SPECTRAL LINE INTERFEROMETRY OF WEAK MACH REFLECTION IN AN IODINE VAPOUR

James Hiron Taylor

June, 1990

A thesis submitted for the degree of Master of Science

of the Australian National University

The contents of this thesis, except where indicated

within the text, are entirely my own work.

ACKNOWLEDGEMENTS

I wish to thank my supervisors, Prof. John Sandeman and Dr. Frank Houwing, for their encouragement and guidance during the course of this work. I would also like to thank Dr. Don Bone for his invaluable assistance with the analysis of the data and general helpfulness in many aspects of the work. Particular thanks to Dr. Frank Houwing, Dr. Will Stefen and Dr. Ian White for reading this thesis and making many useful suggestions and Greg Heath for his help with the colour photography and other graphic work.

I would especially like to thank all my fellow students and able assistants, Toad, Phil, Tim, Wie, Darren, Charles, Trackless etc. and the workshop lads, Graham, David, Macca, Paul, Ian, Brett and Nigel for their help and humour during the long time it has taken to complete this course.

Above all, I wish to thank my family for their support and my wife Karen for her constant cheerfulness, encouragement and help with late night data gathering and the typing of this thesis.

ABSTRACT

Information regarding weak Mach reflection obtained from flow visualization using normal interferometric techniques is limited in resolution by the small fringe shifts produced by the density changes in the flow. Spectral line interferometry causes a greater fringe shift for the same flow conditions, due to the effect known as anomalous dispersion.

An experiment is described where spectral line interferometry in an iodine vapour was used in an attempt to produce interferograms with enhanced fringe shifts across the reflected shock for weak Mach reflection. Successive shots at different detuning from line centre, for a number of iodine spectral lines in the visible, were taken and no overall enhancement effect was observed. Fringe shift enhancement was seen in one particular instance; however, no connection between enhancement and detuning could be shown.

Fringe counting techniques were also used to compare theoretical fringe shifts due to detuning with fringe shifts observed experimentally. The theoretical results obtained agree with the experiment and confirm that the number density of molecular iodine used in the shock tube was too small to produce enhancement of the fringe shifts across the reflected shock.

SPECTRAL LINE INTERFEROMETRY OF WEAK MACH REFLECTION IN AN IODINE VAPOUR

TABLE OF CONTENTS

1. INTRODUCTION

The shock reflection process known as Mach reflection has generated much interest since it was first discovered by Ernst Mach in 1878. Systematic investigation of the shock reflection process, both theoretical and experimental, began in the early forties and is still continuing today. Results that form the foundation of our current knowledge include, among others, the theoretical work of von Neumann (1943), the experimental and theoretical work of the group associated with Bleakney at Princeton (e.g. Bleakney & Taub 1949, Smith 1945); the work of Courant & Friederichs (1948), Liepmann & Roshko (1957) and Landau & Lifshitz (1959); the experiments of Kawamura & Saito (1956), Smith (1959) and Bryson & Gross (1961); the studies by Law & Glass (1971), Ben-Dor & Glass (1979, 1980); the results of Henderson & Lozzi (1975, 1979), Henderson & Gray (1981), Hornung & Kychakoff (1977) and Hornung *et al.* (1979).

The failure of regular reflection for strong shocks in steady and pseudo-steady inviscid flow is now reasonably well understood. However, some questions still remain to be answered, especially in the case of weak Mach reflection, where the effect of downstream conditions on the reflection process is still unclear. It was hoped that this experiment would contribute in some way to the further understanding of the processes involved in weak Mach reflection.

For strong shocks in steady flow, the transition from regular reflection (RR) to Mach reflection (MR) occurs at the mechanical equilibrium/von Neumann criterion (Hornung and Robinson, 1982). For weak shocks the transition occurs at the detachment criterion (Hornung, 1986). Three-shock theory correctly predicts the transition angle for strong shocks and all shock angles for both strong and weak shocks after transition. Two-shock theory predicts all shock angles for both strong and weak shocks up to transition and the transition angle for weak shocks (Bazhenova *et al.*, 1984). In pseudo-steady flow for both strong and weak shocks, the transition from regular to Mach reflection occurs at the detachment criterion (Hornung, 1986). Two-shock theory accurately predicts the transition angle and the shock angles up to

the point of transition, for both strong and weak shocks, but three-shock theory accounts only for the shock angles after transition for strong shocks. For weak shocks, the experimental results for the shock angles deviate from those predicted by three-shock theory (Bazhenova *et al.*, 1984). This is commonly referred to as the "von Neumann" or "Mach" paradox.

Attempts have been made previously to overcome these problems by modifying the von Neumann theory, introducing a microstructure into the region about the triple point using Prandtl-Meyer expansion waves (Bargmann and Montegomery, 1945; Gurderly, 1947) or the inclusion of viscous effects (Sternberg, 1959). No correlation has been achieved with the experimental data using these more complex versions of the basic theory. Also experimental limitations due to conventional interferometric techniques may be contributing to the problem, since unresolvable flow effects could be occurring in the region about the triple point. To address this problem it was decided to use an interferometric technique known as "spectral line interferometry" that produces enhanced fringe shifts for a given density change in the flow when compared to conventional interferometric methods.

The experimental study of weak Mach reflection using flow visualization techniques presents a challenge, since by definition the incident shock is weak and therefore the reflected shock is even weaker. The resultant density changes in the flow due to the reflected shock are, as a consequence, very small. This means that the resolution of the reflected shock and therefore the triple point is limited.

Techniques involving refractivity near a spectral line have obvious advantages over those that assume a constant refractive index for the medium. Anomalous dispersion is the historical name given to the variation of the refractive index about a spectral line. The refractive index increases as the detuning from the spectral line is reduced and it is greater on the long wavelength side than the short wavelength side. The phenomenon was discovered in substances such as the dye Fuchsin and iodine vapour, materials that possess absorption bands in the visible region of the spectrum.

One interferometric technique that utilizes anomalous dispersion is spectral line

interferometry, which was first proposed by Measures (1970) and calls for the use of a narrow band light source tuned to a frequency near that of a selected spectral line. For a gas near an absorption line ν_0, the refractive index n, is given by (Thorne, 1974)

$$n-1=\frac{N.e^2}{16\pi^2\varepsilon_0 m\nu_0}\times\frac{\nu_0-\nu}{(\nu_0-\nu)^2+\left(\frac{\gamma}{4\pi}\right)^2} \qquad (1.1)$$

where N is the number of electron oscillators per unit volume; e is the charge of an electron; ε_0 is the permittivity of free space; m is the electron mass; ν is the frequency and γ is the damping coefficient.

From the above equation, it can be seen that the refractive index will increase as the frequency ν nears the line centre ν_0, since the squared term in the denominator is approaching zero faster than the linear term in the numerator. At line centre, the refractive index is zero. (See figure 1.1.)

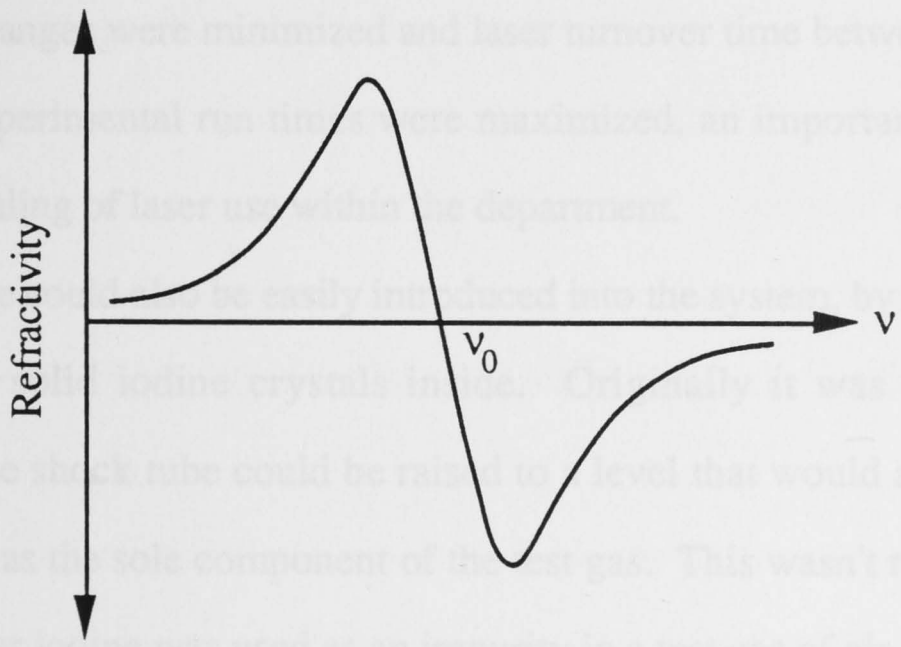

FIGURE 1.1 The refractive index profile about a transition line in a gas.

Application of the technique has been limited experimentally due to a number of strict conditions on the bandwidth and wavelength of the light source. Complications also arise due to the tradeoff between fringe visibility and system sensitivity. Line profile variations can be allowed for in the analysis. Many atomic and molecular systems contain transition lines with linewidths of the order 1.0 - 1.5 GHz. This

requires, for maximum sensitivity of the system, detunings within ~ 1.0 GHz of line centre and for fringe visibility, light source bandwidths much smaller than the detuning. The development of c.w. dye lasers tunable over a great proportion of the visible spectrum and possessing bandwidths of about 1 MHz have solved the inherent problems associated with the technique. Similarly, inexpensive but highly accurate wavemeters are now available that allow the measurement of laser wavelengths to extremely high precision, improving the efficiency of the technique even further.

Molecular iodine was chosen as the test gas principally for the reason already stated above: a multitude of transition lines exist in the visible region of the spectrum (at room temperature), any number of which lie close to the optimum operating wavelength of the laser dye Rhodamine 6G. The reason for selecting transition lines in the spectral region easily covered by the Rhodamine 6G dye was that this dye was being used by the majority of other experiments being conducted in the laboratory at the time of this experiment. Also, the dye is very stable and possesses a long lifetime. This meant dye changes were minimized and laser turnover time between experiments was minimal. Experimental run times were maximized, an important consideration due to tight scheduling of laser use within the department.

Molecular iodine could also be easily introduced into the system, by heating the tube and then placing solid iodine crystals inside. Originally it was hoped that gas temperatures in the shock tube could be raised to a level that would allow the iodine vapour to be used as the sole component of the test gas. This wasn't realized and as a result the molecular iodine was used as an impurity in a test gas of air. This overcame one possibly insurmountable problem, that of low incident shock speed. Low iodine vapour pressures combined with iodine's high molecular weight would have made it extremely difficult to obtain low Mach numbers in the range $1.1 < M_1 < 1.4$, the accepted Mach number interval for the incident shock to produce weak shock reflection. Dissociation of the iodine didn't pose a problem due to the relatively low temperatures generated behind the incident and reflected shocks for this experiment. An upper limit for the gas temperature behind the reflected shock at the operating

conditions used was ~ 800 K. This corresponded to a dissociation percentage for the iodine of ~ 0.3 %.

The purpose of this work was to determine whether spectral line interferometry would produce enhanced fringe shifts under experimental conditions conducive to weak Mach reflection and so provide data on the region about the triple point unaffected by the resolvability limitations of conventional interferometric techniques. A number of shots were completed at different laser detunings from selected iodine spectral lines, with the intention of providing data on the most favourable wavelength location (spectrally) for fringe shift enhancement to occur. Determination of the fringe shift enhancement was made using the fringe shift across the reflected shock.

It was then the intent of the author to obtain comprehensive interferograms of the triple point region using the spectral line interferometric technique at its greatest sensitivity. To this end a 10° wedge was used from the outset of the experiment to produce an extended Mach stem that would allow the region about the triple point to be well clear of any fringe disturbances due to wall effects.

Near the completion of the time allowed for the experiment, it was determined that the enhancement effects due to spectral line interferometry were smaller than had been expected. Absorption and refractive index scans were then attempted to provide an explanation for the results observed for weak Mach reflection in the flow visualization shots.

The following chapters detail the various processes of the investigation. Shock reflection processes are discussed in Chapter 2 assuming inviscid flow. The main emphasis of this experiment is dealing with weak shock reflection, so vibrational and chemical relaxation effects have been ignored as well as viscosity and heat conduction. Laser and molecular spectroscopy are reviewed in Chapters 3 and 4. Chapter 5 describes the experimental apparatus and arrangements used while Chapter 6 provides the theory necessary for the reduction of the experimental data. The results are presented in Chapter 7 and discussed in Chapter 8. Conclusions are drawn in Chapter 9.

2. SHOCK REFLECTION

2.1 The Shock-Jump Relations

An oblique shock may be treated in the same way as a normal shock using the equations of motion if an additional component of velocity is taken into account. If a uniform velocity v is superimposed on the flow field of a normal shock, the resultant velocity ahead of the shock may be adjusted to any direction by varying the magnitude and direction of v. When v is taken to be parallel to the shock (see figure 2.1a), the resultant velocity in front of the shock is $q_1 = \sqrt{u_1^2 + v^2}$ and its angle to the shock is $\alpha = \tan^{-1}(u_1 / v)$. The value of u_2 is always less than u_1 and v is unchanged, so the angle of the flow after the shock is different to that before and the flow turns towards the shock. The angle θ is defined as positive according to figure 2.1b. In figure 2.1b, the flow of figure 2.1a has been rotated so that the initial flow direction is more conventionally aligned.

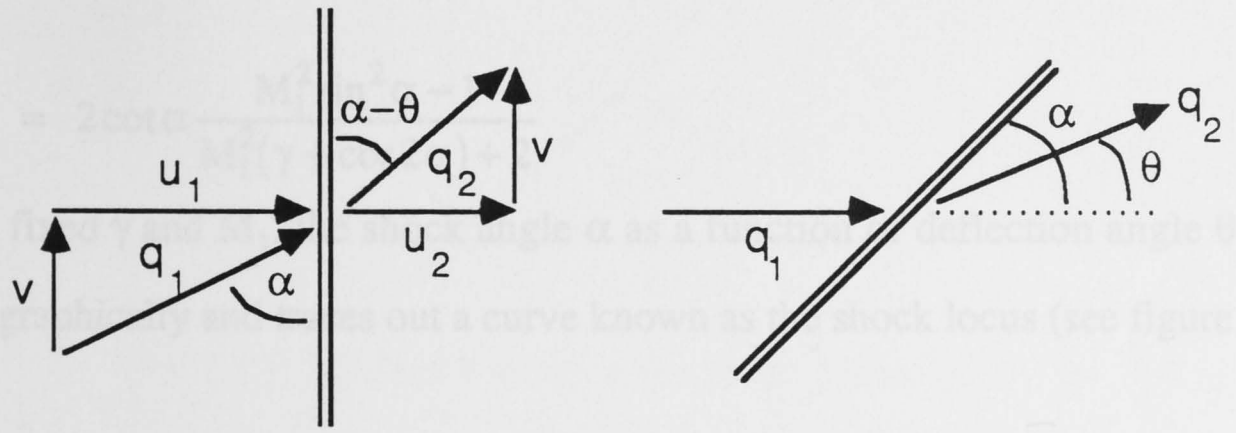

(a) Resolution of velocity components (b) Conventional nomenclature

FIGURE 2.1 Flow through an oblique shock wave.
q is the magnitude of the flow velocity; u and v are the velocity components perpendicular and parallel to the shock respectively; α is the shock angle and θ is the flow deflection angle. The subscripts 1 and 2 denote conditions before and after the shock respectively.

In steady flow through an oblique shock, the downstream conditions (subscript 2) of density ρ, pressure p and temperature T can be related to the upstream conditions (subscript 1) of density and pressure according to Leipmann & Roshko (1957) by the

Rankine-Hugoniot shock jump condition,

$$\frac{\rho_2}{\rho_1} = \frac{(\gamma+1)M_1^2\sin^2\alpha}{(\gamma-1)M_1^2\sin^2\alpha+2} \tag{2.1}$$

$$\frac{p_2}{p_1} = \frac{2\gamma}{(\gamma+1)}\left(M_1^2\sin^2\alpha - 1\right)+1 \tag{2.2}$$

$$\left(\frac{T_2}{T_1}\right)=\frac{a_2^2}{a_1^2}=1+\frac{2(\gamma-1)}{(\gamma+1)^2}\frac{M_1^2\sin^2\alpha-1}{M_1^2\sin^2\alpha}\left(\gamma\ M_1^2\sin^2\alpha+1\right) \tag{2.3}$$

where a is the sound speed of the gas; γ is the ratio of the specific heats of the gas; M_1 is the incident shock Mach number and α is the shock angle.

The relationships between the downstream Mach number M_2, the flow deflection angle θ and the shock angle α, are given by

$$M_2^2\sin^2(\alpha-\theta) = \frac{1+\left(\frac{\gamma-1}{2}\right)M_1^2\sin^2\alpha}{\gamma\ M_1^2\sin^2\alpha-\left(\frac{\gamma-1}{2}\right)} \tag{2.4}$$

$$\tan\theta = 2\cot\alpha\frac{M_1^2\sin^2\alpha-1}{M_1^2(\gamma+\cos2\alpha)+2} \tag{2.5}$$

For a fixed γ and M_1, the shock angle α as a function of deflection angle θ can be plotted graphically and traces out a curve known as the shock locus (see figure 2.2).

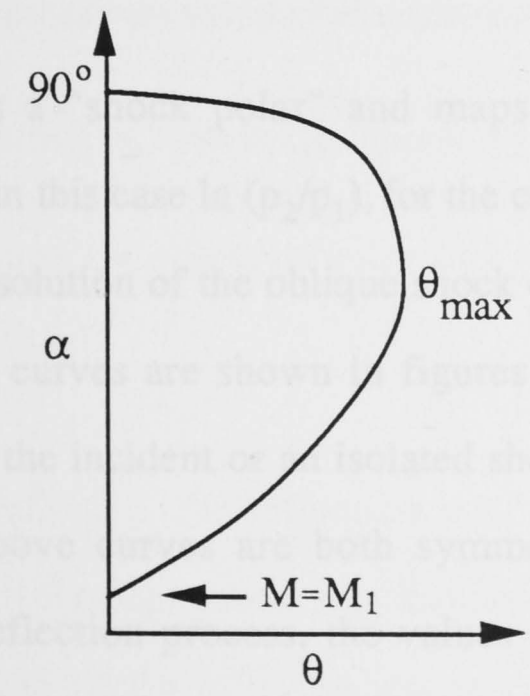

FIGURE 2.2 Shock locus in the (θ , α) plane.

From figure 2.2, as α increases from arcsin $(1/M_1)$, M_2 decreases from a maximum value of M_1 to a value of 1 (the sonic point) just before θ reaches its maximum deflection value θ_{max}. As α increases further, both M_2 and θ decrease until $\theta = 0$ and $\alpha = \pi / 2$, corresponding to a normal shock.

The dependence of p_2 on θ may be found for fixed γ and M_1 if α is eliminated from equations 2.1 and 2.2. Again the solution of the equations can be considered graphically and the result is shown in figure 2.3.

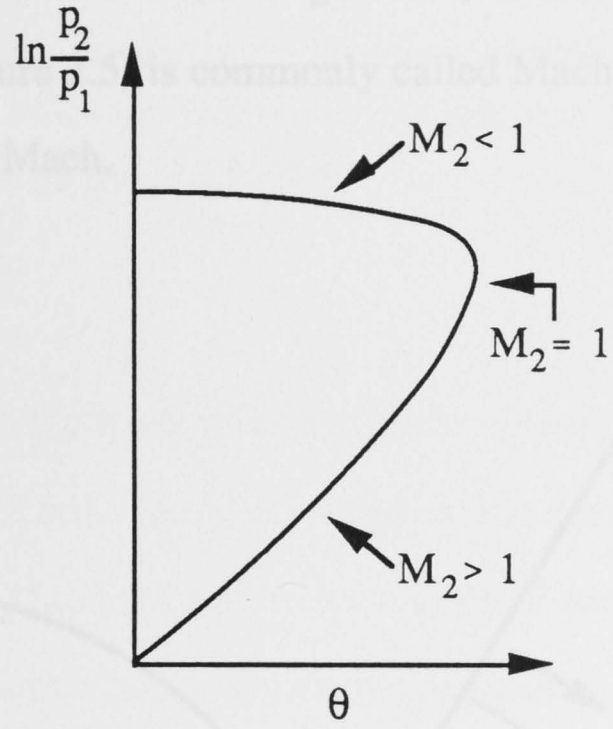

FIGURE 2.3 Shock locus in the (p, θ) plane.

This curve is known as a "shock polar" and maps out all possible values of downstream pressure, or in this case ln (p_2/p_1), for the corresponding flow deflection angle θ according to the solution of the oblique shock equations. Only the positive branch of the respective curves are shown in figures 2.1 and 2.2, since the flow deflection angle through the incident or an isolated shock is always positive in the physical plane. The above curves are both symmetrical about $\theta = 0$. When considering the shock reflection process, the values of the downstream pressure behind both the incident and reflected shocks can be determined graphically from the

solution of the Rankine-Hugoniot shock jump condition using shock polars. The incident shock polar is located about the origin with its base at zero, as in figure 2.3, whereas the base of the reflected shock polar is located at some point on the incident shock polar between the zero and maximum deflection angles of θ as seen in figure 2.7b.

2.2 The Reflection Process and Shock Configurations

When a shock wave propagates along a flat surface that contains a single stationary disturbance (e.g. the apex of a wedge), there are two resultant shock reflection configurations possible. The first (see figure 2.4) is known as regular reflection (RR), the second (see figure 2.5) is commonly called Mach reflection (MR) since it was first studied by Ernst Mach.

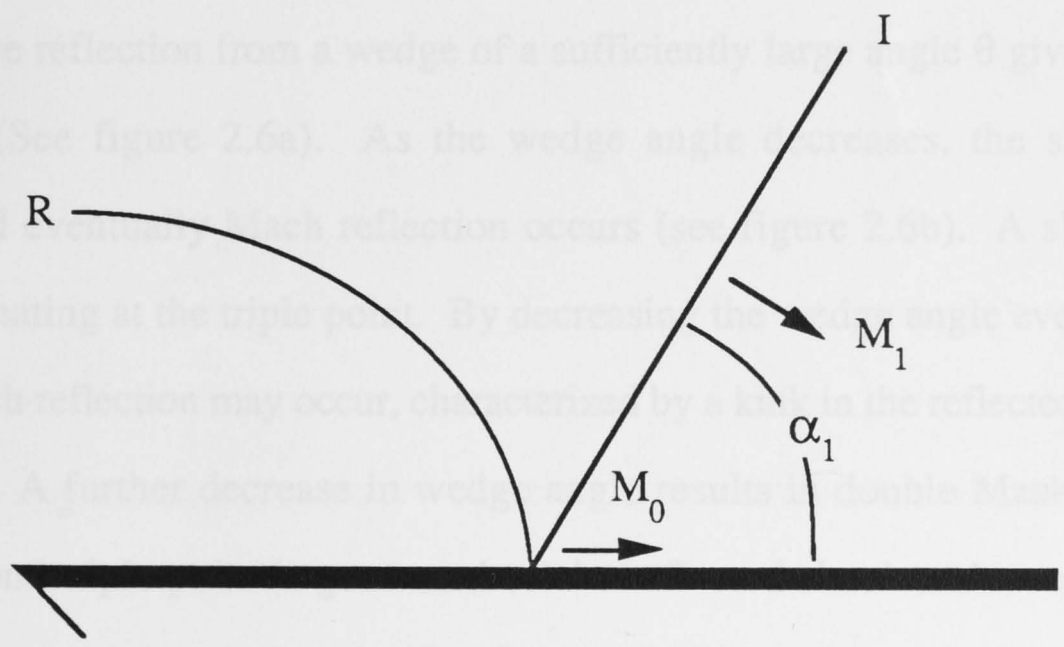

FIGURE 2.4 Regular reflection as seen in the laboratory frame of reference, where I is the incident shock; R is the reflected shock and M_0 is the Mach number of the reflection point with $M_0 = M_1 \sin\alpha$.

When a shock wave is reflected, the reflection configuration (i.e. RR or MR) is determined by the: incident shock angle α_1; incident shock Mach number M_1; specific heat ratio of the shocked gas γ and the Reynolds number of the flow Re.

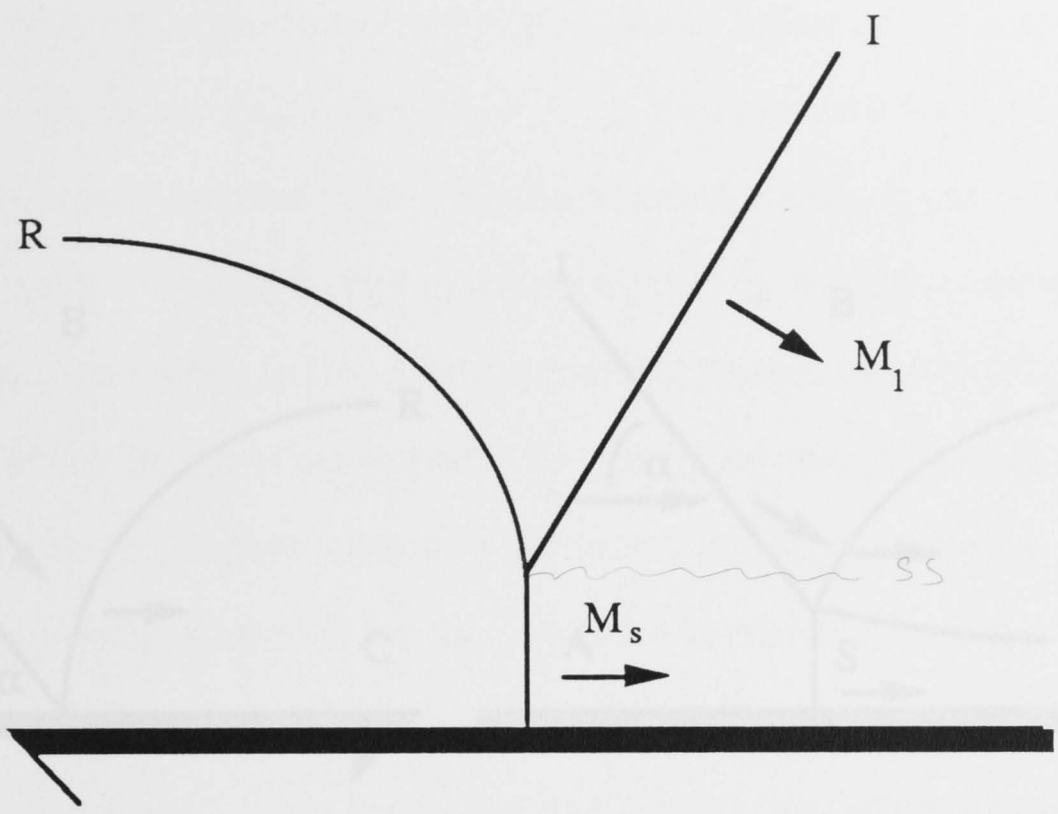

FIGURE 2.5 Mach reflection as seen in the laboratory frame of reference, with M_1 the Mach number of the incident shock and M_s the Mach number of the Mach stem.

Shock wave reflection from a wedge of a sufficiently large angle θ gives a regular reflection. (See figure 2.6a). As the wedge angle decreases, the shock angle increases and eventually Mach reflection occurs (see figure 2.6b). A slipstream is present originating at the triple point. By decreasing the wedge angle even further, a complex Mach reflection may occur, characterized by a kink in the reflected shock (see figure 2.6c). A further decrease in wedge angle results in double Mach reflection, where a second triple point is generated on the reflected shock and a second shock wave and slipstream are produced. (See figure 2.6d.)

Shock reflections in the laboratory have been studied in two ways. The first method is to study the effect in a steady flow. When a wedge is placed in a supersonic wind tunnel, it will interact with the flow (see figures 2.7 and 2.8) to produce a bow shock, which can then be made to strike a surface producing RR or MR. Such a configuration causes a stationary reflection pattern that can be studied over an extended period of time. In figure 2.7a, the incident shock I (the bow shock) deflects the flow through an angle θ_1 and the reflected shock R deflects the flow back

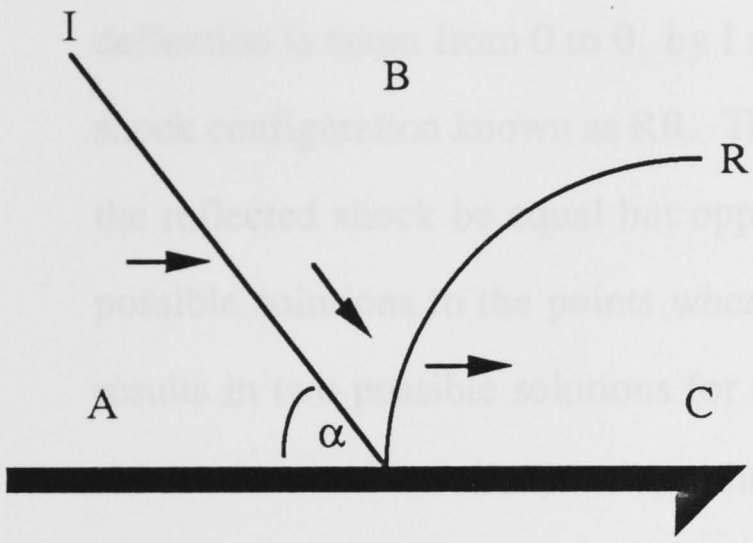

(a) Regular Reflection (RR)

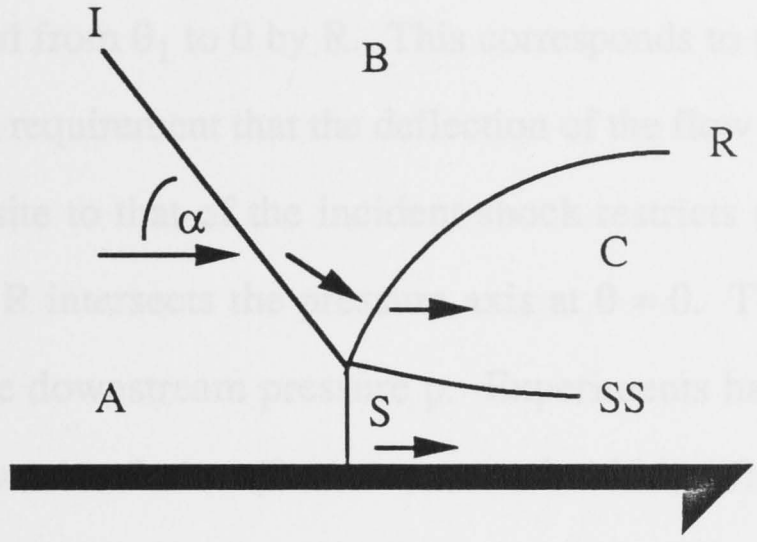

(b) Simple Mach Reflection (SMR)

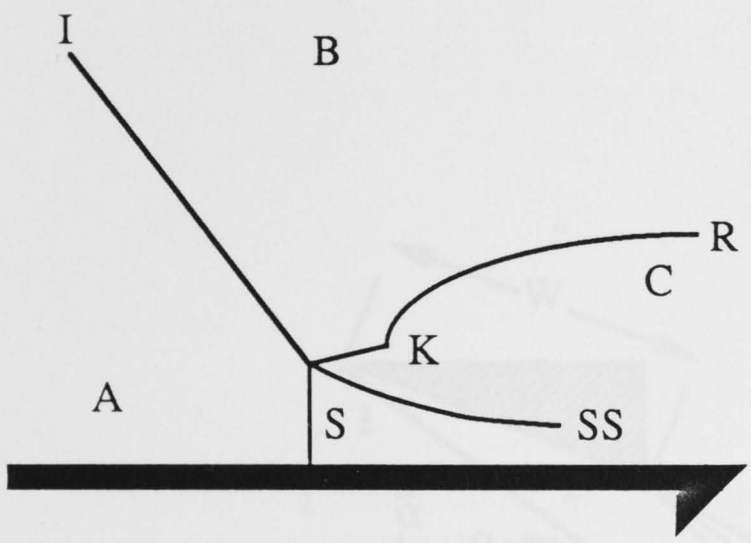

(c) Complex Mach Reflection (CMR)

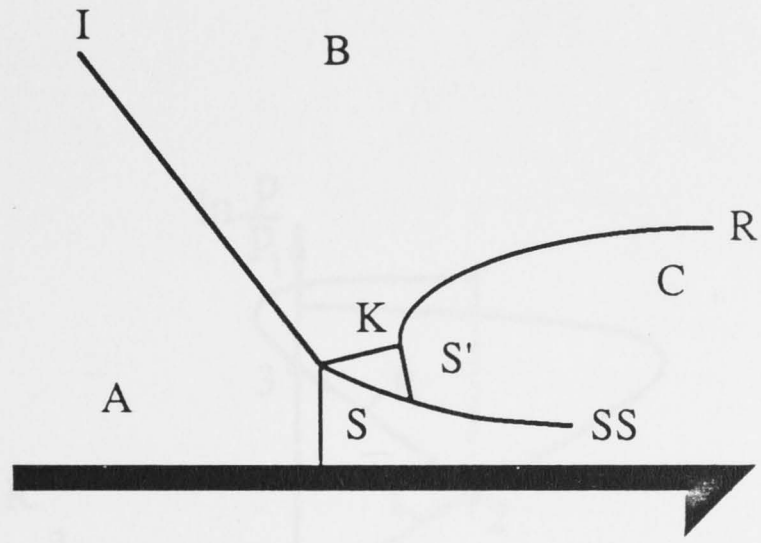

(d) Double Mach Reflection (DMR)

Figure 2.6 Shock Configurations

I = Incident shock
R = Reflected shock
S = Mach stem
K = Kink
SS = Slipstream
S' = Mach stem

to $\theta_2 = 0$. This can be represented in the (p,θ) plane (figure 2.7b). Region 2 lies on the shock locus I, in the area below $M_2 = 1$. A second shock locus is drawn ($M = M_2$) originating from the point (p_2,θ_2) for the reflected shock. It can be seen that the deflection is taken from 0 to θ_1 by I and from θ_1 to 0 by R. This corresponds to the shock configuration known as RR. The requirement that the deflection of the flow by the reflected shock be equal but opposite to that of the incident shock restricts the possible solutions to the points where R intersects the pressure axis at $\theta = 0$. This results in two possible solutions for the downstream pressure p. Experiments have shown that the flow always adopts the weak solution (Bazhenova *et al.*, 1984). Thus for RR, a solution always exists for all angles of initial flow deflection for which the reflected shock polar intersects the zero deflection axis (that is, for all values of $\theta < \theta_d$ where θ_d is the wedge angle for which the reflected shock polar is tangent to the pressure axis).

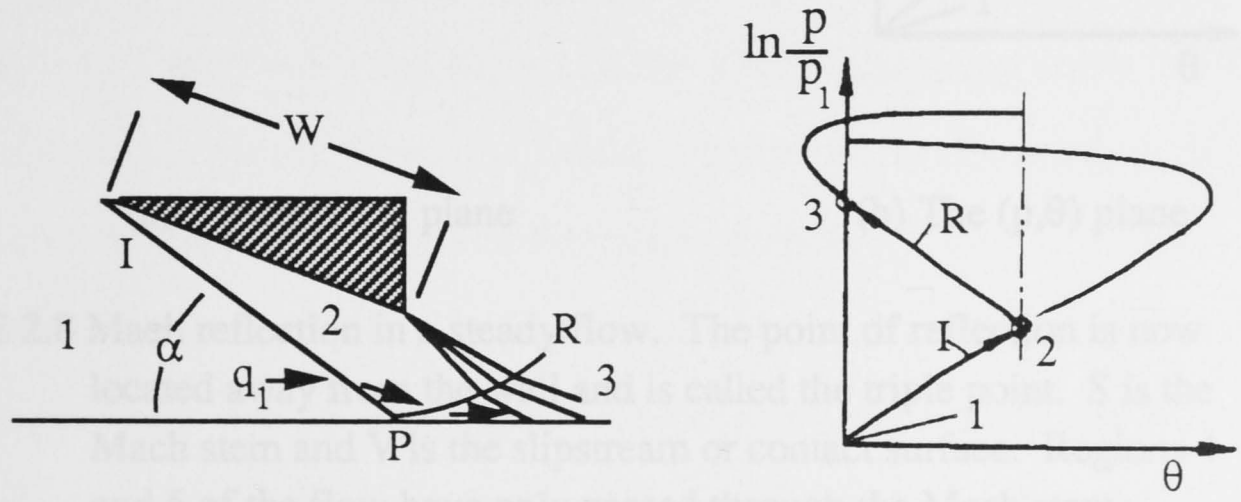

(a) The physical plane (b) The (p,θ) plane

FIGURE 2.7 Regular reflection in a steady flow. I is the incident shock originating at the wedge tip (W is the wedge face); P is the point of reflection; R is the reflected shock and q_1 is the initial flow velocity. The numbers 1, 2 and 3 refer to the pre-shocked, singly shocked and doubly shocked regions of the flow respectively. A Prandtl-Meyer expansion fan is present at the trailing edge of the wedge.

If the incident shock angle α is increased, a critical value is reached, $\alpha = \alpha_d$, beyond which the reflected shock locus R no longer intersects the pressure axis in the (p,θ) plane (see figure 2.8b). The initial flow passes obliquely through the incident shock and is deflected by an angle θ_1. The flow is then redeflected by the reflected shock to an angle $\theta_2 > 0$. (See figure 2.8a) In this situation the flow in region 3 is not parallel to the wall (Hornung, 1986). This requires a nonuniform region across which the transition from $\theta > 0$ to $\theta = 0$ can be accomplished. A near normal shock allows the reflection point P to move off the wall, resulting in a discontinuity forming in the flow (a slipstream or contact surface originating from the reflection point).

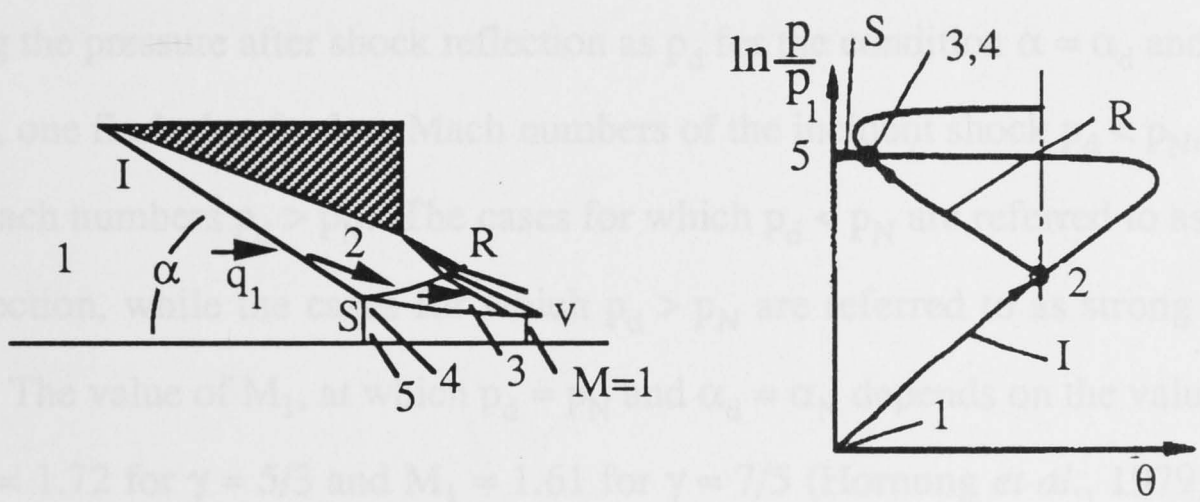

(a) The physical plane (b) The (p,θ) plane

FIGURE 2.8 Mach reflection in a steady flow. The point of reflection is now located away from the wall and is called the triple point. S is the Mach stem and V is the slipstream or contact surface. Regions 4 and 5 of the flow have only passed through the Mach stem.

The gases on either side of the contact surface have different velocities since the gas above the contact surface has been processed by I and R and the gas below has only passed through the normal shock S (Hornung, 1986). Density and entropy differ across the contact surface but the pressure and flow deflection are identical. If the initial flow passing through S is deflected through an angle θ_3, then $\theta_3 = \theta_4$. This

means that the plots of the points representing regions 3 and 4 in the (p,θ) plane (see figure 2.8b) are identical. Therefore, the upper intersection of the reflected shock polar R with the incident shock polar I determines the condition of the intersection of the reflected shock and Mach stem in the physical plane. The "Mach stem" S is represented by the incident shock polar between the points 4 and 5 and is curved as a consequence.

Although RR is not possible for $\alpha > \alpha_d$, MR can occur before the condition $\alpha = \alpha_d$ is reached for a particular class of flows. If one considers the conditions for which MR is possible, it is found that MR cannot occur if $\alpha < \alpha_N$ where α_N is that angle for which I and R intersect on the pressure axis (Hornung *et al.*, 1979). This is known as the von Neumann criterion.

Denoting the pressure after shock reflection as p_d for the condition $\alpha = \alpha_d$ and as p_N for $\alpha = \alpha_N$, one finds that for low Mach numbers of the incident shock $p_d < p_N$, while for high Mach numbers $p_d > p_N$. The cases for which $p_d < p_N$ are referred to as weak shock reflection, while the cases for which $p_d > p_N$ are referred to as strong shock reflection. The value of M_1, at which $p_d = p_N$ and $\alpha_d = \alpha_N$ depends on the value of γ, and is $M_1 = 1.72$ for $\gamma = 5/3$ and $M_1 = 1.61$ for $\gamma = 7/5$ (Hornung *et al.*, 1979). For strong reflection in steady flow, it is found experimentally (Hornung *et al.*, 1979) that transition to MR occurs at the von Neumann criterion.

The second method of study is in unsteady or nonstationary flow, where the reflection process is studied using a shock tube or similar device. In this situation the shock reflection phenomena last only for a fraction of a millisecond and are thus more difficult to describe theoretically.

When a shock wave moving with a velocity q_s strikes a rigid wall at an angle α (that is sufficiently small), it exhibits RR as shown figure 2.9a. The incident shock has a Mach number M_s. By imposing a velocity equal and opposite to that of the reflection point on the system, $q_1 = q_s/\sin\alpha$ (see figure 2.9b), the shocks can be brought to rest in a frame of reference similar to that for steady flow. (In the laboratory frame, the reflection point P moves up the wedge at a constant velocity.) By imposing this

velocity on the system, we can observe the flow as seen in the reference frame fixed with respect to P. In this "pseudo-steady" frame of reference, there is an oblique gas flow moving through I with the gas being deflected through an angle θ_1 with a component of this flow directed towards the reflecting surface. The flow through R is deflected back through some angle, equal but opposite to the original deflection angle θ_1, (i.e. $\theta_2 = 0$) and the flow is redirected back parallel to the reflecting surface.

The presence of only one length scale in the interaction between a shock of finite strength and a flat infinite wedge allows the problem to be treated using self-similarity (von Neumann, 1943). The shock configuration remains constant (i.e. the angles between the shocks and the wedge are unchanged) but d, the distance from the corner to the reflection point, grows linearly with time from the instant the shock strikes the leading edge of the wedge (i.e. the reflected shock is increasing in length). (See figure 2.9c)

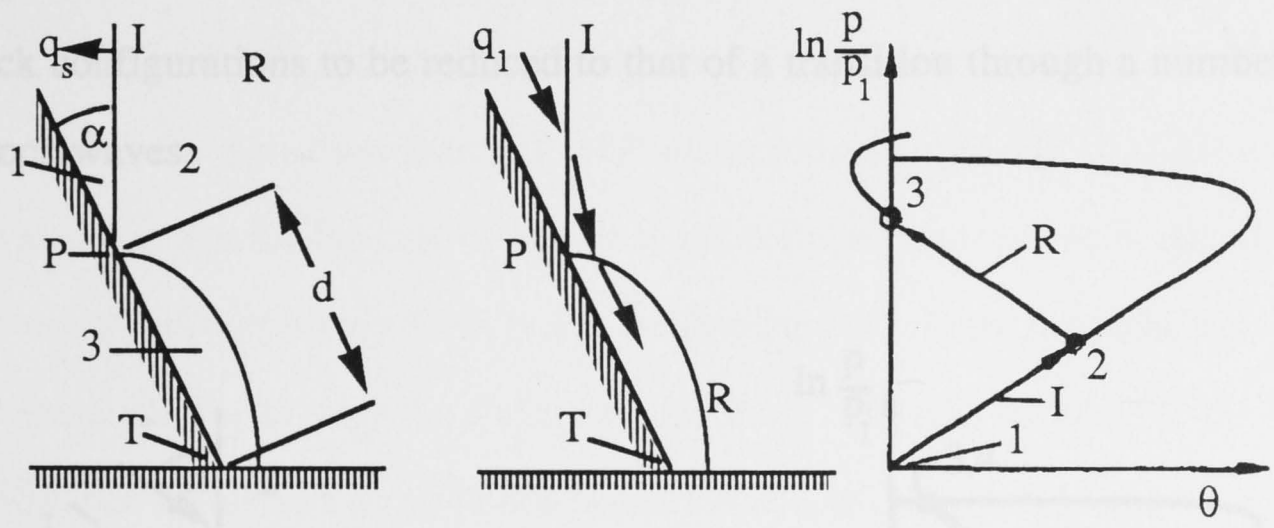

(a) The physical plane (b) The shock frame (c) The (p,θ) plane

FIGURE 2.9 Regular reflection in a "pseudo-steady" flow. T is the corner or wedge tip and d is the distance from the wedge tip to the reflection point

It is therefore possible to attach an inertial frame of reference to the interaction point between the shock and the wedge in the case of RR. Thus, the "pseudo-steady" flow can be considered to be steady about the reflection point P and $M_0 = M_s/\sin\alpha$, where

M_s is the incident shock Mach number ($M_s = q_s/a$ with a being the speed of sound in the unshocked gas). The (p,θ) plane is used again to describe the reflection system and determine the transition criteria. For strong shock reflection in pseudo-steady flow, it is found that RR persists beyond the von Neumann criterion with transition occurring very close to the detachment criterion (Hornung, 1986).

That is, the transition appears to occur when the shock locus R fails to intersect the p-axis. (See figure 2.10.) The triple point P is no longer located on the wedge and moves with a constant velocity q_s, at a constant angle to the surface defined by (Bazhenova *et al.*, 1984),

$$\chi = \tan^{-1} [(a_1 / q_s)^2 - (q_1 / q_s)^2]^{1/2} \qquad (2.6)$$

A contact surface is formed in the flow, the gases on either side of which have different velocities (the gas above the contact surface has been processed by I and R whereas the gas below has only passed through S). The density and entropy differ across the contact surface but the pressure and flow deflection are identical. The "localizing" of the flow region about the triple point in MR allows the treatment of the three shock configurations to be reduced to that of a transition through a number of steady shock waves.

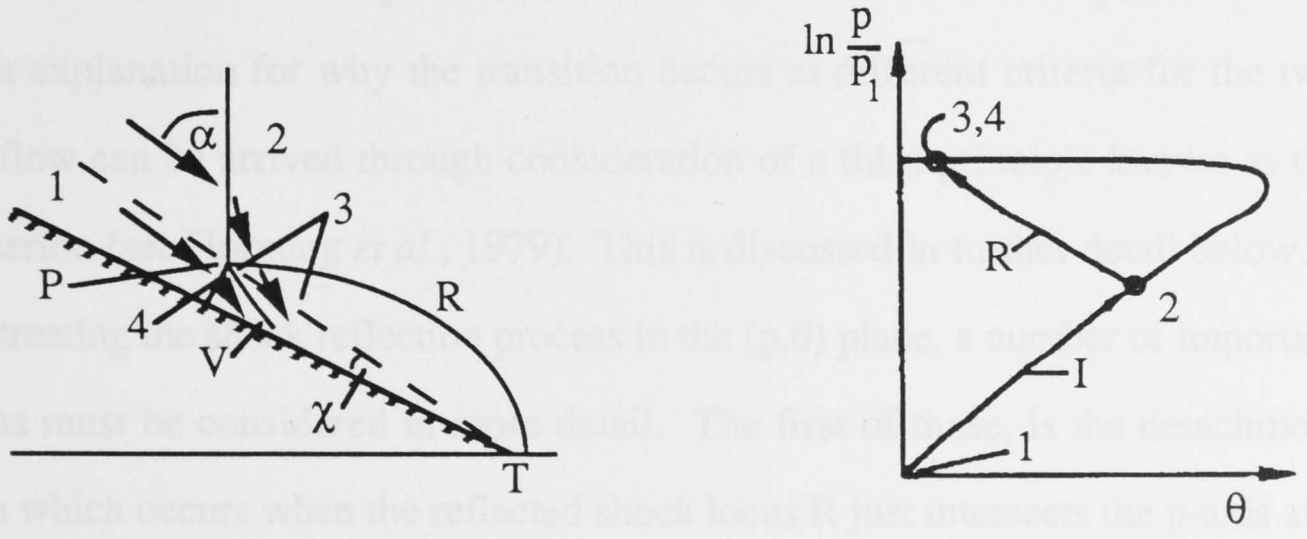

(a) The shock frame (b) The (p,θ) plane

FIGURE 2.10 Mach reflection in a "pseudo-steady" flow. All shocks are joined at the triple point P. V is the slipstream or contact surface, A is the point of contact between the Mach stem and the wedge surface and χ is the angle between the triple point path and the wedge surface.

When the triple point is located adjacent to the wall, the boundary conditions at the wall have to be satisfied and the problem simplifies to the two-shock theory of RR. If the triple point is not adjacent to the wall, the conditions there can only be solved using three-shock theory. The orientation of the triple point configuration is defined relative to the wall (as in equation 2.6) but if this value is unknown then a further condition is necessary, that the Mach stem is straight and normal to the wedge. This is known as the Elementary Theory of Mach Reflection (ETMR). This local treatment of the problem of shock reflection was introduced by von Neumann (1943), and has been developed and extended by many people since.

Thus, the local treatment of shock interactions allows information to be obtained about the flow conditions such as pressure, density etc, behind each shock and the shock angles relative to each other and to some frame of reference (such as the wedge in the case of RR or the path of the triple point in the case of MR). Also, the transition criteria for RR-MR transitions can be determined.

2.3 The Transition from Regular to Mach Reflection

The conditions for transition from RR-MR were discussed briefly in section 2.2, where it was noted that for the case of strong shock reflection, transition occurs at the von Neumann criteria for steady flow, but at the detachment criteria for pseudo-steady flow. An explanation for why the transition occurs at different criteria for the two types of flow can be arrived through consideration of a third principle known as the sonic criterion (see Hornung *et al.*, 1979). This is discussed in further detail below.

When treating the shock reflection process in the (p,θ) plane, a number of important conditions must be considered in more detail. The first of these, is the detachment condition which occurs when the reflected shock locus R just intersects the p-axis at a tangent,

$$\alpha = \alpha_d\,(M_1, \gamma). \qquad (2.7)$$

The pressure at the tangent point may lie above or below the normal-shock value depending on the strength of the reflected shock. The shock reflection is referred to as

"strong" if the pressure at the tangent point is larger than the normal shock value and "weak" if it is less.

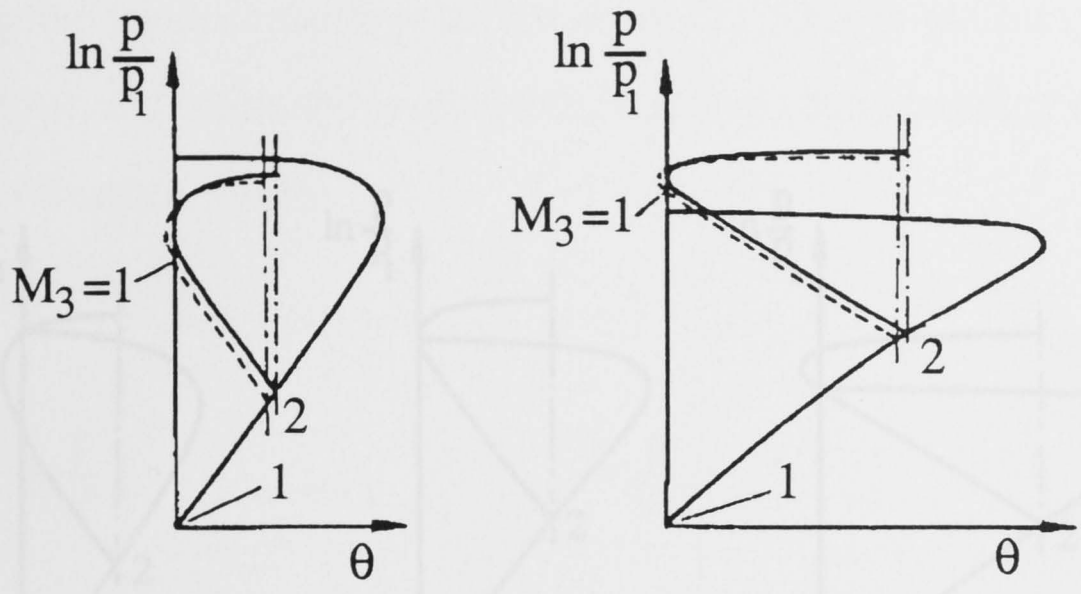

(a) Weak reflection (b) Strong reflection

FIGURE 2.11 The detachment and the sonic conditions in the (p,θ) plane for both weak and strong shock reflections. (The dashed line represents the sonic condition.)

The sonic condition,

$$\alpha = \alpha_s\ (M_1, \gamma), \tag{2.8}$$

occurs when the sonic point of the reflected shock locus intersects the p-axis. This corresponds in the physical plane to the point when transmission of experimental length scales to the reflection point occurs. Both the above conditions in the (p,θ) plane are shown in figure 2.11.

The third important condition is the von Neumann condition which occurs when the reflected shock locus intersects with the normal shock value,

$$\alpha = \alpha_N\ (M_1, \gamma). \tag{2.9}$$

For practical values of γ it is possible that the detachment condition and the von Neumann condition can be equal,

$$\alpha_N\ (M_1, \gamma) = \alpha_d\ (M_1, \gamma). \tag{2.10}$$

This equality is used as the reference point for the determination of shock strength for the shock configuration (i.e. "strong" or "weak" depending on whether the detachment condition is above or below this point (Hornung, 1986) as illustrated in figure 2.12.

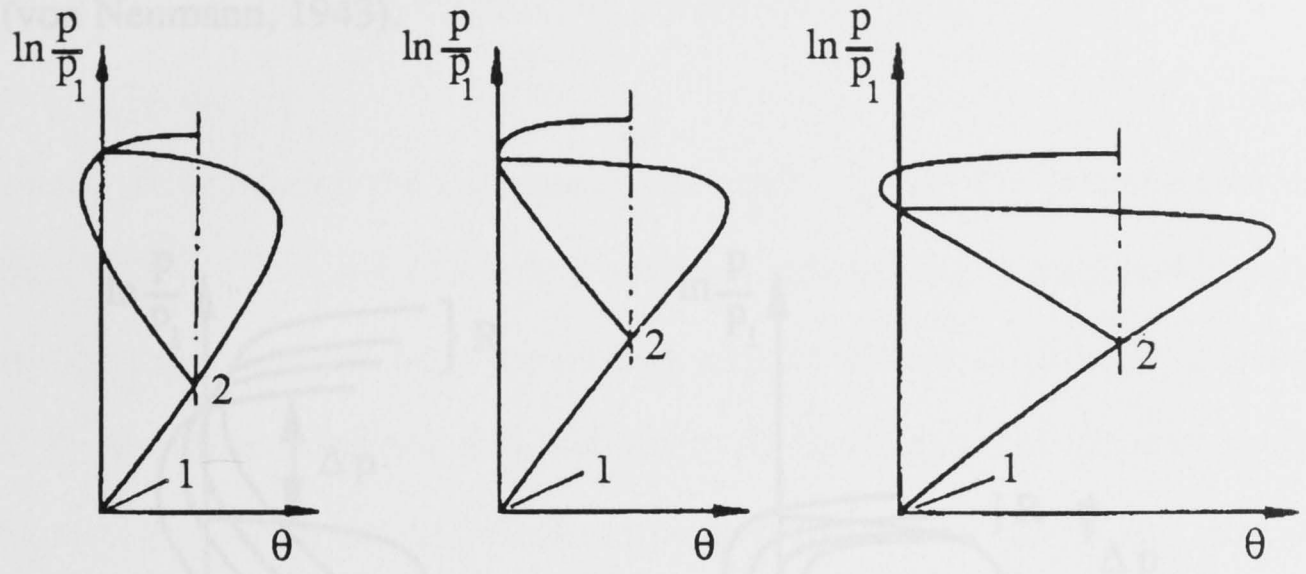

(a) Weak reflection (b) $\alpha_N = \alpha_d$ (c) Strong reflection

FIGURE 2.12 The von Neumann condition in the (p,θ) plane for both weak and strong shock reflection and the point where the von Neumann condition is equal to the detachment condition ($\alpha_N = \alpha_d$).

There are a number of conditions possible where the transition from RR to MR may occur as discussed in section 2.2. They all fall into the region defined by the von Neumann and the detachment criteria,

$$\alpha_N (M_1, \gamma) < \alpha (M_1, \gamma) < \alpha_d (M_1, \gamma) \qquad (2.11)$$

The first possible transition point occurs when the overall flow deflection angle through the incident and the reflected shocks θ_2 is equal to the flow deflection through the Mach stem θ_3, with the limiting condition $\theta_2 = \theta_3 = 0$. This is the minimum angle at which MR can occur and is known as the von Neumann criterion (since this is the predicted angle of transition from three-shock theory) and is denoted by $\alpha_t = \alpha_N$. Henderson and Lozzi (1975) also proposed this criterion and renamed it the

"Mechanical Equilibrium" criterion since no pressure discontinuities exist in the flow during transition if the transition occurs at this condition. The second possible transition point is the detachment condition ($\alpha_t = \alpha_d$), where the reflected shock polar can no longer deflect the flow back through the same angle as it was originally deflected by the incident shock polar (i.e. $\theta_2 \neq 0$). This is the maximum angle possible for RR, and is also the predicted angle of transition according to two-shock theory (von Neumann, 1943).

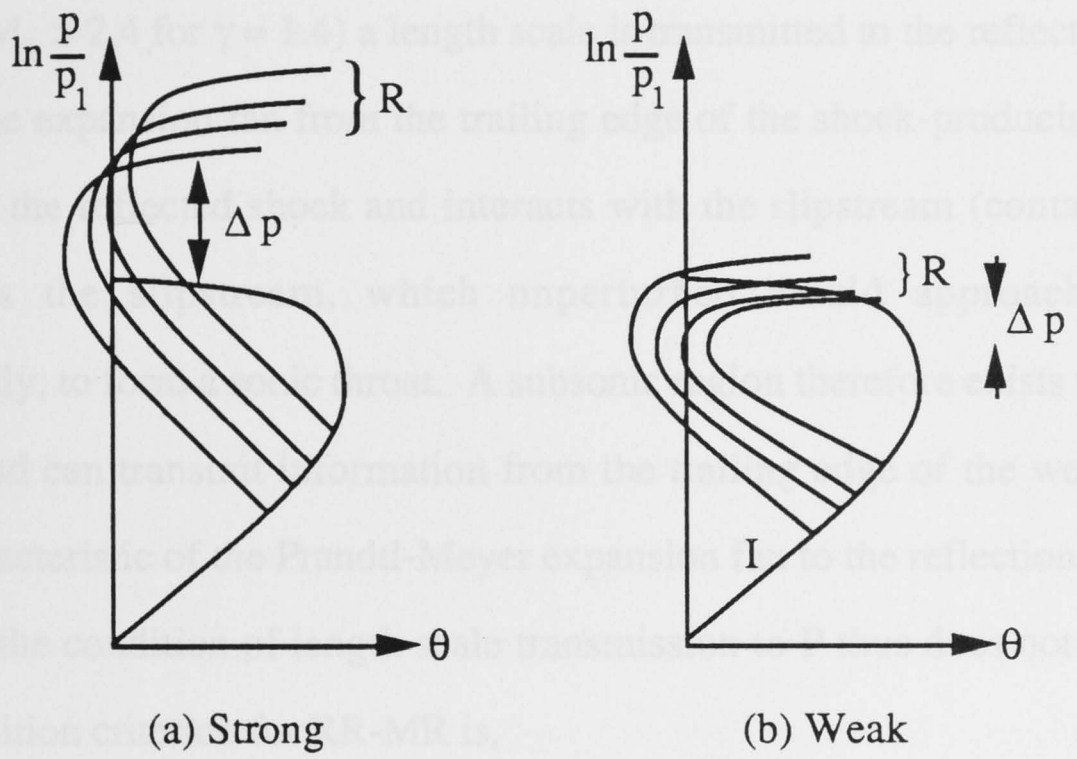

(a) Strong (b) Weak

FIGURE 2.13 Shock polars near transition for both strong and weak shock reflection. Δp is the downstream pressure differential that would occur in the flow during transition from RR to MR according to the detachment criterion.

As α increases, the transition from RR-MR will result in an increase in pressure for weak shock reflection but a decrease in pressure for strong shock reflection according to the detachment criterion as shown in figure 2.13.

An important determining factor in the region of overlap where both RR and MR are theoretically possible is the communication of a length scale to the reflection point P. In the case for RR in pseudo-steady flow (shock reflection of a straight wedge), the

point P is moving at a constant velocity q_1 away from the wedge tip (corner). A compression wave is generated in the flow at the corner as the incident shock passes and travels up the wedge at the local speed of sound relative to the gas. Unless the region behind the reflected shock is subsonic (i.e. $M_3 < 1$, $\alpha > \alpha_{sonic}$), the compression wave will not catch P. Therefore, the region of overlap in the case of pseudo-steady flow is all but eliminated since $\alpha_{sonic} - \alpha_d$ is experimentally unresolvable and the transition criterion for pseudo-steady flow is,

$$\alpha^*_{ps} = \alpha_{sonic} \cong \alpha_{d.} \tag{2.12}$$

For steady flow where the difference between α_N and α_d is experimentally resolvable ($M_1 > 2.4$ for $\gamma = 1.4$) a length scale is transmitted to the reflection point in MR when the expansion fan from the trailing edge of the shock-producing wedge is refracted by the reflected shock and interacts with the slipstream (contact surface). This causes the slipstream, which unperturbed would approach the wall asymptotically, to form a sonic throat. A subsonic region therefore exists upstream of the throat and can transmit information from the trailing edge of the wedge via the leading characteristic of the Prandtl-Meyer expansion fan to the reflection point P. In strong flow the condition of length scale transmission to P thus does not inhibit MR and the transition criterion for RR-MR is,

$$\alpha^*_{st} = \alpha_{N.} \tag{2.13}$$

For the case involving weak shock reflection ($M_1 < 2.4$ for $\gamma = 1.4$) a number of reflection configurations are possible (Hornung, 1986), however for unimpeded flow RR persists up to the detachment condition

$$\alpha = \alpha_d \tag{2.14}$$

2.4 Experimental Studies of Regular and Mach Reflection

As mentioned previously in chapter 1, experimental studies of the shock reflection phenomena were initiated by Ernst Mach (1878) and gained popularity after von Neumann's work. Most of the early work involved weak shocks with shock waves generated by high explosives. As technology improved and the shock tubes became

better, stronger shocks were produced. Complex Mach Reflection, where the flow behind the reflected shock becomes supersonic relative to the triple point, was first observed by Smith (1945). Double Mach Reflection, where the flow behind the reflected shock becomes supersonic relative to the kink as well as the triple point, was discovered by White (1951).

These investigations helped establish a number of facts. For shock reflection by a plane wedge in pseudo-steady flow, it was shown that the path of the triple point had a fixed angle of trajectory. For steady and unsteady flows, the transition angle is different. In steady flow, (for strong shocks) where the shock wave is stationary, attached to a wedge and reflected off either another shock or a wall, the transition occurs at the von Neumann/Mechanical Equilibrium criterion. This is the smallest angle for which Mach reflection can exist and be considered stable. For weak shocks the transition occurs at the detachment criterion. Two-shock theory correctly predicts all shock angles for RR up to the transition point of RR-MR and the transition angle for weak-shock reflection, and three-shock theory accurately determines the shock angles after the transition and the transition angle for strong-shock reflection. Figure 2.14 summarizes the regions where a particular shock reflection configuration exists according to incident Mach number M_1 (for gases with $\gamma = 1.4$) for steady flow.

For pseudo-steady flow, the transition from RR to MR occurs at the detachment criterion, as predicted by two-shock theory. Two-shock theory also accurately predicts all shock angles up to the transition point for both strong and weak shocks but only three-shock theory accounts for the shock angles after the transition for strong shocks. In the case of weak shocks, the difference between the experimental results for the shock reflection angles and those calculated using three-shock theory is known as the "von Neumann" or "Mach" paradox. Figure 2.15 summarizes the regions where a particular shock reflection configuration exists according to incident Mach number M_1 (for gases with $\gamma = 1.4$) for pseudo-steady flow.

Kawamura and Saito (1956) and Sternberg (1959) postulated that the reason for the failure of three-shock theory to correctly predict the shock angles for the Mach

reflection configuration in a pseudo-steady flow for a weak incident shock was that the flow behind the reflected shock is subsonic. This would allow the corner signal from the wedge tip to completely catch the reflected shock resulting in its curvature. If this is so, the MR configuration no longer consisted of three straight shocks and three-shock theory is no longer tenable. They both agreed (within experimental error) that the critical incident Mach number M^*, indicating whether the flow behind the reflected shock was subsonic or supersonic, was $M^* \cong 2.2 - 2.4$. If $M_1 < M^*$, the flow behind the reflected shock was subsonic. When $M_1 > M^*$, the flow behind the reflected shock is supersonic. Therefore, $M^* \cong 2.2 - 2.4$ was the critical Mach number for the valid application of three-shock theory to the MR configuration, that is, the boundary for the classification of strong and weak shocks. For the case involving a weak shock, it has been accepted (Dewey and McMillen, 1985) that the shocks are circular in cross section and their growth appears as a rotation. This invalidates the basic assumption of three-shock theory that shocks are straight.

Another feature of the shock reflection process to gain attention was the apparent shift of the RR-MR transition boundary in favour of RR, that is, RR persisted beyond its theoretical limit. This anomaly generated a number of studies: Bleakney and Taub (1949), Smith (1959) and Walker *et al.* (1981). Walker *et al.* (1981) reproduced the original work done by Bleakney using modern optical methods. They discovered that near the transition a simple two-shock model of the reflection process was invalid. Density discontinuities at or near the region of the two-shock reflection point were observed. These were apparently produced by interaction of the reflected shock and the boundary layer. Hornung *et al.* (1979) proposed that the boundary layer behind the incident shock altered the effective shape of the reflecting surface causing RR to persist beyond its normal boundaries. The variation of transition angle calculated by Hornung and Taylor (1982) for fixed Mach number but varying Reynolds number agreed well with experiment. A number of studies (see Takayama *et al.*, 1981) have shown that roughness of the reflecting surface contributes also to a shift in the transition boundary to larger angles.

Experimental limitations of traditional interferometric techniques may also be contributing to the problem of understanding the inability of three-shock theory to account for shock angles after transition. Unresolvable flow effects such as density discontinuities may also be occurring in the region of the flow about the triple point after the transition to MR as well as at or near the region of the two-shock reflection point for RR. The experiment described in this thesis was designed to provide comprehensive data on the Mach reflection configuration and the surrounding flow region using an interferometric technique known as "spectral line interferometry" as well as determining if this technique that has been utilized in a number of other fields can be applied successfully to flow visualization in the shock tube.

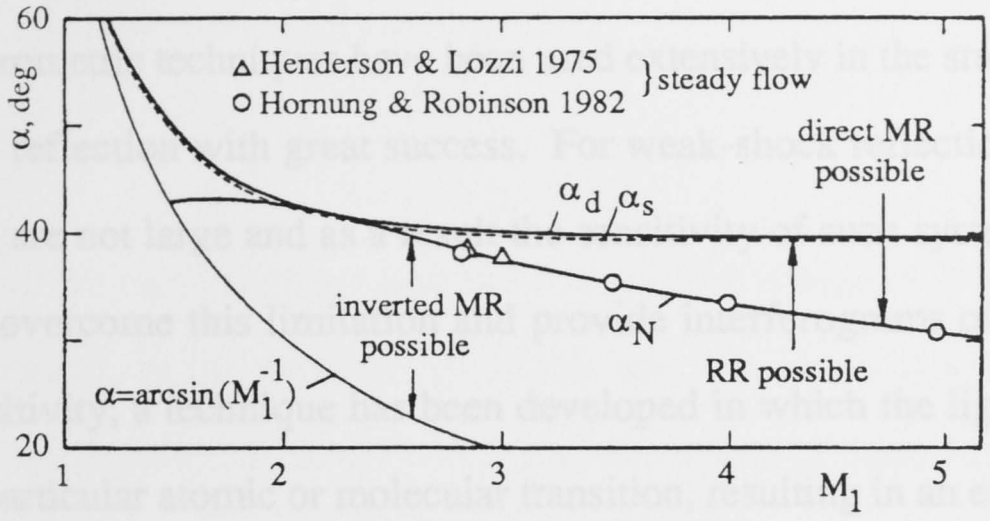

FIGURE 2.14 The existence of a particular shock reflection configuration in the (M_1,α) plane for steady flow. Important values of the function $\alpha\,(M_1)$ for $\gamma = 1.4$ are shown. The **Δ** and **O** symbols represent observed failure of RR in steady flow. Figure taken from Hornung (1986).

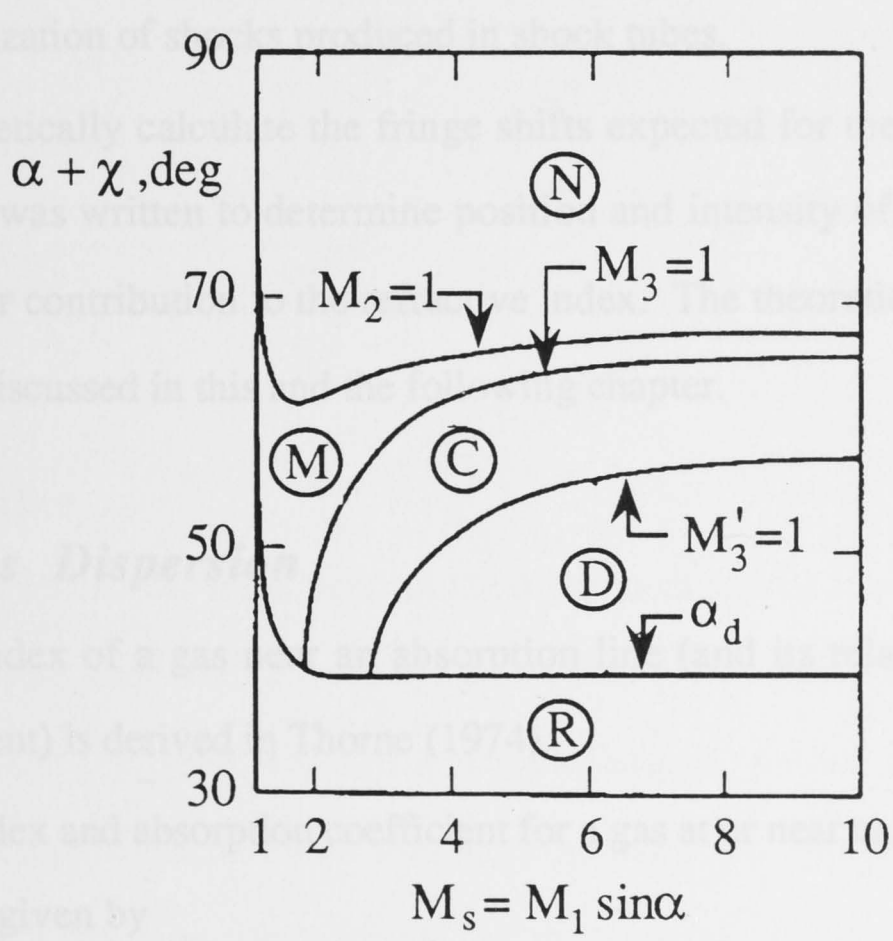

FIGURE 2.15 The regions for psuedo-steady flow ($\gamma = 1.4$) where a particular shock reflection configuration exists. (After Ben-Dor 1978.) R = regular, M = Mach, C = complex, D = double and N = no reflection. M_3^I is the Mach number relative to the second triple point. Figure taken from Hornung (1986).

3. LASER SPECTROSCOPY

Optical interferometric techniques have been used extensively in the study of shock waves and shock reflection with great success. For weak-shock reflection however, density gradients are not large and as a result the sensitivity of such systems is poor. In an attempt to overcome this limitation and provide interferograms of previously unattainable sensitivity, a technique has been developed in which the light source is tuned close to a particular atomic or molecular transition, resulting in an enhancement of the sensitivity of the system due to the increase in refractive index near the transition (Measures, 1970). This increase in refractive index of a gas or vapour about an atomic or molecular transition is known as anomalous dispersion, and is determined by the transition probability of the absorption line in question. A major aim of this experiment was the investigation of the applicability of the technique of spectral line interferometry, a technique that makes use of the anomalous dispersion effect, to the visualization of shocks produced in shock tubes.

In order to theoretically calculate the fringe shifts expected for the experiment, a computer program was written to determine position and intensity of the absorption lines as well as their contribution to the refractive index. The theoretical background to this program is discussed in this and the following chapter.

3.1 Anomalous Dispersion

The refractive index of a gas near an absorption line (and its relationship to the absorption coefficient) is derived in Thorne (1974).

The refractive index and absorption coefficient for a gas at or near an absorption line of frequency ν_0, is given by

$$n-1=\frac{N.e^2}{16\pi^2\varepsilon_0 m\nu_0}.\frac{\nu_0-\nu}{(\nu_0-\nu)^2+\left(\frac{\gamma}{4\pi}\right)^2} \qquad (3.1)$$

and

$$K = \frac{4\pi\nu_0\kappa}{c} = \frac{N.e^2}{4\pi\varepsilon_0 mc}.\frac{\frac{\gamma}{4\pi}}{(\nu_0-\nu)^2+\left(\frac{\gamma}{4\pi}\right)^2} \tag{3.2}$$

where N is the electron oscillators per unit volume, e is the charge of the electron, m is the electron mass, ε_0 is the permittivity of free space, ν is the frequency of the oscillations and γ is the damping factor covering all conditions of damping

The above two equations can be rewritten in terms of the oscillator strength f_j of a particular transition of frequency ν_j by setting the number of classical oscillators N equal to $N_j f_j$ where N_j is the number density of atoms or molecules in the lower state of the transition being considered.(f_j is the effective number of electrons per atom or molecular for that particular transition). Equation 3.1 and 3.2 then become

$$n_\nu - 1 = \frac{e^2}{16\pi^2\varepsilon_0 m}.\frac{N_j f_j}{\nu_j}.\frac{\nu_j-\nu}{(\nu_j-\nu)^2+\left(\frac{\gamma}{4\pi}\right)^2} \tag{3.3}$$

and

$$K = \frac{e^2}{4\pi\varepsilon_0 mc}.N_j f_j.\frac{\frac{\gamma}{4\pi}}{(\nu_j-\nu)^2+\left(\frac{\gamma}{4\pi}\right)^2} \tag{3.4}$$

3.2 Line Profiles

For any atomic or molecular transition, an ideal monochromatic line does not exist. Every transition is associated with a finite spread of energy and thus frequency. Three processes contribute to the finite width of a spectral line: (a) natural broadening, (b) Doppler broadening and (c) interactions with adjacent particles. In the solid state, this last broadening effect can take many forms, but in this work only the gas state is of interest and so pressure broadening is the important factor.

Using an instrument of infinite resolving power to scan a spectral line would result in an output signal I_ν that was proportional to the incident intensity; then figure 3.1 in emission and figure 3.2 in absorption would result.

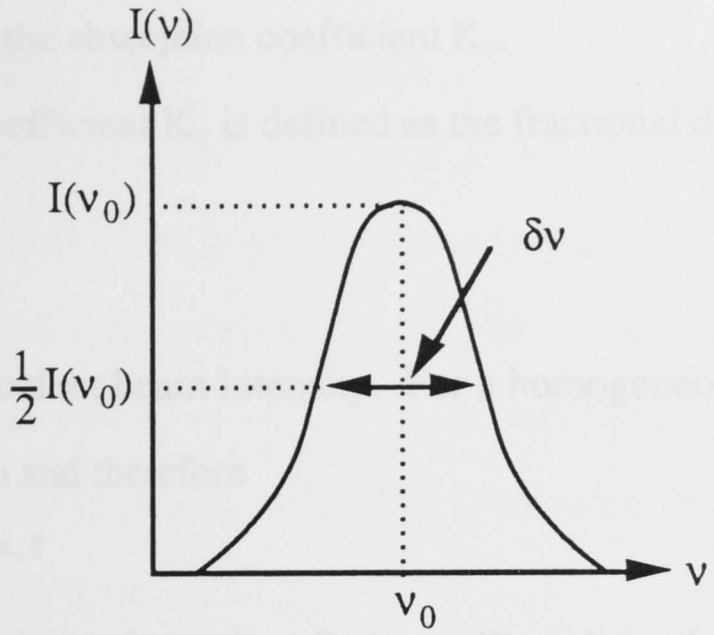

FIGURE 3.1 Emission line profile.

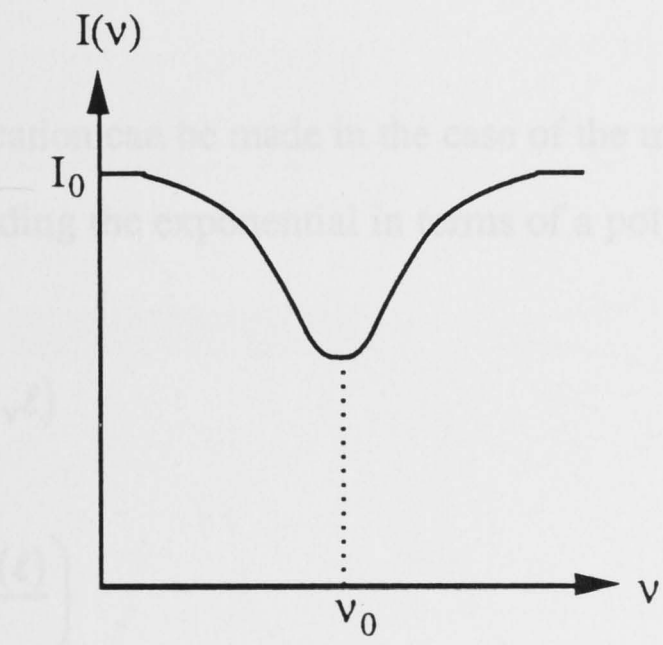

FIGURE 3.2 Absorption line profile.

These curves are typical for emission and absorption and have a distinct shape due to the frequency dependence of the emission and absorption co-efficients, j_ν and k_ν respectively, of the gas. The two profiles below are for optically thin media. For the the case of emission in an optically thin gas, we can assume that the medium does not re-absorb radiation emitted from its deeper layers. If the gas is optically thin in absorption, we have that the optical depth $K_\nu \ell$, (where ℓ is the thickness of the absorbing layers) is much less than one. Assuming the gas is optically thin, then the emissivity j_ν is proportional to I_ν, the emitted radiation intensity, and figure 3.1 is therefore also a plot of j_ν. For the case of absorption, we can consider figure 3.2 for

the calculation of the absorption coefficient K_ν.

The absorption coefficient K_ν is defined as the fractional decrease in intensity per unit path length

$$-dI_\nu = I_0 \kappa \; d\ell \tag{3.5}$$

where I_0 is the incident beam intensity. For a homogeneous medium κ_ν is a constant for all the medium and therefore

$$I_\nu(\ell) = I(0).e^{-\kappa_\nu \ell} \tag{3.6}$$

where $I_\nu(\ell)$ is the beam intensity after travelling through the absorbing layers ℓ and I_0=I(0) with

$$\kappa_\nu = \frac{1}{\ell} \ln\left(\frac{I(0)}{I_\nu(\ell)}\right). \tag{3.7}$$

However, a simplification can be made in the case of the medium being optically thin, $\kappa_\nu \ell << 1$. By expanding the exponential in terms of a polynomial and neglecting the higher order terms,

$$I_\nu(\ell) = I(0).(1 - \kappa_\nu \ell) \tag{3.8}$$

and

$$\kappa_\nu = \frac{1}{\ell} \cdot \left(\frac{I(0) - I_\nu(\ell)}{I(0)}\right) \tag{3.9}$$

Therefore, the profile of κ_ν is identical to the dip in figure 3.2. The importance of a broadening mechanism is generally denoted by its width δ_ν, which is the full width of the spectral line at half its peak intensity (FWHM). However, this value is not a complete description of the line profile since it doesn't account for the wings of the spectral line. The wings of the spectral line are the region of the line profile (absorption and emission) greater than one width δ_ν from the line centre.

3.3 Broadening Processes

3.3.1 Natural Broadening

As stated in section 3.2, every transition is associated with a finite spread of energy and therefore frequency. If we consider this in a quantum mechanical sense, there are two distinct energy levels. These levels cannot be infinitely narrow since, according

to Heisenberg's Uncertainty Principle, $\Delta E \,.\, \Delta t \cong \hbar$ and therefore the energy spread is $\Delta E \cong \hbar \,/\, \Delta t$, where t is taken to be the probability associated with finding the atom in a particular given state. This is given by the mean lifetime of the state τ and results in a frequency spread for the state j of $\delta\nu_j = 1 \,/\, 2\pi\tau_j$. Obviously this means for ground or metastable states with $\tau_j \rightarrow \infty$ that $\delta\nu_j$ is negligible. However, for upper states with finite lifetime of the order 10^{-6} to 10^{-9} there is a corresponding frequency spread which is of the order 0.1 to 100 Mhz.

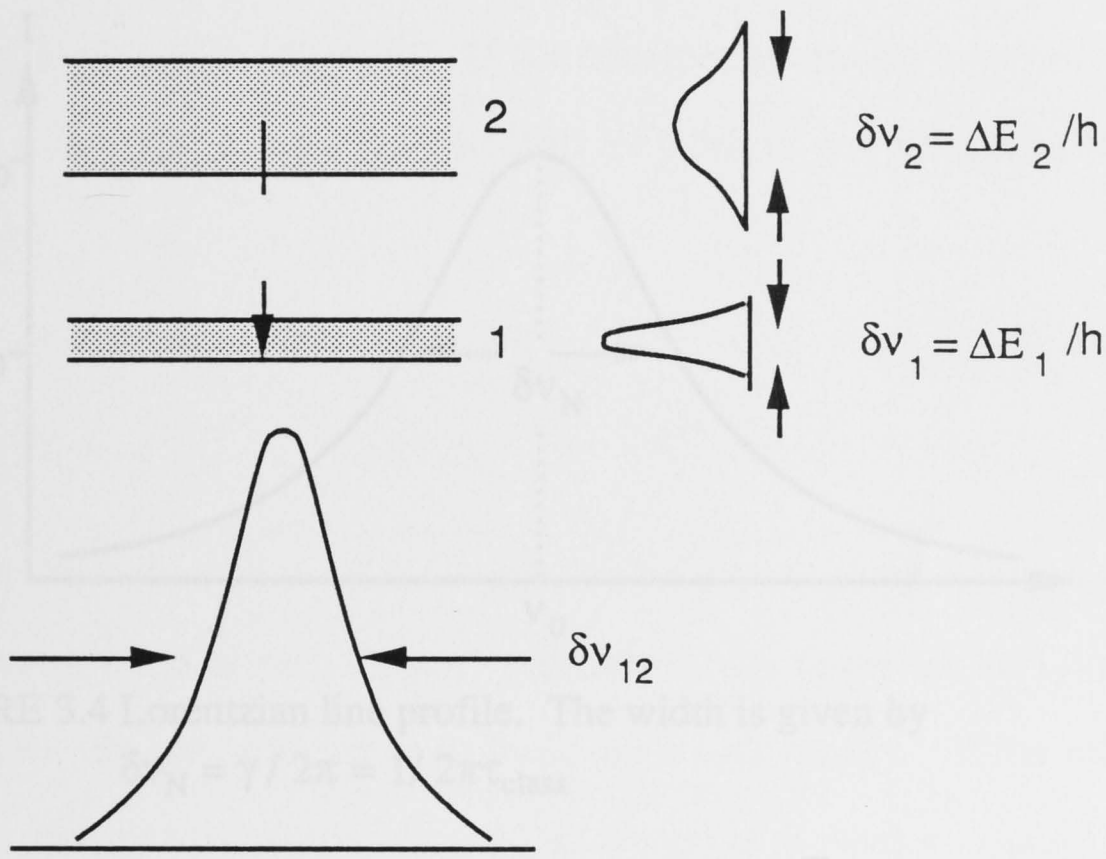

FIGURE 3.3 Natural broadening of the spectral line. Each energy level is expanded according to the probability distribution shown on the right. The width of the spectral line is given by $\delta\nu_{12} = \delta\nu_1 + \delta\nu_2$

In the absence of collisions the mean lifetime of a particular state is related to the Einstein A coefficient for spontaneous emission $\tau_2 = 1 \,/\, A_{21}$ and if one or more transitions are possible, then $\tau_2 = 1 / \sum_i A_{2i}$. This means that the spontaneous emission is proportional to frequency cubed (i.e. $A_{21} \propto \nu^3$), the natural broadening effect is greater in the ultra-violet region than in the infra-red. In the visible region,

natural broadening is usually a couple of orders of magnitude less than the Doppler broadening. However, the natural broadening has a Lorentzian profile (see figure 3.4) and thus still has a significant contribution in the wings of a spectral line. A classical approach gives the spectral line width value as

$$\delta\nu_n = \frac{\gamma}{4\pi} = \frac{1}{2\pi\tau_{class}} \tag{3.10}$$

where $\tau_{class} = 1 / \gamma$ with γ being the classical damping coefficient. This corresponds to a Lorentzian profile.

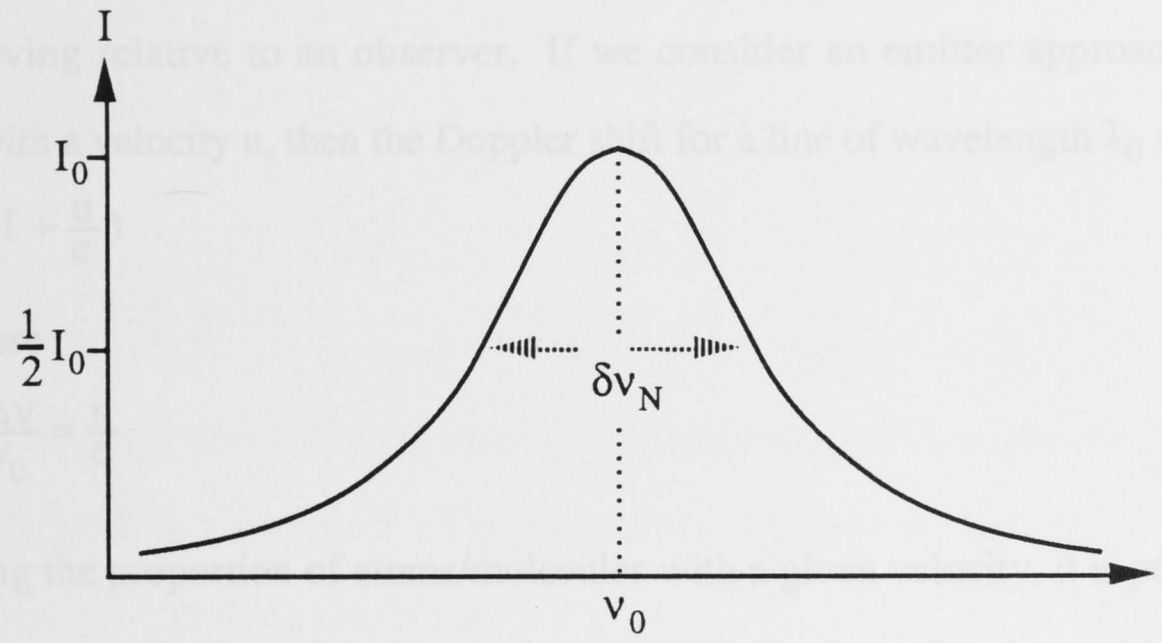

FIGURE 3.4 Lorentzian line profile. The width is given by
$\delta\nu_N = \gamma / 2\pi = 1/ 2\pi\tau_{class}$

A full quantum mechanical approach also yields a Lorentzian profile and if in figure 3.3 only state (2) is broadened, then $\gamma_{class} = 1/\tau_{class}$ becomes $\gamma_2 = 1/\tau_2$. This implies $\delta\nu_N = 1/2\pi\tau_2$, which is identical to the width value determined using a classical approach. If, as in an experiment, level (1) had a finite lifetime τ_1, then the associated frequency spread $\delta\nu_1$ would also contribute to the overall line width. Convoluting the two Lorentzians produces another Lorentzian profile

$$\gamma = \gamma_1 + \gamma_2 = \frac{1}{\tau_1} + \frac{1}{\tau_2} \tag{3.11}$$

However, this Lorentzian has an increased line width

$$\delta\nu_N = \frac{1}{2\pi\tau_1} + \frac{1}{2\pi\tau_2} = \delta\nu_1 + \delta\nu_2 \tag{3.12}$$

The contribution from natural broadening to the observed linewidths of the iodine at the experimental conditions of interest was small compared to the individual contributions from Doppler and pressure broadening discussed in the next two chapters.

3.3.2 Doppler Broadening

The most significant line broadening effect during this experiment was due to the well known Doppler effect, that is, the apparent shift in wavelength of a signal from a source moving relative to an observer. If we consider an emitter approaching the observer with a velocity u, then the Doppler shift for a line of wavelength λ_0 will be

$$\lambda = \lambda_0 \left(1 + \frac{u}{c}\right) \tag{3.13}$$

and therefore

$$\frac{-\Delta\lambda}{\lambda_0} = \frac{\Delta\nu}{\nu_0} = \frac{u}{c} \tag{3.14}$$

By knowing the proportion of atoms/molecules with a given velocity, it is possible to calculate the contribution of each velocity segment u + du to the spectral line at the corresponding wavelength and hence to build up a line profile. If the motion is entirely thermal and the assumption is made that the gas is in thermal equilibrium at a temperature T, then the velocity distribution will simply be a Maxwellian one with

$$dn_u = \frac{n}{(\alpha\sqrt{\pi}) \,.\, e^{-u^2/\alpha^2}}\, du \tag{3.15}$$

where dn_u is the fraction of atoms/molecules having a velocity between u and u + du, along the axis of sight. The most probable velocity α is given by

$$\alpha = \sqrt{\frac{2kT}{m}} = \sqrt{\frac{2RT}{M}} \tag{3.16}$$

with m the atomic mass and M the atomic number. Substituting u from equation (3.14) into equation (3.15), we have for the fraction of atoms emitting in the frequency interval ν to ν +dν

$$\frac{dn_\nu}{n} = \frac{1}{\alpha\sqrt{\pi}} \cdot e^{-c^2(\Delta\nu)^2/\nu_0^2\alpha^2} \cdot \frac{c}{\nu_0}\, d\nu \tag{3.17}$$

The intensity at ν will be proportional to dn_ν so it is possible for the line profile to be written in terms of the central intensity I_0

$$I_\nu = I_0 \cdot e^{-c^2(\nu_0-\nu)^2/\nu_0^2\alpha^2} \tag{3.18}$$

This is a Gaussian distribution about ν_0, with a line width determined by α. The half-value width $\delta\nu_D$ is calculated from $I_\nu = (1/2)\, I(0)$ so

$$\ln 2 = \frac{c^2}{\nu_0^2\alpha^2} \cdot (\nu_0 - \nu_{1/2})^2 \tag{3.19}$$

Now $\delta\nu_D = 2\,|\,\nu_0 - \nu_{1/2}\,|$, so

$$\delta\nu_D = 2 \cdot \frac{\nu_0\alpha}{c} \cdot \sqrt{\ln 2} \tag{3.20}$$

and therefore

$$\delta\nu_D = \frac{2\nu_0}{c} \cdot \sqrt{\frac{2RT \ln 2}{M}} \tag{3.21}$$

It should be noted that while the Doppler or Gaussian profile shown in figure 3.5, has a greater peak intensity than a Lorentzian, for the same area under the curve, it falls off more and rapidly in the wings.

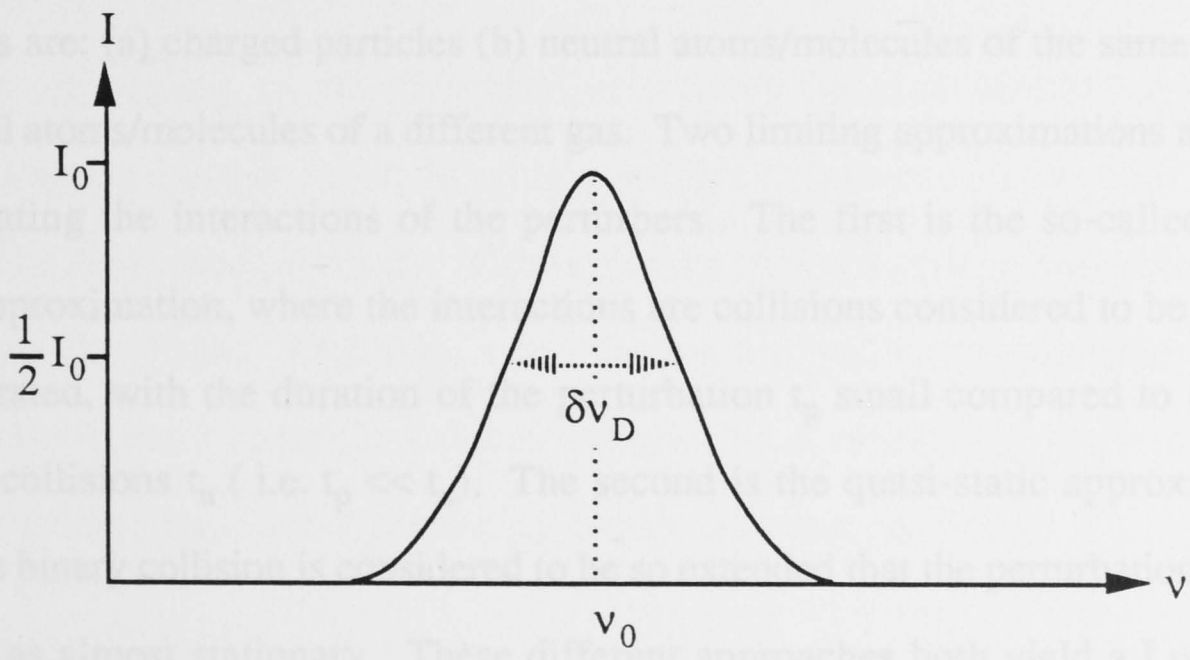

FIGURE 3.5 Doppler line profile. The width is given by
$\delta\nu_D = 7.16\text{E-}7\ \nu_0\ (T / M)^{1/2}$

3.3.3 Pressure Broadening

When the pressure of an absorbing or emitting gas is increased, the spectral lines become broadened and in many cases shifted (Thorne, 1974). An example of this effect is seen in figure 3.6. Sometimes additional lines will appear due to forbidden transitions becoming possible. The perturbing effects of broadening, shifting and mixing energy levels are due to interactions with other particles.

Iodine spectral lines were very sensitive to pressure broadening effects caused by the addition of a buffer gas to the shock tube. A buffer gas was needed in the shock tube to produce the slow shock speeds required for the occurrence of weak Mach reflection, since the iodine vapour pressure achieved experimentally was too low. This pressure broadening effect imposed a severe limitation on the experiment. Shock tube fill pressures could not exceed approximately 10 KPa. This pressure limitation meant an upper limit existed on the amount of buffer gas that could be added to the shock tube. As a result the shock speed was too fast for the occurrence of weak Mach reflection. However, since the major aim of this experiment was the investigation of the spectral line interferometric technique, the slightly high shock speeds were an unavoidable.

Pressure broadening can be classified either by the type of perturber or by the approximations made in the method of treating the perturbation. Different types of perturbers are: (a) charged particles (b) neutral atoms/molecules of the same gas and (c) neutral atoms/molecules of a different gas. Two limiting approximations are made when treating the interactions of the perturbers. The first is the so-called binary impact approximation, where the interactions are collisions considered to be discrete and separated, with the duration of the perturbation t_p small compared to the time between collisions t_u (i.e. $t_p << t_u$). The second is the quasi-static approximation, where the binary collision is considered to be so extended that the perturbation may be regarded as almost stationary. These different approaches both yield a Lorentzian profile that has a width a couple of orders of magnitude greater than that for natural broadening.

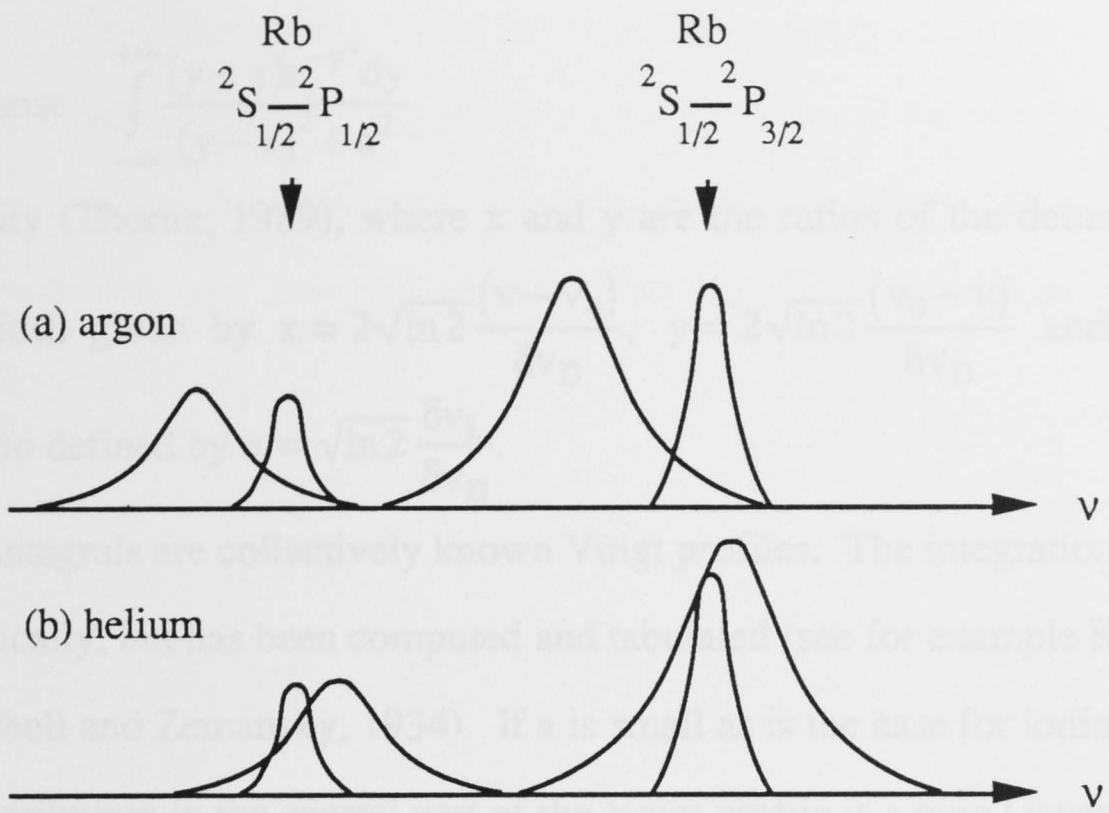

FIGURE 3.6 Rubidium lines broadened by (a) argon and (b) helium. In each case the narrow curves represents the rubidium principal series doublet at low pressure and the broadened curves represent the doublet at 12 atm. inert gas pressure.

3.4 The Convolution of Gaussian and Lorentzian Profiles

Pressure broadening of a spectral line yields a Lorentzian profile (Thorne, 1974). The combination of natural and pressure broadening is also a Lorentzian profile; however, the line width is greater. That is,

$\gamma = \gamma_n + \gamma_{coll}$ with $\gamma_{coll} >> \gamma_n$.

Doppler broadening, on the other hand, produces a Gaussian profile and it can be seen that a spectral line in reality is going to exhibit broadening effects from all three of the above mentioned processes. This is true for iodine where pressure broadening effects were significant. Therefore, a real spectral line will be a combination of both Gaussian and Lorentzian profiles. Since it is possible to express line profiles in terms of line intensities, the result of combining the two different profiles is

$$k = \text{const} \cdot \int_{-\infty}^{+\infty} \frac{e^{-y^2} dy}{(y-x)^2 + a^2} \qquad (3.22)$$

in absorption and

$$n-1 = \text{const} \cdot \int_{-\infty}^{+\infty} \frac{(y-x)e^{-y^2}dy}{(y-x)^2+a^2} \qquad (3.23)$$

in refractivity (Thorne, 1989), where x and y are the ratios of the detuning to the Doppler width given by $x = 2\sqrt{\ln 2}\,\frac{(\nu-\nu_0)}{\delta\nu_D}$, $y = 2\sqrt{\ln 2}\,\frac{(\nu_0-\nu)}{\delta\nu_D}$ and a is the damping ratio defined by $a = \sqrt{\ln 2}\,\frac{\delta\nu_L}{\delta\nu_D}$.

The two integrals are collectively known Voigt profiles. The integration cannot be done analytically, but has been computed and tabulated (see for example Kuhn, 1969 and/or Mitchell and Zemansky, 1934). If a is small as is the case for iodine, then the intensity distribution in the central part of the Voigt profile is a pure Gaussian but the wings of the line would be due to the Lorentzian component.

3.5 Experimental Linewidths

Typical temperatures obtained for preshock conditions during the experiment were in the interval 58-68 °C. This corresponded to a range in the Doppler widths (using equation (3.36) with M = 253.80 grams and $\nu_0 = 5.255 \times 10^5$ GHz [λ = 570.520 nm]) of 0.423-0.436 GHz. Observed linewidths were of the order of 1.1 GHz over the entire temperature interval and this was approximately 2.6 times greater than the calculated Doppler widths. Pressure broadening was therefore a contributor to the experimental linewidth and a Voigt profile was assumed for the lineshape of the observed spectral lines. The method of Measures (1970) was used to calculate the theoretical Voigt profile linewidths, allowing the contribution due to pressure broadening to be determined. The Lorentzian linewidth was calculated using an iterative process that matched the theoretical Voigt profile linewidth to the observed Voigt profile linewidth (using the known value of the Doppler linewidth and the varying the Lorentzian linewidth to produce the desired result). This yielded typical values for the Lorentzian linewidth and therefore the pressure broadening of 0.08 GHz. The pressure broadening was 5.3 times less than the Doppler broadening, ($\alpha \sim$ 0.19) on the average, indicating that the dominant broadening process, for pressures

less than 9.98 KPa (100 mbars), could be attributed to Doppler effects. This meant that individual pressure broadening processes in this pressure range were significant but small enough for their effects to be considered as a whole and therefore the individual contributions from resonance, Van Der Waals and quadratic Stark broadening were ignored.

4. MOLECULAR SPECTROSCOPY

As mentioned in the introduction to the previous chapter, a computer program was written to determine position and intensity of the absorption lines as well as their contribution to the refractive index (i.e. to theoretically calculate the expected fringe shifts for the experiment). The theoretical background to this program, with respect to the determination of spectral line position, population number density and oscillator strength is discussed in this chapter. Most of the description given in this chapter is based on the theory presented by Herzberg (1950) and Banwell (1972)

4.1 Electronic and Total Energy

When considering the motion of a diatomic molecule, it can be assumed to a good first approximation that the three forms of motion of the molecule act independently of each other; thus, the total energy of the molecule is simply the sum of three independent energy functions

independent energy functions

$$E_{TOTAL} = E_E + E_V + E_R \tag{4.1}$$

where E_E is the electronic energy; E_v is the vibrational energy; E_R is the rotational energy. Often it is convenient to deal in units of wavenumber and one thus defines

$$T = T_e + G + F$$
$$= \frac{E_E}{hc} + \frac{E_V}{hc} + \frac{E_R}{hc} \tag{4.2}$$

where T_e, G and F are known as the electronic, vibrational rotational energy terms, respectively. For example, iodine has rotational energy separations of 1-2 cm^{-1}, whereas the vibrational energy separations for iodine are approximately 200 cm^{-1}.

If equation 4.1 is the total energy of the system, then the change in the total energy is

$$\Delta E_{TOTAL} = \Delta E_E + \Delta E_V + \Delta E_R \tag{4.3}$$

with the approximate orders of magnitude for the change

$$\Delta E_E \approx \Delta E_V * 10^3 \approx \Delta E_R * 10^6 \tag{4.4}$$

It can be seen from the above equations that vibrational changes show a coarse

structure and the rotational changes a fine structure overlayed on the electronic spectra of the molecule. As an illustration, two different electronic states with their associated vibrational and rotational lines are shown in figure 4.1. The diagram is not drawn to scale since the energy separation between the rotational levels, in comparison to the energy separation between the vibrational levels, is very much smaller than shown.

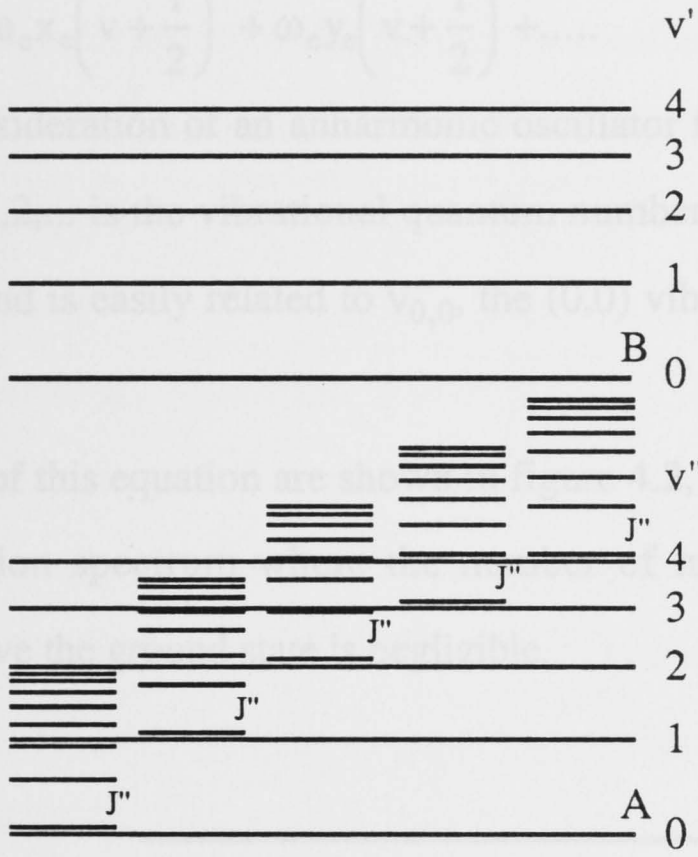

FIGURE 4.1 Vibrational and rotational levels of two electronic states A and B of a molecule (only the first few rotational and vibrational levels are shown).

4.2 Vibrational Structure

From equation 4.2 the wavenumbers of the spectral lines corresponding to an electronic transition in emission or absorption are given by

$$\nu = T' - T'' = (T_e' - T_e'') + (G' - G'') + (F' + F''), \qquad (4.5)$$

where the single prime letters refer to the upper state and the double prime to the lower state. Rewriting equation (4.6) we obtain

$$\nu = \nu_E + \nu_V + \nu_R. \qquad (4.6)$$

When considering the vibrational coarse structure of a given molecule's spectra, we can ignore the contribution from the rotational energies. Considering that $\nu_E = T_e' - T_e''$ is a constant for a given electronic transition and ignoring the rotational

contribution so $\nu_R = F' - F'' = 0$, we have

$$\nu = \nu_e + \omega_e'\left(v'+\frac{1}{2}\right) - \omega_e'x_e'\left(v'+\frac{1}{2}\right)^2 + \omega_e'y_e'\left(v'+\frac{1}{2}\right)^3 - \ldots\ldots$$
$$-\left[\omega_e''\left(v''+\frac{1}{2}\right) - \omega_e''x_e''\left(v''+\frac{1}{2}\right)^2 + \omega_e''y_e''\left(v''+\frac{1}{2}\right)^3 - \ldots\ldots\right] \quad (4.7)$$

where

$$\nu_v = \omega_e\left(v+\frac{1}{2}\right) - \omega_e x_e\left(v+\frac{1}{2}\right)^2 + \omega_e y_e\left(v+\frac{1}{2}\right)^3 + \ldots\ldots \quad (4.8)$$

derives from the consideration of an anharmonic oscillator for a vibrating diatomic molecule and $v = 0,1,2,...$ is the vibrational quantum number. ν_e is called the origin of the band system and is easily related to $\nu_{0,0}$, the (0,0) vibrational transition of an electronic transition.

The energy levels of this equation are shown in figure 4.2, for two arbitrary values of ν_e, in an absorption spectrum where the number of molecules in the higher vibrational levels above the ground state is negligible.

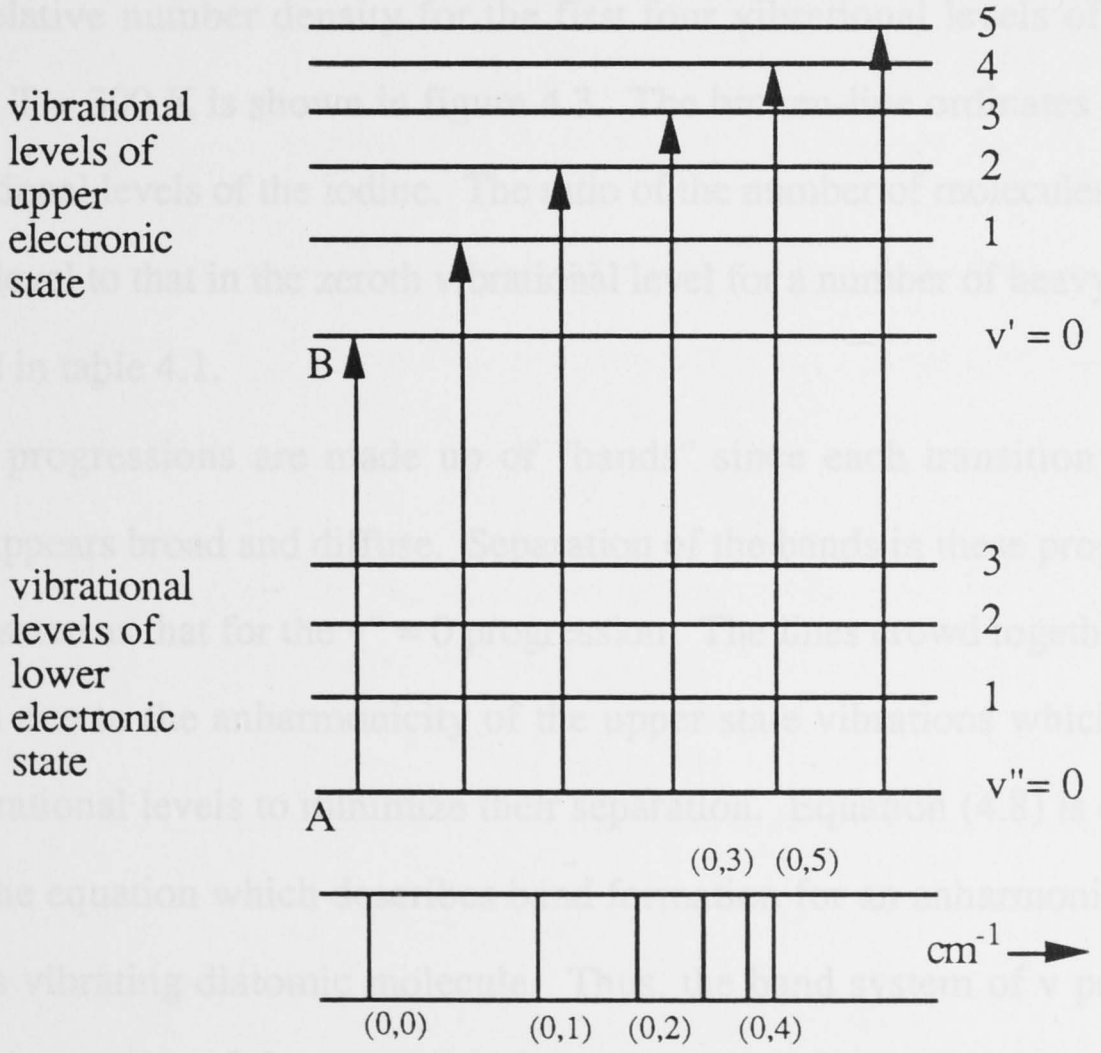

FIGURE 4.2 The vibrational coarse structure of the band formed during electronic absorption from the ground state v" = 0 to a higher state.

In theory there is no real selection rule for vibrational transitions coupled with an electronic transition for either emission or absorption and thus it is possible for a molecular spectrum to exhibit a great many vibrational progressions. However, in general only a single v' progression exists in absorption spectra at low temperatures due to the fact that the number of molecules in higher excited vibrational levels above the ground state is very small. However, if the vibrational quanta in the ground state are small, as is the case for some of the heavier molecules such as I_2 or when the temperature is high, then the number of molecules existing in these higher vibrational levels will be greater and so it will be possible for a number of other progressions besides v" = 0 to be present.

According to the Maxwell-Boltzmann distribution law, the number of molecules dN_E that have a classical vibrational energy level between E+dE is proportional to $e^{-E/kT}$, where k is Boltzmann's constant and T is absolute temperature. The fall off in the number of molecules in higher vibrational levels is very rapid even for heavy molecules such as I_2. This fall off is even greater for molecules such as H_2, N_2, O_2, etc. The relative number density for the first four vibrational levels of the iodine molecule at T = 300 K is shown in figure 4.3. The broken-line ordinates correspond to the vibrational levels of the iodine. The ratio of the number of molecules in the first vibrational level to that in the zeroth vibrational level for a number of heavy molecules is displayed in table 4.1.

These v' progressions are made up of "bands" since each transition under low resolution appears broad and diffuse. Separation of the bands in these progressions is exactly the same as that for the v" = 0 progression. The lines crowd together at higher frequencies due to the anharmonicity of the upper state vibrations which cause the excited vibrational levels to minimize their separation. Equation (4.8) is empirically similar to the equation which describes band formation for an anharmonic oscillator model for a vibrating diatomic molecule. Thus, the band system of v progressions represents the totality of the transitions between two different electronic states of a diatomic molecule.

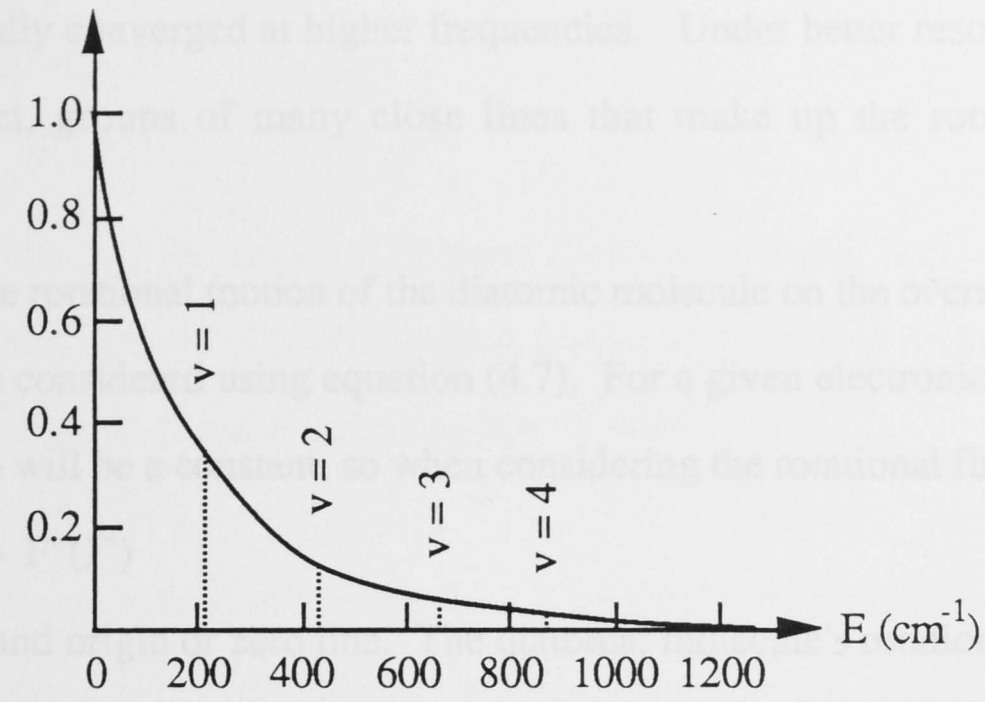

FIGURE 4.3 The Boltzmann factor and thermal distribution of vibrational levels for I_2. Figure taken from Herzberg (1950).

TABLE 4.1 The ratio of the number of molecules in the first vibrational level to that in the zeroth vibrational level for T=300 K and T=1000 K.

Gas	$\Delta G_{1/2}$ (cm)$^{-1}$	$\exp(-\Delta G_{1/2}\, hc/kT)$	
		For 300 K	For 1000 K
H_2	4160.2	2.16×10^{-9}	2.51×10^{-3}
HCl	2885.9	9.77×10^{-7}	1.57×10^{-2}
N_2	2330.7	1.40×10^{-5}	3.50×10^{-2}
CO	2143.2	3.43×10^{-5}	4.58×10^{-2}
O_2	1556.4	5.74×10^{-4}	1.07×10^{-1}
S_2	721.6	3.14×10^{-2}	3.54×10^{-1}
Cl_2	556.9	6.92×10^{-2}	4.49×10^{-1}
I_2	213.2	3.60×10^{-1}	7.36×10^{-1}

4.3 Rotational Structure

In the previous section it was seen that the coarse structure produced by vibrational energy considerations of a diatomic molecule resulted in v progressions, a series of

bands that gradually converged at higher frequencies. Under better resolution these bands are, in fact, groups of many close lines that make up the rotational fine structure.

The effect of the rotational motion of the diatomic molecule on the overall energy of the system can be considered using equation (4.7). For a given electronic-vibrational transition $\nu_E + \nu_V$ will be a constant, so when considering the rotational fine structure,

$$\nu = \nu_0 + F'(J') - F''(J'') \tag{4.9}$$

where ν_0 is the band origin or zero line. The diatomic molecule's rotational period is long compared to its vibrational period and when approximating its motion by a rotating rigid symmetric top model, an average value is taken for the internuclear distance. Allowing for the possibility of centrifugal distortion due to the speed of rotation, the energy levels of a non-rigid rotating diatomic molecule are given by

$$F_v(J) = \frac{h}{8\pi^2 c I_B} J(J+1) + \left(\frac{h}{8\pi^2 c I_A} - \frac{h}{8\pi^2 c I_B} \right) \Lambda^2 - D_v J^2 (J+1)^2 + .. \text{ for } J = 0,1,2,.. \tag{4.10}$$

where I_B is the mean moment of inertia of the molecule about an axis perpendicular to the internuclear axis, J is the rotational quantum number, I_A is moment of inertia of the electrons about the internuclear axis, Λ is the quantum number of the angular momentum of the electrons about the internuclear axis and $D_v J^2(J+1)^2$ is the term added to take into account the influence of centrifugal force. If we rewrite $B_v = \frac{h}{8\pi^2 c I_B}$ as the rotational constant and $A = \frac{h}{8\pi^2 c I_A}$ we have

$$F_v(J) = B_v J(J+1) + (A - B_v)\Lambda^2 - D_v J^2 (J+1)^2 + ... \text{ for } J = 0,1,2,... \tag{4.11}$$

Obviously the angular momentum Λ is a constant for a given electronic-vibrational transition and can be ignored when considering possible rotational transitions if the appropriate ν_0 is chosen for $\nu = \nu_0 + F'(J') - F''(J'')$.

Also, we define $F_v(J)$ to be the value of the rotational term value measured from the rotational level having $J = 0$ and so

$$F_v(J) = B_v J(J+1) - D_v J^2 (J+1)^2 + ... \tag{4.12}$$

Therefore, rewriting equation (4.9) we obtain

$$\nu = \nu_0 + B_\nu'J'(J'+1) - D_\nu'J'^2(J'+1)^2 + \ldots\ldots$$
$$-\left(B_\nu''J''(J''+1) - D_\nu''J''^2(J''+1)^2 + \ldots\ldots\right) \qquad (4.13)$$

The selection rules will be the same as those for the symmetric top; i.e. the upper and lower levels must have different electronic angular momentum Λ (as is this case for iodine) and that if one of these states has $\Lambda \neq 0$, then

$\Delta J = 0, \pm 1\,;\ J = 0 \not\leftrightarrow J = 0$

If both electronic states have $\Delta = 0$ as in a $\Sigma \leftrightarrow \Sigma$ transition, then the $\Delta J = 0$ transition is forbidden and only $J = \pm 1$ will appear. A letter designation is assigned to each ΔJ value depending on whether it is positive or negative,

ΔJ :	-2	-1	0	+1	+2
	O	P	Q	R	S

but in this case we will be dealing only with what is known as the P, Q and R branches due to the above mentioned selection rules.

If we consider each of the branches separately, we have

$$P:\ \nu_P = \nu_0 + F_\nu'(J+1) - F_\nu''(J) \qquad \Delta J = -1 \qquad (4.14)$$

$$Q:\ \nu_Q = \nu_0 + F_\nu'(J) - F_\nu''(J) \qquad \Delta J = 0 \qquad (4.15)$$

$$R:\ \nu_R = \nu_0 + F_\nu'(J-1) - F_\nu''(J) \qquad \Delta J = +1 \qquad (4.16)$$

where J is equal to J" for the above equations. The P and R-branch equations can be combined into the same formula, given by

$$\nu = \nu_0 + (B_\nu' + B_\nu'')m + (B_\nu' - B_\nu'')m^2 \qquad \text{where } m = \pm 1, \pm 2, ..$$
$$\text{with } m = -\text{ve for P}$$
$$m = +\text{ve for R} \qquad (4.17)$$

The graphical representation of the above equation (i.e. no Q-branch) is known to be parabolic in shape and can be represented as a Fortrat Diagram (figure 4.4). It is parabolic because of the quadratic term $(B_\nu' - B_\nu'')m^2$ which will cause one of either the P or R-branches to turn back on itself, thus forming what is known as a band head. A band head is produced in the R-branch if $B_\nu' > B_\nu''$ and in the P-branch when $B_\nu' < B_\nu''$. When the R-branch contains the band head, the head will lie on the

short wavelength side of the band origin and the overall band is said to be shaded to the red. When the P-branch contains the band head, the head will lie on the long wavelength side of the band origin and the band is said to be shaded to the violet. Note also that the Q-branch, when present and plotted on the Fortrat Diagram, always follows the shaded side of the band. The m value corresponding to the band head, that is, the vertex of the Fortrat parabola, is given by

$$m_{vertex} = \frac{-(B_v' + B_v'')}{2(B_v' - B_v'')} \tag{4.18}$$

which is derived from equation (4.17) and is the integer value closest to that calculated from the above equation.

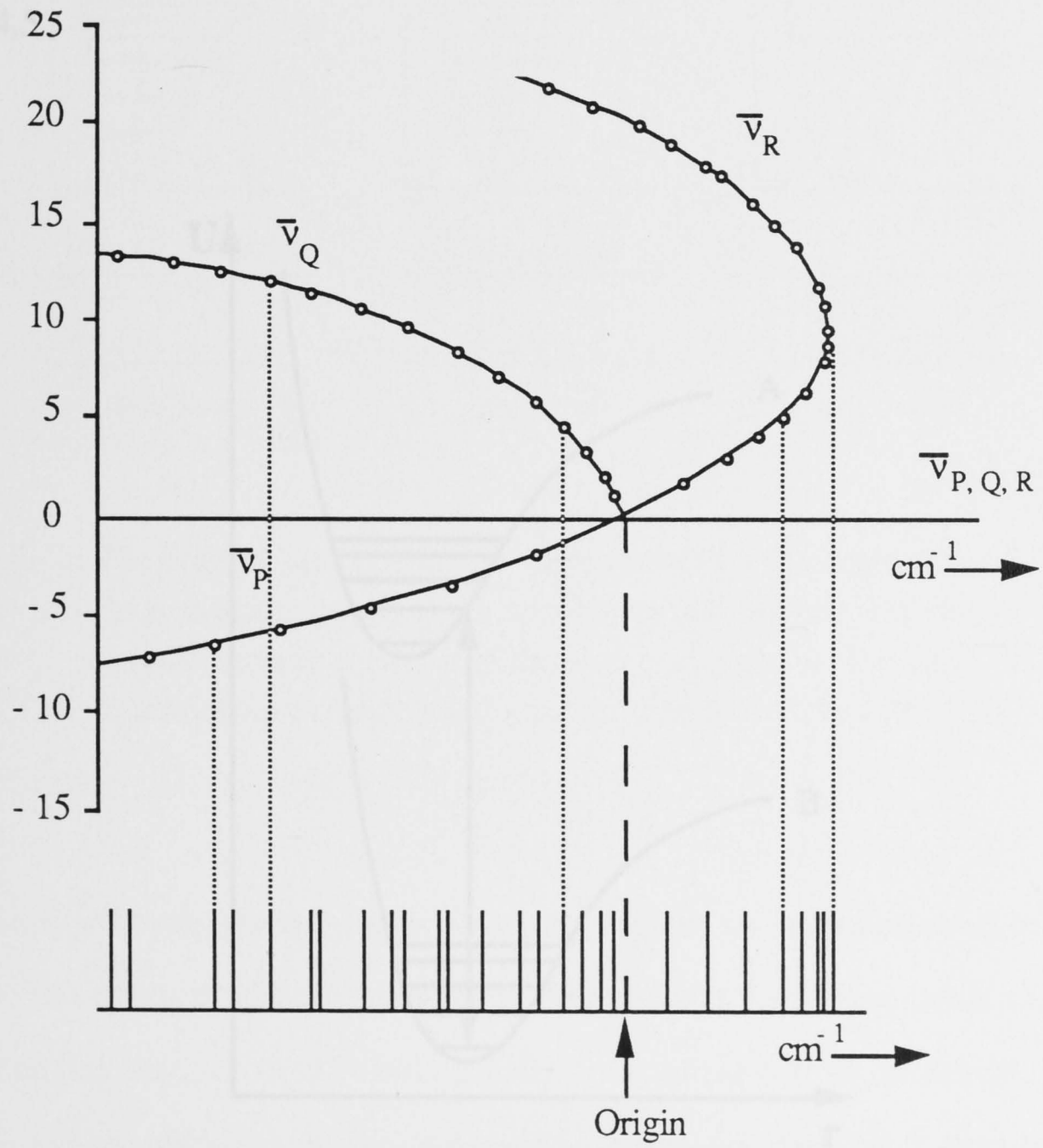

FIGURE 4.4 A Fortrat diagram drawn for a 10% difference between B' and B" values with B'< B". Figure taken from Banwell (1972).

4.4 Intensity Distribution in Electronic Bands

4.4.1 Intensity Distribution in Vibrational Structure

Quantum mechanics imposes no limitation on the vibrational quantum number during an electronic transition. However, the spectrum does not exhibit uniform intensity across the v progressions. In some spectra the (0,0) transition is stronger, whereas in other spectra the (0,v') transitions are stronger for higher order values of v'. This can be understood by considering the Frank-Condon Principle, which states that an electronic transition takes place so rapidly that the vibrating diatomic molecule has no time to alter its internuclear distance and so when plotted on a potential energy vs internuclear distance graph, the transitions can be considered to be vertical. (See figure 4.5.)

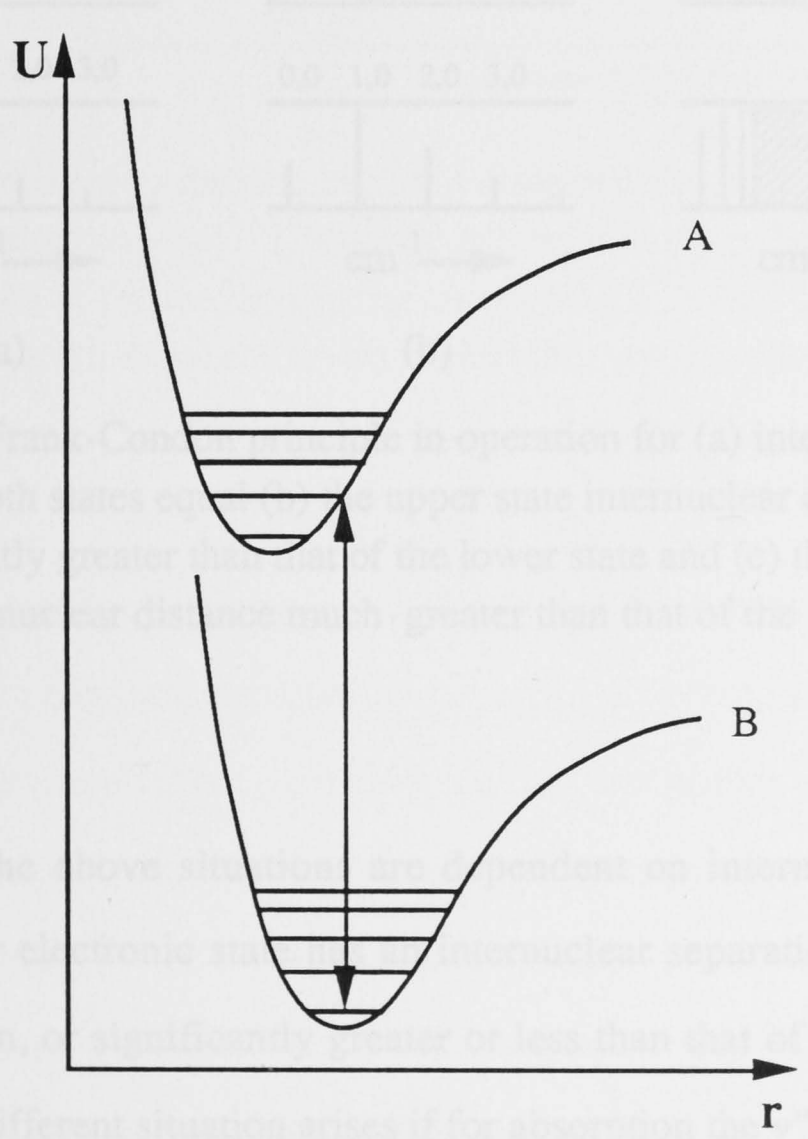

FIGURE 4.5 An electronic transition from an upper electronic state A to a lower electronic state B with a change in vibrational quantum number due to the Frank-Condon principle.

If we consider only absorption from the v" = 0 state for simplicity, three typical situations can result, as shown in figure 4.6.

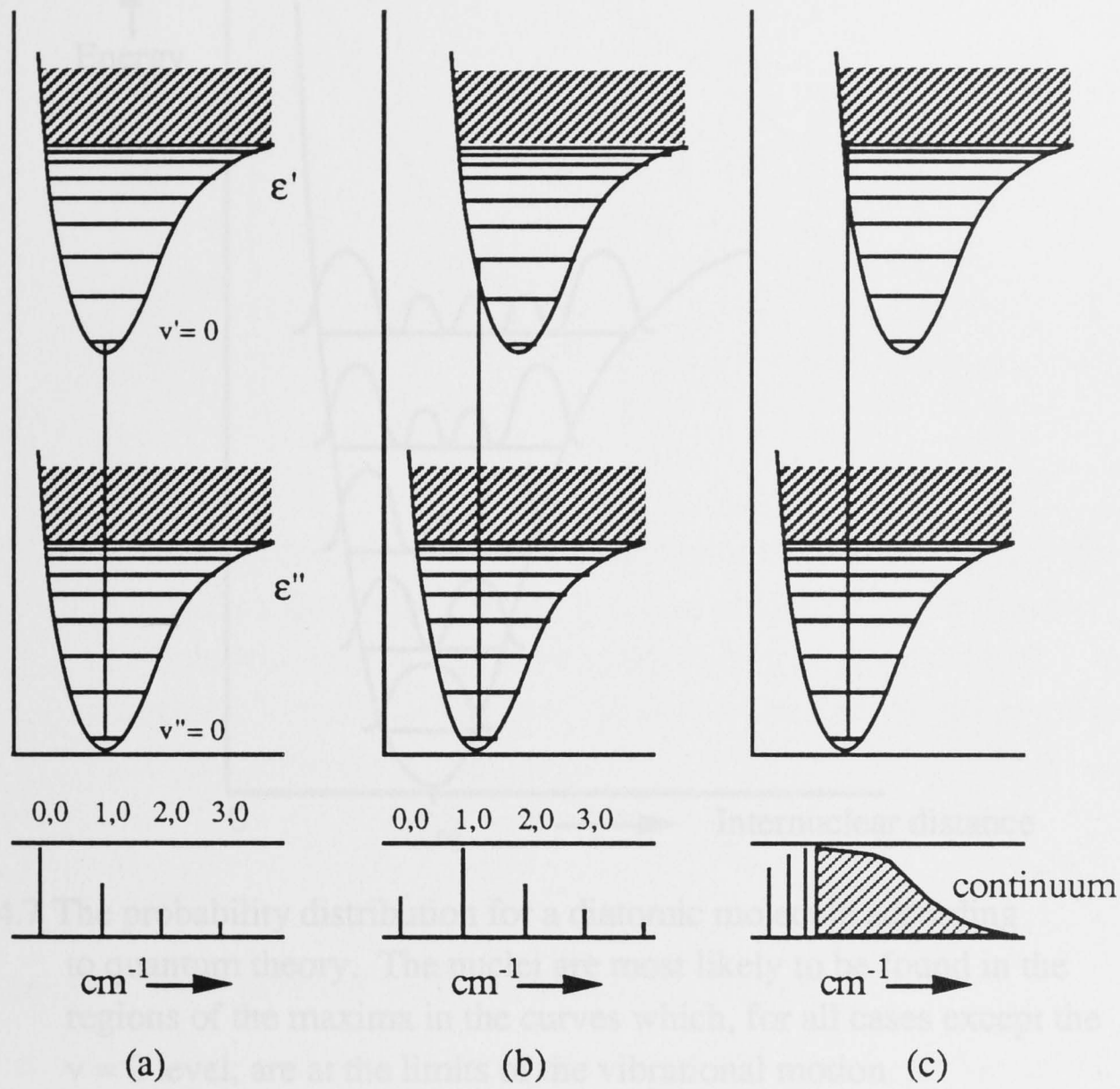

FIGURE 4.6 The Frank-Condon principle in operation for (a) internuclear distances in both states equal (b) the upper state internuclear distance slightly greater than that of the lower state and (c) the upper state internuclear distance much greater than that of the lower state.

Obviously all the above situations are dependent on internuclear distance and whether the upper electronic state has an internuclear separation equal to, slightly greater or less than, or significantly greater or less than that of the lower electronic state. A slightly different situation arises if for absorption the v" = 0 vibrational state is not the only one populated. The result is similar to what is observed for emission from higher order vibrational levels. At these higher vibrational levels the molecules

have equal probability of being at the end points of the vibration (see figure 4.7).

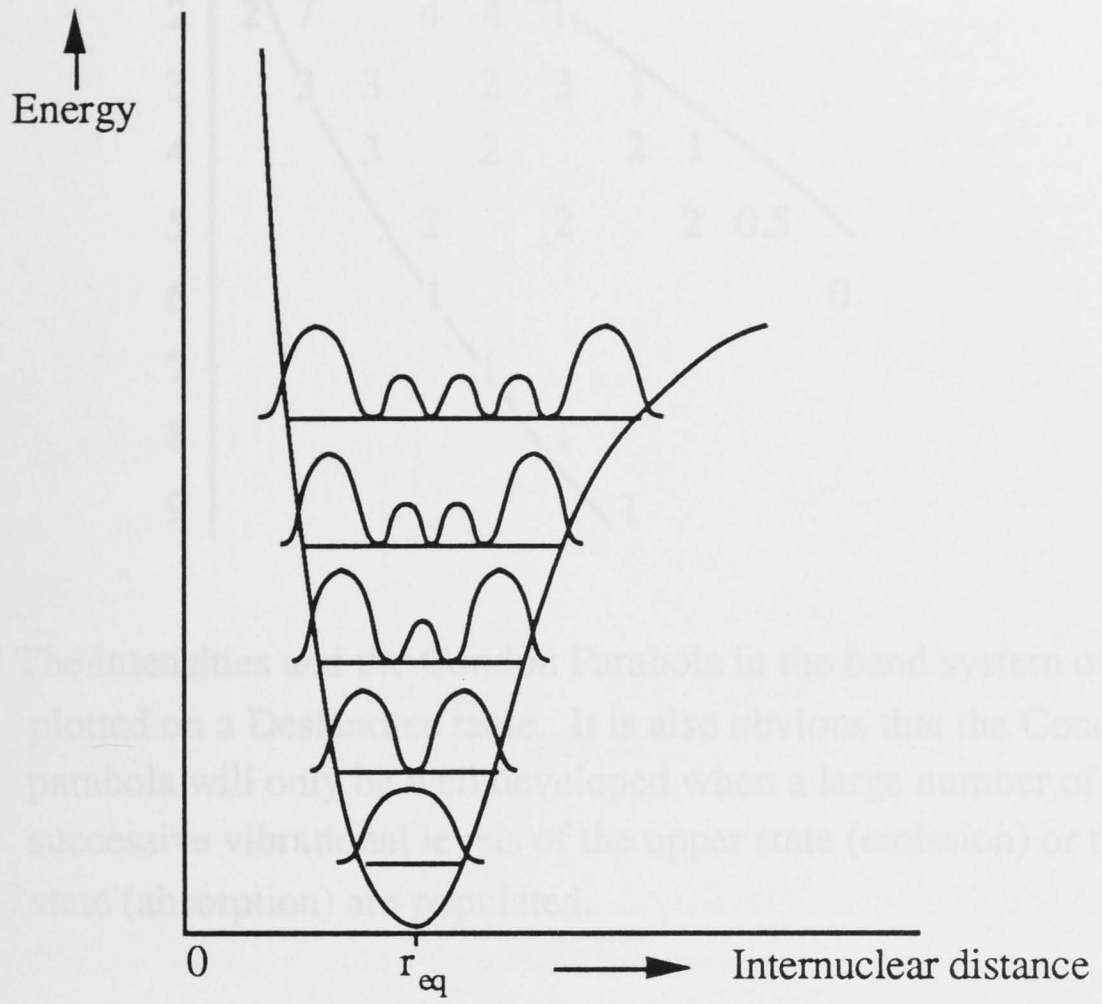

FIGURE 4.7 The probability distribution for a diatomic molecule according to quantum theory. The nuclei are most likely to be found in the regions of the maxima in the curves which, for all cases except the v = 0 level, are at the limits of the vibrational motion.

Therefore, it is possible in emission or absorption from higher vibrational levels $v' > 0$, $v'' > 0$ for the resultant transition to have two different final vibrational states, differing in quantum number but equal in transition probability and thus intensity. If the intensities from such an electronic transition are plotted on a Deslandres table where the upper vibrational level quantum number is drawn against the lower vibrational level quantum number (v' vs v''), then by joining the most intense bands in the array, a parabolic curve is obtained whose principle axis is the main diagonal. This is known as the Condon parabola and is shown in figure 4.8.

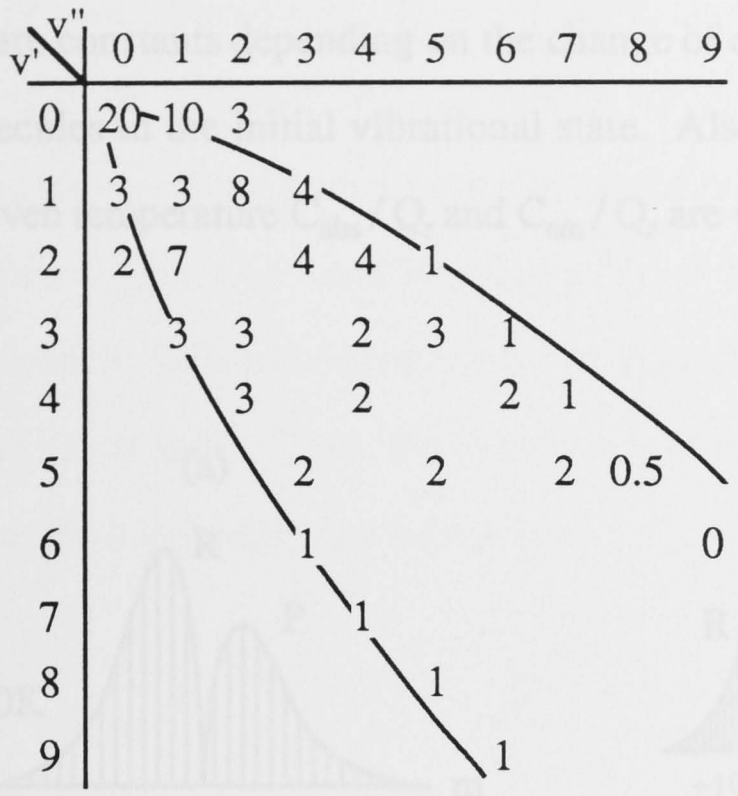

FIGURE 4.8 The intensities and the Condon Parabola in the band system of PN plotted on a Deslandres table. It is also obvious that the Condon parabola will only be well developed when a large number of successive vibrational levels of the upper state (emission) or the lower state (absorption) are populated.

4.4.2 Intensity Distribution in Rotational Structure

For the rotational fine structure in the branches of the electronic bands, the line intensities vary in the same manner as the branches of the purely rotation-vibration bands in the infra-red. For an electronic transition where both the electronic states involved possess zero electronic angular momentum, $\Lambda = 0$, a $\Sigma \leftrightarrow \Sigma$ transition results, which is distinguishable by the fact that only a P and R-branch exist in the spectrum. In each branch there is an intensity maximum which lies at higher J values for greater temperature and smaller rotational constant B_v (see figure 4.9).

The intensity relationships for these branches are quantitatively given by

$$I_{abs} = \frac{C_{abs} \cdot \nu}{Q_r} \cdot (J' + J'' + 1). e^{-B''J''(J'' + 1)hc / kT} \qquad (4.19)$$

and

$$I_{em} = \frac{C_{em} \cdot \nu}{Q_r} \cdot (J' + J'' + 1). e^{-B'J'(J' + 1)hc / kT} \qquad (4.20)$$

where C_{abs} and C_{em} are constants depending on the change of dipole moment and the total number of molecules in the initial vibrational state. Also for a given rotation-vibration band at a given temperature C_{abs} / Q_r and C_{em} / Q_r are very nearly constants.

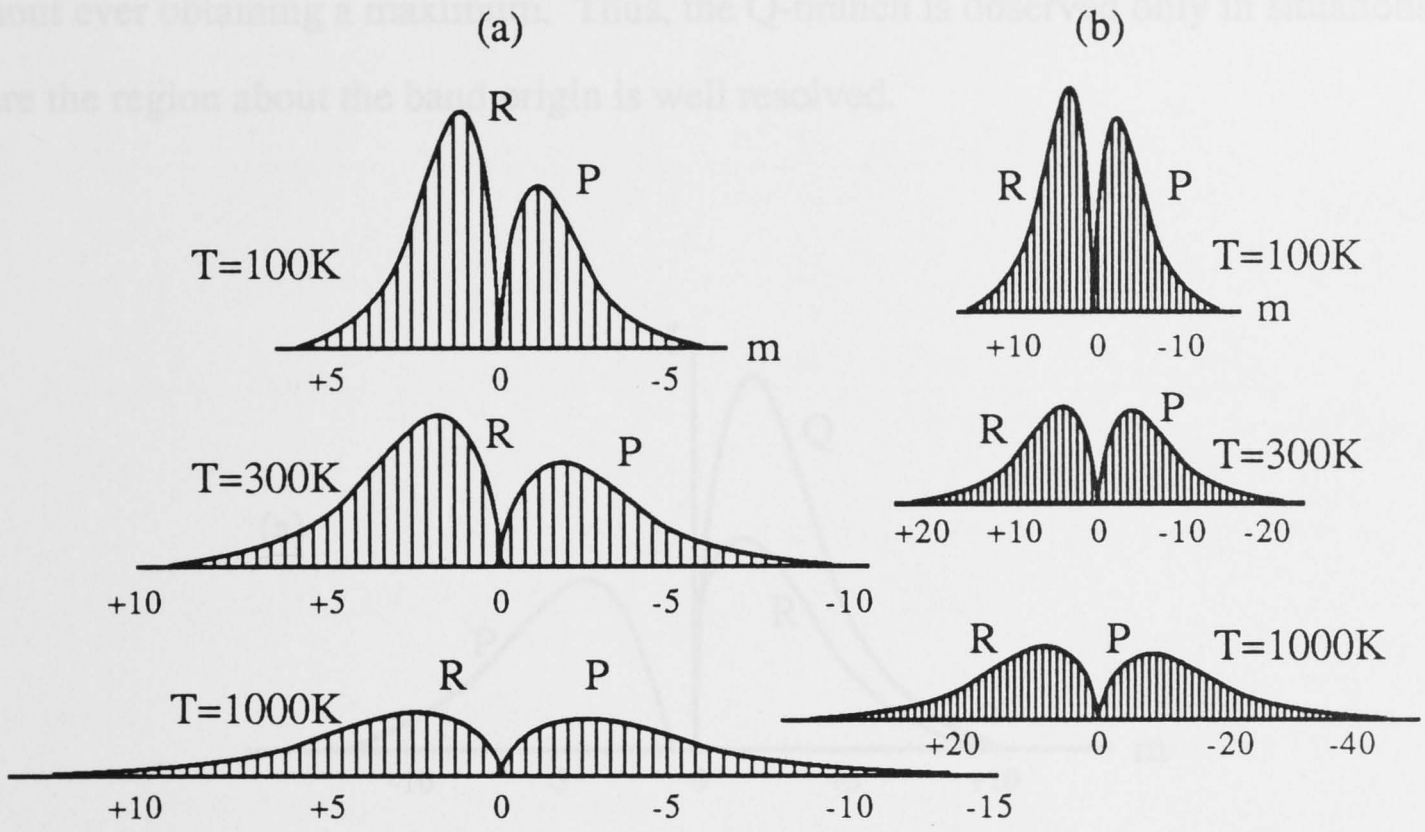

FIGURE 4.9 The intensity distribution in rotation-vibration bands for absorption at T=100 K, T=300 K and T=1000 K with (a) B=10.44 cm^{-1} and (b) B=2 cm^{-1}. The lines are drawn assuming a constant B for both the upper and lower states that is similiar.

If the electronic quantum number Λ for one of the electronic states involved in the transition is not equal to zero, as is the case for the ${}^3\Pi_{0u^+} \leftrightarrow {}^1\Sigma_g^+$ transition in iodine then the spectrum will appear to be different. The intensity distributions of the P and R-branches will remain the same but in addition a Q-branch will appear (see figure 4.10) whose intensity distribution will rely on whether the transition involves a positive, negative or null change in the electronic angular momentum. The first case represents a ${}^1\Pi \rightarrow {}^1\Sigma$ transition similar to that in the I_2 molecule being used in this experiment. The R-branch is slightly stronger than the P-branch and a Q-branch, if present, will be approximately twice the intensity of the corresponding lines in the P

and R-branches. In the reverse transition, $^1\Sigma \rightarrow {}^1\Pi$, the P-branch line intensities will be slightly stronger than the R-branch intensities with the Q-branch remaining the same. The second case involves both electronic states with electronic angular momentum being nonzero (i.e. $\Lambda = 1$ and is called a $^1\Pi \rightarrow {}^1\Pi$ transition). In this circumstance the Q-branch decreases significantly in intensity from the beginning without ever obtaining a maximum. Thus, the Q-branch is observed only in situations where the region about the band origin is well resolved.

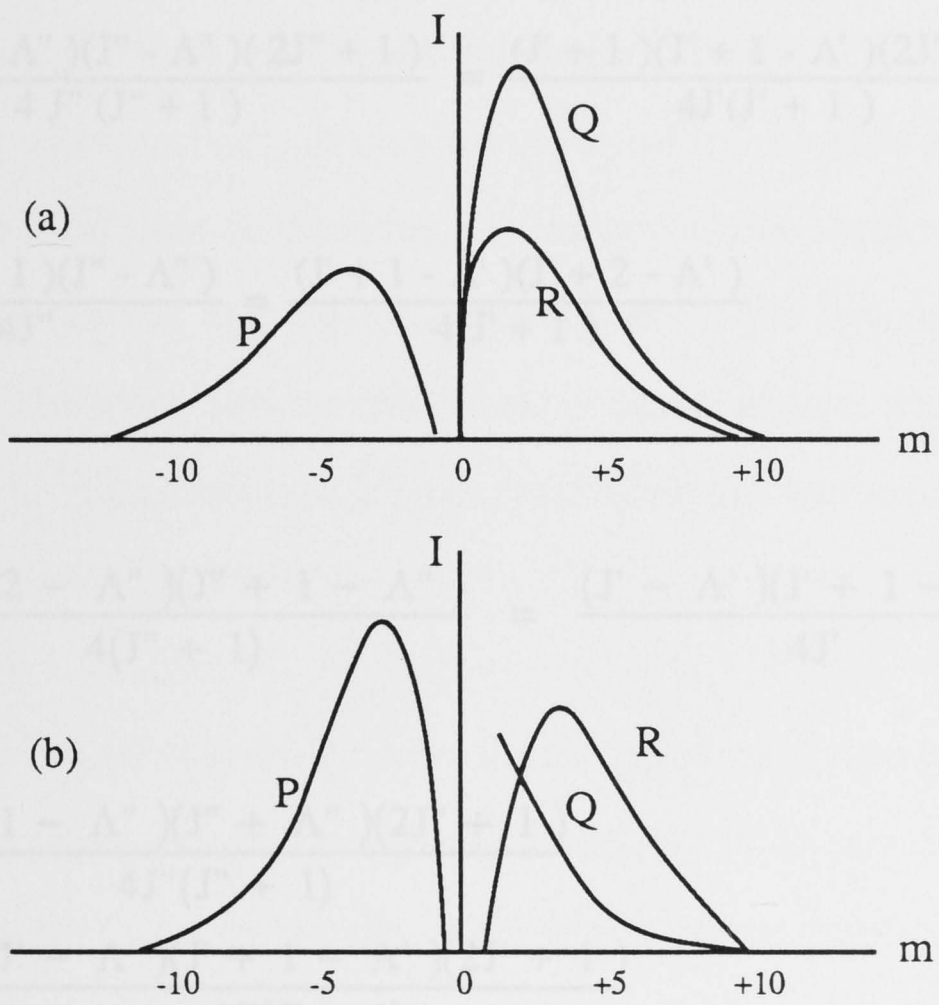

FIGURE 4.10 The intensity distribution in emission for bands with a Q-branch. (a) $^1\Pi$ - $^1\Sigma$ transition and (b) $^1\Pi$ - $^1\Pi$ transition.

The line intensities in thermal equilibrium can be expressed, apart from a constant and a frequency factor, as the product of the line strength and the Boltzmann factor. The values of S_J are given by the following Honl-London formulae.

For $\Delta\Lambda = 0$,

$$S_J^R = \frac{(J'' + 1 + \Lambda'')(J'' + 1 - \Lambda'')}{J'' + 1} = \frac{(J' + \Lambda')(J' - \Lambda')}{J'} \qquad (4.21a)$$

$$S_J^Q = \frac{(2J'' + 1)\Lambda''^2}{J''(J'' + 1)} = \frac{(2J' + 1)\Lambda'^2}{J'(J' + 1)} \qquad (4.21b)$$

$$S_J^P = \frac{(J'' + \Lambda'')(J'' - \Lambda'')}{J''} = \frac{(J' + 1 + \Lambda')(J' + 1 - \Lambda')}{J' + 1} \qquad (4.21c)$$

For $\Delta\Lambda = +1$,

$$S_J^R = \frac{(J'' + 2 + \Lambda'')(J'' + 1 + \Lambda'')}{4(J'' + 1)} = \frac{(J' + \Lambda')(J' - 1 + \Lambda')}{4J'} \qquad (4.22a)$$

$$S_J^Q = \frac{(J'' + 1 + \Lambda'')(J'' - \Lambda'')(2J'' + 1)}{4J''(J'' + 1)} = \frac{(J' + 1)(J' + 1 - \Lambda')(2J' + 1)}{4J'(J' + 1)} \qquad (4.22b)$$

$$S_J^P = \frac{(J'' - \Lambda'' - 1)(J'' - \Lambda'')}{4J''} = \frac{(J' + 1 - \Lambda')(J' + 2 - \Lambda')}{4(J' + 1)} \qquad (4.22c)$$

For $\Delta\Lambda = -1$,

$$S_J^R = \frac{(J'' + 2 - \Lambda'')(J'' + 1 - \Lambda'')}{4(J'' + 1)} = \frac{(J' - \Lambda')(J' + 1 - \Lambda')}{4J'} \qquad (4.23a)$$

$$S_J^Q = \frac{(J'' + 1 - \Lambda'')(J'' + \Lambda'')(2J'' + 1)}{4J''(J'' + 1)} = \frac{(J' - \Lambda')(J' + 1 - \Lambda')(2J' + 1)}{4J'(J' + 1)} \qquad (4.23b)$$

$$S_J^P = \frac{(J'' - 1 + \Lambda'')(J'' + \Lambda'')}{4J''} = \frac{(J' + 1 + \Lambda')(J' + 2 + \Lambda')}{4'(J' + 1)} \qquad (4.23c)$$

The only restriction on the above formulae is that they are valid only for the case where there is noninteraction of the rotation and electronic motions. The electronic spectrum exhibits only one other feature and that is an intensity alternation in the rotational line intensities. This line intensity alternation is similar to that observed in Raman spectra for homonuclear molecules. Due to nuclear spin interaction the odd

numbered or the even numbered rotational states have a greater statistical weight and are thus higher in transition probability. Also, these states known as strong and weak states are symmetric (s) and antisymmetric (a) or vice versa depending on the statistics of the nuclei. This results in one further transition rule of s $\mapsto$ a which holds for electronic transitions and produces this line intensity alternation in the rotational branches.

4.5 Electronic Angular Momentum

In general, the classification of molecular electronic states is analogous to that for atomic energy states which are "pure" electronic states. The electronic orbital angular momentum L in an atom is a constant since the motion of the electrons takes place in a spherically symmetric electric field and the electron spin can be neglected,. However, in a diatomic molecule the only symmetry that exists is the symmetry about the internuclear axis. Therefore, only the component of orbital angular momentum about this axis is constant. A precession of L takes place about the internuclear axis with a constant component $M_L h/2\pi$, where

$M_L = L, L - 1, L - 2, ..., -L$

Reversing the electric field doesn't change the energy of the system but will change M_L to $-M_L$ and therefore states differing only in the sign of M_L are degenerate (i.e. have the same energy). As the electric field of the system becomes stronger, L precesses at a greater rate while M_L remains well defined. Therefore, it is appropriate to classify electronic states of diatomic molecules according to the value of $|M_L|$ and so we define $\Lambda = |M_L|$. Λ represents the component of orbital angular momentum about the internuclear axis and its magnitude is given by $\Lambda h/2\pi$ (see figure 4.11). Λ also only takes the values,

$\Lambda = 0, 1, 2, ..., L$

According to whether L = 0, 1, 2, ..., the corresponding molecular state is designated a Σ , Π , Δ , Φ , ... state. All other states except for the Σ state ($\Lambda = 0$) are doubly degenerate.

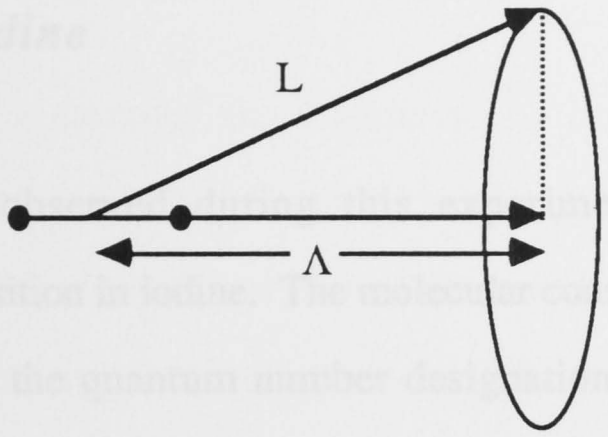

FIGURE 4.11 The precession of orbital angular momentum L about the internuclear axis.

If the electron spin is taken into account, the spin of individual electrons will form a resultant S which will be either integral or half integral depending on whether the total number of electrons for the molecule is even or odd, respectively. For a Σ state S is fixed in space as long as the molecule is not rotating, since S is not affected by the electric field. For other states, however, with $\Lambda \neq 0$ there is an internal magnetic field in the direction of the internuclear axis resulting from the orbital motion of the electrons. This can cause a coupling between the rotational and electronic motions (discussed in the next section) that results in a precession of S about the electric field direction (i.e. along the internuclear axis) with a constant component M_s with a magnitude $M_s h/2\pi$. For molecules, M_s is denoted by Σ, which is not to be confused with the molecular state having zero orbital angular momentum:

$\Sigma = S, S - 1, S - 2, ..., -S$

There are $2S + 1$ possible states since S can be negative; however, it is not defined for states with $\Lambda = 0$ (i.e. Σ states). A state with $\Lambda \neq 0$ will split into $2S + 1$ different energy levels. Therefore, a state with $\Lambda \neq 0$ is a multiple with $2S + 1$ components. If $\Lambda = 0$, then there is no magnetic field in the direction of the internuclear axis and Σ is undefined and no splitting will occur. Σ states are singlets as long as the molecule is not rotating.

4.6 Molecular Iodine

4.6.1 Coupling

The spectral lines observed during this experiment corresponded to the $B^3\Pi_{0u^+} \leftrightarrow X^1\Sigma_g^+$ transition in iodine. The molecular constants for this transition are shown in table 4.2 and the quantum number designations for the absorption lines scanned are shown in table 4.3. The Π state is a doubly degenerate, positive, odd triplet (Λ=1, S=1) and the Σ state is a non-degenerate, positive, even singlet (Λ=0, S=0). Iodine is a homonuclear molecule and therefore possesses two types of symmetry; (i) symmetry about any plane passing through both nuclei and (ii) centre symmetry about the midpoint of the internuclear axis. The states are classified by the sign change in their electronic eigenfunctions when reflected about both these symmetry points. Positive means the electronic eigenfunctions remain unchanged after reflection about (i) and negative means the electronic eigenfunctions change in sign. An even (g) sign indicates the electronic eigenfunctions remain unchanged after reflection about (ii) and odd (u) indicates the electronic eigenfunctions change sign. Since iodine is a homonuclear molecule the nuclear spin affects the observed band spectra causing an intensity alternation (Herzberg, 1950) in the ratio of (I + 1) / I for the even / odd numbered rotational levels making up the rotational fine structure. For iodine the nuclear spin I = 5/2. Therefore the intensity alternation is in the ratio of 7 : 5 for the even : odd states.

In a molecule, coupling occurs between the rotational and electronic motions causing alterations in the energy levels of the molecular system and resulting in further selection rules becoming important when considering possible transitions. The different angular momenta in the molecule, electronic spin, electronic orbital angular momentum, and angular momentum of nuclear rotation, form a resultant that is always designated **J**. Different modes of coupling occur for different molecular states and are treated in a manner first done by Hund (1927).

The $^1\Sigma_g^+$ state for iodine exhibits no coupling since both the spin **S** and the orbital angular momentum **L** of the electrons are zero. The $^3\Pi_{0u^+}$ state corresponds to

Hund's case (a) or (c).

For Hund's case (a) it is assumed that the interaction between the nuclear rotation and the electronic motion (orbital and spin) is weak whereas the electronic motion itself is coupled very strongly to the line joining the nuclei. The coupling is similar to that of a symmetric top, except $\mathbf{\Lambda}$ is replaced by $\mathbf{\Omega}$. The rotational energy for case (a) is identical to that of a symmetric top with $\mathbf{\Omega}$ as the angular momentum about the internuclear axis (Herzberg, 1950). Neglecting the centrifugal stretching terms (see equation (4.11))

$$F_v(J) = B_v\left[J(J+1) - \Omega^2\right] \tag{4.24}$$

where $A\Omega^2$ is omitted since it is a constant for a given electronic state and is therefore included in the electronic energy. For a given multiplet term, B_v is also a constant for each multiplet component except when the multiplet splitting is large. Ω is an integral or half-integral depending on whether the number of electrons is even or odd respectively and J is an integral when Ω is an integral since $\mathbf{\Omega}$ is the component of **J**. **J** also cannot be less than its component $\mathbf{\Omega}$. and levels with $J < \Omega$ do not occur. Therefore for a given Ω

$$J = \Omega, \Omega+1, \Omega+2, \ldots \tag{4.25}$$

Under certain circumstances, particularly for heavy molecules such as iodine, the interaction between **L** and **S** maybe stronger than the interaction with the internuclear axis. $\mathbf{\Lambda}$ and $\mathbf{\Sigma}$ are undefined for this case and instead **L** and **S** first form a resultant J_a which is then coupled to the internuclear axis by the component Ω. The electronic angular momentum Ω and the rotational nuclear angular momentum **N** form the resultant angular momentum **J** just as in case (a). This is Hund's case (c). Equations (4.25) and (4.26) give the rotational energy levels and their J values as for case (a). For the transition from case (a) to case (c), the only change involves the splitting of the ${}^3\Pi_{0u^+}$ state into two zero (0) states, a 0^+ and a 0^- state, which in case (c) are independent of each other, as are the other multiplet components.

4.6.2 Selection Rules

(i) General Selection Rules

For the quantum number J, the total angular momentum, the selection rule is

$$\Delta J=0, \pm 1, \text{ with the restriction } J = 0 \not\leftrightarrow J = 0 \tag{4.26}$$

The symmetry selection rules only allow positive terms to combine with negative terms and vice versa

$$+ \leftrightarrow -, \quad + \not\leftrightarrow +, \quad - \not\leftrightarrow - \tag{4.27}$$

and for identical nuclei (i.e.: iodine), symmetric terms can combine only with symmetric terms and anti-symmetric terms can combine only with anti-symmetric terms

$$s \leftrightarrow s, \quad a \leftrightarrow a, \quad s \not\leftrightarrow a \tag{4.28}$$

Finally for the case of a molecule with nuclei of like charge (i.e. iodine), even electronic states only combine only with odd electronic states

$$g \leftrightarrow u, \quad g \not\leftrightarrow g, \quad u \not\leftrightarrow u \tag{4.29}$$

(ii) Selection Rules for Hund's Case (a)

There are selection rules that hold for both Hund's case (a) and (b) but not for other coupling cases. In cases (a) and (b), the quantum number Λ is defined and

$$\Delta\Lambda = 0, \pm 1 \tag{4.30}$$

This corresponds to the selection rule for M_L in atoms in an electric or magnetic field and means that Σ–Σ, Σ–Π, Π–Π, Π–Δ, ... transitions are allowed: however, transitions such as Σ–Δ, Σ–Φ, Π–Φ, ... are not. Furthermore, Σ^+ states cannot combine with Σ^- states; that is

$$\Sigma^+ \leftrightarrow \Sigma^+, \quad \Sigma^- \leftrightarrow \Sigma^-, \quad \Sigma^+ \not\leftrightarrow \Sigma^- \tag{4.31}$$

however, both Σ^+ and Σ^- states can combine with Π states. The resultant spin **S** is defined for (a) and (b) and therefore the selection rule for the associated quantum number is

$$\Delta S = 0 \tag{4.32}$$

This implies that only states of the same multiplicity can combine with each other, however, for increasing interaction between **S** and $\boldsymbol{\Lambda}$ (i.e. increasing nuclear charge),

this rule holds less and less rigorously, as is the case for the $B^3\Pi_{0u^+} \leftrightarrow X^1\Sigma_g^+$ transition in iodine.

(iii) Selection Rules for Hund's Case (c)

In Hund's case (c) only the quantum number Ω, the total electronic angular momentum about the internuclear axis is well defined. The selection rule for this quantum number is

$$\Delta\Omega = 0, \pm 1 \tag{4.33}$$

The analogue of equation (4.32) also holds,

$$0^+ \leftrightarrow 0^+, \quad 0^- \leftrightarrow 0^-, \quad 0^+ \not\leftrightarrow 0^- \tag{4.34}$$

and if both states have $\Omega = 0$ (not the case for iodine), then no Q-branch occurs.

(iv) Violation of Approximate Selection Rules

The selection rule, $\Delta S = 0$, holds less strictly with increasing spin-orbit interaction (i.e. increasing nuclear charge) and singlet-triplet intercombinations have been observed for molecules as relatively light as CO (Herzberg, 1950). For heavier molecules such as iodine, the $^3\Pi$ - $^1\Sigma$ transitions (Cameron bands) represent fairly intense absorption and emission bands (transition to Hund's case (c)). If the $^3\Pi$ state belongs to Hund's case (b), nine branches are possible in the $^3\Pi$ - $^1\Sigma$ bands. However, for large multiplet splitting, (i.e. iodine) as case (a) and finally case (c) are approached, only the sub-bands $^3\Pi_0$ - $^1\Sigma$ (with two bands) and $^3\Pi_1$ - $^1\Sigma$ (with three branches) occur due to the selection rule $\Delta\Omega = 0, \pm 1$.

4.6.3 Molecular Constants, Quantum Numbers and other such things

TABLE 4.2 Molecular constants for the $B^3\Pi_{0u^+} \leftrightarrow X^1\Sigma_g^+$ transition in iodine

State	T_e	w_e	$w_e x_e$	$w_e y_e$	B_e	α_e	r_e (10^{-1})	$\nu_{0,0}$
$B^3\Pi_{0u^+}$	15769.01	125.69	0.764	0	0.02903	0.000158	3.016	
$X^1\Sigma_{g^+}$	0	214.50	0.614	-0.000895	0.03737	0.000113	2.666	15598.3

TABLE 4.3 Quantum number designation for absorption lines scanned

Wavelength (nm)	v"	v'	J"	J'	Branch
570.521	0	16	0	1	R
570.519	0	16	1	2	R
570.519	0	16	2	3	R
570.520	0	16	3	4	R
570.521	0	16	4	5	R
570.523	0	16	5	6	R
570.525	0	16	6	7	R
570.981	0	16	38	39	R
571.225	1	18	21	20	P

The Frank-Condon factors and R-centroid values (computed using a rotationless potential curve) for the vibrational transitions v" = 0-5 to v' = 0-67 (J" = J' = 0 and J" = J' = 100) for iodine are given in Brewer and Tellinghuisen (1971) and Tellinghuisen (1978). The band origins of the vibrational transitions (for the relatively well populated lower vibrational levels of v" = 0-5) for iodine in the 560-600 nm wavelength region of Rhodamine 6G are given in table 4.4.

4.7 The Computer Code

4.7.1 General Description

For a given electro-vibrational transition, the wavenumber values for each rotational transition line were calculated using equations (4.14), (4.15) and (4.16) over a pre-determined interval of values for the rotational quantum number J. The contribution from the electrons and the centrifugal force were neglected. Molelcular constants were taken from Herzberg and Huber (1979).

From the calculated rotational line wavenumbers, an interval over the wavenumber range between the lowest to the highest value was determined. This interval was then divided into a number of points about each transition line using a given rotational linewidth and an integer value (the number of points in the wavenumber interval was

Table 4.4
Band origins of iodine in the
560-600 nm wavelength region
of the spectrum

Wavelength (nm)	v"	v'	Wavelength (nm)	v"	v'	Wavelength (nm)	v"	v'
599.693	0	9	588.445	2	16	592.863	4	19
595.716	0	10	585.015	2	17	589.555	4	20
591.85	0	11	581.68	2	18	586.341	4	21
588.092	0	12	578.44	2	19	583.219	4	22
584.437	0	13	575.291	2	20	580.186	4	23
580.885	0	14	572.23	2	21	577.239	4	24
577.431	0	15	569.256	2	22	574.378	4	25
574.072	0	16	566.366	2	23	571.6	4	26
570.807	0	17	563.558	2	24	568.902	4	27
567.633	0	18	560.831	2	25	566.283	4	28
564.546	0	19				563.741	4	29
561.546	0	20	599.458	3	15	561.274	4	30
			595.839	3	16			
595.564	1	12	592.322	3	17	596.89	5	20
591.817	1	13	588.905	3	18	593.596	5	21
588.174	1	14	585.583	3	19	590.396	5	22
584.633	1	15	582.356	3	20	587.288	5	23
581.19	1	16	579.22	3	21	584.27	5	24
577.844	1	17	576.173	3	22	581.338	5	25
574.591	1	18	573.213	3	23	578.492	5	26
571.429	1	19	570.337	3	24	575.729	5	27
568.355	1	20	567.543	3	25	573.047	5	28
565.367	1	21	564.83	3	26	570.444	5	29
562.464	1	22	562.196	3	27	567.918	5	30
						565.468	5	31
595.605	2	14	599.771	4	17	563.092	5	32
591.974	2	15	596.267	4	18	560.788	5	33

greater for larger integer values). The optical depth and fringe shift values were then calculated at these points.

For the initial given J value, beginning at the first point in the wavenumber interval, the optical depth and refractivity contributions were determined from the P, Q and R-branch rotational transition lines by passing the values for; the line centre frequency of the line being considered, the detuning of the wavenumber point from that line centre, the collisional broadening width, the doppler width, the oscillator strength and the pathlength of the medium to a subroutine that determined a single value for the optical depth and the fringe shift for that point assuming the Voigt profiles shown in equations (3.23) and (3.24) and using the equations (A3) and (A4) for the actual calculations. The value of J was then incremented in unit steps and the above process repeated until the final value of J was reached. Each optical depth and refractivity value calculated was summed until a final value was attained that represented all the contributions of the transition lines considered to the optical depth and fringe shift value at that point (wavenumber). The process was then repeated over the range of J for the next point (wavenumber) and so on until the optical depth and refractivity for the entire wavenumber interval of interest was determined. Physically the optical depth value is a measure of the absolute absorption and the fringe shift, a measure of the absolute refractivity at that point. To determine theoretically the fringe shift obtained when scanning the dye laser over a frequency range, the fringe shift difference between adjacent points (wavenumbers) is taken and then summed to produce the total fringe shift that would occur. To determine theoretically the fringe shift obtained across the reflected shock, the fringe shift value is determined for the wavenumber point, pre-reflected shock at a temperature of T_1 and post-reflected shock at a temperature of T_2 ($T_1 < T_2$). The difference in the fringe shift values is the fringe shift that theoretically should occur at that wavelength (wavenumber).

4.7.2 Flow Diagram, Listing and Sample Output

A flow diagram, listing and output of the code is included on the next few pages.

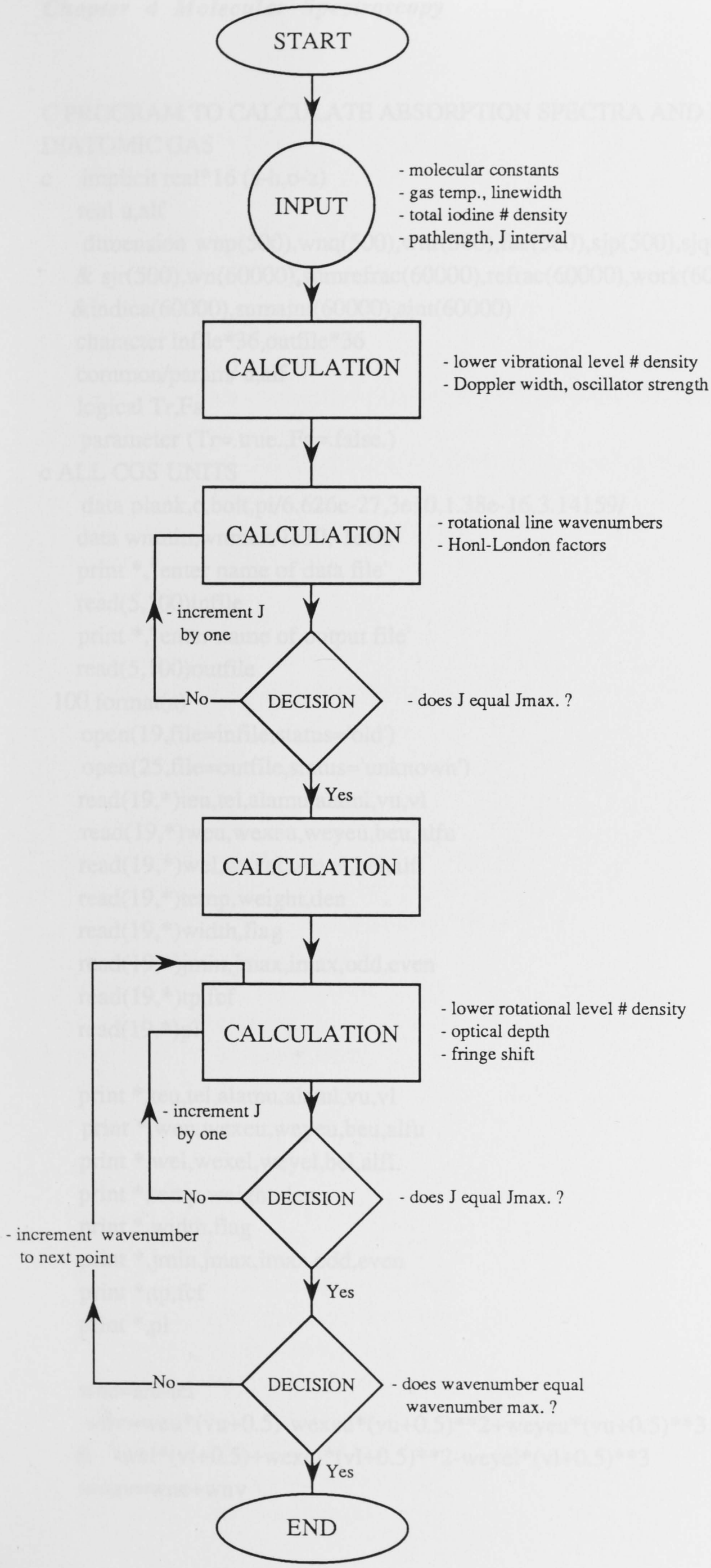

Figure 4.12 Flow chart

```
C PROGRAM TO CALCULATE ABSORPTION SPECTRA AND DISPERSION OF
DIATOMIC GAS
c     implicit real*16 (a-h,o-z)
      real u,alf
       dimension wnp(500),wnq(500),wnr(500),fac(500),sjp(500),sjq(500),
     & sjr(500),wn(60000),sumrefrac(60000),refrac(60000),work(60000),
     &indica(60000),sumaint(60000),aint(60000)
      character infile*36,outfile*36
      common/param/ u,alf
      logical Tr,Fa
       parameter (Tr=.true.,Fa=.false.)
c ALL CGS UNITS
       data plank,c,bolt,pi/6.626e-27,3e10,1.38e-16,3.14159/
      data wnmin,wnmax/1e30,-1e30/
      print *,' enter name of data file'
      read(5,100)infile
      print *,' enter name of output file'
      read(5,100)outfile
  100 format(a)
       open(19,file=infile,status='old')
       open(25,file=outfile,status='unknown')
      read(19,*)teu,tel,alamu,alaml,vu,vl
       read(19,*)weu,wexeu,weyeu,beu,alfu
      read(19,*)wel,wexel,weyel,bel,alfl
      read(19,*)temp,weight,den
      read(19,*)width,flag
      read(19,*)jmin,jmax,imax,odd,even
      read(19,*)tp,fcf
      read(19,*)pl

      print *,teu,tel,alamu,alaml,vu,vl
       print *,weu,wexeu,weyeu,beu,alfu
      print *,wel,wexel,weyel,bel,alfl
      print *,temp,weight,den
      print *,width,flag
      print *,jmin,jmax,imax,odd,even
      print *,tp,fcf
      print *,pl

      wne=teu-tel
       wnv=weu*(vu+0.5)-wexeu*(vu+0.5)**2+weyeu*(vu+0.5)**3
     &   -wel*(vl+0.5)+wexel*(vl+0.5)**2-weyel*(vl+0.5)**3
       wnev=wne+wnv
```

```
      bvu=beu-alfu*(vu+0.5)
      bvl=bel-alfl*(vl+0.5)
      part=(bolt*temp)/(plank*c*bvl)
      parvib=0.0
      w0=wel-wexel+0.75*weyel
      w0x0=wexel-1.5*weyel
      w0y0=weyel
      ivmax=w0/(2*w0x0)
      do 987 iv=0,ivmax
      argvib=(((w0*iv)-(w0x0*iv**2)+(w0y0*iv**3))*plank*c)/(bolt*temp)
  987 parvib=parvib+exp(-argvib)
      argvl=(((w0*vl)-(w0x0*vl**2)+(w0y0*vl**3))*plank*c)/(bolt*temp)
      denvl=(den*exp(-argvl))/parvib
      dopplr=wnev*7.16e-7*sqrt(temp/weight)
      a=sqrt(alog(2.))*width/dopplr
      print *,dopplr,a
      approx=sqrt(1+a*a)
      aaaaaa=approx*dopplr
      osc=4.7019290E+29*wnev*fcf*tp

      jjdj=jmax-jmin+1
      do 1 jj=1,jjdj
      j=jmin+jj-1
      wnp(jj)=wnev+bvu*j*(j+1)-bvl*(j+1)*(j+2)
      wnq(jj)=wnev+bvu*j*(j+1)-bvl*j*(j+1)
      wnr(jj)=wnev+bvu*(j+1)*(j+2)-bvl*j*(j+1)
      print *,wnp(jj),wnq(jj),wnr(jj)
      arg=bvl*j*(j+1)*plank*c/(bolt*temp)
      fac(jj)=denvl*exp(-arg)
      sjp(jj)=sjj(-1,j+1,alamu,alaml)
      sjq(jj)=sjj( 0,j  ,alamu,alaml)
      sjr(jj)=sjj( 1,j,alamu,alaml)

c     test if j odd or even
      testit=j*1./2.-j/2
c      print *,' testit=',testit,'    j=',j
      if(testit.gt.0.25)fac(jj)=fac(jj)*odd/part
      if(testit.lt.0.25)fac(jj)=fac(jj)*even/part
      if(wnp(jj).lt.wnmin)wnmin=wnp(jj)
      if(wnq(jj).lt.wnmin)wnmin=wnq(jj)
      if(wnr(jj).lt.wnmin)wnmin=wnr(jj)
      if(wnp(jj).gt.wnmax)wnmax=wnp(jj)
      if(wnq(jj).gt.wnmax)wnmax=wnq(jj)
    1 if(wnr(jj).gt.wnmax)wnmax=wnr(jj)
```

```
      jjjmmm=sqrt(part/2)-0.5
      print *,'jjjmmm = ',jjjmmm
      rmmm=-(bvu+bvl)/(2*(bvu-bvl))
      print *,'rmmm = ',rmmm
      print *,wnmin,wnmax
      num=0
      do 30 j=1,jjdj
      do 31 i=0,2*imax
      num=num+1
      wn(num)=wnp(j)+(i-imax)*aaaaaa*6/imax
      num=num+1
      wn(num)=wnq(j)+(i-imax)*aaaaaa*6/imax
      num=num+1
      wn(num)=wnr(j)+(i-imax)*aaaaaa*6/imax
   31 continue
   30 continue
      pl=pl/100
      dopplr=c*dopplr
      width=c*width
      npts=num
      call sort(wn,work,indica,npts)

      do 4 i=1,npts
      k=0.
      sumrefrac(0)=0.
      sumaint(0)=0
      do 5 j=1,jjdj

      k=k+1
      freqp=c*wnp(j)
      delwnp=c*(wn(i)-wnp(j))
      pop=(fac(j+1)*sjp(j))*1.0E+06
       sumrefrac(k)=sumrefrac(k-1)+abdis(tr,'FS',delwnp,
     +width,dopplr,pop,osc,pl,freqp)
       sumaint(k)=sumaint(k-1)+abdis(fa,'OD',delwnp,
     +width,dopplr,pop,osc,pl,freqp)

      k=k+1
      freqq=c*wnq(j)
      delwnq=c*(wn(i)-wnq(j))
      pop=(fac(j+1)*sjq(j))*1.0E+06
       sumrefrac(k)=sumrefrac(k-1)+flag*abdis(tr,'FS',delwnq,
     +width,dopplr,pop,osc,pl,freqq)
```

```
      sumaint(k)=sumaint(k-1)+flag*abdis(fa,'OD',delwnq,
     +width,dopplr,pop,osc,pl,freqq)

      k=k+1
      freqr=c*wnr(j)
      delwnr=c*(wn(i)-wnr(j))
      pop=(fac(j+1)*sjr(j))*1.0E+06
       sumrefrac(k)=sumrefrac(k-1)+abdis(tr,'FS',delwnr,
     +width,dopplr,pop,osc,pl,freqr)
       sumaint(k)=sumaint(k-1)+abdis(fa,'OD',delwnr,
     +width,dopplr,pop,osc,pl,freqr)

    5 continue
      refrac(i)=sumrefrac(k)
      aint(i)=sumaint(k)
    4 continue
      write(25,500)npts
  500 format(i5)
      do 400 i=1,npts
  400 write(25,501)wn(i),aint(i),refrac(i)
  501 format(3(2x,g15.9))
      stop
      end
      function sjj(jdelj,j,alamu,alaml)
c     implicit real*16 (a-h,o-z)
      dellam=alamu-alaml
      if(dellam)1,2,3
    1 if(jdelj)4,5,6
    4 sjj=(j-1+alaml)*(j+alaml)/(4*j)
      return
    5 sjj=0.0
      if(j.ne.0)sjj=(j+1-alaml)*(j+alaml)*(2*j+1)/(4*j*(j+1))
      return
    6 sjj=(j+2-alaml)*(j+1-alaml)/(4*(j+1))
      return
c
c

    2 if(jdelj)7,8,9
    7 sjj=(j+alaml)*(j-alaml)/j
      return
    8 sjj=0.0
      if(j.ne.0.0)sjj=(2*j+1)*alaml*alaml/(j*(j+1))
      return
```

```
   9 sjj=(j+1+alaml)*(j+1-alaml)/(j+1)
     return
c

c
   3 if(jdelj)10,11,12
  10 sjj=(j-1-alaml)*(j-alaml)/(4*j)
     return
  11 sjj=0.0
     if(j.ne.0.0)sjj=(j+1+alaml)*(j-alaml)*(2*j+1)/(4*j*(j+1))
     return
  12 sjj=(j+2+alaml)*(j+1+alaml)/(4*(j+1))
     return
c
     end

************************************************************************
**
* FUNCTION NAME: AbDis      version 1.1 8th Feb 1990              *
* Calculate the refractive index as a function of temperature for a  *
* given set of atomic and experimental parameters.                   *
************************************************************************
**
*
      real function abdis(disp,option,D,G,B,N,f,l,nu0)
     implicit none
     logical Tr,Fa
      parameter (Tr=.true.,Fa=.false.)
     real r0/2.817939e-15/      !classical electron radius
     real c /2.9979246e8/       !speed of light
     real pi/3.141592654/
     real k/1.38062e-23/        !Boltzmanns const.
     real umu/1.66043e-27/      !unified mass unit
     real D                    !detuning in calculation
     real G                    !collisional FWHM at T=T,T0  [Hz]
     real B                    !FWHM doppler width Hz
     real N                    !atomic population [per cu. m]
     real u                    !detuning parameter
     real f                    !oscillator strength
     real l                    !pathlength [m]
     real alf                  !ratio of linewidths
     real nu0                   !centre frequency
```

```
      real tlth/1.6651092/      !2*sqrt(ln(2))
      real lo,hi               !limits on the integral
      real aerr/5e-5/           !absolute error limit
      real rerr/5e-5/           !relative error limit
      real error               !estimated error returned
      integer ier              !error parameter
      real intgrl              !value of the integral
      character*2 option        !disp display mode option
      real DCADRE               !integration function from IMSL
      logical disp             !true if dispersion calculation
*
      External FunA,FunD
      common/param/ u,alf
*
1     format(a,$)
2     format(a2)
36    format(a36)
*
      alf=G/B
      lo=-15*(alf+1)
      Hi=+15*(alf+1)
      u=D*TLTH/B
      if(disp) then
       Intgrl=DCADRE(funD,lo,hi,aerr,rerr,error,ier)
       if(option.eq.'SE') then     !sellmeier error
        abdis=-intgrl*D*TLTH/(PI**0.5*B)
       elseif(option.eq.'FS') then !Fringe shift
        abdis=intgrl*N*f*L*r0*C*TLTH/(4*PI**1.5*B)
       elseif(option.eq.'MP') then !Measures P
        abdis=1E7*intgrl*r0*c*sqrt(pi)
       endif
      else
       Intgrl=DCADRE(funA,lo,hi,aerr,rerr,error,ier)
       if(option.eq.'OD') then     !optical depth
        abdis=intgrl*N*f*L*r0*c*alf*TLTH/(2*PI**1.5*B)
       elseif(option.eq.'A') then !absorption
        abdis=exp(-intgrl*N*f*L*r0*c*alf*TLTH/(2*PI**1.5*B))
       elseif(option.eq.'MH') then !Measures H
        abdis=1E7*intgrl*r0*c*alf/sqrt(pi)
       endif
      endif
      return
      end
*
```

```
*
**********************************************************************
* FUNCTION NAME: FunD       Vers 1.1  30th Aug 85            *
* calculates the integrand for the program Voigt, dispersion    *
**********************************************************************
*
    real function funD(s)
    implicit none
    real s          !velocity parameter
    real u,alf
*
    common/param/ u,alf
*
    funD=(s-u)/((s-u)**2+alf**2)*exp(-s**2)
D      write(*,*) ' funD,s,u,alf: ',funD,s,u,alf
    return
    end
*
*
**********************************************************************
* FUNCTION NAME: FunA       Vers 1.1  30th Aug 85            *
* calculates the integrand for the program Voigt, absorption    *
**********************************************************************
*
    real function funA(s)
    implicit none
    real s          !velocity parameter
    real u,alf
*
    common/param/ u,alf
*
    funA=exp(-s**2)/((s-u)**2+alf**2)
D      write(*,*) ' funA,s,u,alf: ',funA,s,u,alf
    return
    end

    subroutine sort(wn,work,indica,npts)
c   implicit real*16 (a-h,o-z)
    dimension wn(1),work(1)
    integer indica(1)
     print *,' npts = ',npts
    do 1 i=1,npts
    indica(i)=-10
```

```
   1 work(i)=wn(i)
     do 6 m=1,npts
     amin=1e30
     do 2 i=1,npts
     if(i.eq.indica(i))go to 2
     if(work(i).gt.amin)go to 2
     ihold=i
     amin=work(i)
   2 continue
     wn(m)=amin
   6 indica(ihold)=ihold
c     do 7 i=1,npts
c   7 print *,wn(i)
     return
     end
```

The output below is written to the computer screen immediately the program commences and is at first a confirmation of the data supplied; the molecular constants; the temperature; the total iodine number density; the Gaussian linewidth; the interval for J; the oscillator strength and the pathlength. The calculated rotational transition lines are then shown arranged in their respective branches (i.e. P, Q and R), followed finally by the calculated values for; the J value for the rotational line containing the highest number density; the value for J at the bandhead (rounded to the nearest integer); the maximum and minimum wavenumber value in the interval and the number of points in the interval.

```
15769.01     0.0000000E+00  1.000000     0.0000000E+00   16.00000
0.0000000E+00
125.6900     0.7640000     0.0000000E+00  2.9030001E-02  1.5800000E-04
214.5000     0.6140000    -8.9500000E-04  3.7370000E-02  1.1300000E-04
323.0000      253.8000     5.9780001E+16
4.0000002E-03   1.000000
0         5          5  5.000000      7.000000
1.2000000E-36  7.1330001E-03
5.080000
1.4157803E-02  0.2352214
17527.72      17527.80      17527.85
17527.63      17527.78      17527.88
17527.51      17527.73      17527.89
17527.37      17527.67      17527.88
17527.21      17527.58      17527.85
17527.03      17527.47      17527.79
jjjmmm =         54
rmmm =    2.926244
17527.03      17527.89
npts =         198
```

Below is a small sample of the output data file of the theoretical calculation for the (16,0) vibrational, 0-5 rotational transition. The first number is the number of points in the wavenumber interval. The first column is wavenumber (cm^{-1}), the second column is optical depth and the third column is fringe shift.

198

17526.9375	0.487273719E-04	0.569889834E-02
17526.9551	0.528538803E-04	0.588452118E-02
17526.9727	0.576848543E-04	0.608647475E-02
17526.9902	0.634228418E-04	0.630768435E-02
17527.0078	0.703566620E-04	0.655196141E-02
17527.0254	0.789117839E-04	0.682440354E-02
17527.0430	0.897396021E-04	0.713203987E-02
17527.0605	0.103884726E-03	0.748492545E-02
17527.0781	0.123119782E-03	0.789811835E-02
17527.0957	0.150673106E-03	0.839547534E-02
17527.1133	0.192988518E-03	0.901766494E-02
17527.1211	0.219787849E-03	0.935205724E-02
17527.1387	0.314261735E-03	0.103089456E-01
17527.1563	0.517148583E-03	0.117722070E-01
17527.1738	0.112744432E-02	0.145206051E-01
17527.1914	0.681330543E-02	0.230435077E-01
17527.2090	0.758793503E-01	0.815153588E-02
17527.2266	0.684550358E-02	-.668209512E-02
17527.2441	0.119548873E-02	0.202229782E-02
17527.2617	0.629803981E-03	0.509723369E-02
17527.2793	0.489665603E-03	0.707913423E-02
17527.2813	0.484574819E-03	0.727677485E-02
17527.2969	0.497381610E-03	0.884575769E-02
17527.2988	0.505738019E-03	0.904925819E-02
17527.3164	0.678829674E-03	0.111474106E-01
17527.3340	0.129888079E-02	0.144873606E-01
17527.3516	0.726769865E-02	0.238417350E-01
17527.3691	0.799035579E-01	0.854187366E-02
17527.3848	0.105021764E-01	-.881147664E-02
17527.3867	0.729861390E-02	-.670178002E-02
17527.4023	0.150697480E-02	0.224909768E-02
17527.4043	0.136293913E-02	0.282518263E-02
17527.4199	0.812176208E-03	0.614474574E-02
17527.4219	0.781423296E-03	0.646749465E-02
17527.4219	0.781423296E-03	0.646749465E-02
17527.4375	0.662173494E-03	0.875945389E-02
17527.4395	0.658682548E-03	0.902743638E-02

Chapter 5. METHODOLOGY

5.1 The Shock Tube

5.1.1. Design and Operation

The experiment was conducted in the A.N.U. Department of Physics and Theoretical Physics only non-free-piston shock tube. This tube was chosen because of the requirement for weak Mach reflection of a very slow incident shock speed.

The shock tube, shown in figure 5.1, can be broken down into two parts: (i) the high pressure reservoir, which is made of mild steel and has a circular cross-section with an internal diameter of 50 mm and (ii) the shock tube, constructed of welded angle aluminium with a square cross-section and an internal width of 50.8 mm (2"). The two sections are separated by a diaphragm and connected to a single rotary vacuum pump.

Fixed into the end of the high pressure reservoir that attaches to the shock tube was a mechanical pricker that is spring loaded and triggered by pulling up a stop. This pricker pierces the diaphragm, allowing the expansion into the shock tube of the high pressure driver gas. The test section was bolted onto the end of the shock tube with an end plate fixed to the back of it. The test section windows were made of quartz polished to flatness of $\lambda/4$ with a diameter of 60 mm.

Four lengths of resistance wire (each with a diameter of 3 mm) sheathed in insulating woven fiberglass tubing were wired in parallel to a welding power supply (3.6 amps, 35 volts, ~ 500 watts) and wrapped around the entire length of the shock tube. This was covered by multiple layers of aluminium foil in an attempt to minimize heat radiation from the tube to the surrounding room and maximize the heat input into the tube from the heating coils.

The operation of the tube was extremely simple. The welding power supply was turned on approximately one hour before the tube was to be first fired for the day. (Initially the tube was heated for two hours and then allowed to cool for one hour, heated again for one hour etc., but after a thermistor gauge was installed in the back

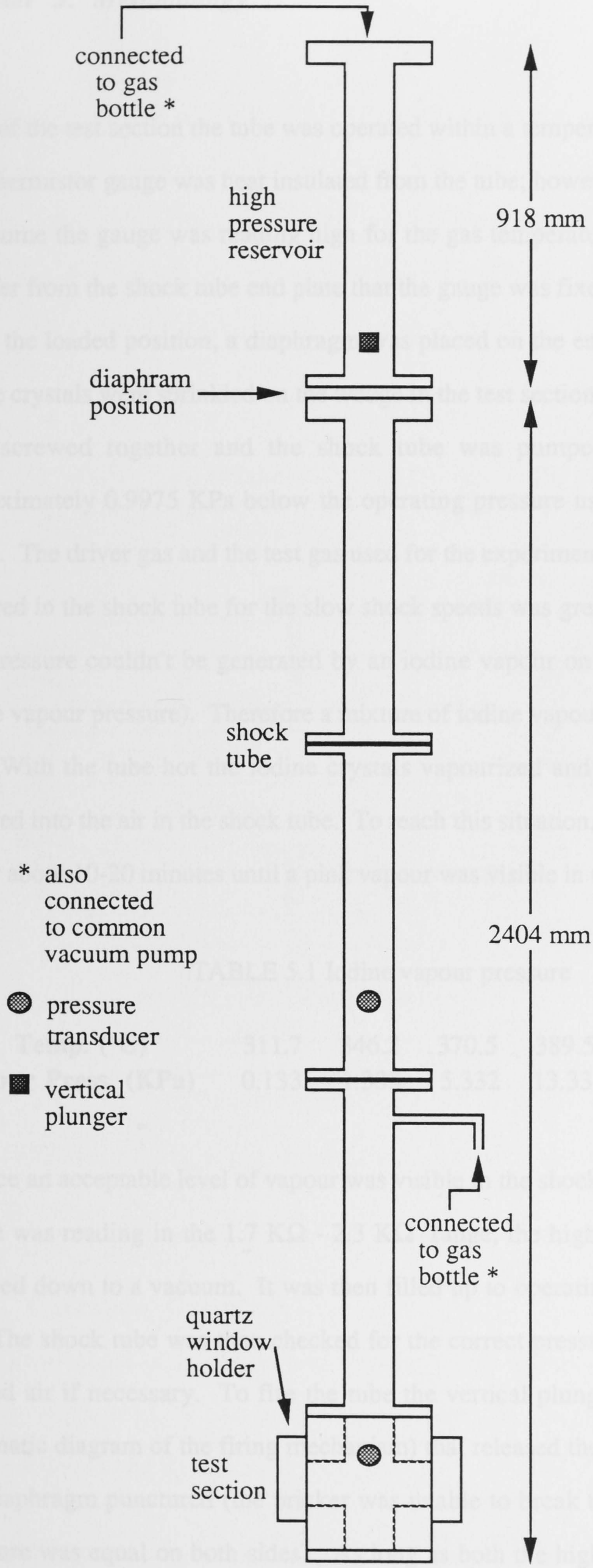

FIGURE 5.1
Schematic diagram of the Shock tube

plate of the test section the tube was operated within a temperature range of 55-70 °C. The thermistor gauge was heat insulated from the tube; however, it is only reasonable to assume the gauge was reading high for the gas temperature due to radiative heat transfer from the shock tube end plate that the gauge was fixed into. The pricker was set in the loaded position, a diaphragm was placed on the end of the shock tube and iodine crystals were sprinkled on the wedge in the test section. The two sections were then screwed together and the shock tube was pumped down to a pressure approximately 0.9975 KPa below the operating pressure using the common rotary pump. The driver gas and the test gas used for the experiment were air. The pressure required in the shock tube for the slow shock speeds was greater than 50.65 KPa and this pressure couldn't be generated by an iodine vapour only (see table 5.1 for the iodine vapour pressure). Therefore a mixture of iodine vapour air was used as the test gas. With the tube hot the iodine crystals vapourized and the iodine vapour then diffused into the air in the shock tube. To reach this situation, the tube was allowed to sit for about 10-20 minutes until a pink vapour was visible in the test section.

TABLE 5.1 Iodine vapour pressure

Temp. (°C)	311.7	346.2	370.5	389.5	432.8	456.0
Vapour Press. (KPa)	0.133	1.333	5.332	13.33	53.32	101.308

Once an acceptable level of vapour was visible in the shock tube and the thermistor gauge was reading in the 1.7 KΩ - 2.3 KΩ range, the high pressure reservoir was pumped down to a vacuum. It was then filled up to operating pressure with bottled air. The shock tube was then checked for the correct pressure and topped up using bottled air if necessary. To fire the tube the vertical plunger (see figure 5.2 for a schematic diagram of the firing mechanism) that released the pricker was pulled and the diaphragm punctured (the pricker was unable to break the diaphragm when the pressure was equal on both sides). As long as both the high pressure reservoir and the shock tube didn't leak, the tube could be left in the "ready to fire" mode safely for

an indefinite period of time. This allowed one person to run the tube and the experimental instruments with ease. Once fired, the tube was opened in two places: (i) the reservoir/shock tube connection and (ii) the end plate on the test section. The shock tube was cleaned of diaphragm fragments and iodine vapour. Turn around time between shots, once the tube was at operating temperature, was about 10-20 minutes.

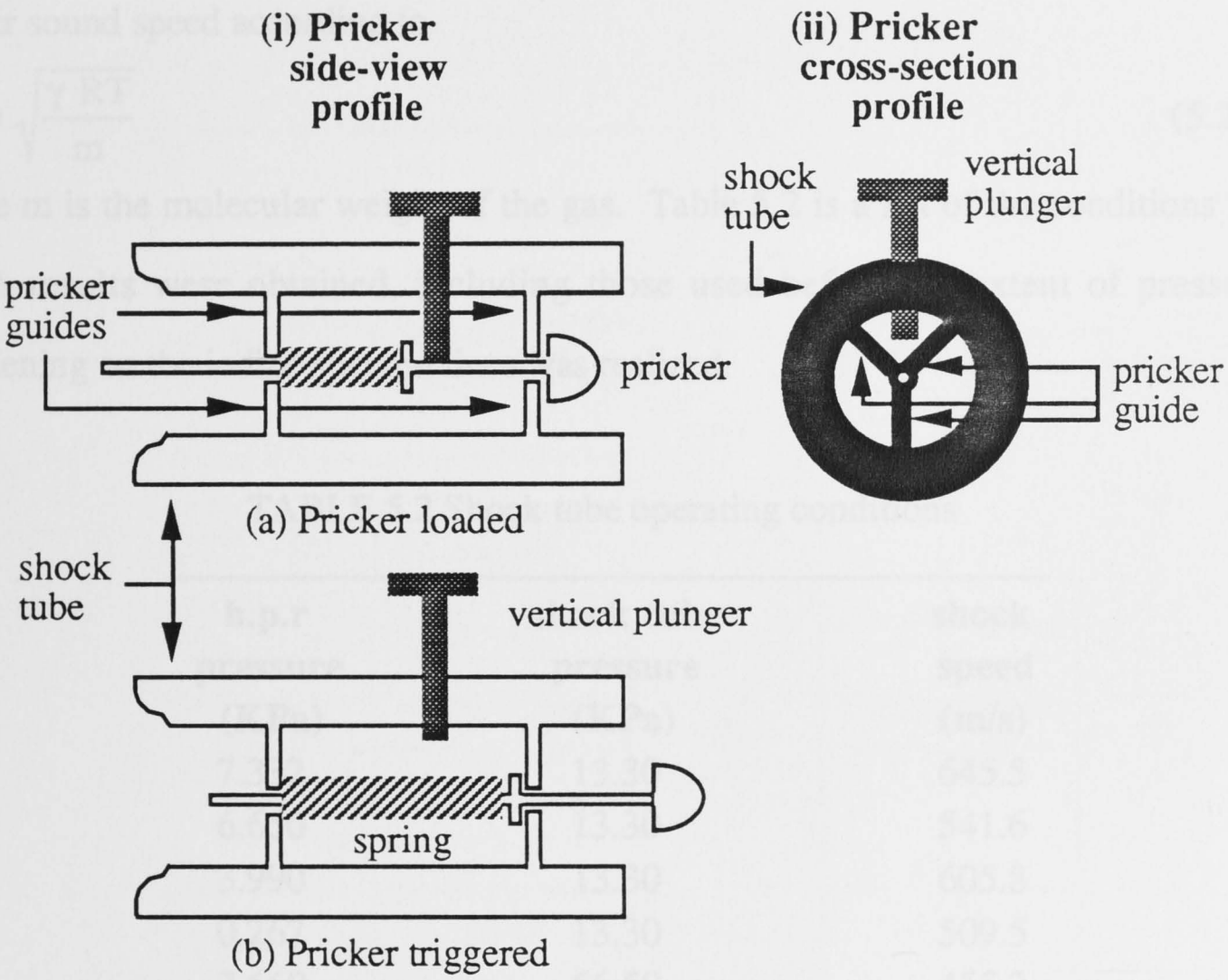

FIGURE 5.2 The pricker mechanism used to fire the shock tube

5.1.2 Operating Condition

For an ideal gas in a constant area shock tube, the relationship between parameters such as shock velocity and initial test gas pressure are given by the "shock tube equation (Glass and Patterson, 1955):

$$\frac{P_5}{P_1} = \gamma_1 M_s^2 \left[1 - \left(\frac{\gamma_5 - 1}{2} \right) . \frac{u_s}{a_5} \right]^{\frac{-2\gamma_5}{\gamma_5 - 1}}, \qquad (5.1)$$

where P_5 and P_1 are the respective pressures of the driver gas and the initial test gas,

γ is the ratio of the specific heats of the gas, M_s is the Mach number of the shock, u_s is the velocity of the shock and a_5 is the sound speed of the driver gas. While equation (5.1) is not as accurate for real gases, it does give a qualitative idea about the variation of shock velocity with the other parameters. The selection of the driver gas is dictated by the shock velocity required. For slow shocks, a driver gas that possesses a low sound speed is needed. The higher molecular weight produces a slower sound speed according to

$$a = \sqrt{\frac{\gamma RT}{m}} \tag{5.2}$$

where m is the molecular weight of the gas. Table 5.2 is a list of the conditions for which results were obtained, including those used before the extent of pressure broadening on the iodine spectral lines was realized.

TABLE 5.2 Shock tube operating conditions

h.p.r pressure (KPa)	**shock tube pressure (KPa)**	**shock speed (m/s)**
7.332	13.30	645.5
6.650	13.30	541.6
3.990	13.30	605.8
0.267	13.30	509.5
2.660	66.50	455.2
2.660	119.7	426.3
0.665	119.7	398.1

5.1.3 Timing and Event Triggering

As shown in figure 5.3, the timing of the shock was done by two pressure transducers spaced approximately 810 mm apart with the #2 pressure transducer about 39 mm from the centre of test section windows (see figure 5.1). Both pressure signals were sent to a Phillips model PM 3302 digital cathode ray oscilloscope (CRO) with the #2 pressure signal that was amplified being used as the trigger for both the

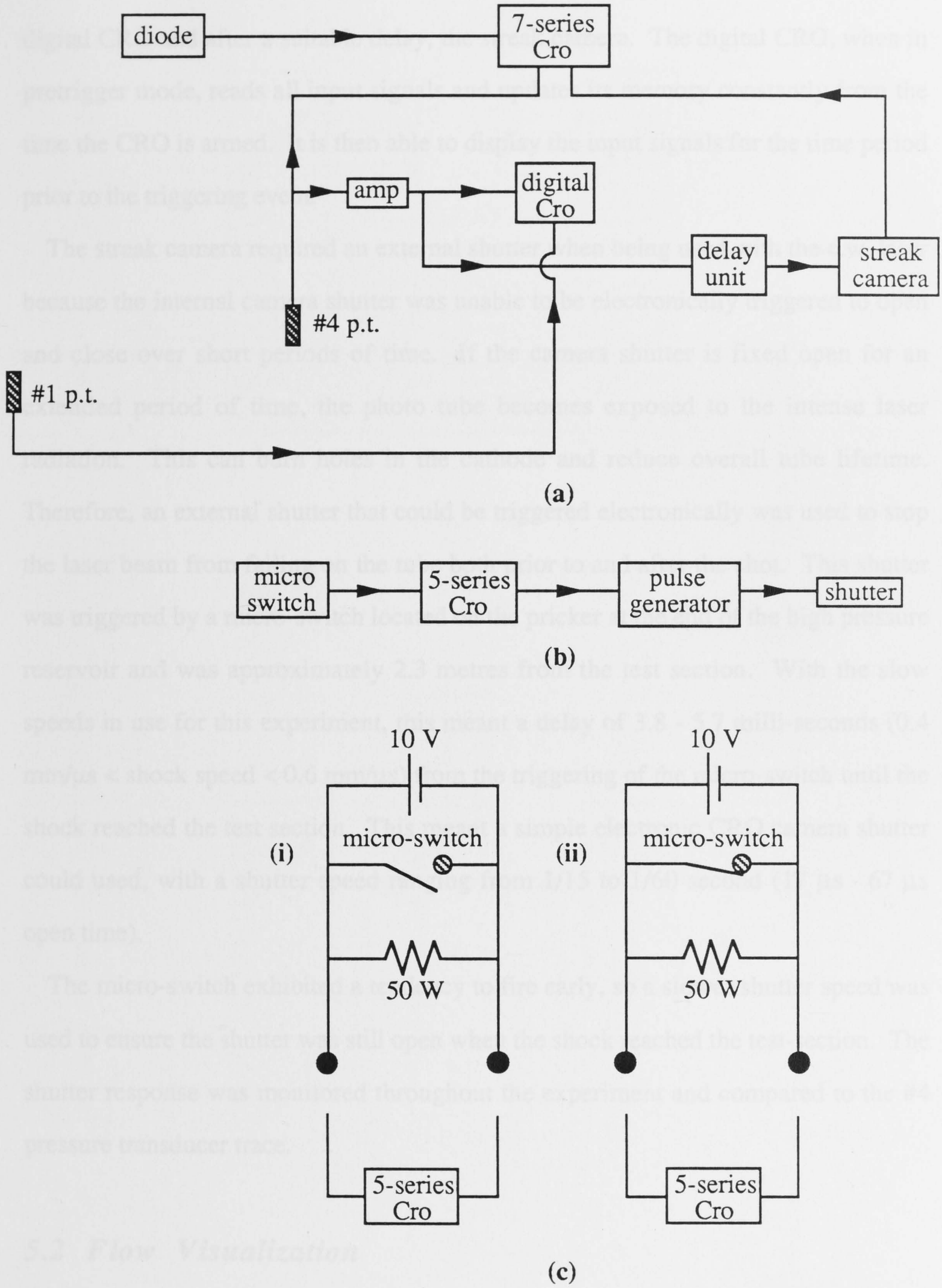

FIGURE 5.3 Schematic diagrams of shock tube electronics.
(a) Shock timing and camera triggering.
(b) External shutter triggering.
(c) Micro-switch design; (i) loaded & (ii) fired.

digital CRO and after a suitable delay, the streak camera. The digital CRO, when in pretrigger mode, reads all input signals and updates its memory constantly from the time the CRO is armed. It is then able to display the input signals for the time period prior to the triggering event.

The streak camera required an external shutter when being used with the c.w. laser because the internal camera shutter was unable to be electronically triggered to open and close over short periods of time. If the camera shutter is fixed open for an extended period of time, the photo tube becomes exposed to the intense laser radiation. This can burn holes in the cathode and reduce overall tube lifetime. Therefore, an external shutter that could be triggered electronically was used to stop the laser beam from falling on the tube both prior to and after the shot. This shutter was triggered by a micro-switch located on the pricker at the end of the high pressure reservoir and was approximately 2.3 metres from the test section. With the slow speeds in use for this experiment, this meant a delay of 3.8 - 5.7 milli-seconds (0.4 mm/μs < shock speed < 0.6 mm/μs) from the triggering of the micro-switch until the shock reached the test section. This meant a simple electronic CRO camera shutter could used, with a shutter speed ranging from 1/15 to 1/60 second (17 μs - 67 μs open time).

The micro-switch exhibited a tendency to fire early, so a slower shutter speed was used to ensure the shutter was still open when the shock reached the test-section. The shutter response was monitored throughout the experiment and compared to the #4 pressure transducer trace.

5.2 Flow Visualization

5.2.1 Optical System

Observation of the shock was achieved using density gradients in the flow. A Mach-Zehnder interferometer (MZ), shown in figure 5.4, was used to produce spatially resolved interferograms of the flow. The shock appeared as a shift in the position of the interference fringes focussed in the test section.

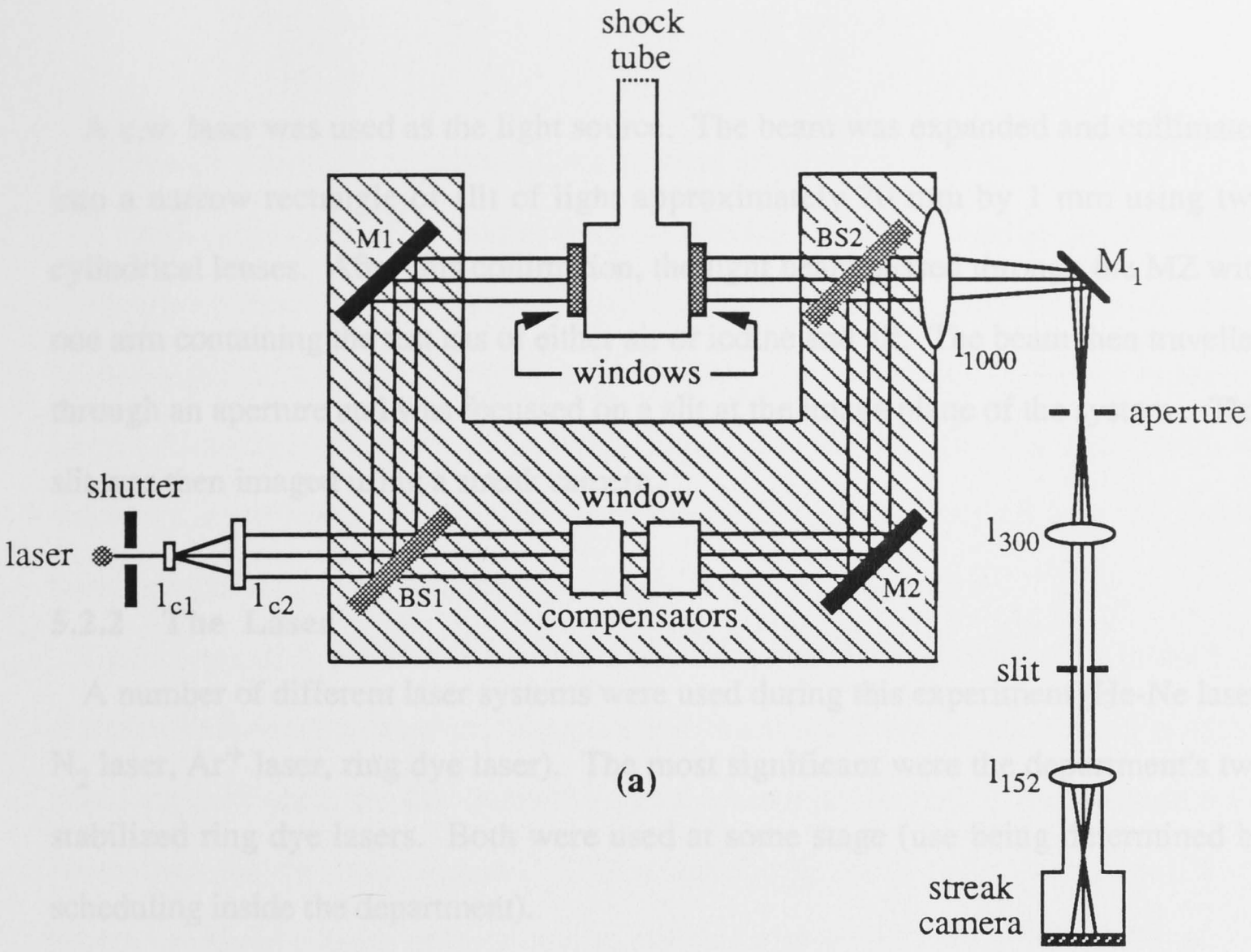

(a)

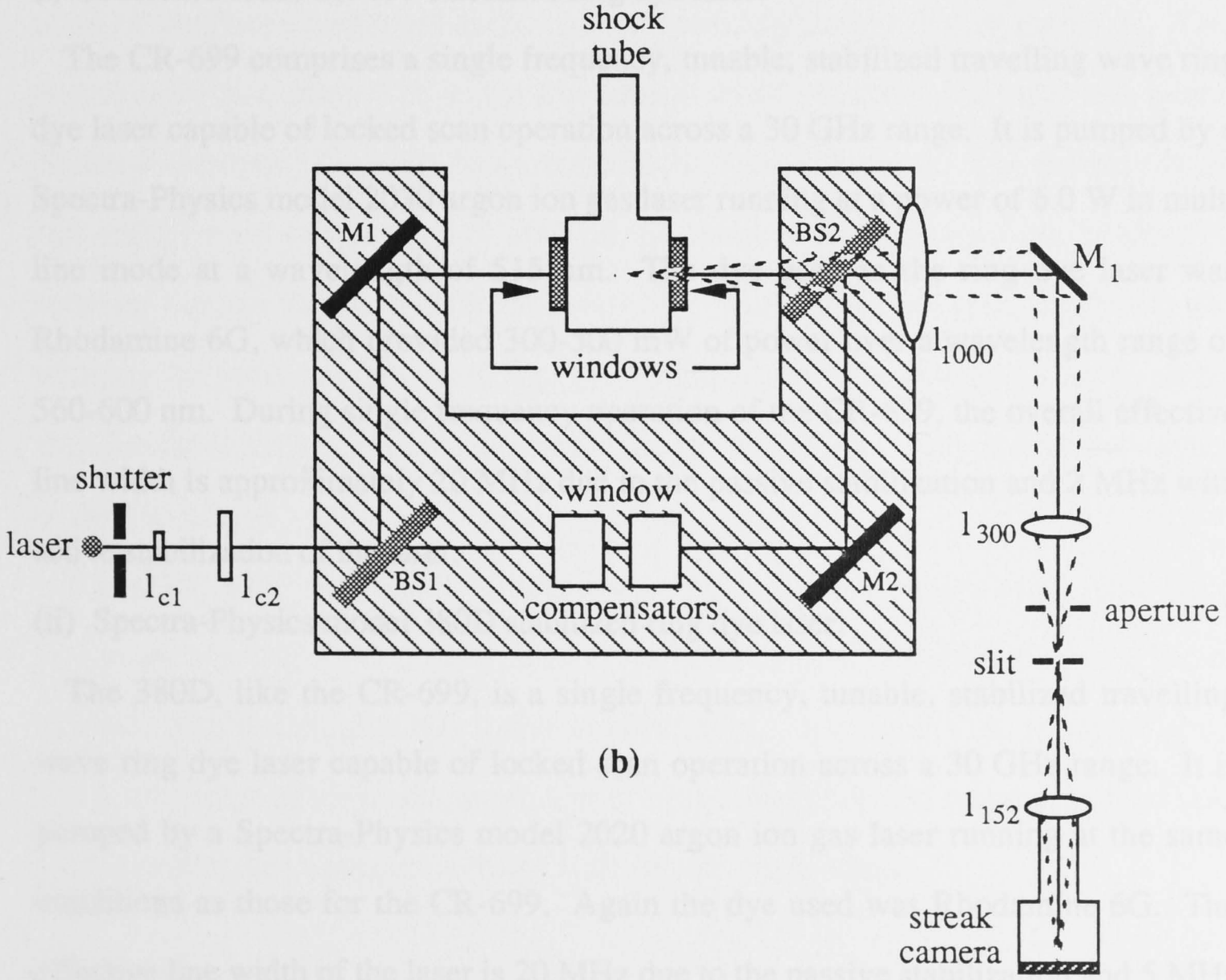

(b)

FIGURE 5.4 Optical arrangements for flow visualization
(a) Ray optics
(b) Imaging

A c.w. laser was used as the light source. The beam was expanded and collimated into a narrow rectangle or slit of light approximately 70 mm by 1 mm using two cylindrical lenses. After this collimation, the light beam passed through the MZ with one arm containing the test gas of either air or iodine and air. The beam then travelled through an aperture and was focussed on a slit at the image plane of the system . This slit was then imaged using a streak camera.

5.2.2 The Laser

A number of different laser systems were used during this experiment (He-Ne laser, N_2 laser, Ar^+ laser, ring dye laser). The most significant were the department's two stabilized ring dye lasers. Both were used at some stage (use being determined by scheduling inside the department).

(i) Coherent Model CR-699 stabilized ring dye laser.

The CR-699 comprises a single frequency, tunable, stabilized travelling wave ring dye laser capable of locked scan operation across a 30 GHz range. It is pumped by a Spectra-Physics model 2030 argon ion gas laser running at a power of 6.0 W in multi line mode at a wavelength of 515 nm. The dye used in the ring dye laser was Rhodamine 6G, which provided 300-500 mW of power over a wavelength range of 560-600 nm. During single frequency operation of the CR-699, the overall effective line width is approximately 20 MHz due to the passive stabilization and 2 MHz with active stabilization of the laser.

(ii) Spectra-Physics model 380D stabilized ring dye laser.

The 380D, like the CR-699, is a single frequency, tunable, stabilized travelling wave ring dye laser capable of locked scan operation across a 30 GHz range. It is pumped by a Spectra-Physics model 2020 argon ion gas laser running at the same conditions as those for the CR-699. Again the dye used was Rhodamine 6G. The effective line width of the laser is 20 MHz due to the passive stabilization and 5 MHz with active stabilization of the laser. Both laser systems linewidths, during either passive or active stabilization, were considerably narrower than the spectral lines

encountered during the experiment, which were greater than 1 GHz.

A small percentage of the output from the dye laser was also used as the input beam for a wavemeter. The wavemeter is a wavelength measuring device that utilizes a scanning Michelson interferometer to compare the wavelength of a known reference from a Helium-Neon laser (632.81627 nm at 288 K and 101.308 KPa) with the unknown input beam. The He-Ne interference fringes are counted over the time it takes to measure a known number of fringes from the input beam.

Laser beam divergence was a major problem during this experiment due to the long distance between the laser exit aperture and the shock tube. A number of possible solutions were tried, the first being the use of a single-mode optic fibre to transmit the beam over the distance required. Unfortunately, the only optic fibre of sufficient length produced a beam of poor quality that had a speckled appearance in the output plane of the fibre (the pattern could also be altered by simply flexing the fibre). Two people were also needed to adjust the beam intensity because the input and output planes of the optic fibre were on separate floors of the laboratory. The second system was simply a set of mirrors that allowed the beam to travel down a gap in the wall between the two floors. The beam divergence was minimized, after much trial and error, by the positioning of two long focal length lenses. These were placed in such a way that the beam waist was minimized at the first cylinderical lens and the test section of the shock tube.

Coupled with the beam divergence problem was laser beam intensity. Unfortunately, there was no way around this problem and therefore a balance had to be made with the shock tube's iodine concentration. Too much iodine vapour in the shock tube (high absorption) caused loss of fringe resolution and contrast and too little iodine vapour didn't produce a fringe shift enhancement effect.

5.2.3 The Mach-Zehnder Interferometer

The interferometer used for the experiment was a Carl Zeiss Mach-Zehnder (MZ)

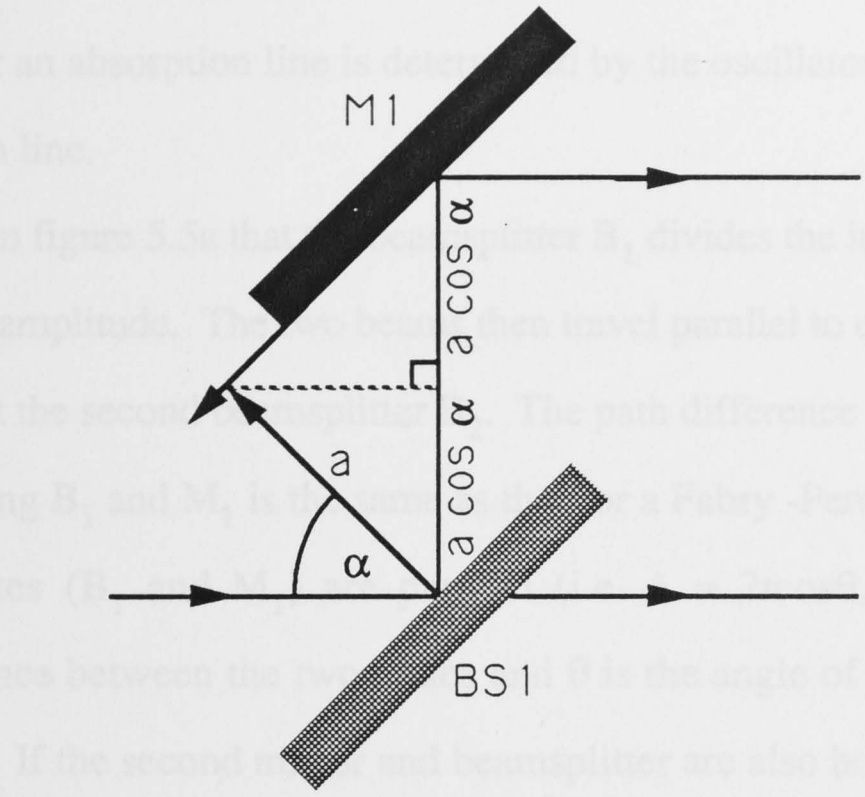

(a)

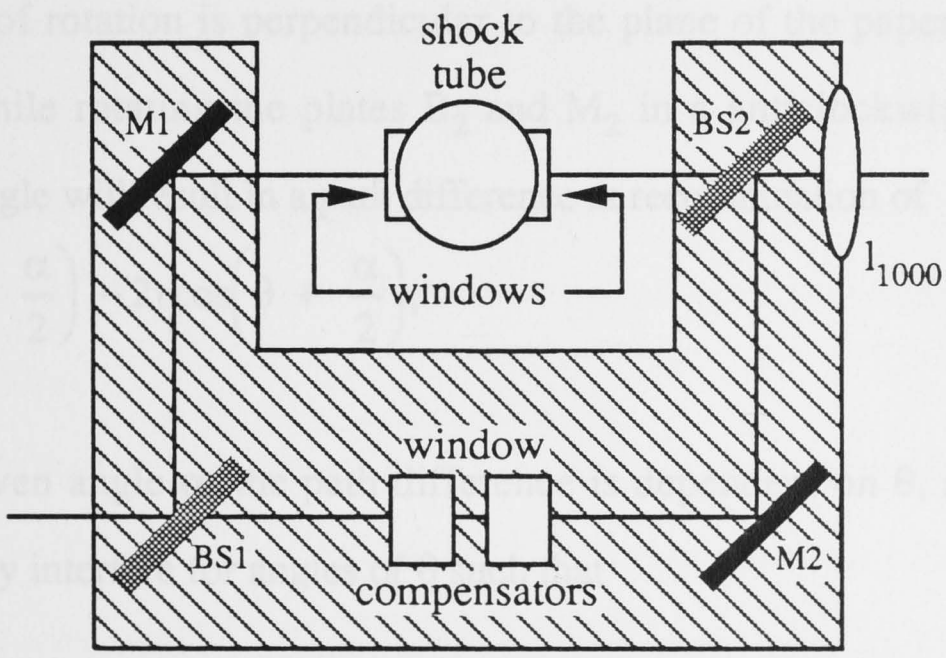

(b)

FIGURE 5.5 The Mach-Zehnder Interferometer
(a) Path difference between the two parallel beams
(b) Schematic diagram

interferometer. The MZ is a refractometer that is related to spectroscopy through the fact that the variation of refractive index for the gas or vapour (in the test arm of the interferometer) near an absorption line is determined by the oscillator strength of that particular absorption line.

It can be seen from figure 5.5a that the beamsplitter B_1 divides the incident light into two beams of equal amplitude. The two beams then travel parallel to each other before being recombined at the second beamsplitter B_2. The path difference between the two beams after traversing B_1 and M_1 is the same as that for a Fabry -Perot interferometer when the two plates (B_1 and M_1) are parallel (i.e. $\Delta = 2t\cos\theta$, where t is the perpendicular distance between the two plates and θ is the angle of incidence in the plane of the paper). If the second mirror and beamsplitter are also both parallel to B_1 (and therefore M_1), then the second pair of reflections will introduce a similar path increment into the lower beam. The net path difference after recombination, therefore, is zero for any angle of incidence. Rotating the plates B_1 and M_1 in a clockwise direction (the axis of rotation is perpendicular to the plane of the paper) through a small angle $\alpha/2$ while rotating the plates B_2 and M_2 in a anticlockwise direction through the same angle will result in a path difference at recombination of

$$\Delta = 2t\cos\left(\theta - \frac{\alpha}{2}\right) - 2t\cos\left(\theta + \frac{\alpha}{2}\right), \qquad (5.3)$$

$$\cong 2t\alpha\sin\theta.$$

Therefore, for a given angle α, the path difference is dependent on θ, and the two beams constructively interfere for angles of θ such that

$$\Delta = 2t\alpha\sin\theta = n\lambda. \qquad (5.4)$$

Since the system is not axially symmetric (i.e. Δ depends on the wedge angle α), the interference fringes are straight lines parallel to the edge of the wedge and also since both the beams are travelling in the same direction after recombination, the fringes are focussed at infinity or in the focal plane of a lens.

5.2.4 The Streak Camera

Spectral line interferometry requires that the laser bandwidth be smaller than the

detuning from the line centre. The only laser available that satisfied this narrow linewidth requirement was a c.w. laser. This in turn dictated the means of capturing the resultant flow visualization image. A streak/framing camera was chosen as this produced the best result.

The camera used was a Hadland Imacon model 790 image converter camera that could be used in either a streak or framing mode dependent on the type of "plug in" unit used with the camera.

As mentioned previously in section 5.2.2 laser intensity was a problem due to the distance between the exit aperture of the laser and the shock tube. The slowest framing speed possible for the Imacon was 2.5 x 10^4 frames/second, which meant that the maximum exposure duration for the camera in framing mode was 8 μsec/frame. The slowest streak speed possible was 1 μs/mm, resulting in a maximum exposure duration of 70 μsec.

The optical set-up for framing camera operation involved a full illumination of the test section whereas a slit arrangement is used in conjunction with the streak camera. This maximized the experiment's available light by focussing the light down to a slit at the image plane of the optical system (the object plane of the camera). Therefore, the camera was used in streak mode to maximize the light intensity and produce better resolved interferograms.

The streak camera had a streak speed of 0.1-1 μs/mm, which resulted in a streak recording time of 7 to 70 μsecs, adjustable by a 10 turn potentiometer. The resolution of the system was approximately 12 line pairs/mm. The image produced by the streak camera was an interferogram which recorded the changes of the interference pattern along the slit as a function of time.

5.3 Narrow Band Absorption and Refractive Index Measurements

5.3.1 Optical System (Narrow band absorption)

Iodine absorption profiles were obtained with an optical system similar to that used

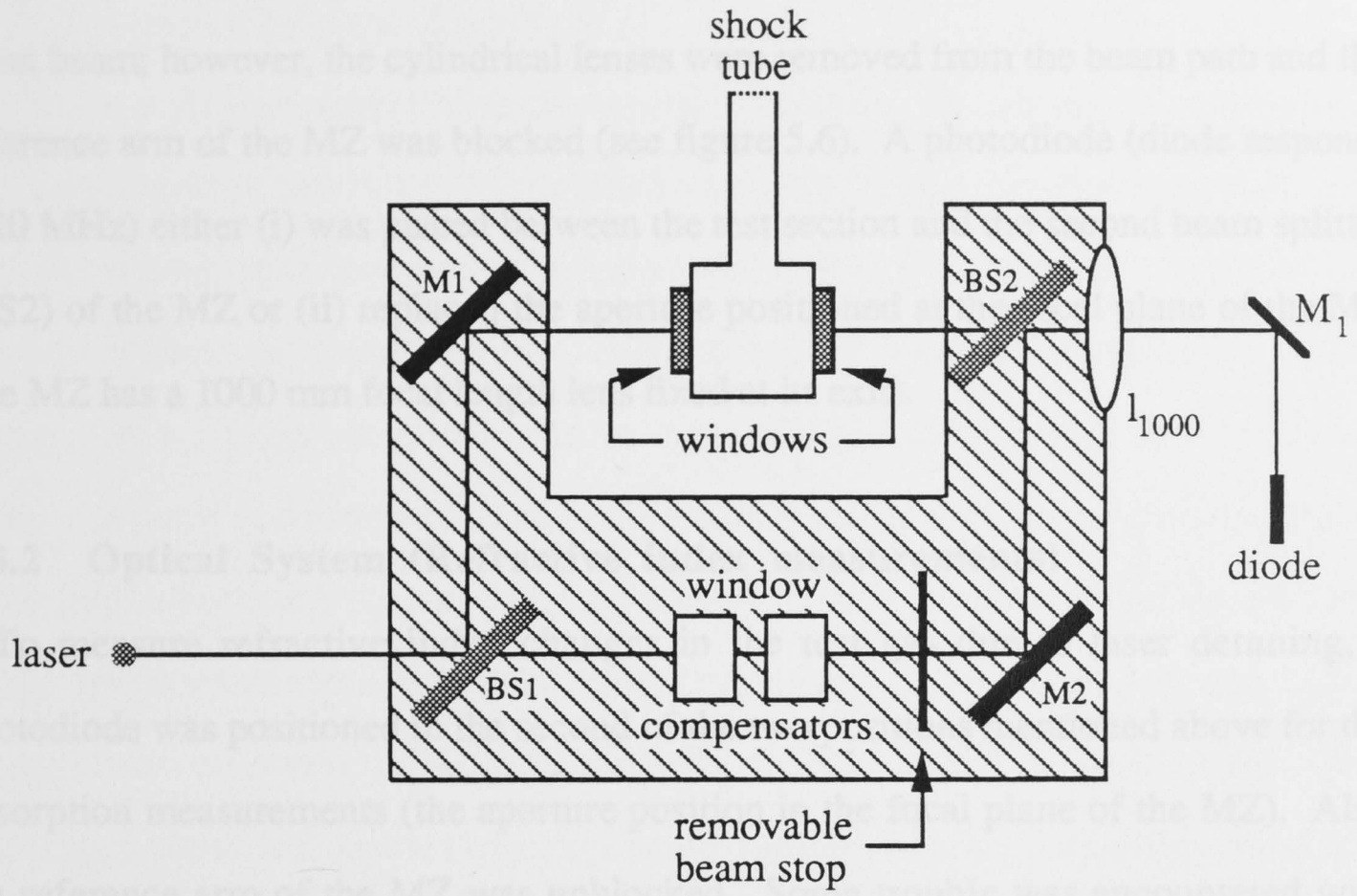

FIGURE 5.6 Optical arrangements for absorption and refractive index measurements.
(a) Position 1
(b) Position 2

for flow visualization (section 5.1.1). The c.w. ring dye laser again provided the input beam; however, the cylindrical lenses were removed from the beam path and the reference arm of the MZ was blocked (see figure 5.6). A photodiode (diode response > 20 MHz) either (i) was placed between the test section and the second beam splitter (BS2) of the MZ or (ii) replaced the aperture positioned at the focal plane of the MZ (the MZ has a 1000 mm focal length lens fixed at its exit).

5.3.2 Optical System (Refractive index measurements)

To measure refractive index changes in the test gas due to laser detuning, a photodiode was positioned in the second of the two positions mentioned above for the absorption measurements (the aperture position in the focal plane of the MZ). Also the reference arm of the MZ was unblocked. Some trouble was encountered with beam size (more than one fringe across the beam profile even with infinite fringe separation) and spurious fringe movement due to convection currents from the hot shock tube causing density changes in the reference arm of the MZ.

Chapter 6. DATA REDUCTION

6.1 Fringe Pattern Analysis

To allow comparisons to be made between the shots, the relevant interferograms were digitized and treated to a fringe-pattern analysis using a two-dimensional Fourier transform program developed by Bone *et al.* (1986). Figure 6.1 shows the set-up used to digitize the interferograms. This technique permits the separation of the desired information components from the unwanted components in the Fourier transform plane (the positive and negative exponential parts of the sinusoidal intensity from each other and from some of the spurious intensity contributions) since all the terms are found as strongly peaked functions centred at the origin, $\pm \nu_0$ and $\pm 2\nu_0$. There is also an overall noise component contributing across the entire plane. The underlying phase is recovered by a process of selective filtering, retransformation and fringe matching that retains only the components due to the positive exponential part of the fringe system.

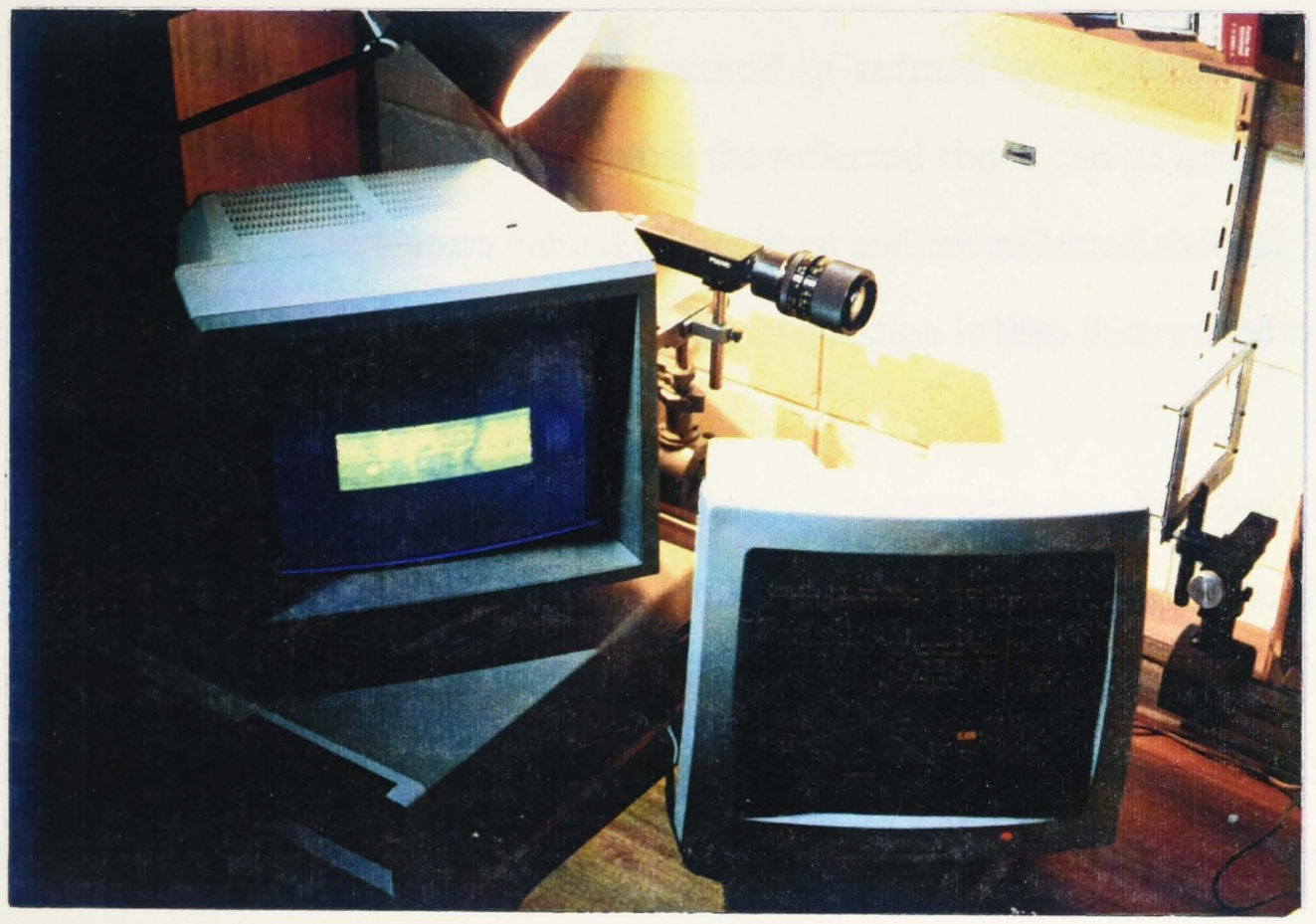

FIGURE 6.1 A photo of the equipment used in the digitization process. This included a computer, two screens, (one was a graphics screen), a video camera and an optical mount for the interferogram.

6.2 Theoretical Fringe Shifts across the Reflected Shock

As already stated, the refractive index of the test gas was experimentally determined using Mach-Zehnder Interferometry. The relationship between the position of a fringe at the focal plane of the test gas and the refractive index of the gas is given by Huber (1971) as

$$p\lambda = \alpha y + (n - 1)L - (n' - 1)L' \qquad (6.1)$$

where $(n - 1)L$ is the path length of the test arm, $(n' - 1)L'$ is the path length in the reference arm, y is the position of the fringe, measured in the observation plane and α is the angle between the test and the reference beams of the interferometer.

For a particular wavelength λ, a change in the refractive index Δn produces a change in fringe order Δp at position y of

$$\lambda \Delta p = \Delta n L \qquad (6.2)$$

where L is the length of the test arm.

When calculating the fringe shift across the reflected shock for a set wavelength, the change in refractive index of the gas is, from equation 6.2, dependent on the change in iodine number density only. Using the method of refractivity calculation (see Appendix A) the theoretical fringe shift across the reflected shock can be determined from knowledge of the temperature behind the incident and the reflected shocks. The number density of the molecular iodine transition in question is then determined from the Boltzmann distribution (see Appendix B).

It is assumed that even though a temperature increase occurs across both the incident and reflected shocks, no increase in iodine vapour pressure takes place. This is due to the temperature behind the shock in question attaining a maximum for only a short time duration before it quickly decreases to some equilibrium value. The vapourization of more iodine crystals is therefore assumed negligible. The only change that takes place across the shock, therefore, is a redistribution of the total iodine population in accordance with the Boltzmann distribution.

6.3 Absorption and Refractive Index Measurements

The absorption and refractive index profiles were obtained by scanning the ring dye lasers and so were spatially resolved. (Scanning the lasers involved a slow variation of the laser wavelength by a rotation of a Brewster prism while maintaining a narrow linewidth with the active stabilization on.)

When considering the line profiles obtained during the experiment, a deconvolution of the observed line profile and the instrument function of the laser and the photo - diode is required. Throughout the experiment (at all operating conditions), linewidths of the order 1 GHz were observed for all iodine spectral lines. The linewidths of the ring dye lasers were of the order 20 MHz for passive stabilization, or 2-5 MHz for active stabilization. The response time of the photo-diode used was of the order of micro-seconds. This meant the instrument functions of both the lasers and the diode were effectively delta functions compared to the spectral line profiles and so no de-convolution of the observed line profiles was required.

6.4 Theoretical Fringe Shifts for a Scanned Spectral Line

The calculations involved for the determination of the gas refractivity (n - 1) at a particular wavelength λ are included in the appendices. This involves the calculation of the refractivity from data obtained for the number density of the iodine, oscillator strength of the vibrational transition and the spectral line profile. In these calculations, observed temperatures, pressures and linewidths from the experiment are used and a Voigt profile is assumed. In assuming a Voigt profile, both the Gaussian (doppler) and the Lorentzian (pressure) linewidths are needed. The doppler width was calculated from the temperature of the gas using equation (3.35), whereas the Lorentzian width was determined using equation (A3) for optical depth and varying the value for a (the ratio between the Lorentzian and doppler linewidths) so as to produce the observed optical depth (at line centre) and observed linewidth for the transition.

Using equation (6.2), the calculated refractivities were used for the resultant

theoretical fringe shifts due to detuning through a spectral line. However, equation (6.2) is valid only for a constant wavelength. Since the wavelength detunings were all of the order of 5-10 MHz (0.0055 nm < $\Delta\lambda$ < 0.011 nm), the assumption of a constant wavelength leads to an error in the value obtained for the fringe shift of 1 in 57000 or smaller. Therefore, equation (6.2) was used with the wavelength taken to be the wavelength of the line centre λ_0.

Chapter 7. EXPERIMENTAL RESULTS

The results obtained have been divided into separate sections according to the experimental techniques used. Section 7.1 details the results obtained for the absorption profiles and refractive index measurements. Section 7.2 includes the results acquired using the flow visualization. This involves the original interferograms, the resulting digitized and filtered interferograms and the experimentally determined fringe shifts. In each section, the results are accompanied by their respective high pressure reservoir (h.p.r.) or driver gas and shock tube (s.t.) pressures, gas temperature, shock velocity, Mach number and laser wavelength, where appropriate.

7.1 Absorption and Refractive Index Measurements

Molecular iodine is known to possess many transition lines in the visible spectrum. Preliminary calculations and absorption scans were completed to determine the position of those transitions that fell in the region of maximum laser output for the dye Rhodamine 6G (λ_{max} = 571 nm). Once a number of suitable transition lines were selected, laser scans were performed to determine the exact position and absorption strength of the lines. The area about each spectral line was also checked for adjacent or overlapping absorption line profiles, with the aim of finding an isolated, resolvable spectral line and bandhead. (An isolated bandhead refers to the region on the non-shaded side of the bandhead being free of any overlapping absorption profile.)

There existed two major regions of interest in the spectrum for the possible use of spectral line interferometry. The first region was just to the non-shaded side of a vibrational bandhead and the second was in the vicinity of an isolated line possessing a reasonably high J value. On the non-shaded side of the bandhead, it was thought all the negative components of the refractive indices of the closely positioned and overlapping spectral lines comprising the bandhead would sum to produce an overall greater refractive index on that side of the bandhead compared to the individual lines themselves or any isolated line at a higher J value. The isolated line would possibly

have its negative component of refractive index cancelled by the positive component of an adjacent line or vice versa. However, the isolated line possesses (at higher J values) a significantly increased population (according to the Boltzmann distribution) and therefore refractive index when compared to any single line near the bandhead. Therefore, the possibility of significant fringe shift enhancement existed in both these regions of the spectrum.

For the $^3\Pi_{0u^+} \leftrightarrow ^1\Sigma_g^+$ transition, one bandhead, corresponding to the (16,0) vibrational transition, was found at λ = 570.519 nm and had an absorption-clear region on its non-shaded side. (See figure 7.1.) Two isolated spectral lines were determined, with the first at λ = 570.981 nm (v' = 16, v" = 0, J' = 39, J" = 38) and the second at λ = 571.225 nm (v' = 18, v" = 1, J' = 21, J" = 20). Both are R-branch transitions. (See figures 7.2 and 7.3.)

In the process of scanning the absorption profiles in the regions of interest, pressure broadening was found to be the major contributor to the line widths observed. (See figures 7.4, 7.5 and 7.6.) Linewidths of the order 1.0 to 1.5 GHz were common to all absorption line profiles for total shock pressures up to approximately 13 KPa. Significant broadening of the linewidths occurred after this, up to a pressure of about 40 KPa, where a distinct absorption line profile was no longer present. Absorption still occurred but over a wider range of frequencies and at a lower peak value for the line centre.

The use of a different fill gas with iodine to increase shock tube pressure didn't reduce the pressure broadening significantly enough to justify changing the additive gas in the shock tube for the shots involving weak Mach reflection. The additive gas used in the shock tube for all scans shown here was air. Helium was tried and made no appreciable difference to the line profiles observed for the same total pressure. For air, a total shock tube gas pressure greater than 11 KPa caused considerable broadening of the iodine absorption line profile, whereas for a buffer gas of helium, this didn't occur until approximately 14 KPa.

It was assumed that unless a reasonable absorption profile existed for a given

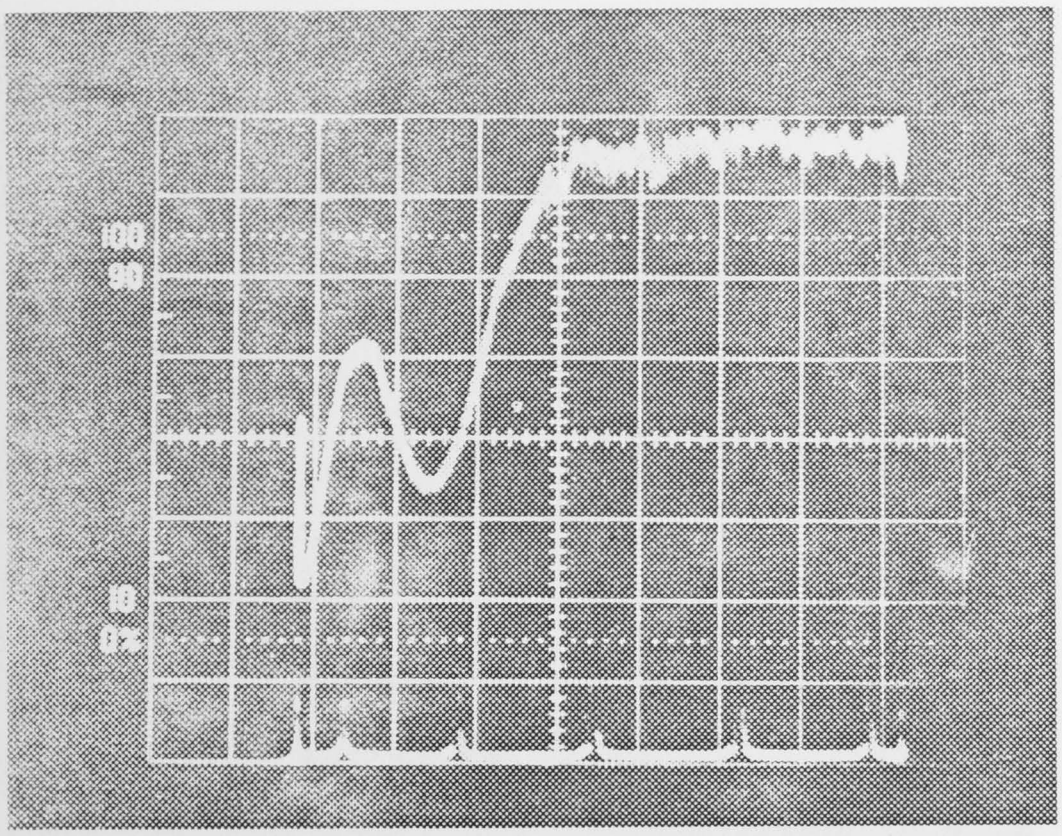

(i)

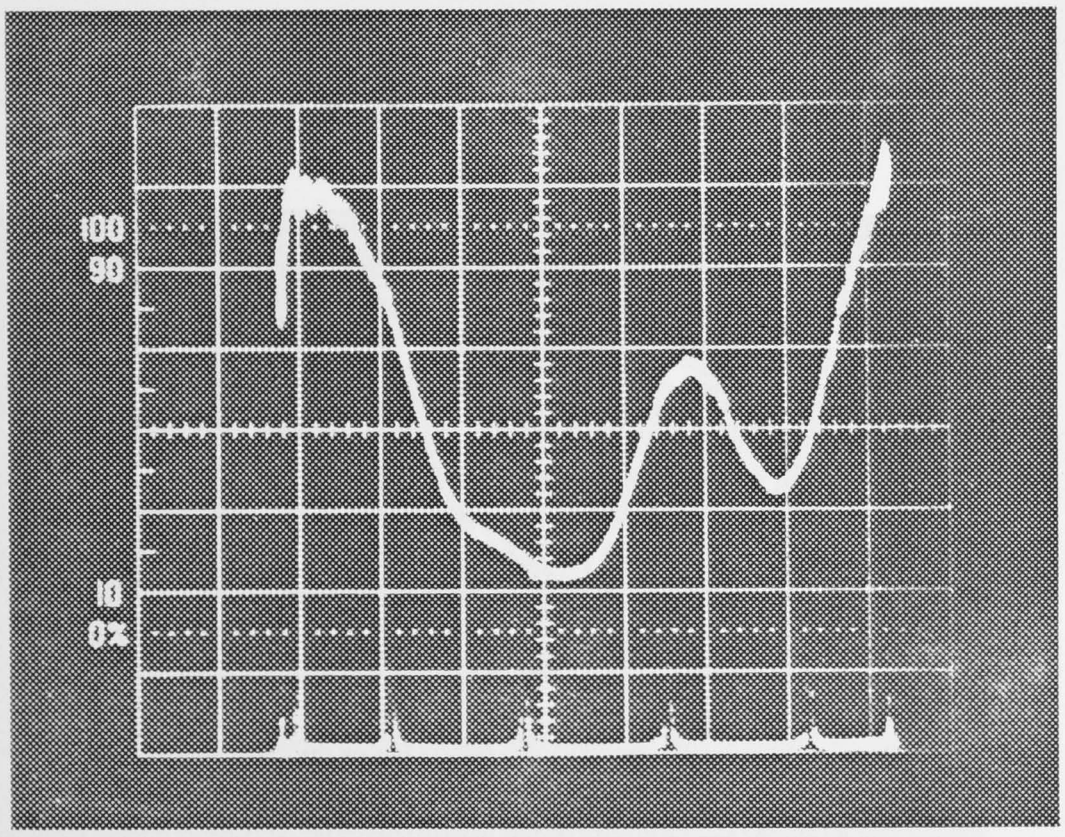

(ii)

FIGURE 7.1 Absorption trace of the region about the bandhead $\lambda_{bh} = 570.519$ nm. The markers are 1.5 GHz (~ 0.002 nm) apart. This is the same for all absorption and refractive index scans.
(i) Scan centre wavelength is $\lambda_0 = 570.517$ nm.
(ii) Scan centre wavelength is $\lambda_0 = 570.522$ nm.

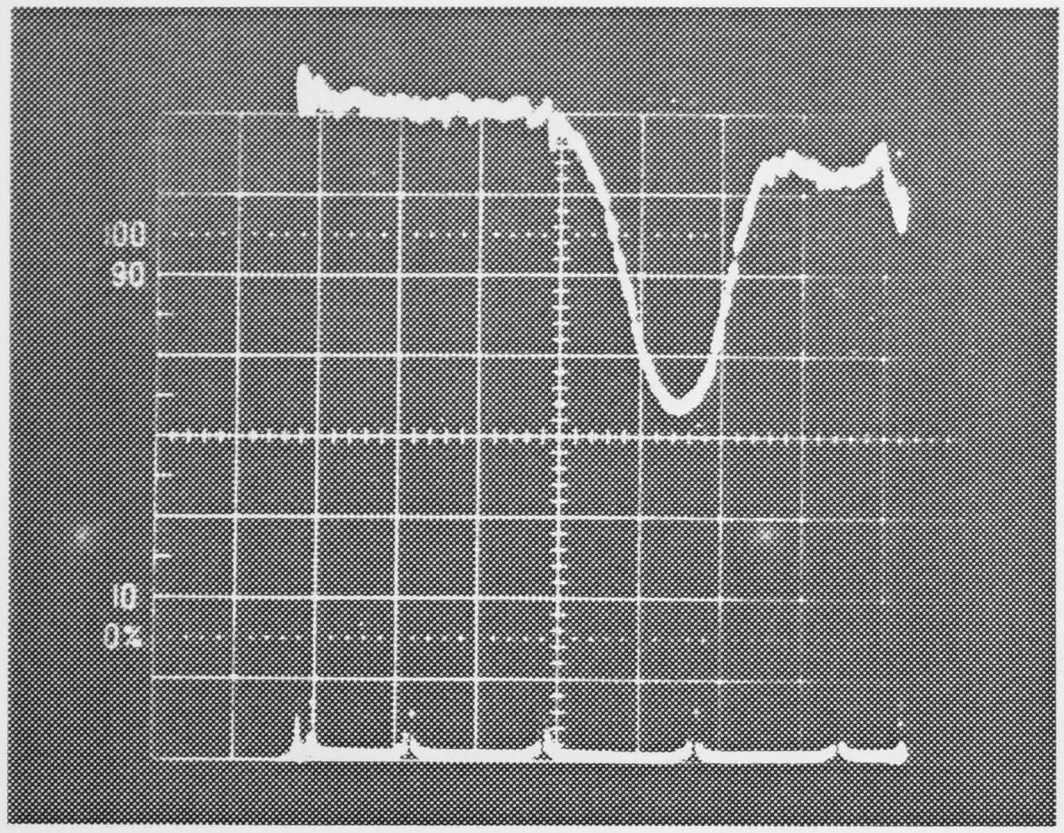

FIGURE 7.2 Absorption trace of the region about the isolated spectral line $\lambda = 571.226$ nm.

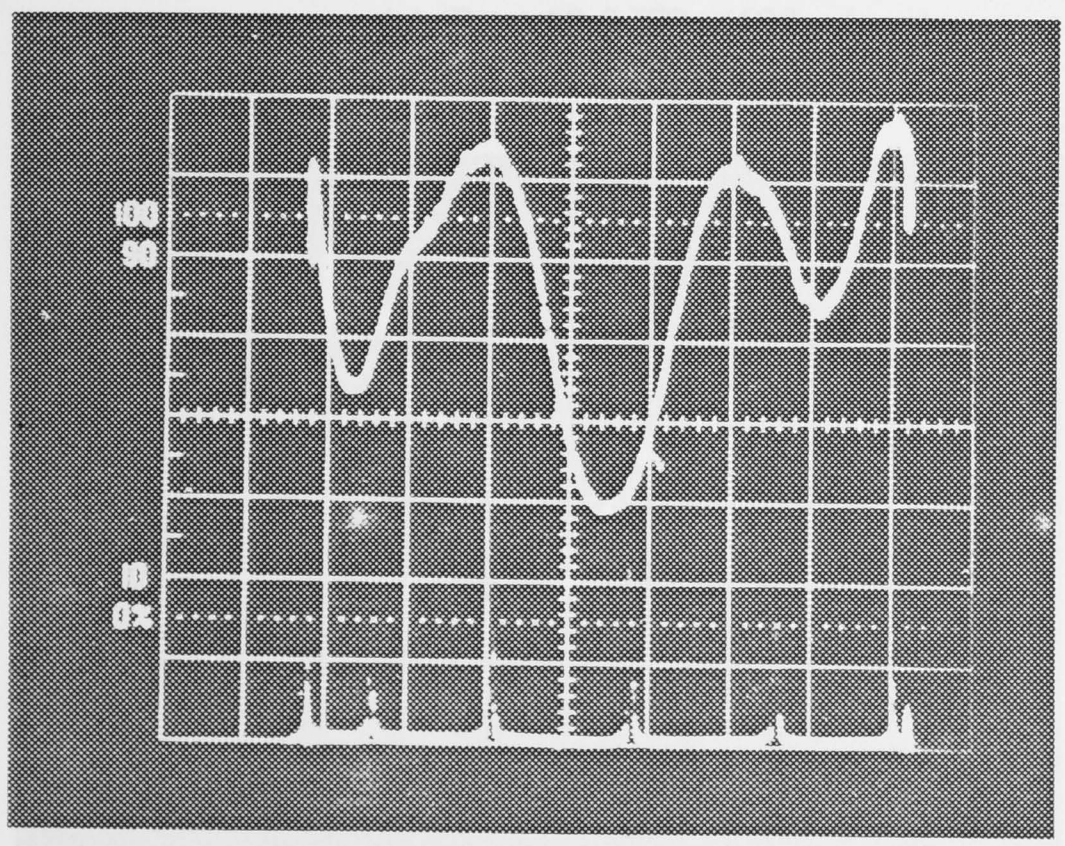

FIGURE 7.3 Absorption trace of the region about the isolated spectral line $\lambda = 570.984$ nm.

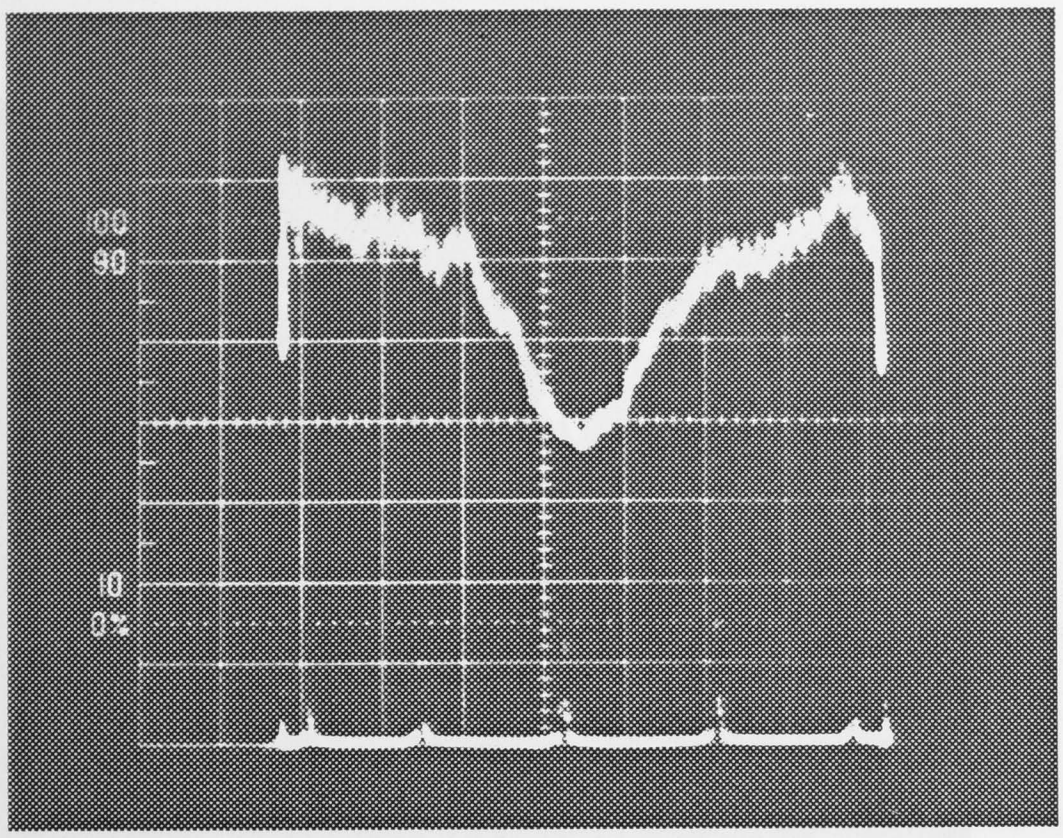

FIGURE 7.4 (i) P_T = 13.2 KPa (132 mbars). Absorption profile linewidth variation with buffer gas pressure for the spectral line λ = 571.225 nm.

(i) P_T = 13.2 KPa (132 mbars)
(ii) P_T = 15.0 KPa (150 mbars)
(iii) P_T = 16.6 KPa (166 mbars)
(iv) P_T = 18.5 KPa (185 mbars)
(v) P_T > 60.0 KPa (600 mbars)

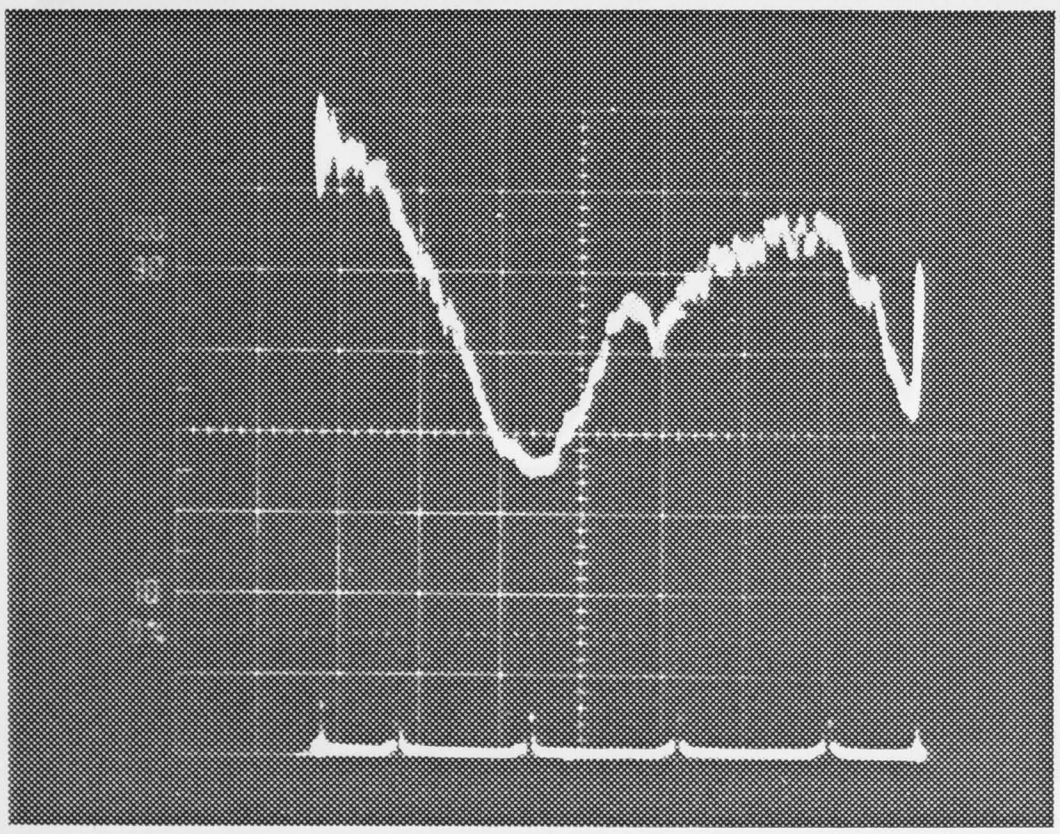

FIGURE 7.4 (ii) P_T = 15.0 KPa (150 mbars)

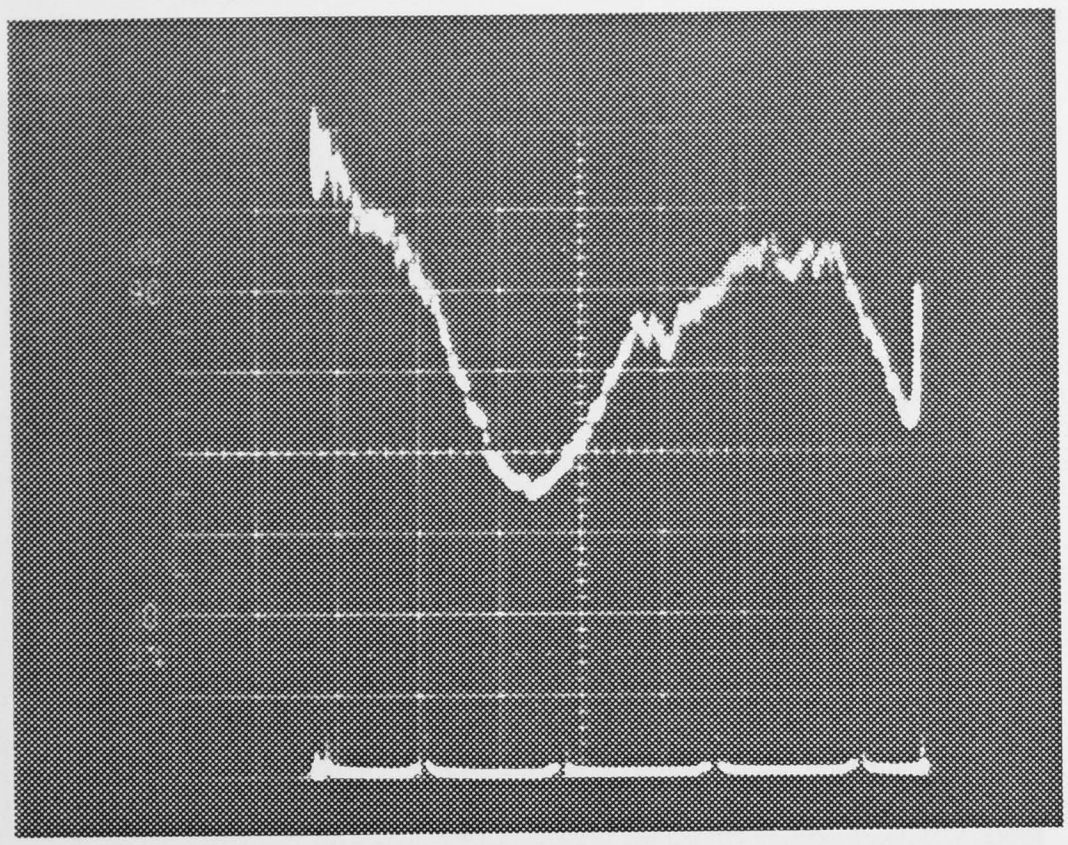

FIGURE 7.4 (iii) P_T = 16.6 KPa (166 mbars)

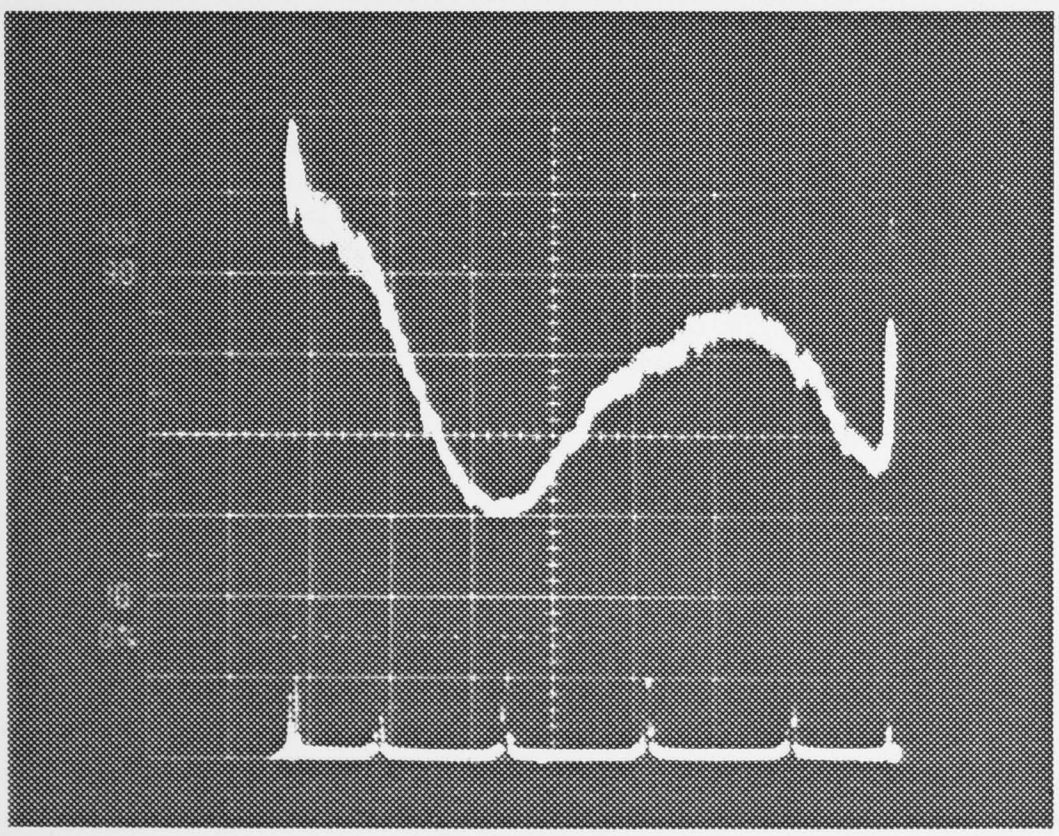

FIGURE 7.4 (iv) P_T = 18.5 KPa (185 mbars)

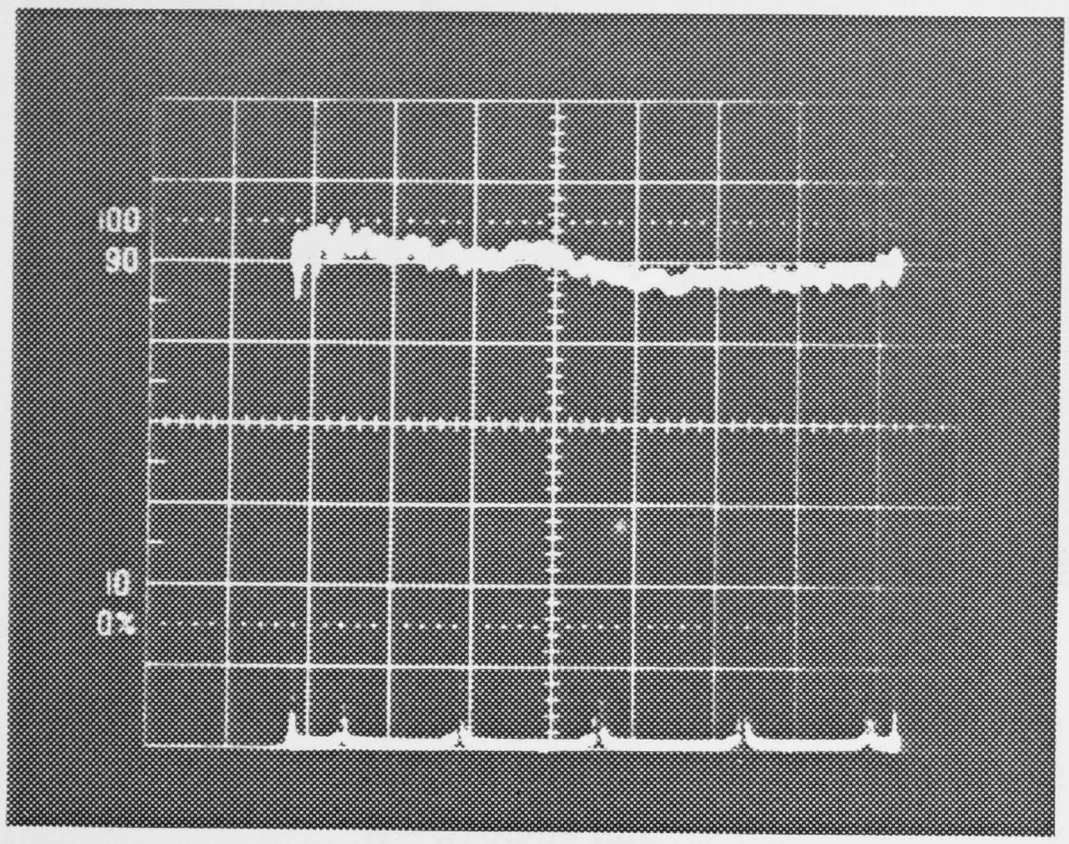

FIGURE 7.4 (v) P_T > 60.0 KPa (600 mbars).

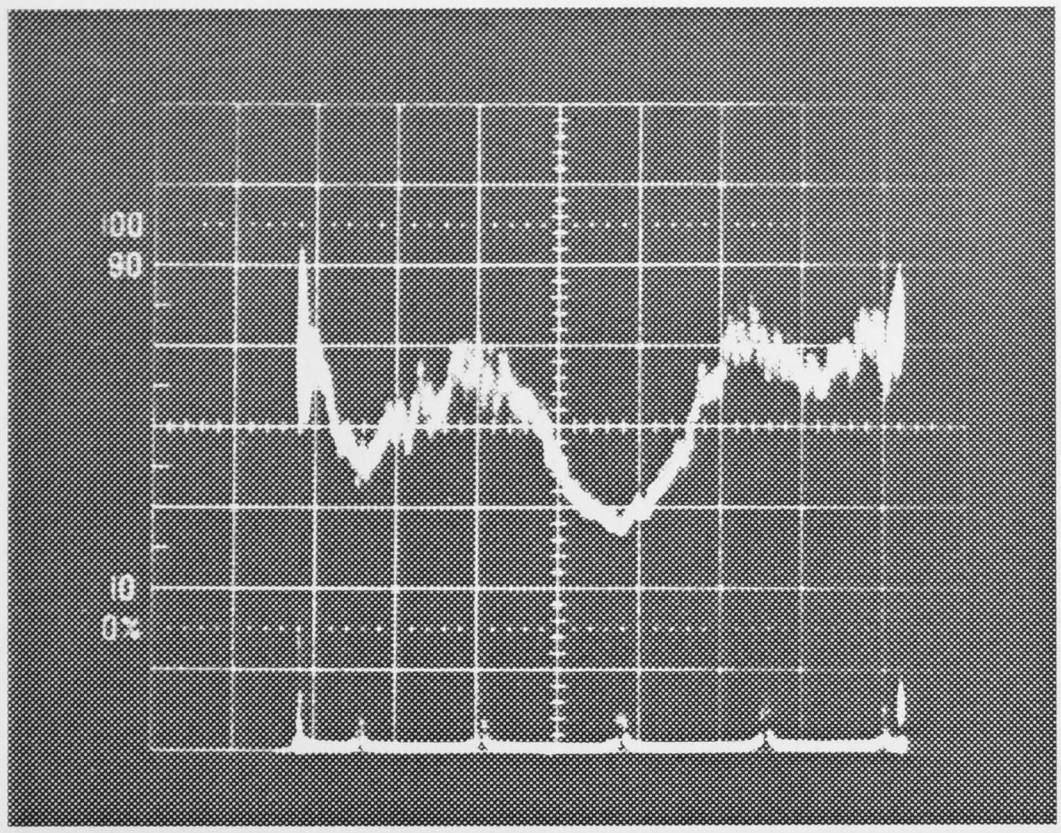

FIGURE 7.5 (i) P_T = 10.0 KPa (100 mbars). Absorption profile linewidth variation with buffer gas pressure for the spectral line λ = 570.984 nm.

(i) P_T = 10.0 KPa (100 mbars)

(ii) P_T = 16.9 KPa (169 mbars)

(iii) P_T = 25.0 KPa (250 mbars)

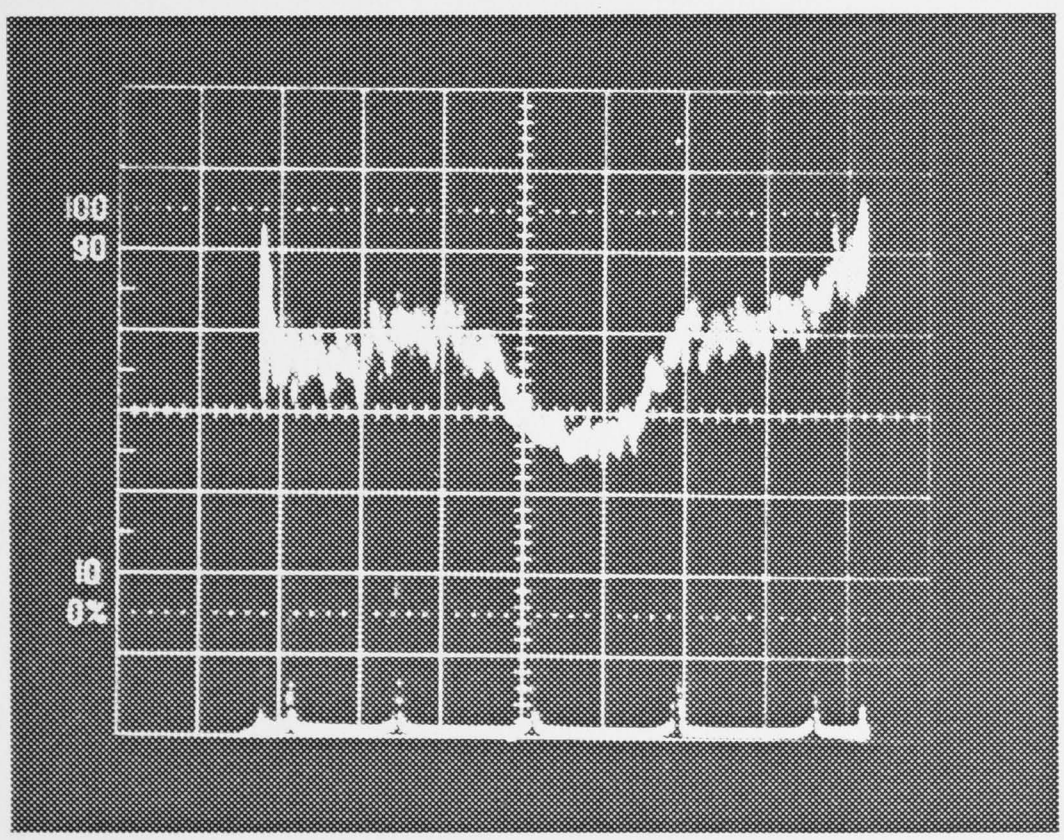

FIGURE 7.5 (ii) P_T = 16.9 KPa (169 mbars)

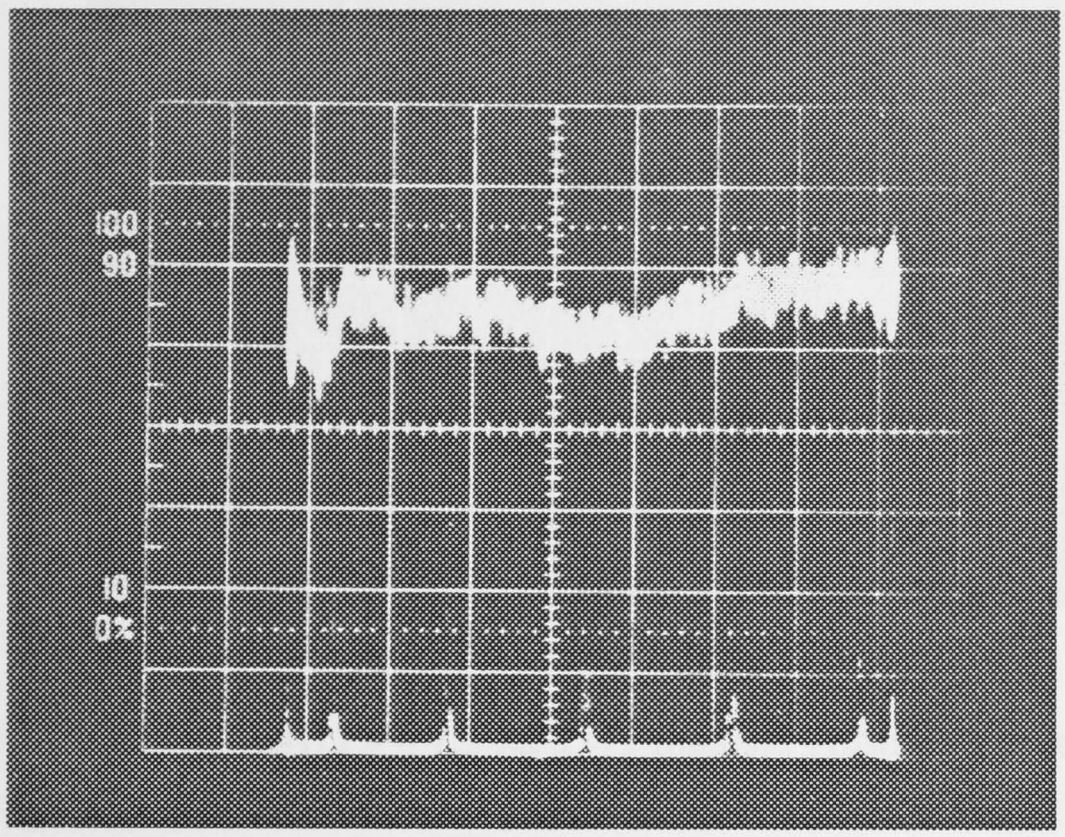

FIGURE 7.5 (iii) P_T = 25.0 KPa (250 mbars)

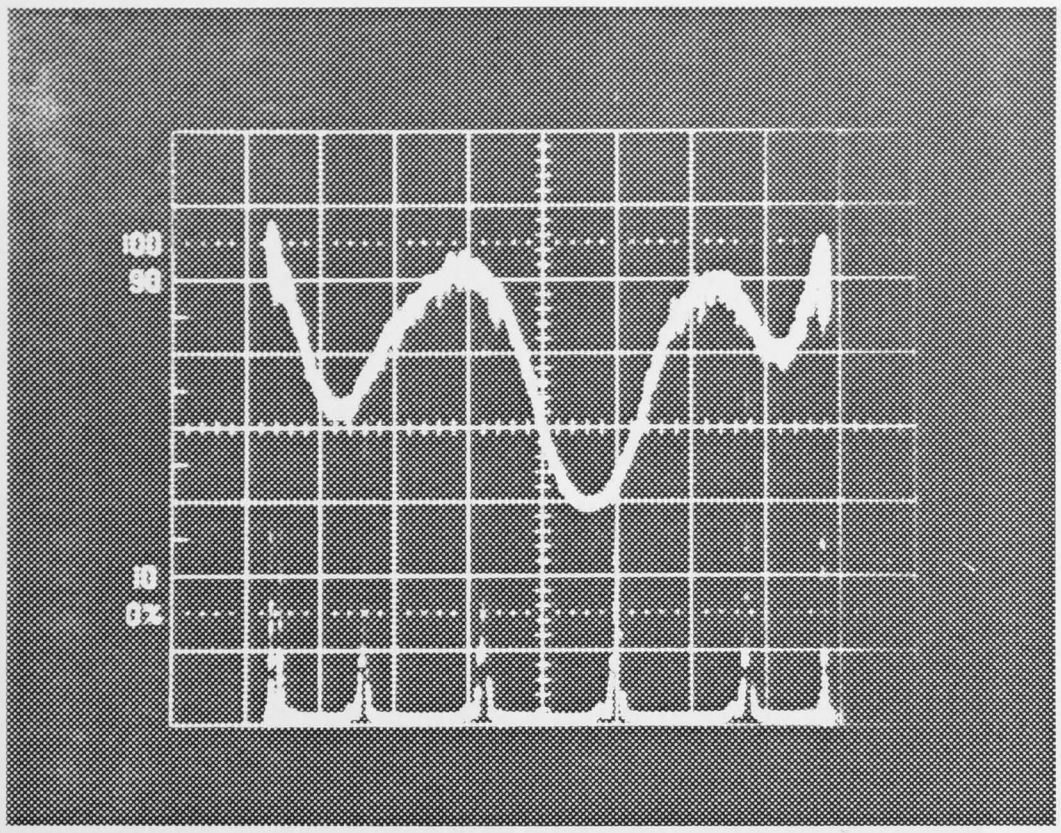

FIGURE 7.6 (i) P_T = 7.3 KPa (73 mbars). Absorption profile linewidth variation with buffer gas pressure for the spectral line λ = 570.984 nm.

(i) P_T = 7.3 KPa (73 mbars)

(ii) P_T = 31.4 KPa (314 mbars)

(iii) P_T > 80.0 KPa (800 mbars)

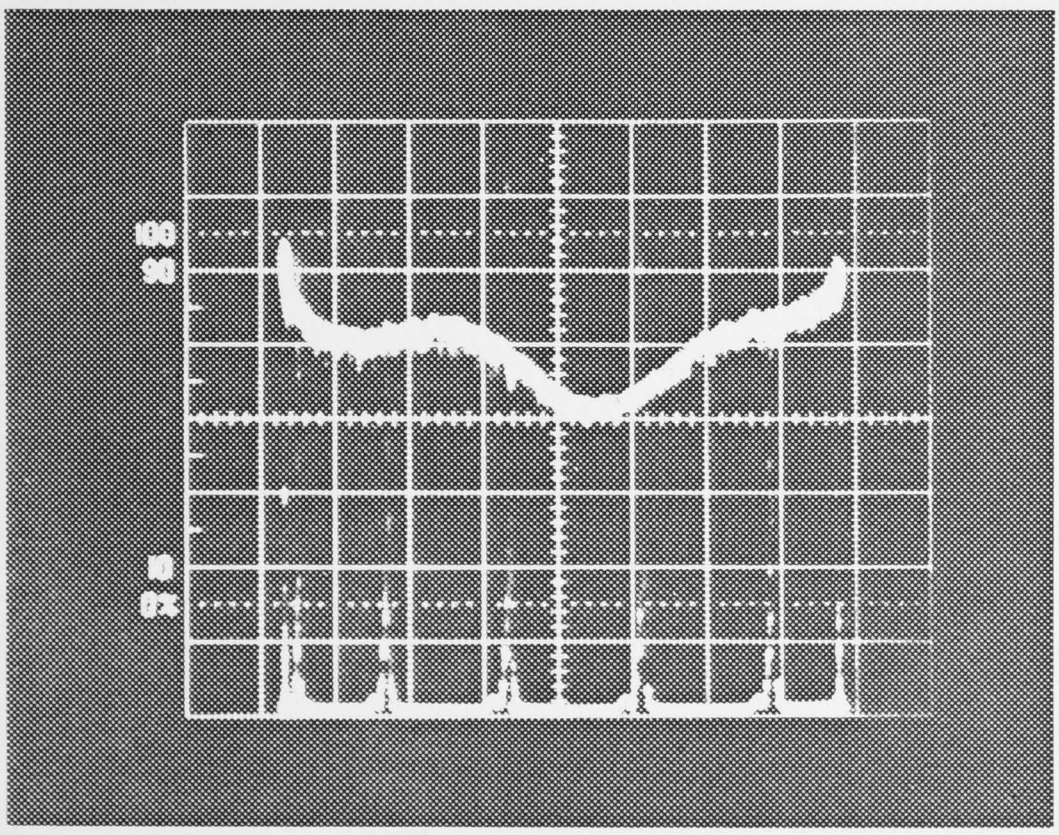

FIGURE 7.6 (ii) P_T = 31.4 KPa (314 mbars)

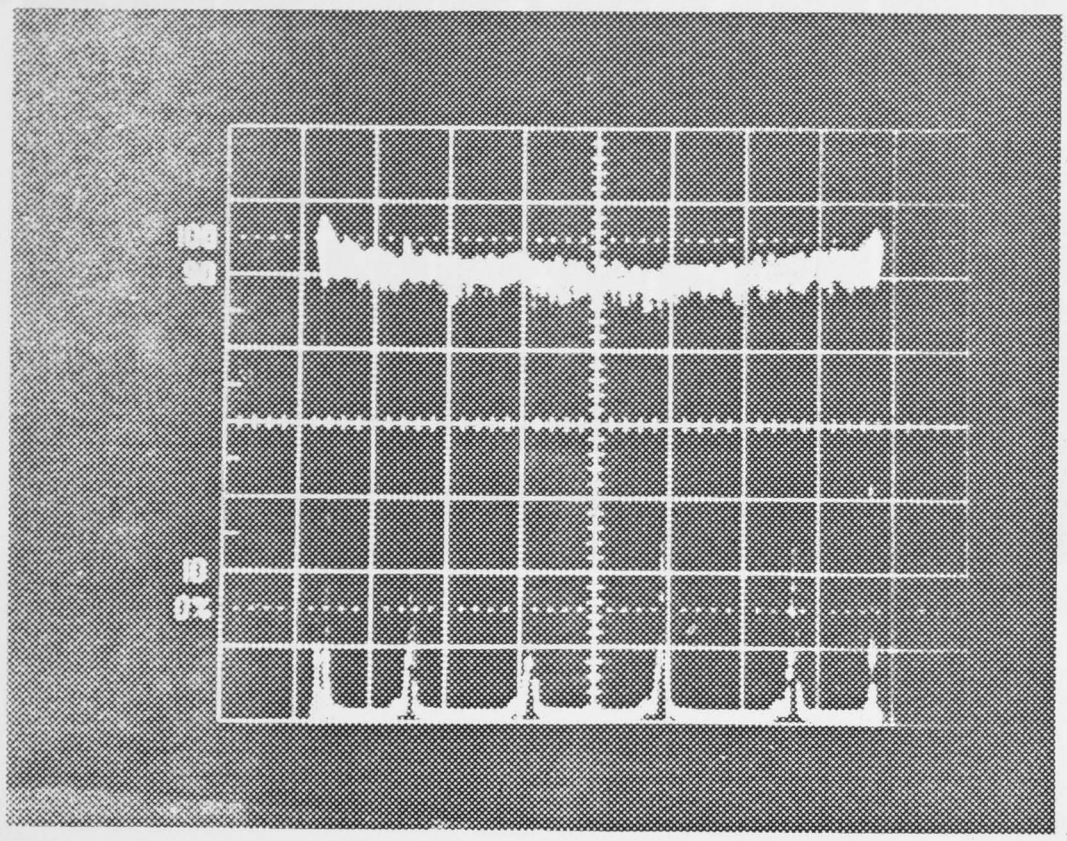

FIGURE 7.6 (iii) P_T > 80.0 KPa (800 mbars).

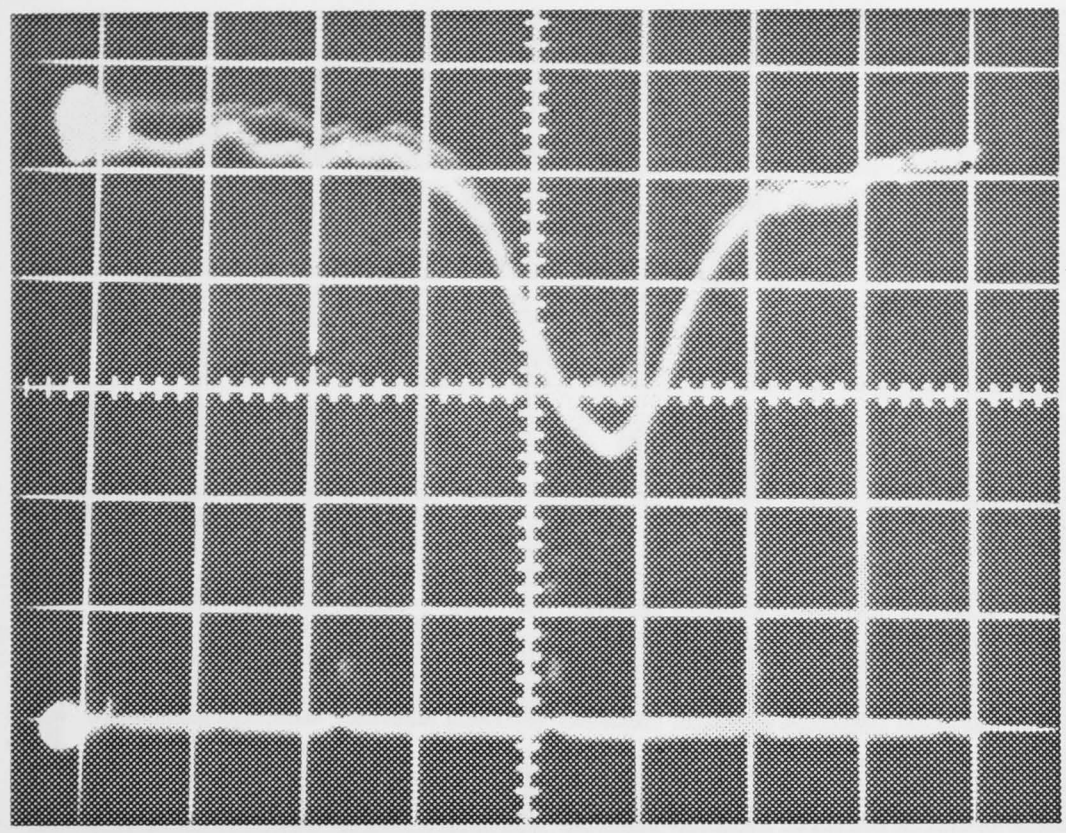

(i)

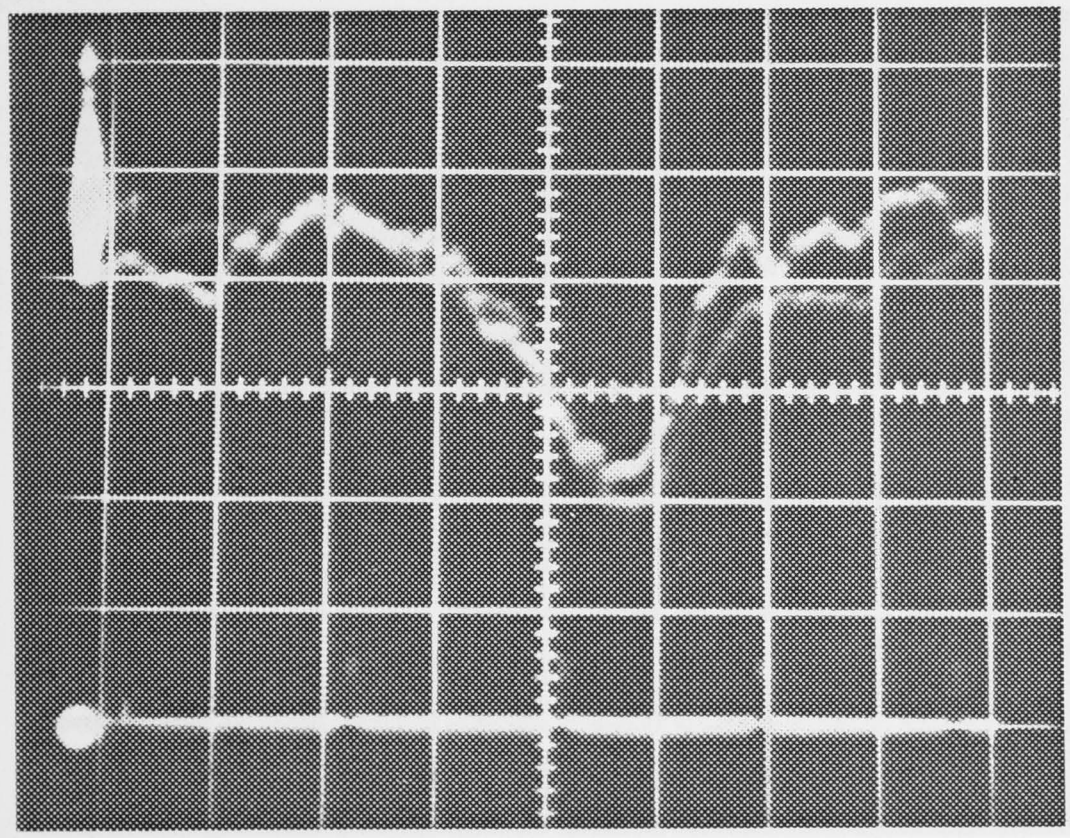

(ii)

FIGURE 7.7 Laser scans for the spectral line $\lambda = 571.225$ nm.
Gas temperature = 45 °C
Iodine vapour pressure = 0.19 KPa (1.9 mbars)
(i) Absorption scan, $P_T = 8.5$ KPa (85 mbars)
(ii) Refractive index scan, $P_T = 9.4$ KPa (94 mbars)

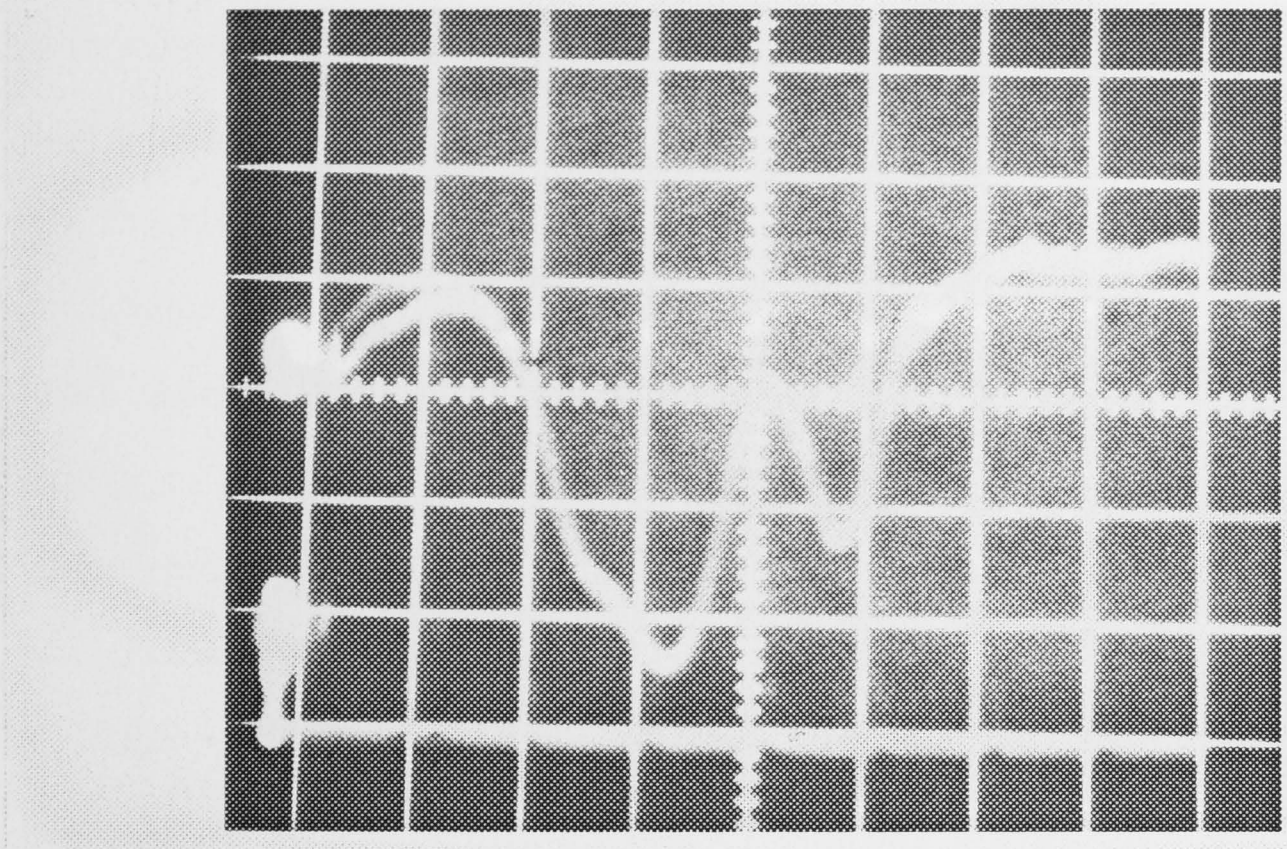

(i)

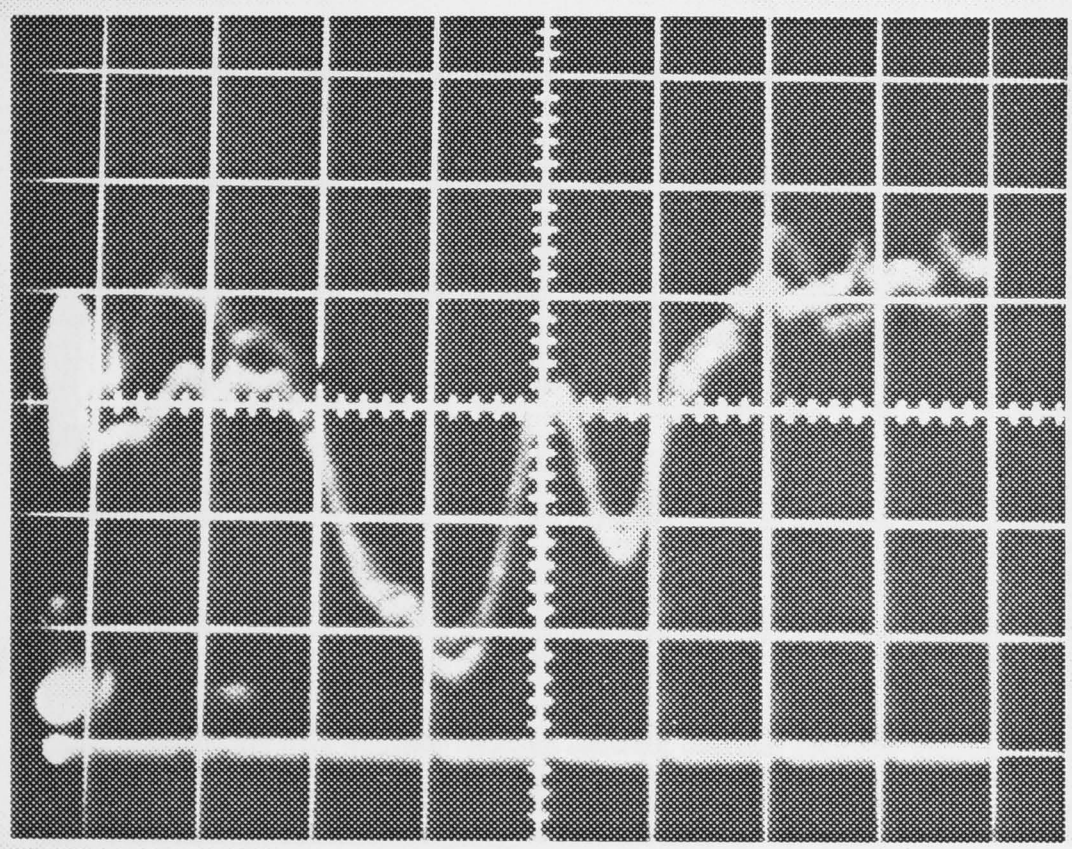

(ii)

FIGURE 7.8 Laser scans for the spectral line $\lambda = 570.519$ nm.
Gas temperature = 48 °C
Iodine vapour pressure = 0.25 KPa (2.5 mbars)
(i) Absorption scan, $P_T = 8.8$ KPa (88 mbars)
(ii) Refractive index scan, $P_T = 9.3$ KPa (93 mbars)

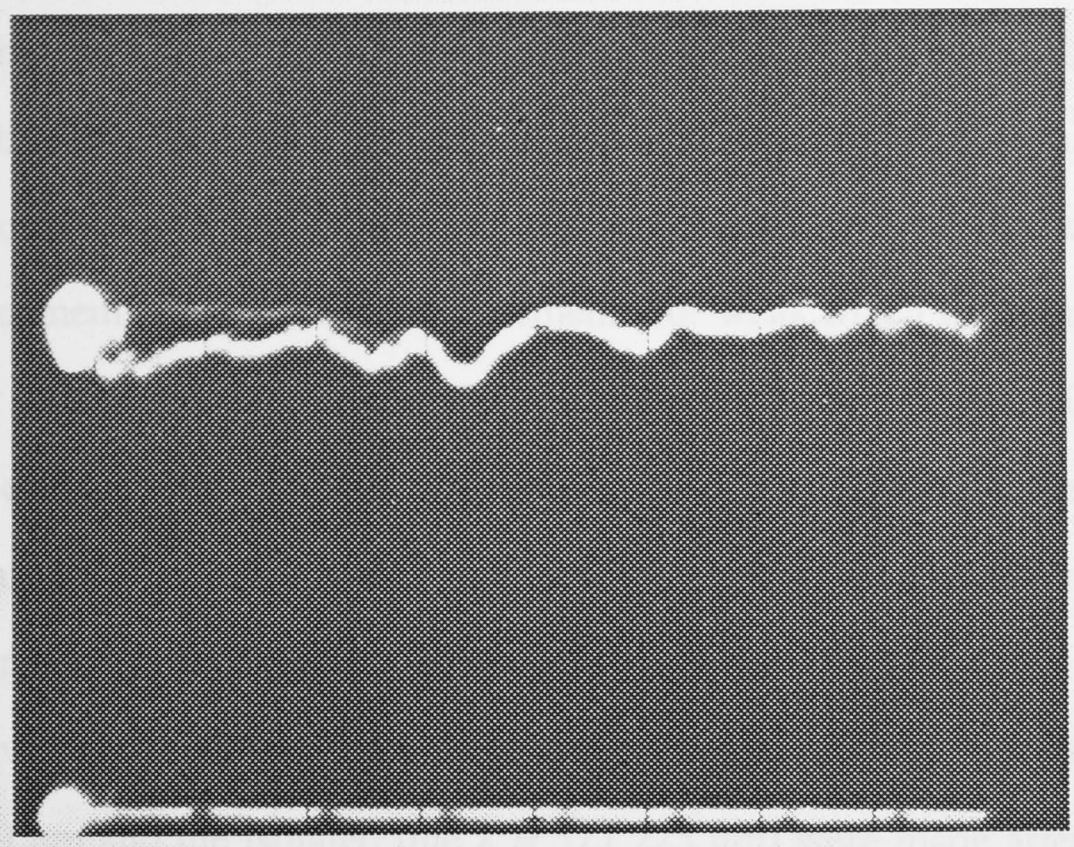

(i)

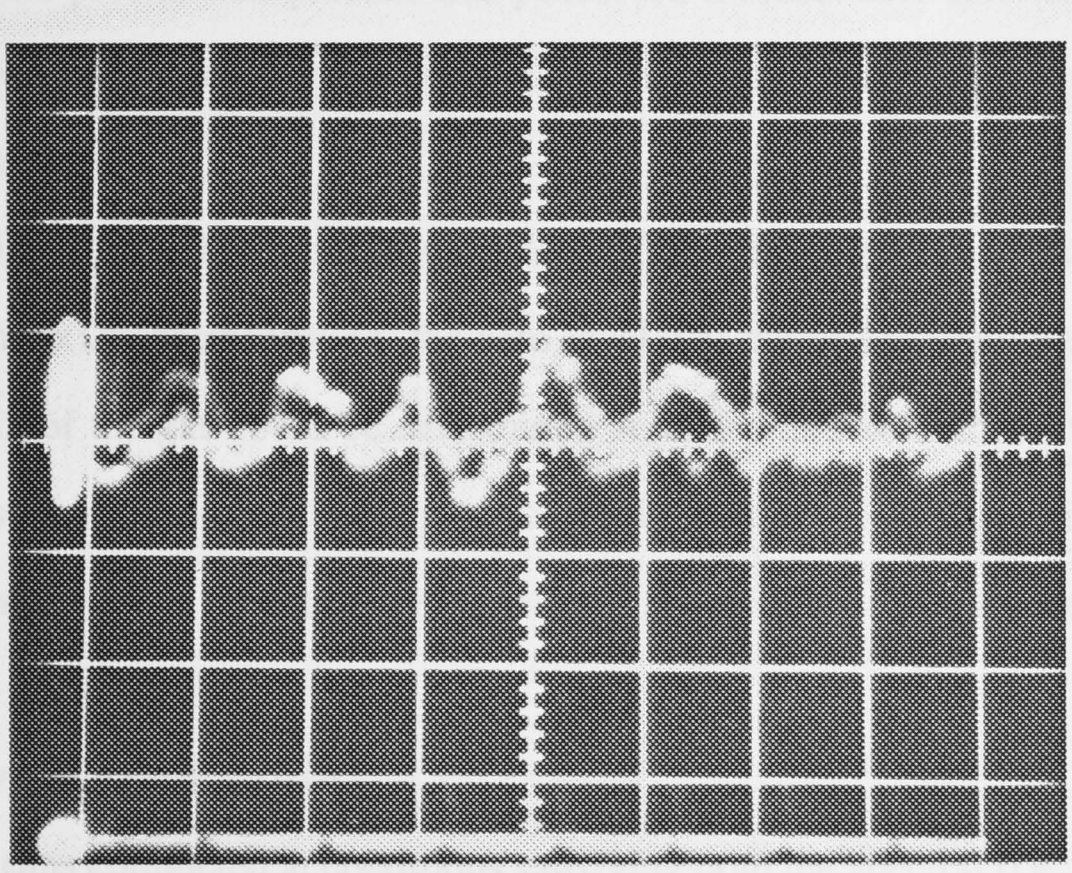

(ii)

FIGURE 7.9 Laser scans for the spectral line $\lambda = 570.519$ nm.
Gas temperature = 25 °C
Iodine vapour pressure = 0.0 KPa (0 mbars)
(i) Absorption scan, $P_T = 0.7$ KPa (7 mbars)
(ii) Refractive index scan $P_T = 1.9$ KPa (19 mbars)

transition, then the enhancement effects due to the refractive index variation about the line would be negligible. This meant a maximum pressure of no more than 10 KPa in the shock tube. A smaller additive gas pressure would have been better for fringe shift enhancement. The pressure requirements for weak Mach reflection, however, were better suited to shock tube pressures of the order of 90 KPa. This forced a compromise to be reached with the shock tube operating conditions. All shots attempted after the significance of pressure broadening was determined were at a shock tube pressure of 10 KPa.

Refractive index measurements about the spectral lines in question (the bandhead λ = 570.519 nm and the isolated line λ = 571.225 nm) were made after all shots of weak Mach reflection in the shock tube had been completed (see figures 7.7, 7.8 and 7.9). An absorption scan was made in conjunction with every refractive index scan to insure the line profile was present and possessed a reasonable linewidth and peak absorption value. Figure 7.9 has been included as a reference scan (no iodine was present in the tube).

The CRO scale division settings were different for each type of scan (absorption or refractive index). For absorption, the zero level was carefully monitored so that the optical depth of the gas could be determined and used as a reference for theoretical calculations of optical depth. The position of the zero level for the refractive index scans was unimportant because only the relative fringe shift was being measured.

7.2 Flow Visualization

The only runs completed at conditions satisfying both the spectral (i.e. low pressure broadening) and slow shock speed requirements were in the series starting at Shot #364 and finishing with Shot #387 (see figures 7.10 to 7.16.). The equivalent series of shots for the spectral line λ = 571.225 nm was unable to be completed at the same time as that for the (16,0) bandhead because of equipment failure occurring after shot #371 (the last shot in the (16,0) bandhead series). A departmental timetable calling for the relocation of the tunable ring dye lasers, amongst other things, prevented

completion of the isolated line series of shots at a later date.

The interferograms obtained were digitized and filtered according to the process mentioned in section 6.1. The resultant filtered interferograms are displayed below the originals. The shots are presented in increasing order of wavelength. For comparisons of the enhanced fringe shift effects for different wavelength detunings, vertical slices were taken of the digitized interferograms at different distances behind the incident shock (i.e. 5, 10, 15 and 20 mm) and an average fringe shift was determined. (These are also presented with their respective interferograms.) Table 7.1 shows the laser wavelength for each shot.

The fringe shift across the reflected shock, for a particular distance behind the incident shock, was taken from the individual plot of the vertical slice for that particular distance and is shown in table 7.2. In all, four vertical slices were taken behind the incident shock to generate a reasonable value for the average fringe shift. The four separate plots of the vertical slices taken for shot #365 have been included here as an example as well as the overlaid plot of the four vertical slices. Only the overlaid plot has been included for all other shots.

TABLE 7.1 Wavelength vs Shot #

Wavelength (nm)	**Shot #**
570.513	371
570.515	364
570.517	365
570.519	368
570.521	369
570.523	370
632.8	387

The laser wavelength for this series of shots varied from 570.513 nm to 570.523 nm. The bandhead was at 570.517 nm, with a number of overlapping absorption lines existing between there and 570.523 nm. A second absorption maximum lay at

570.520 nm. The wavelength of the HeNe laser (λ = 632.8 nm) is included as a reference for comparison of the enhanced fringe shifts with the unenhanced fringe shifts across the reflected shock. The incident shock speed is faster by approximately 17% than the average for the other shots but the Mach number is comparable. (The sound speed in a test gas of air is greater than that for a test gas mix of air and iodine.) Therefore, the reflected shock will also be of comparable strength and the resultant fringe shift should give a good indication of the size of the fringe shift due solely to density changes in the air.

A table (Table 7.3) has been included at the end of this section, listing all the details concerning the operating conditions, sound speeds, etc. for each shot except for shot #393. This shot was not analysed but is included as it was a similar shot to shot #387 and exhibits some interesting features.

It should also be noted that the fringe shift across the reflected shock shouldn't vary with distance behind the incident shock, except for a slight general weakening that will affect all the shots equally.

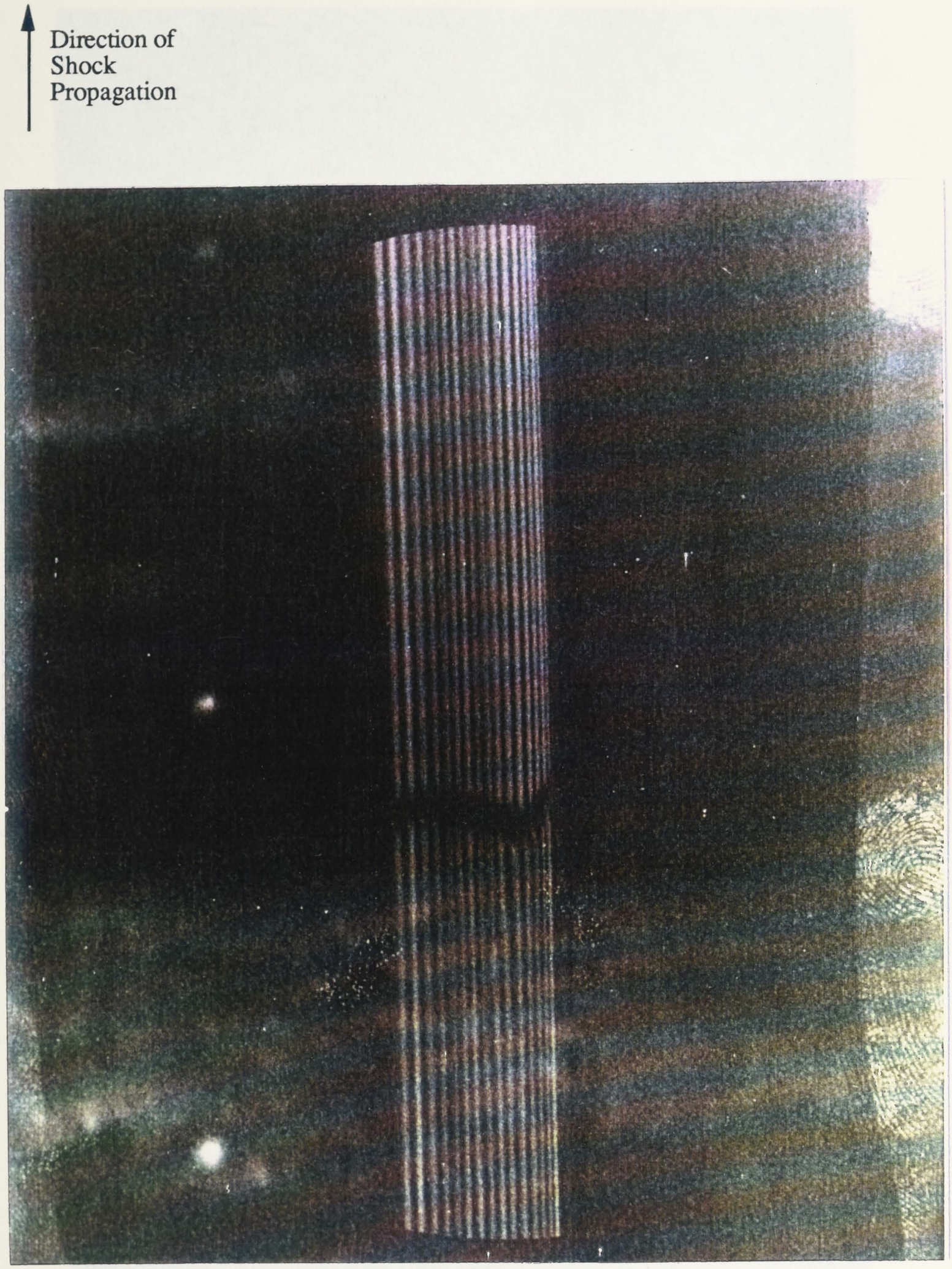

FIGURE 7.10a Shot #371, The original interferogram.
Gas temperature = 62° C
Iodine vapour pressure = 0.667 KPa
Shock velocity = 506.3 m/s
Mach # = 1.7
Laser wavelength = 570.513 nm

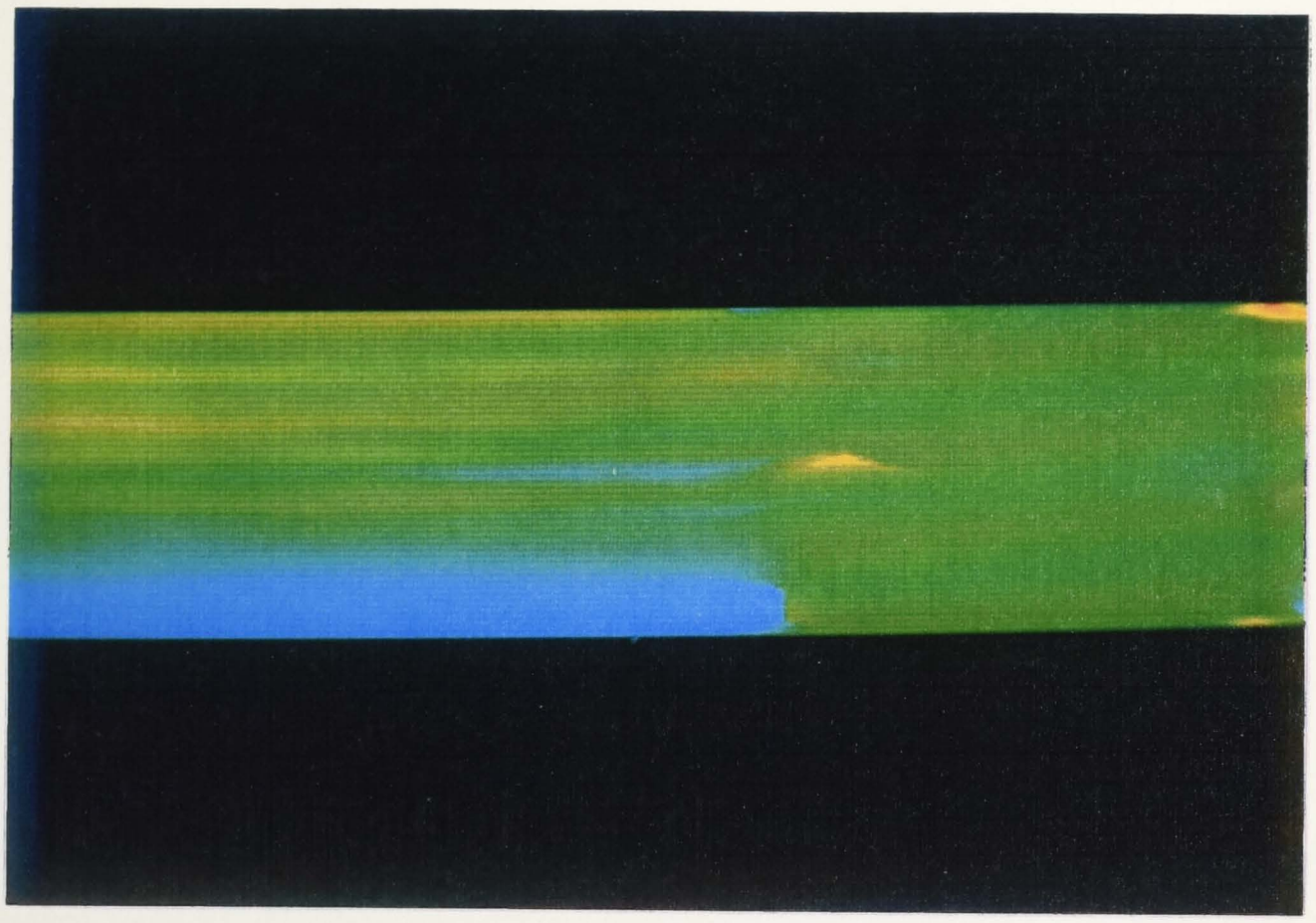

FIGURE 7.10b Shot #371, The filtered picture.
(1 - 256 pixel display)

Direction of
Shock
Propagation

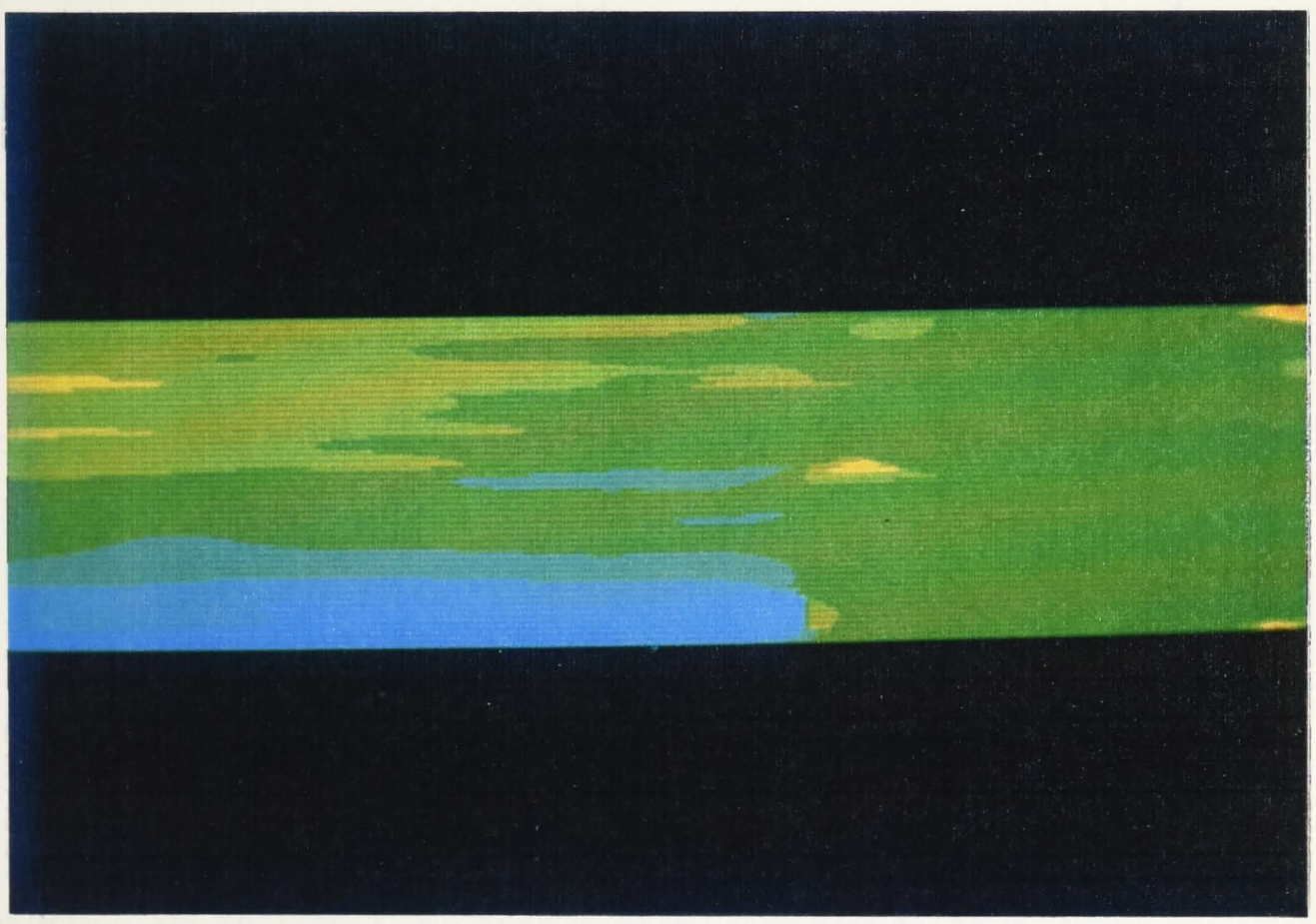

FIGURE 7.10c Shot #371, The filtered picture.
(1 - 56 pixel display)

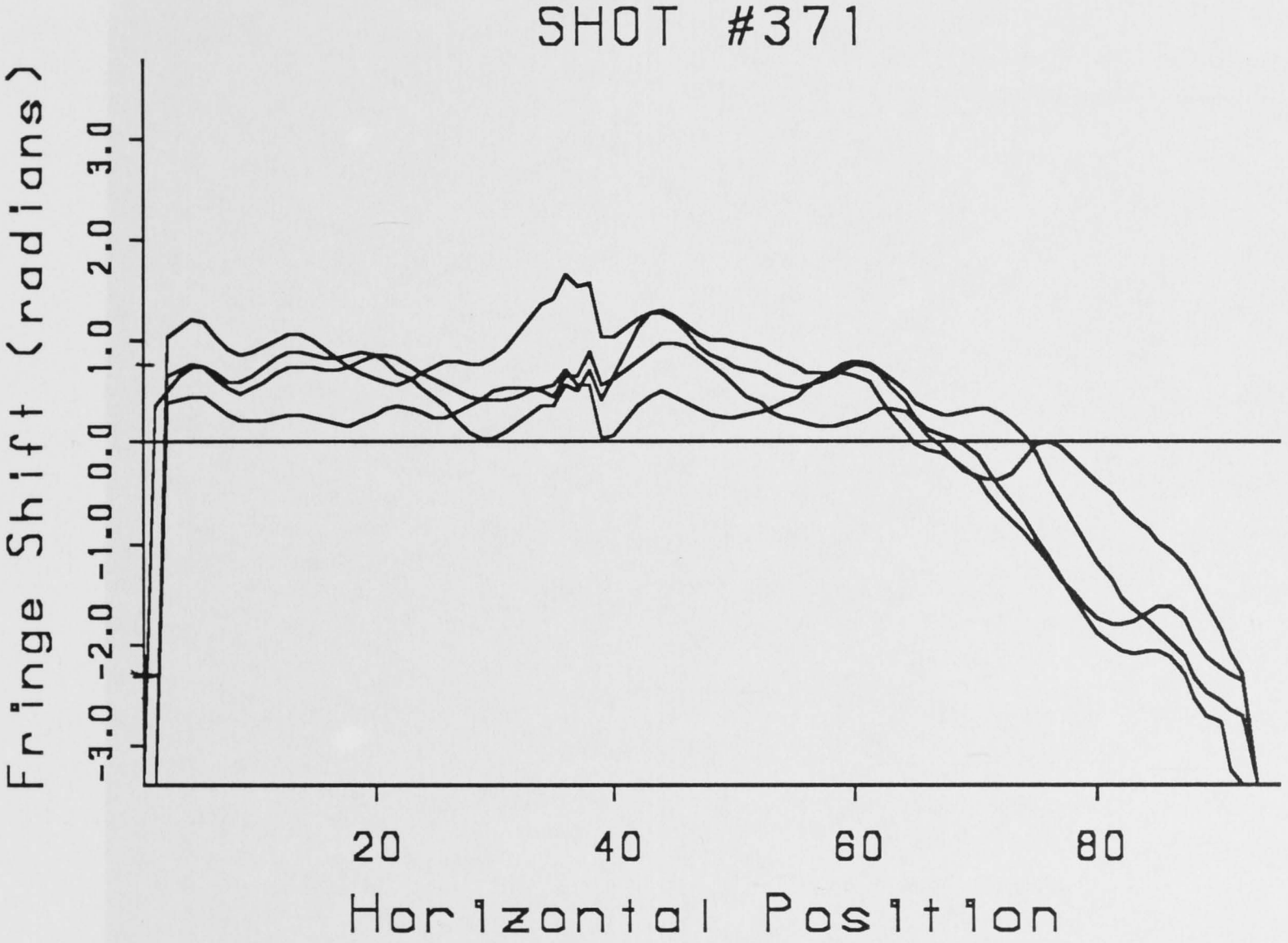

FIGURE 7.10d Shot #371, An overlay of the four vertical slices taken at 5, 10, 15 and 20 mm behind the incident shock. This gives the phase shift across the reflected shock. The horizontal position is given in pixels.

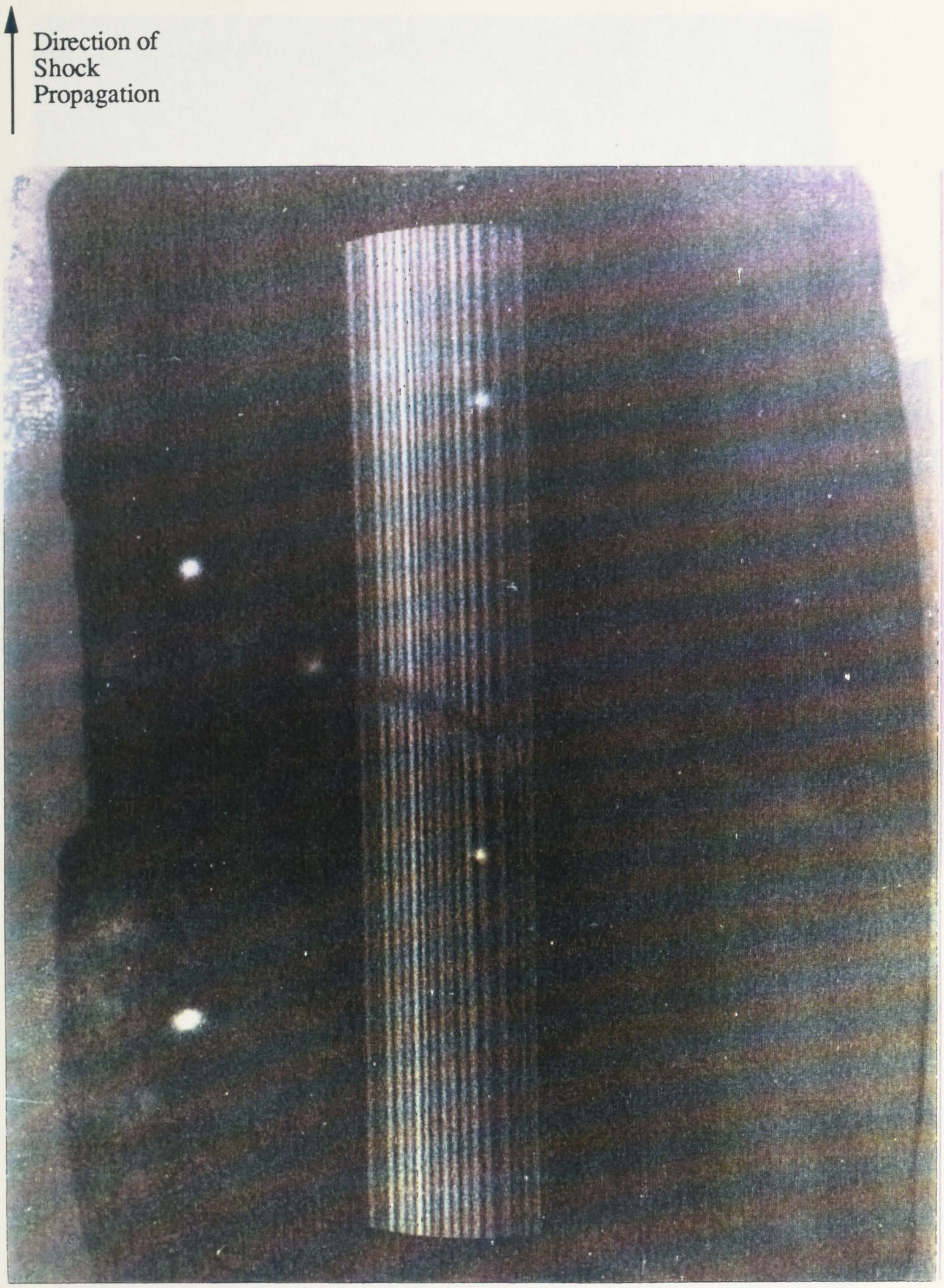

FIGURE 7.11a Shot #364, The original interferogram.
Gas temperature = 68° C
Iodine vapour pressure = 1.07 KPa
Shock velocity = 509.4 m/s
Mach # = 1.86
Laser wavelength = 570.515 nm

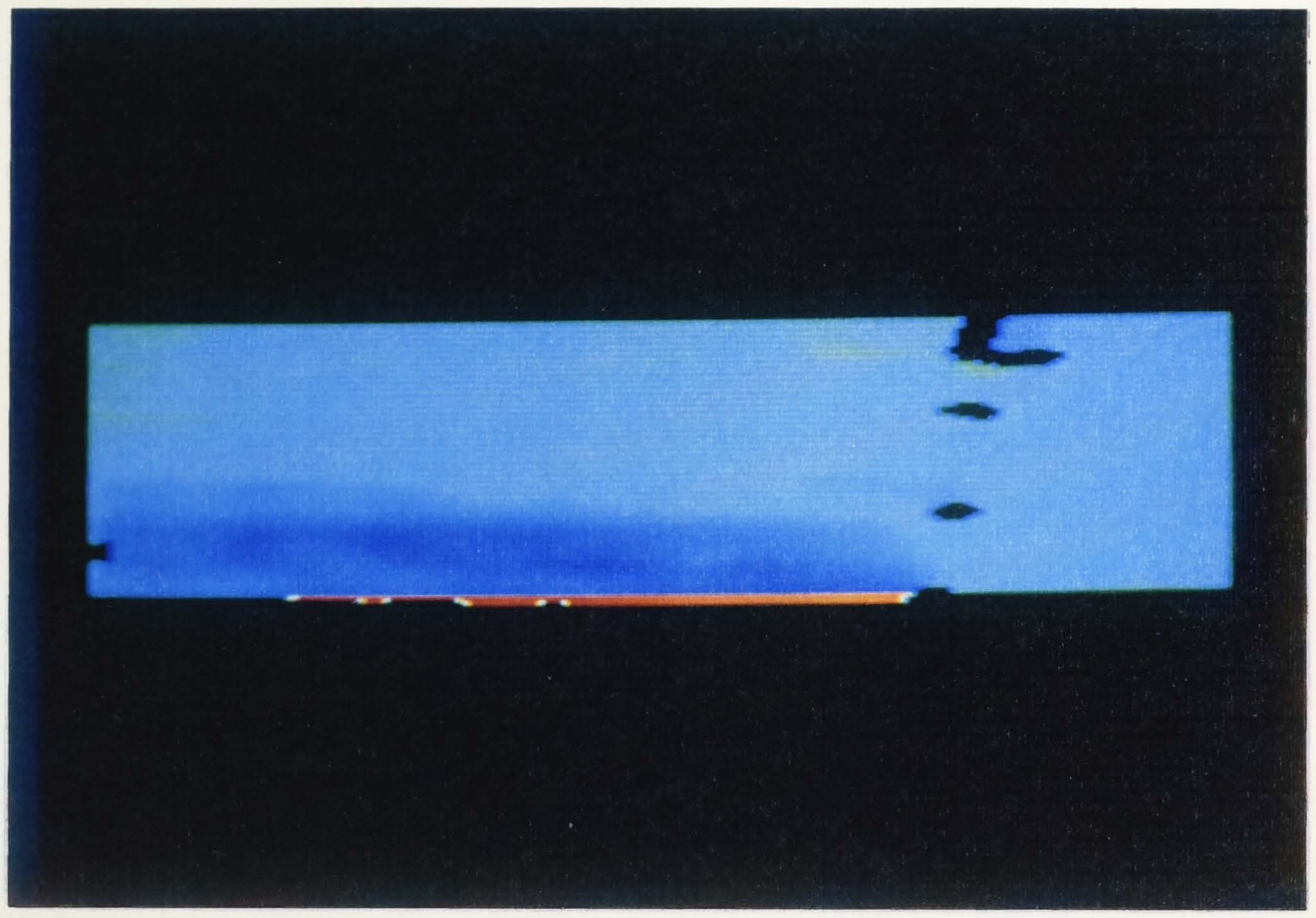

FIGURE 7.11b Shot #364, The filtered picture.
(1 - 256 pixel display)

Direction of
Shock
Propagation

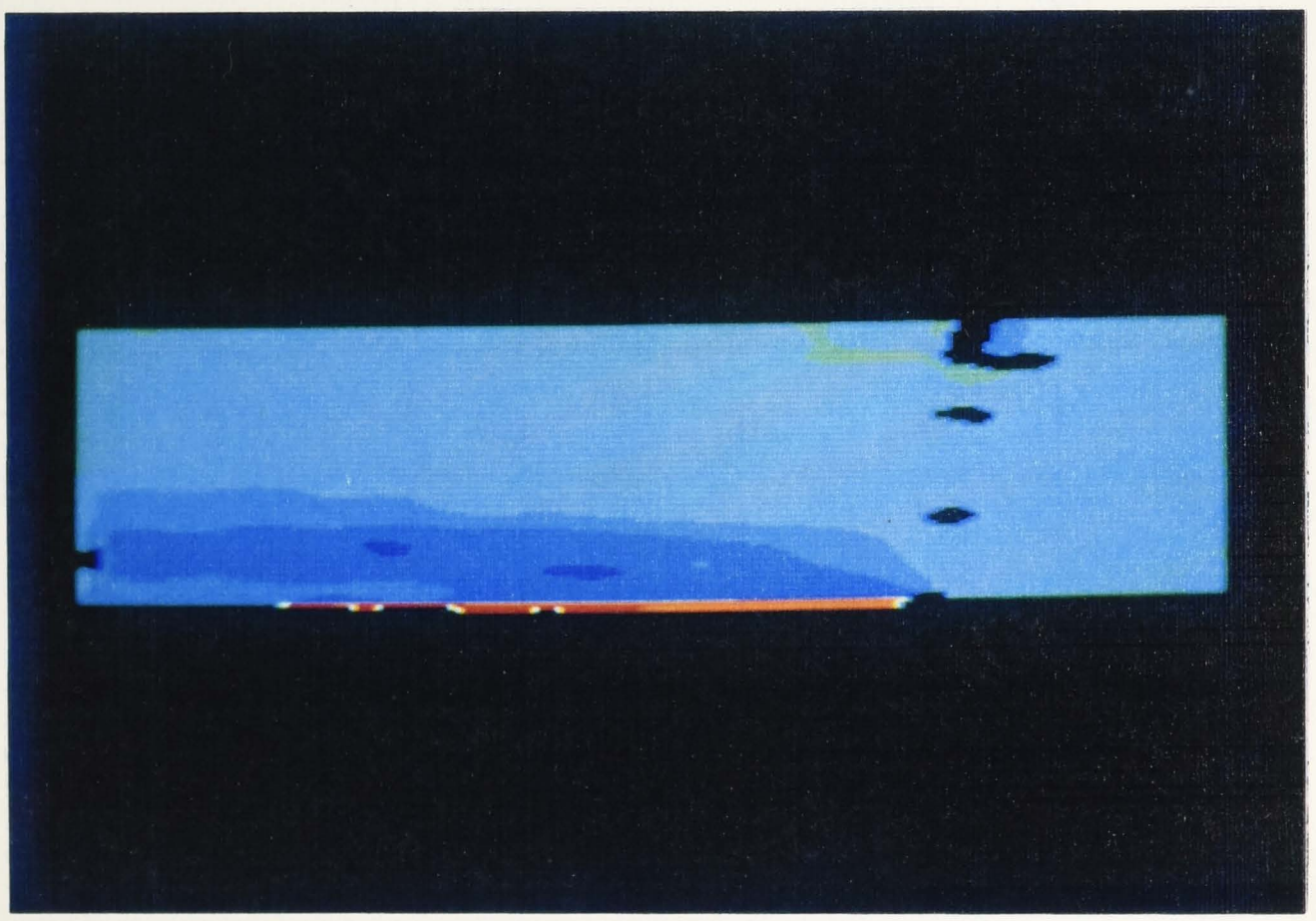

FIGURE 7.11c Shot #364, The filtered picture.
(1 - 56 pixel display)

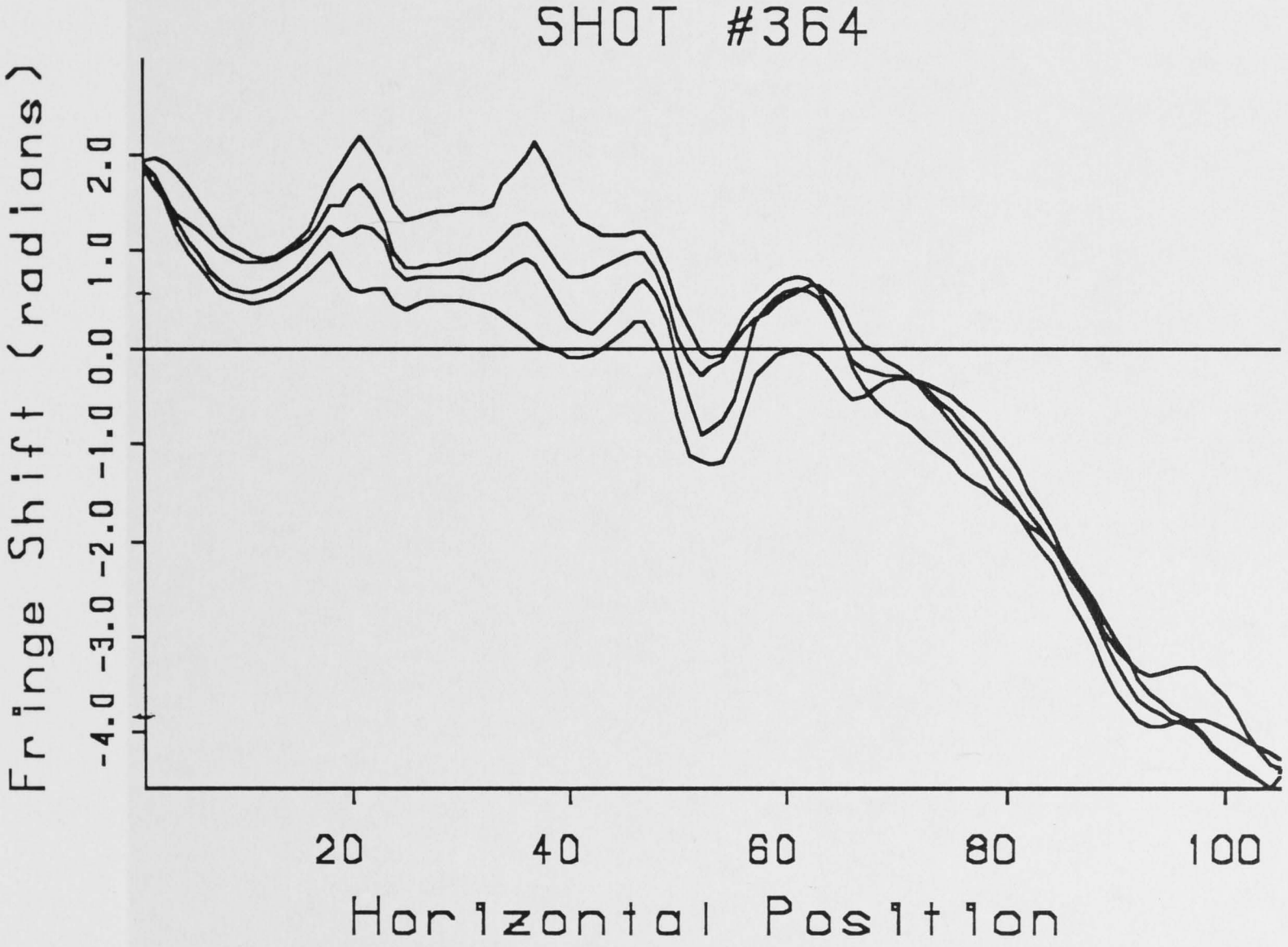

FIGURE 7.11d Shot #364, An overlay of the four vertical slices taken at 5, 10, 15 and 20 mm behind the incident shock. This gives the phase shift across the reflected shock. The horizontal position is given in pixels.

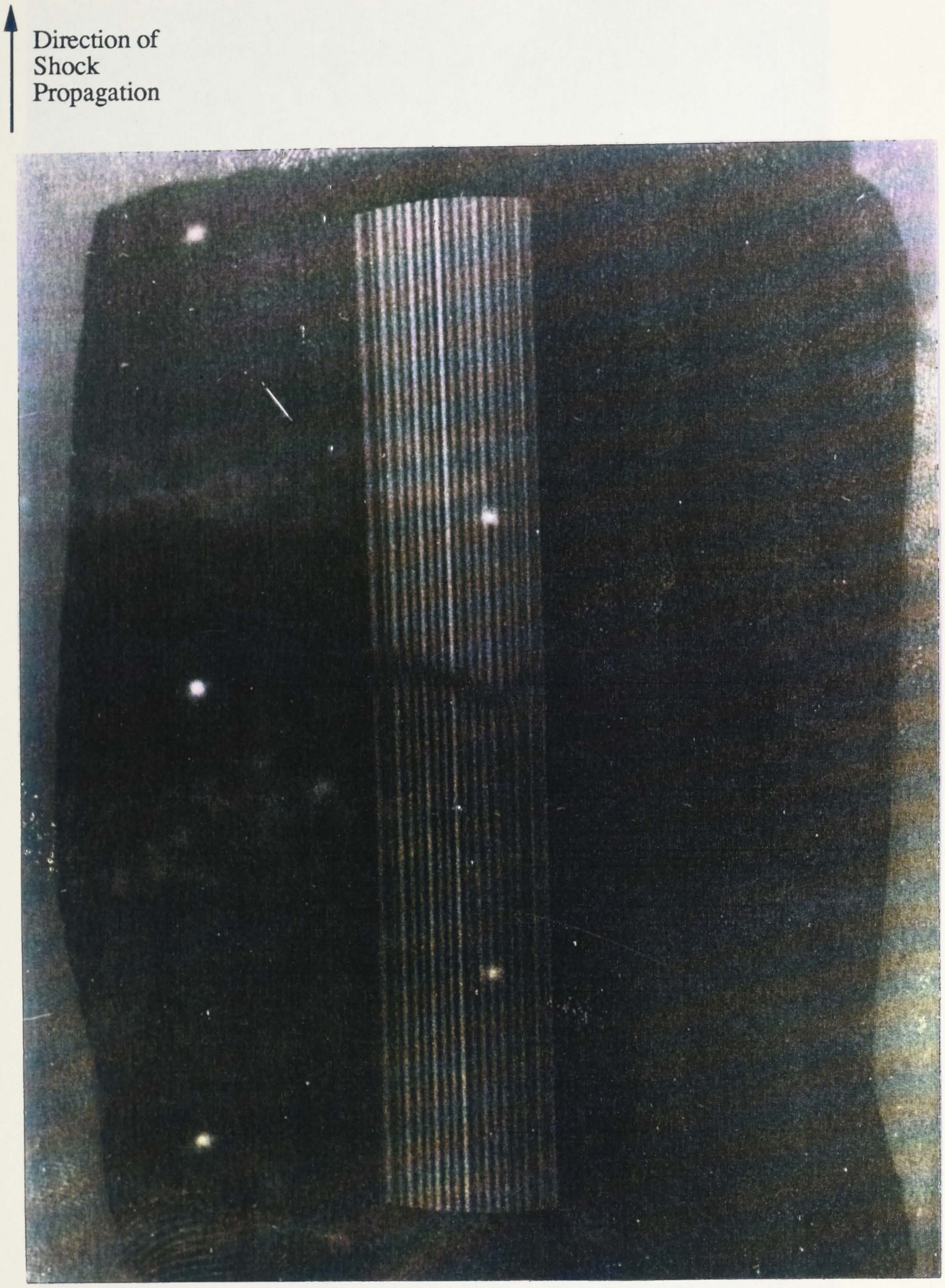

FIGURE 7.12a Shot #365, The original interferogram.
Gas temperature = 66° C
Iodine vapour pressure = 0.866 KPa
Shock velocity = 506.3 m/s
Mach # = 1.77
Laser wavelength = 570.517 nm

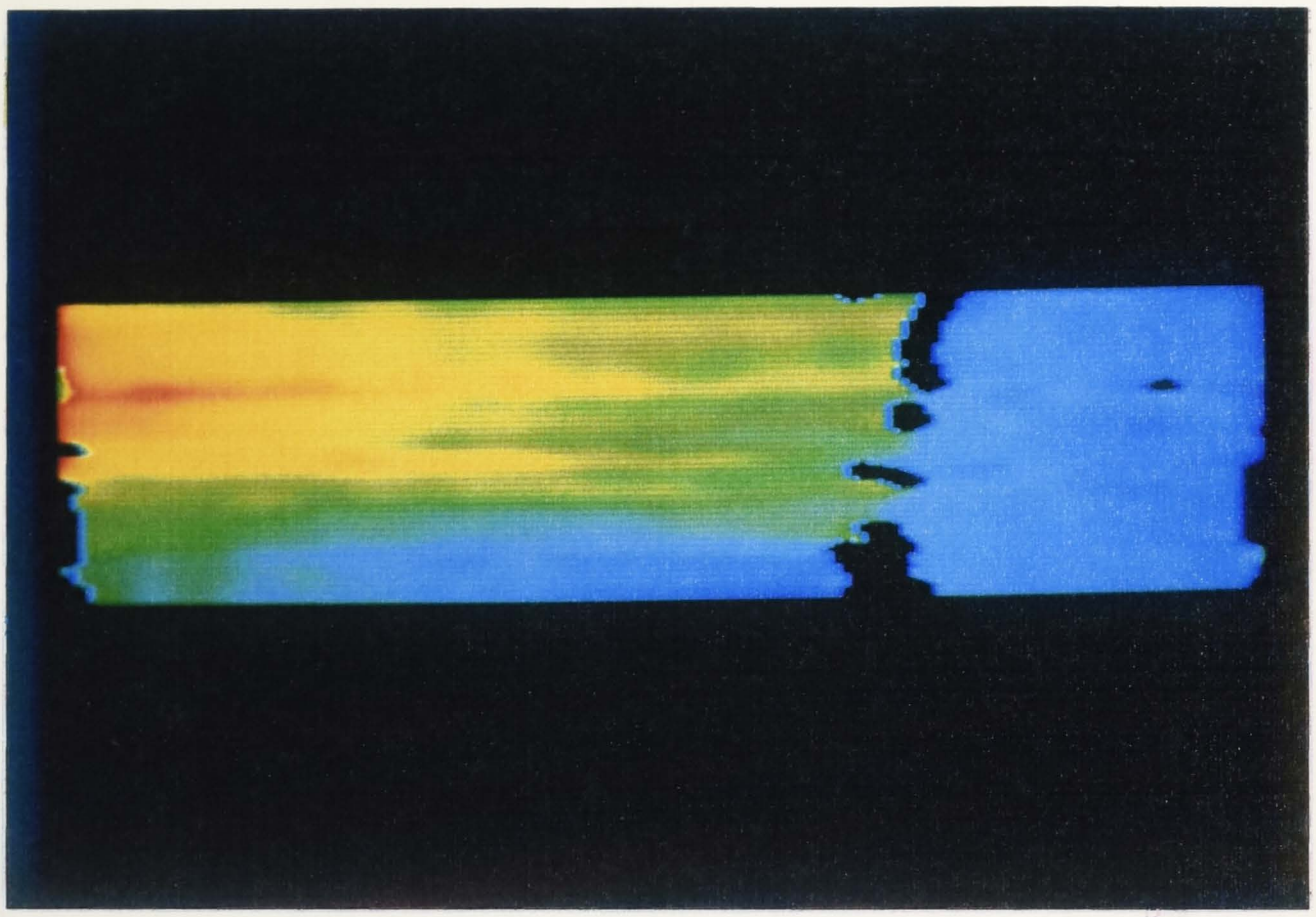

FIGURE 7.12b Shot #365, The filtered picture.
(1 - 256 pixel display)

Direction of
Shock
Propagation

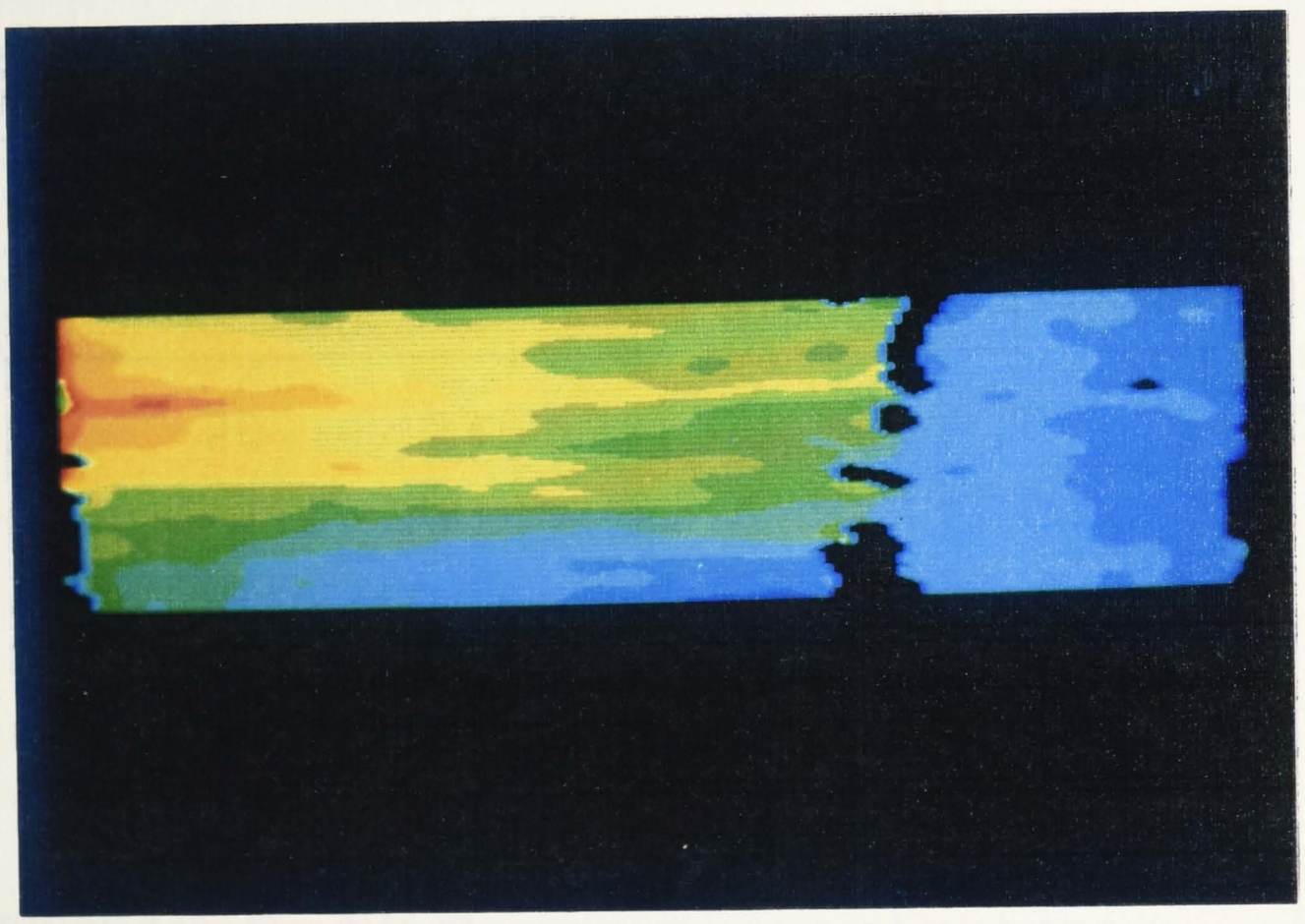

FIGURE 7.12c Shot #365, The filtered picture.
(1 - 56 pixel display)

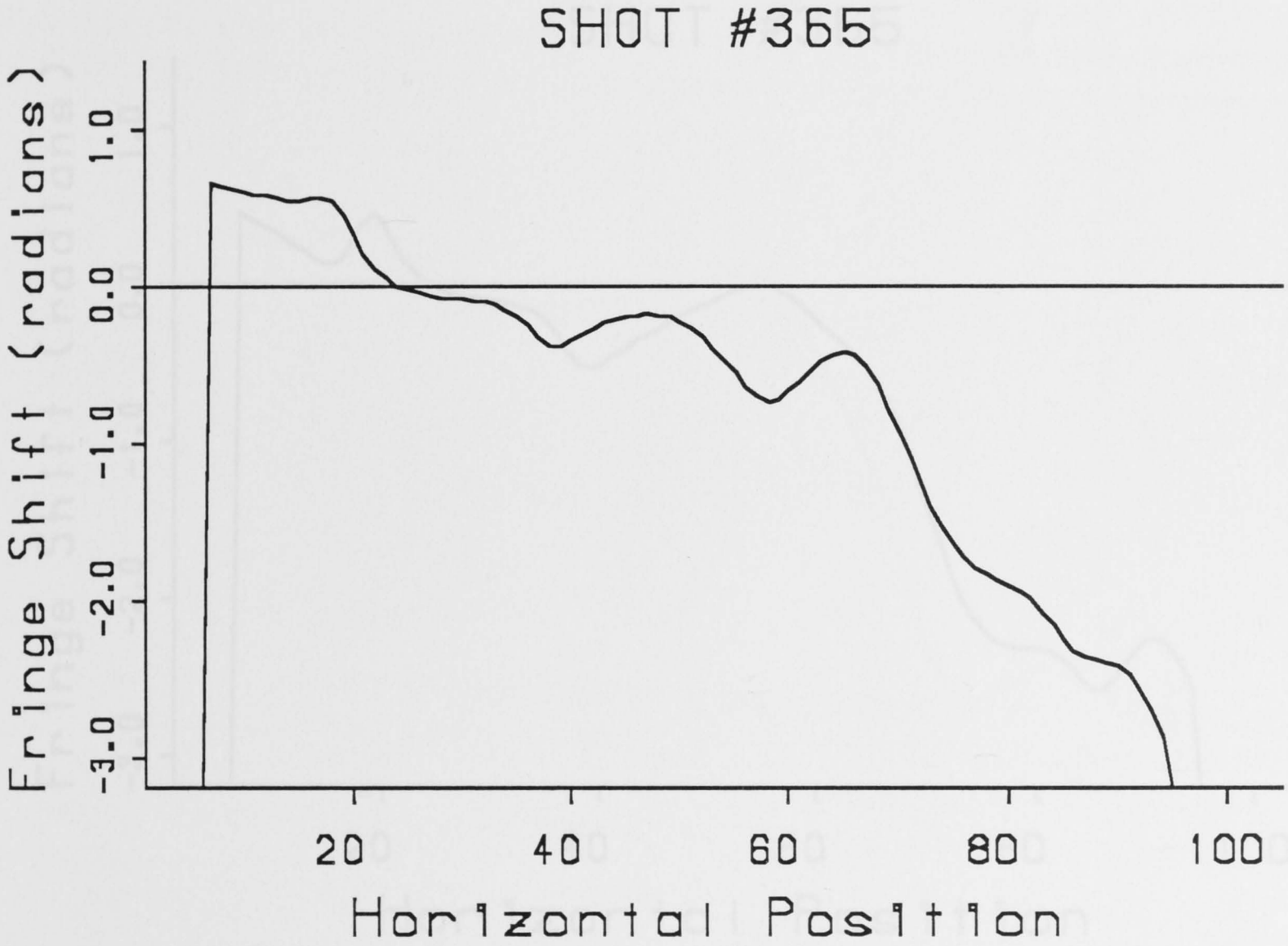

FIGURE 7.12d Shot #365, The vertical slice taken at 5 mm behind the incident shock. This gives the phase shift across the reflected shock. The horizontal position is given in pixels.

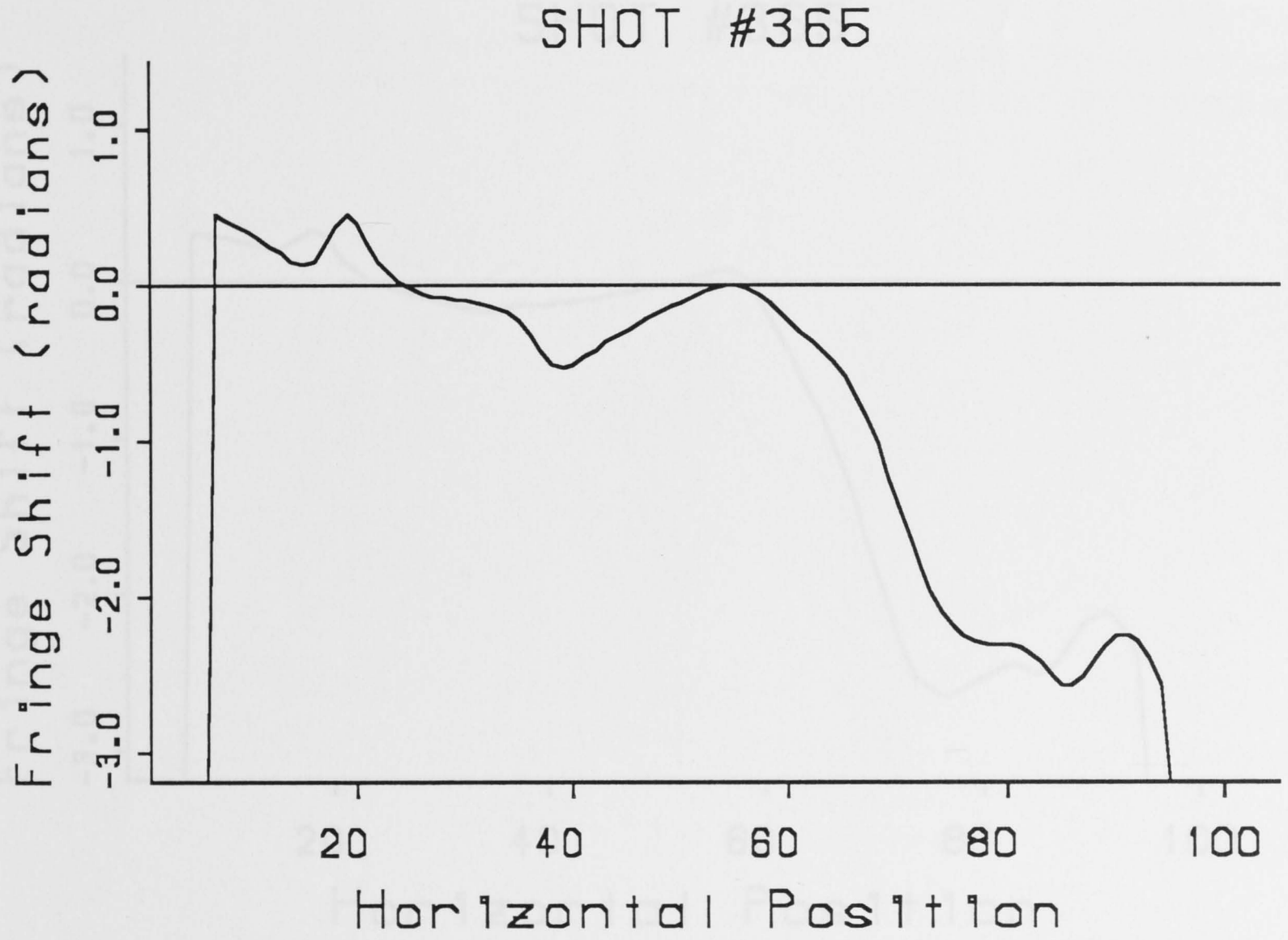

FIGURE 7.12e Shot #365, The vertical slice taken at 10 mm behind the incident shock. This gives the phase shift across the reflected shock. The horizontal position is given in pixels.

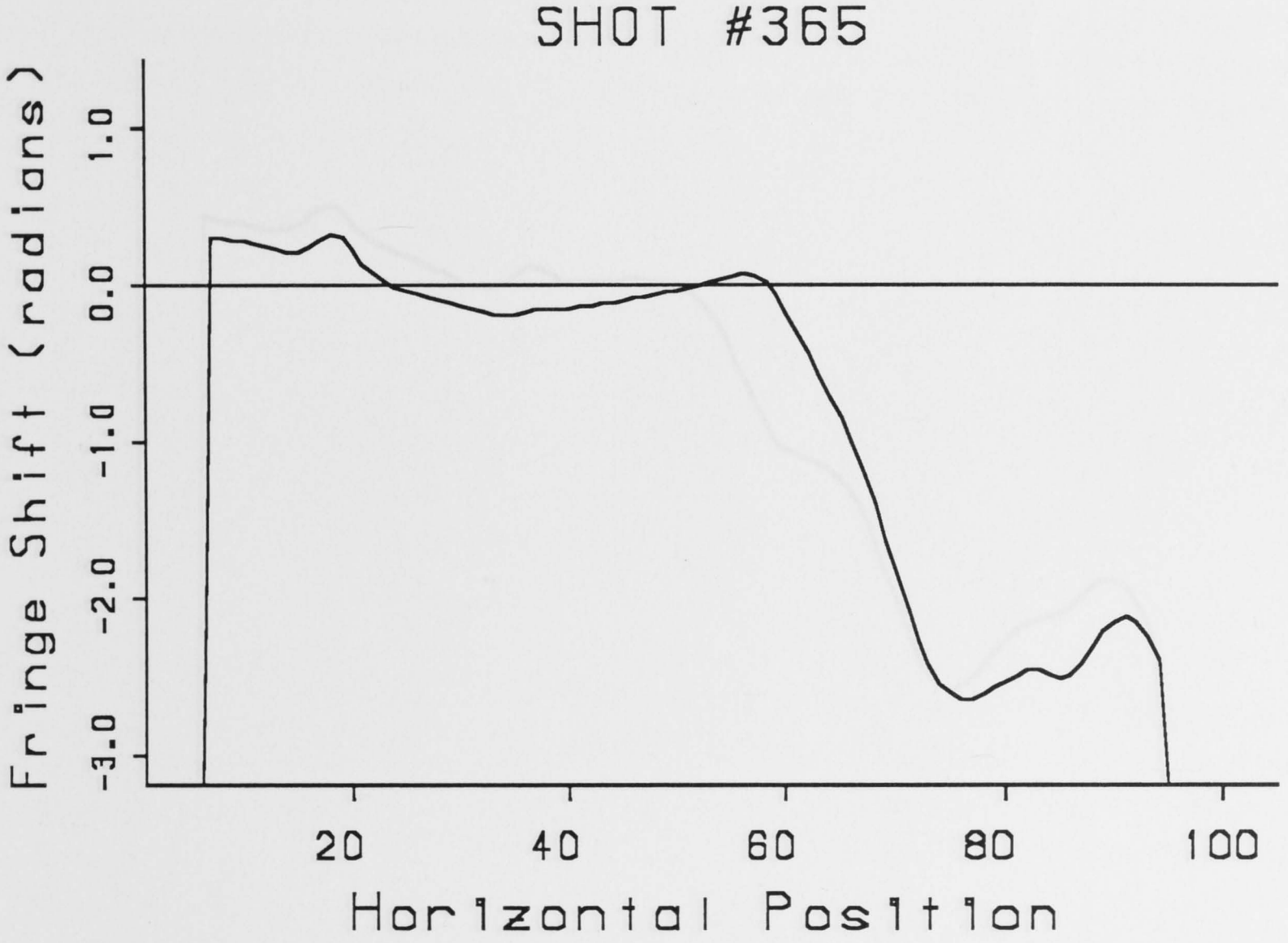

FIGURE 7.12f Shot #365, The vertical slice taken at 15 mm behind the incident shock. This gives the phase shift across the reflected shock. The horizontal position is given in pixels.

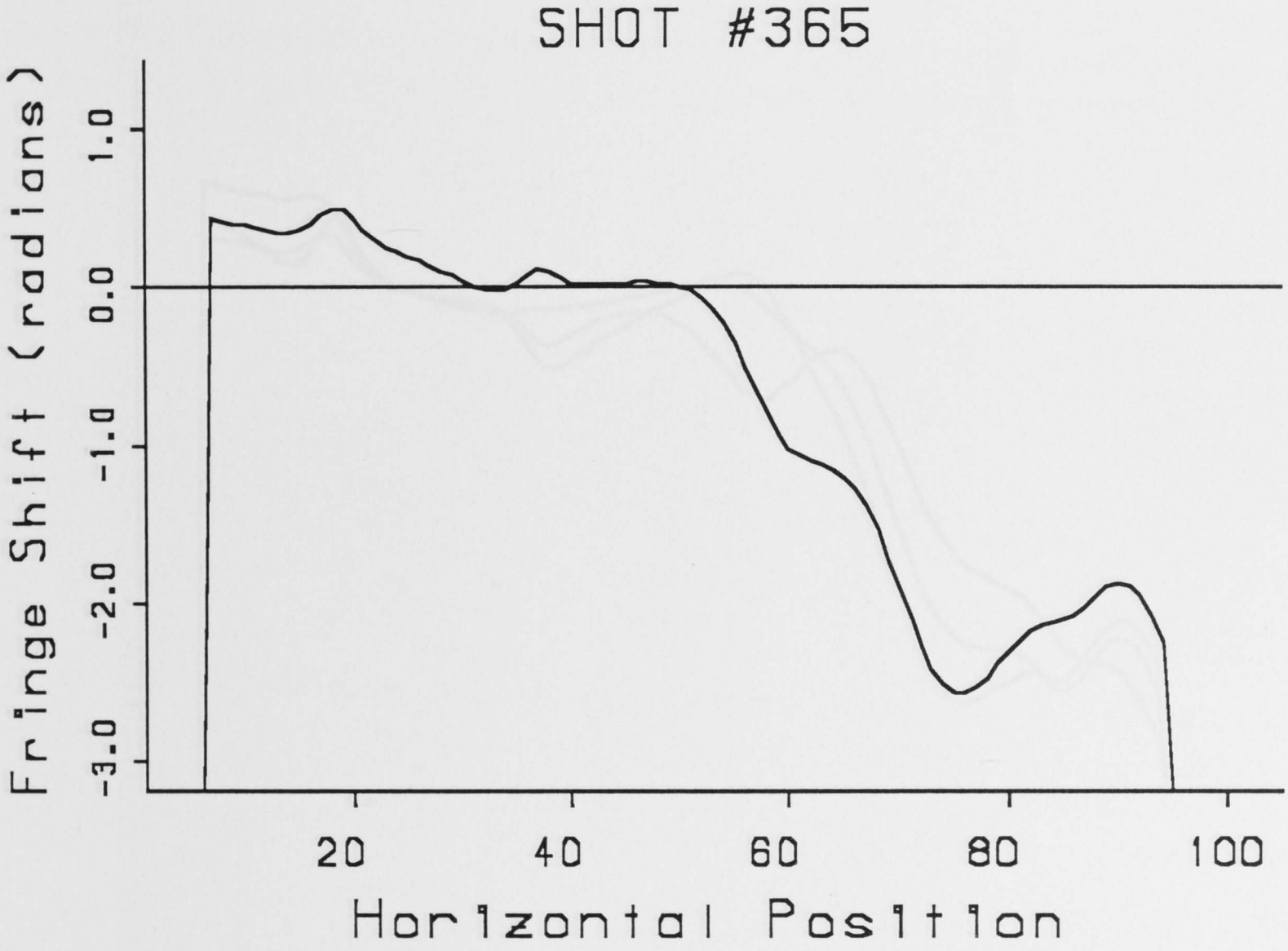

FIGURE 7.12g Shot #365, The vertical slice taken at 20 mm behind the incident shock. This gives the phase shift across the reflected shock. The horizontal position is given in pixels

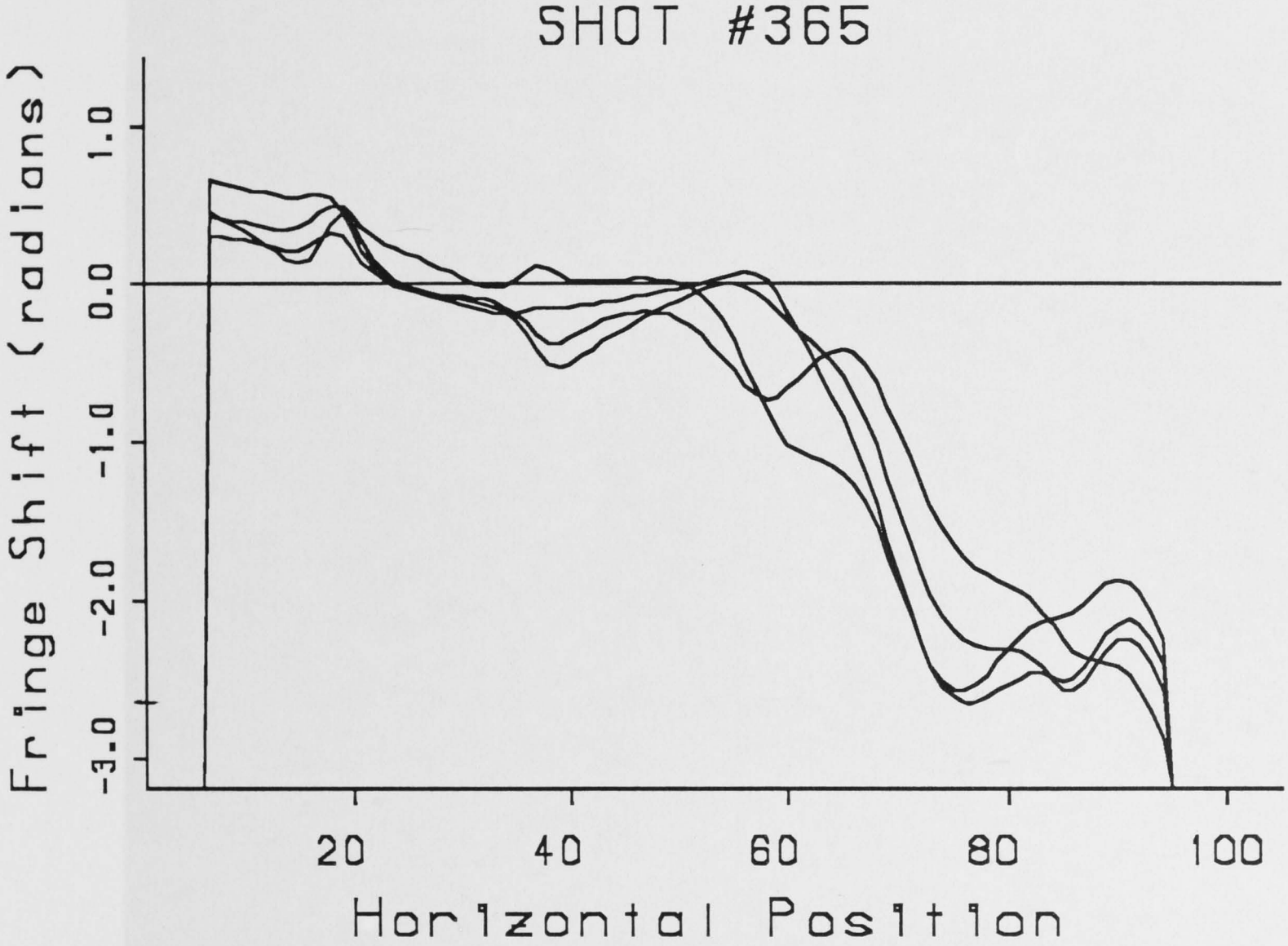

FIGURE 7.12h Shot #365, An overlay of the four vertical slices taken at 5, 10, 15 and 20 mm behind the incident shock. This gives the phase shift across the reflected shock. The horizontal position is given in pixels

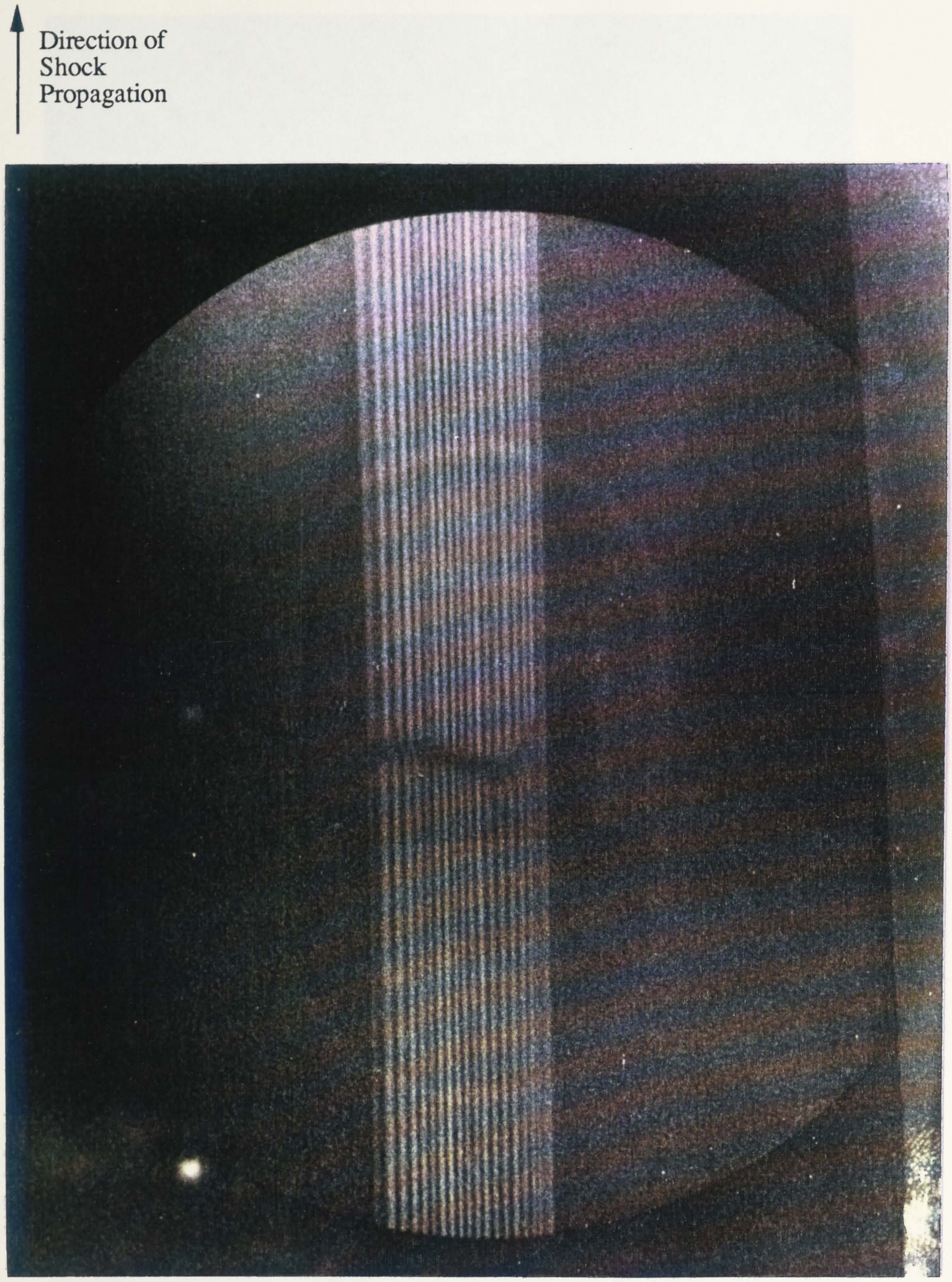

FIGURE 7.13a Shot #368, The original interferogram.
Gas temperature = 58° C
Iodine vapour pressure = 0.533 KPa
Shock velocity = 509.4 m/s
Mach # = 1.65
Laser wavelength = 570.519 nm

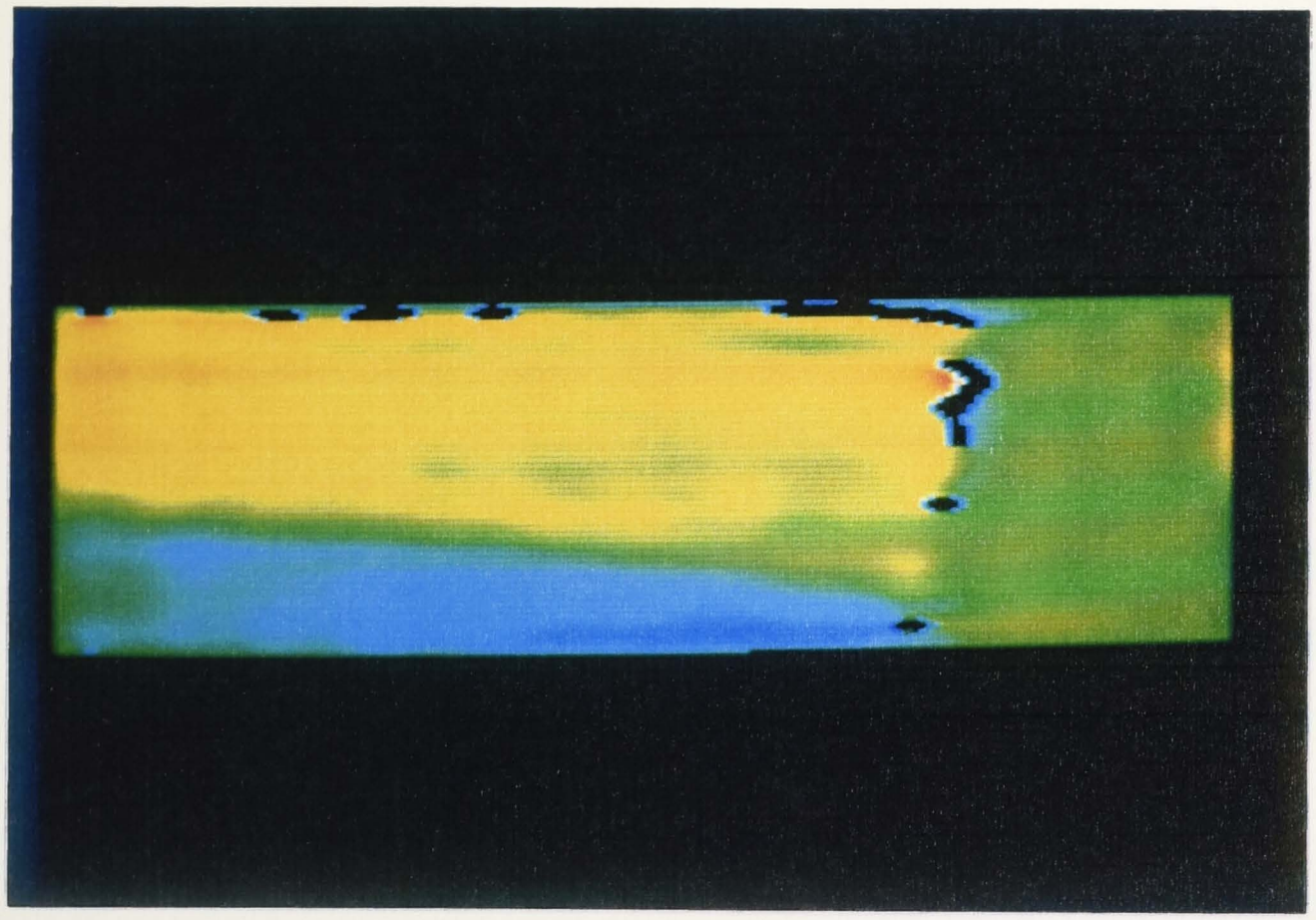

FIGURE 7.13b Shot #368, The filtered picture.
(1 - 256 pixel display)

Direction of
Shock
Propagation

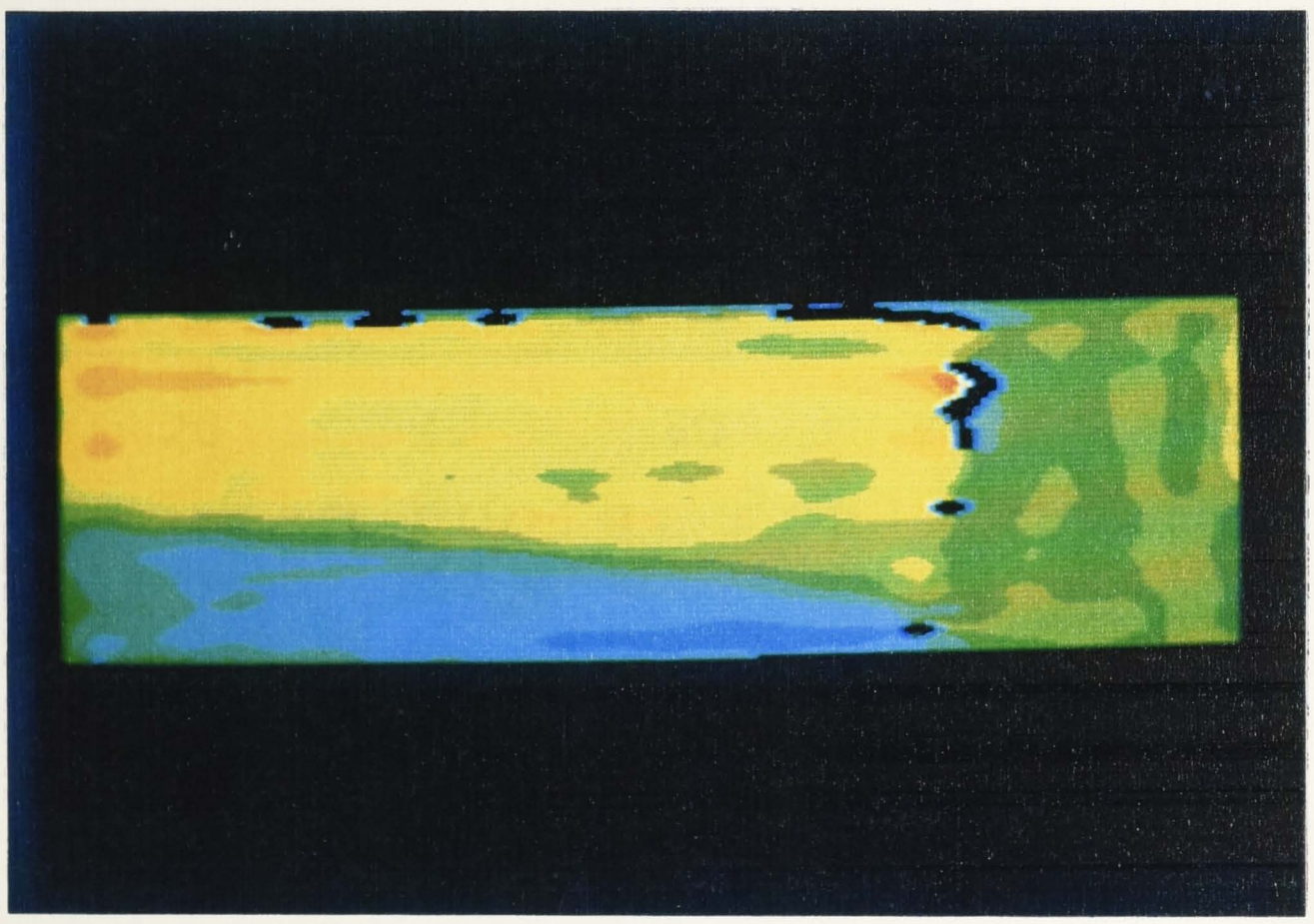

FIGURE 7.13c Shot #368, The filtered picture.
(1 - 56 pixel display)

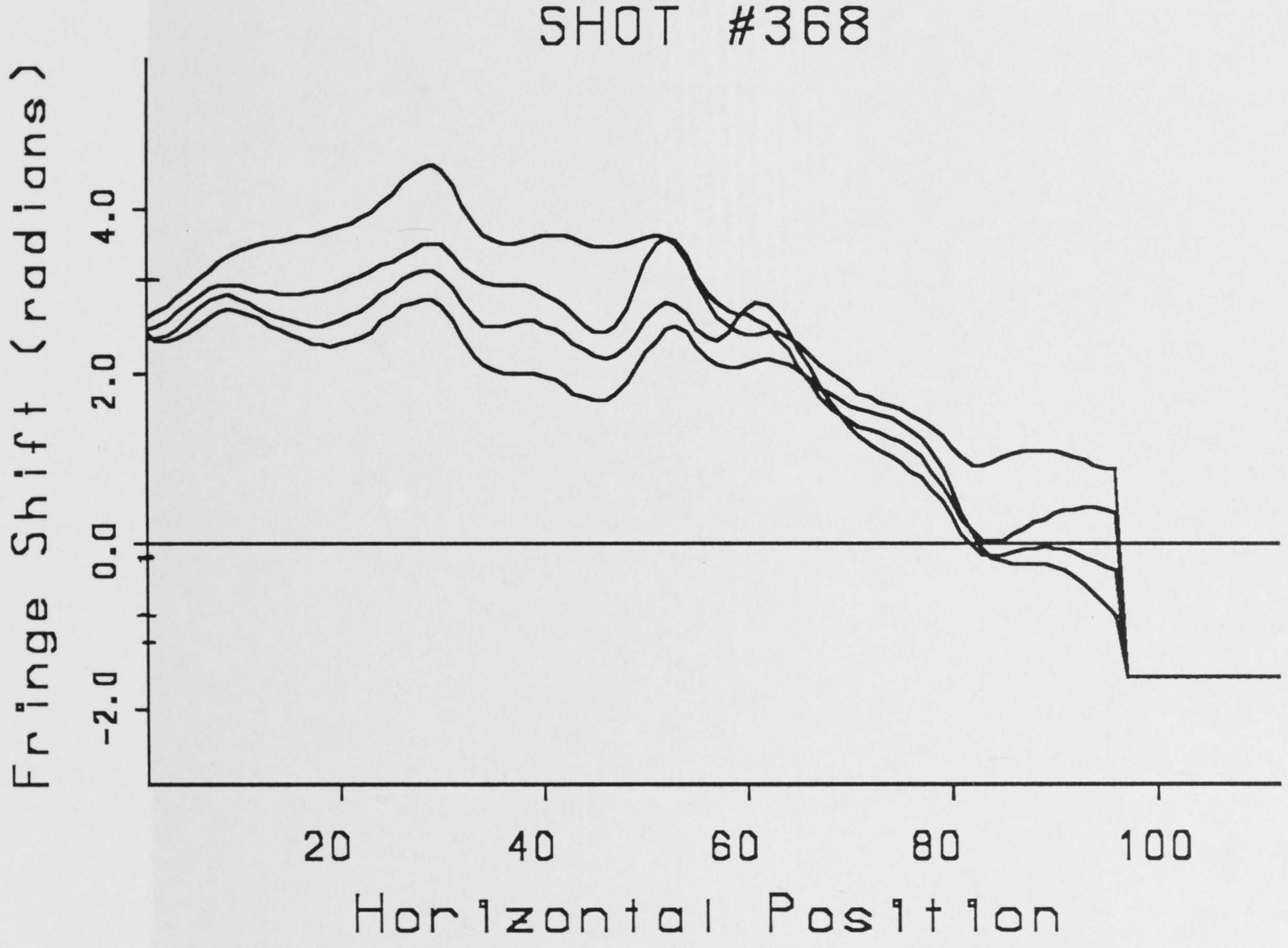

FIGURE 7.13d Shot #368, An overlay of the four vertical slices taken at 5, 10, 15 and 20 mm behind the incident shock. This gives the phase shift across the reflected shock. The horizontal position is given in pixels.

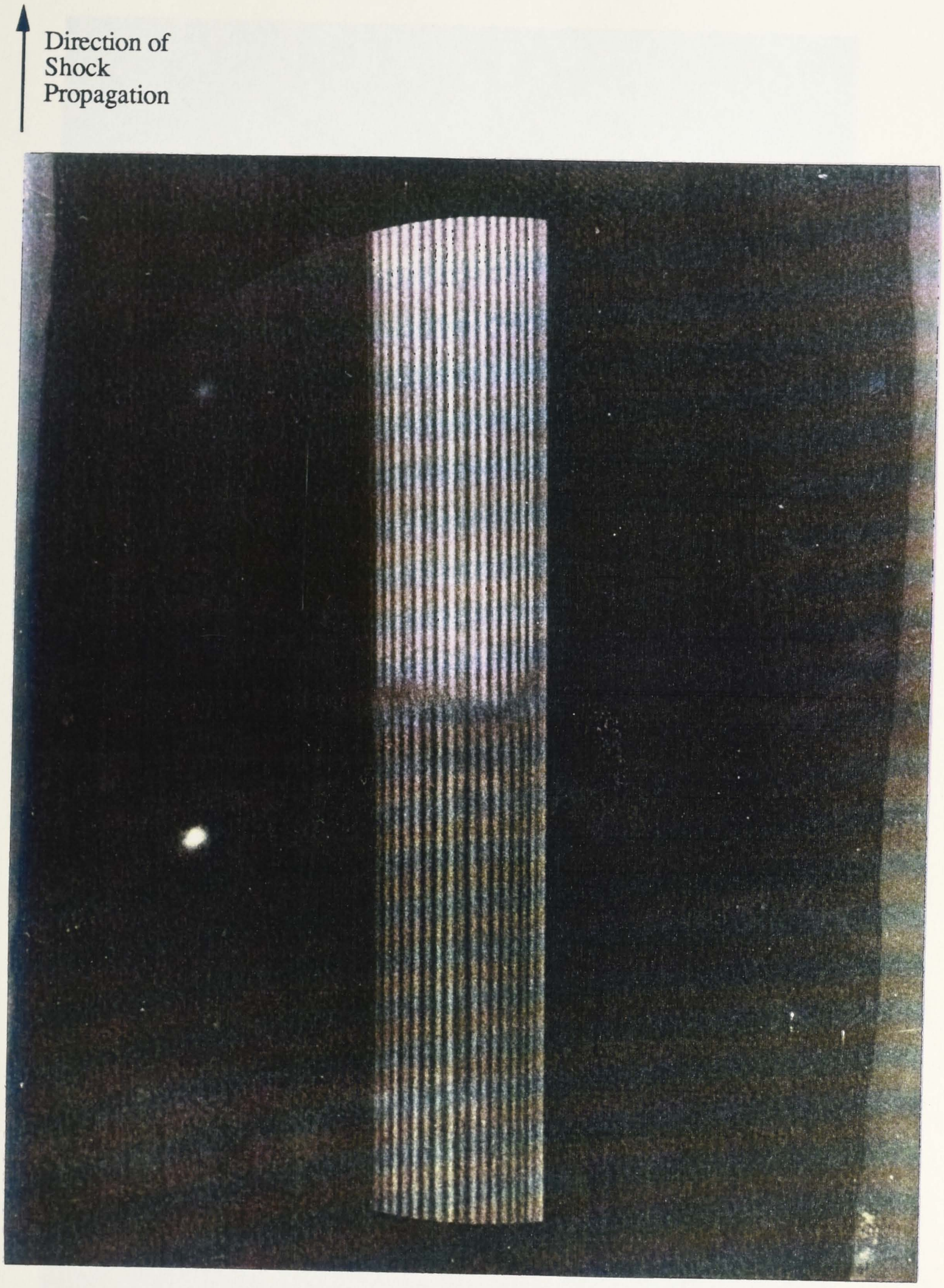

FIGURE 7.14a Shot #369, The original interferogram.
Gas temperature = 59° C
Iodine vapour pressure = 0.60 KPa
Shock velocity = 512.7 m/s
Mach # = 1.69
Laser wavelength = 570.521 nm

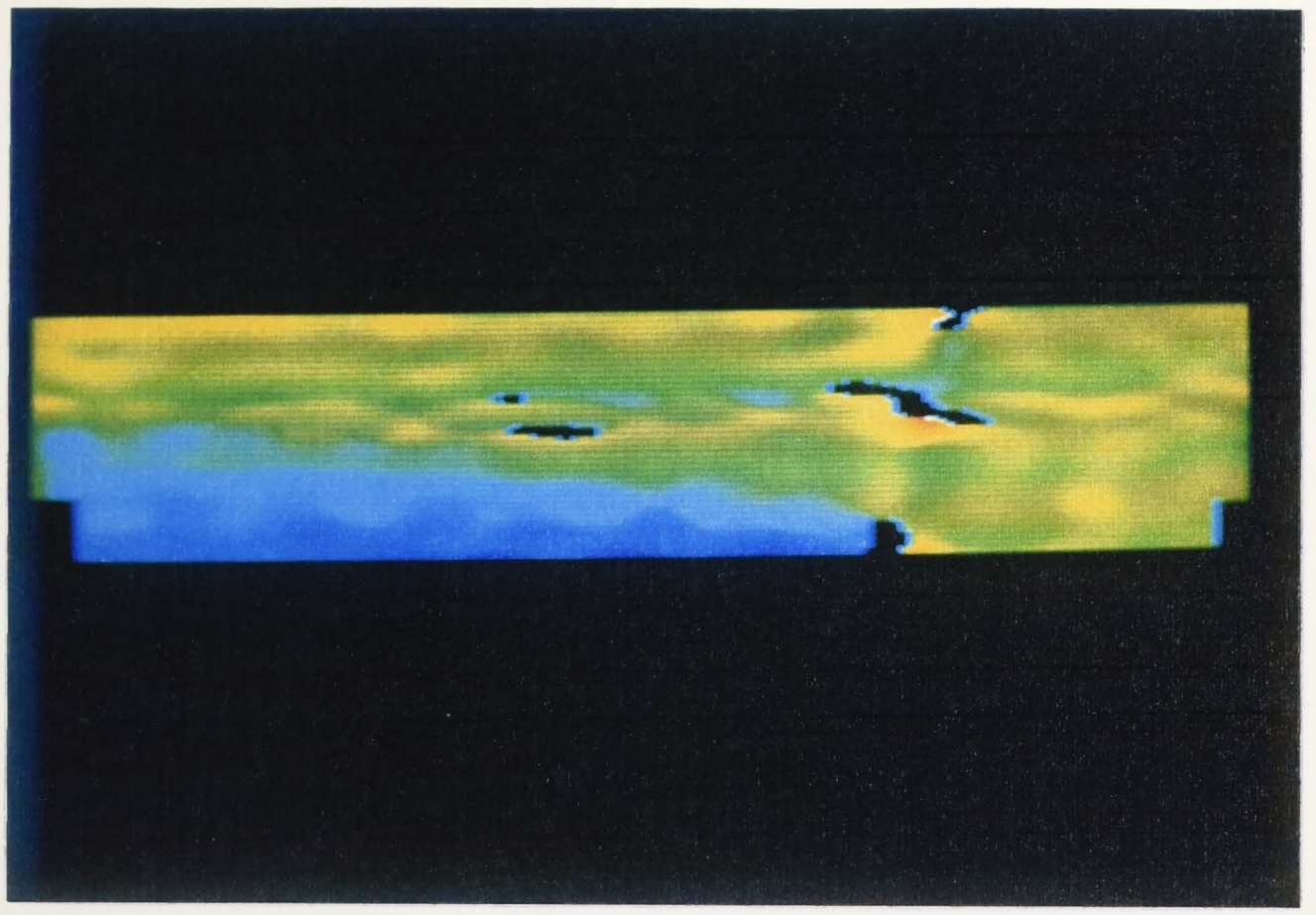

FIGURE 7.14b Shot #369, The filtered picture.
(1 - 256 pixel display)

Direction of
Shock
Propagation

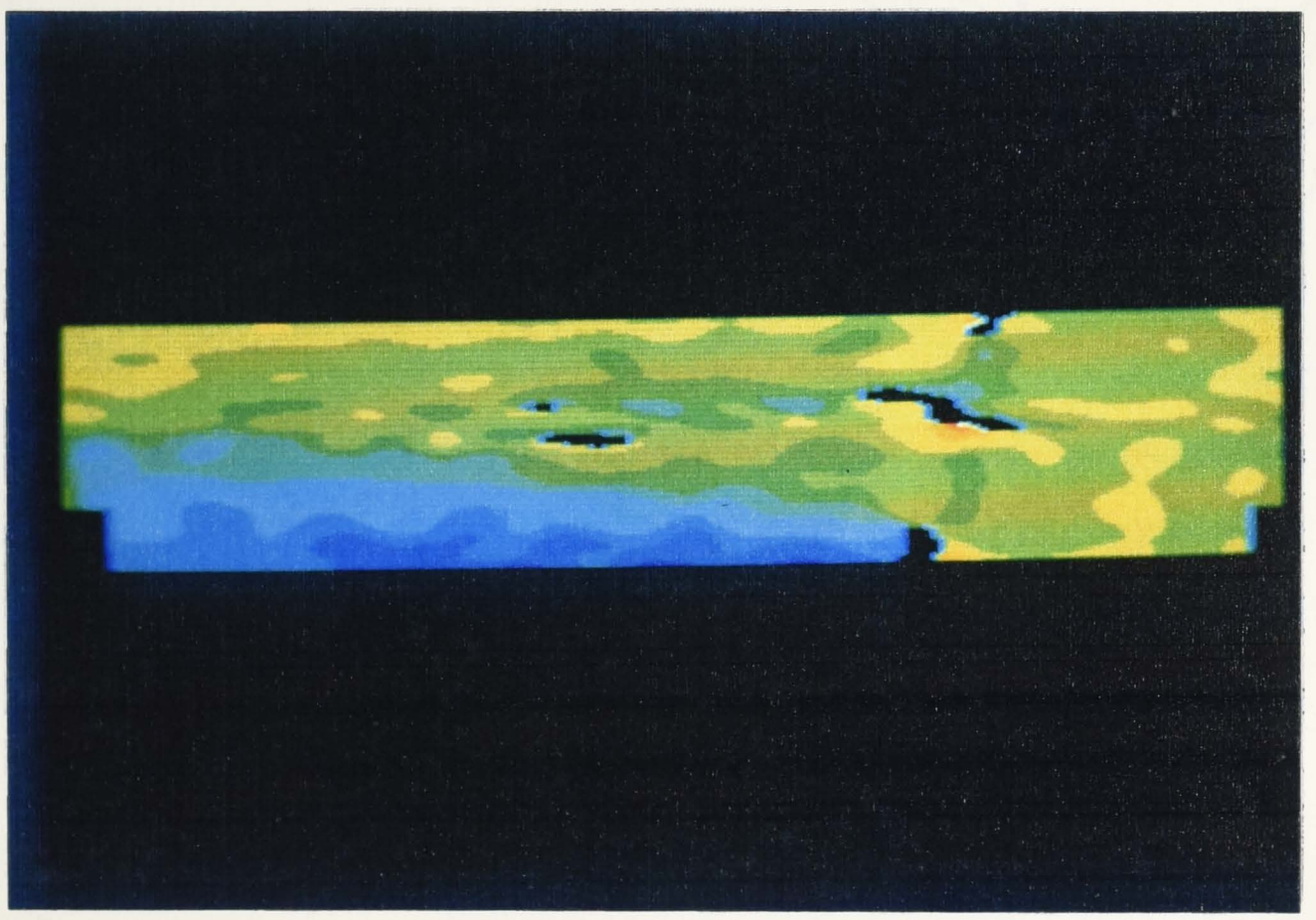

FIGURE 7.14c Shot #369, The filtered picture.
(1 - 56 pixel display)

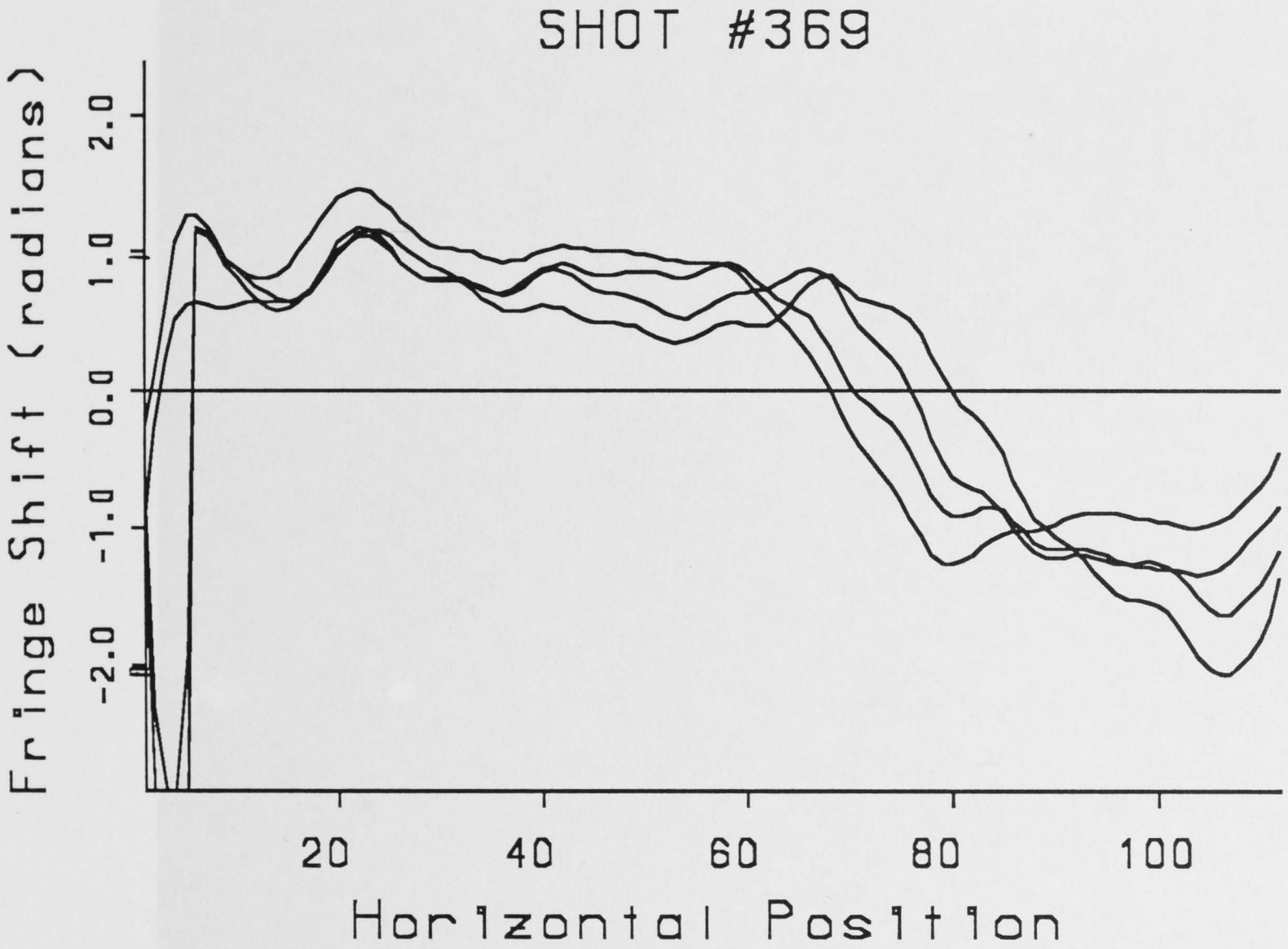

FIGURE 7.14d Shot #369, An overlay of the four vertical slices taken at 5, 10, 15 and 20 mm behind the incident shock. This gives the phase shift across the reflected shock. The horizontal position is given in pixels.

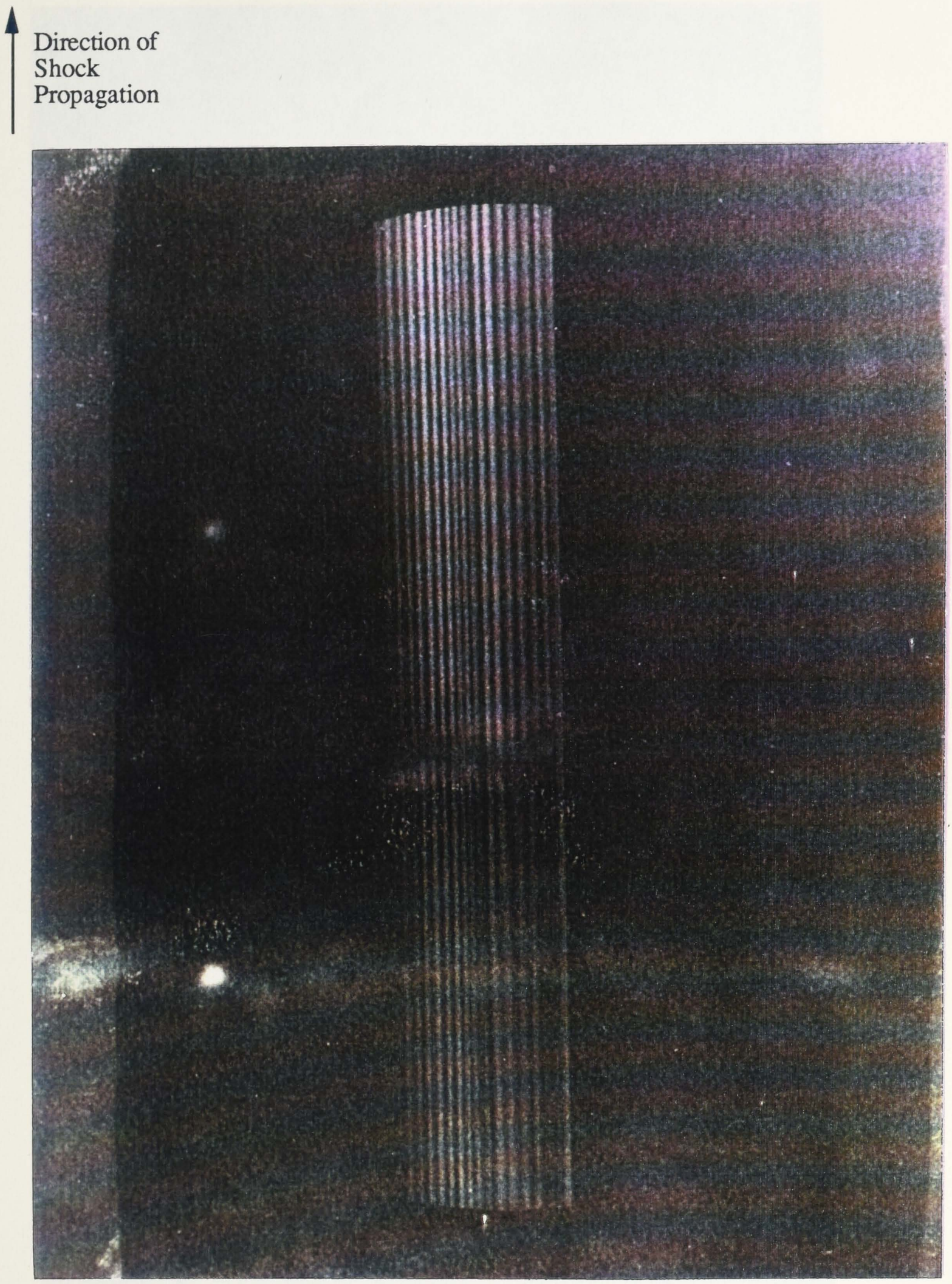

FIGURE 7.15a Shot #370, The original interferogram.
Gas temperature = 63° C
Iodine vapour pressure = 0.706 KPa
Shock velocity = 512.7 m/s
Mach # = 1.73
Laser wavelength = 570.523 nm

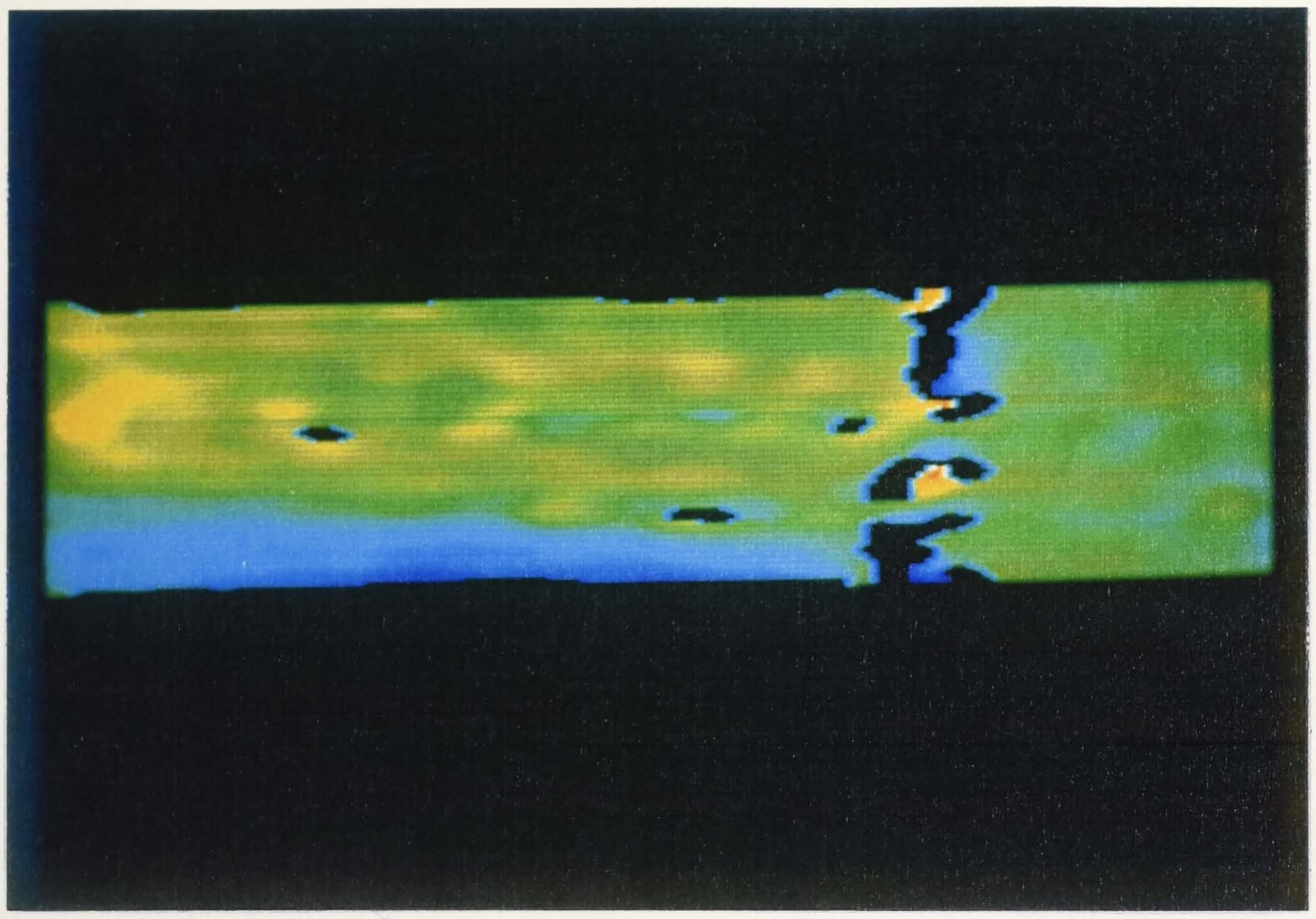

FIGURE 7.15b Shot #370, The filtered picture.
(1 - 256 pixel display)

Direction of
Shock
Propagation

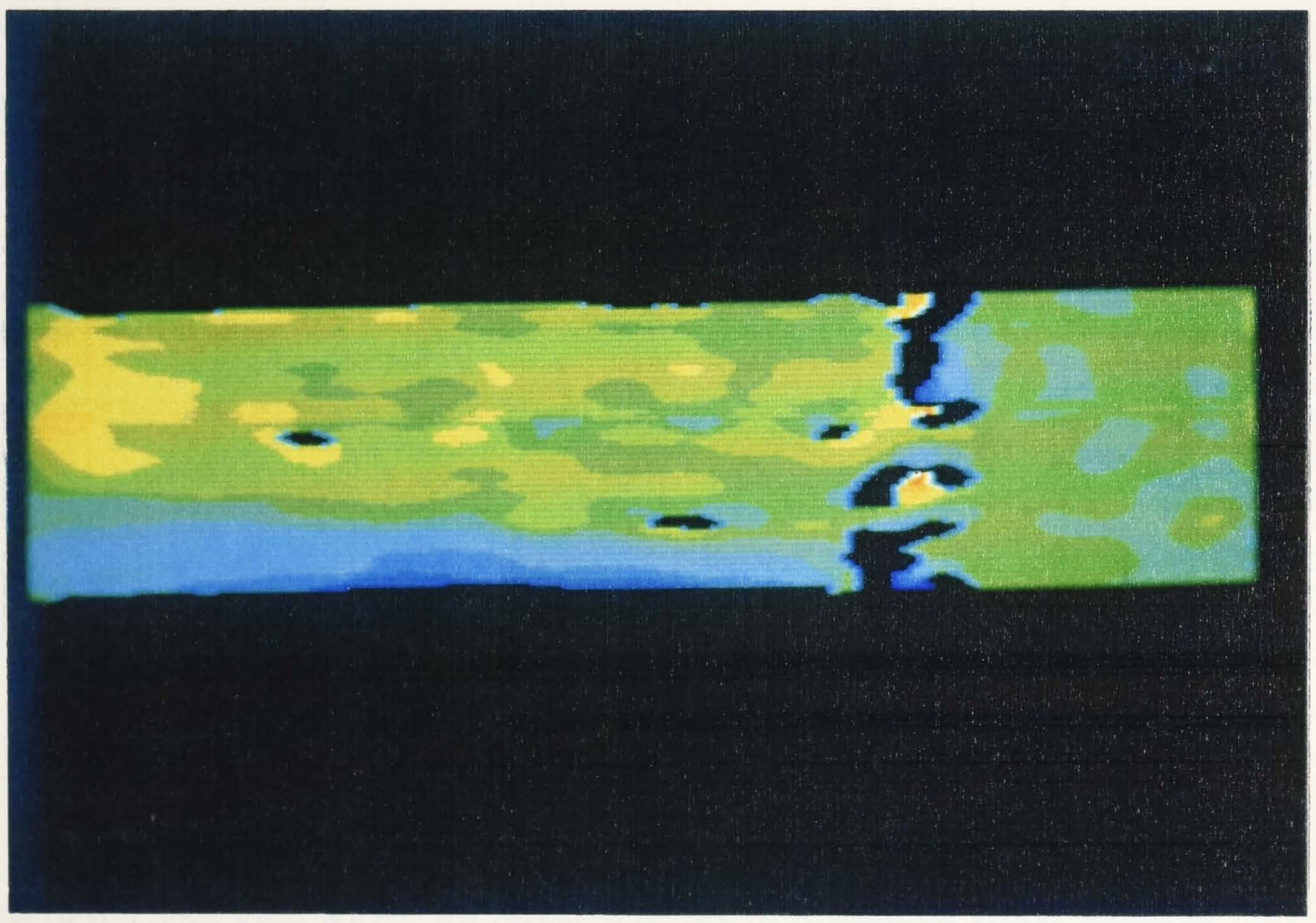

FIGURE 7.15c Shot #370, The filtered picture.
(1 - 56 pixel display)

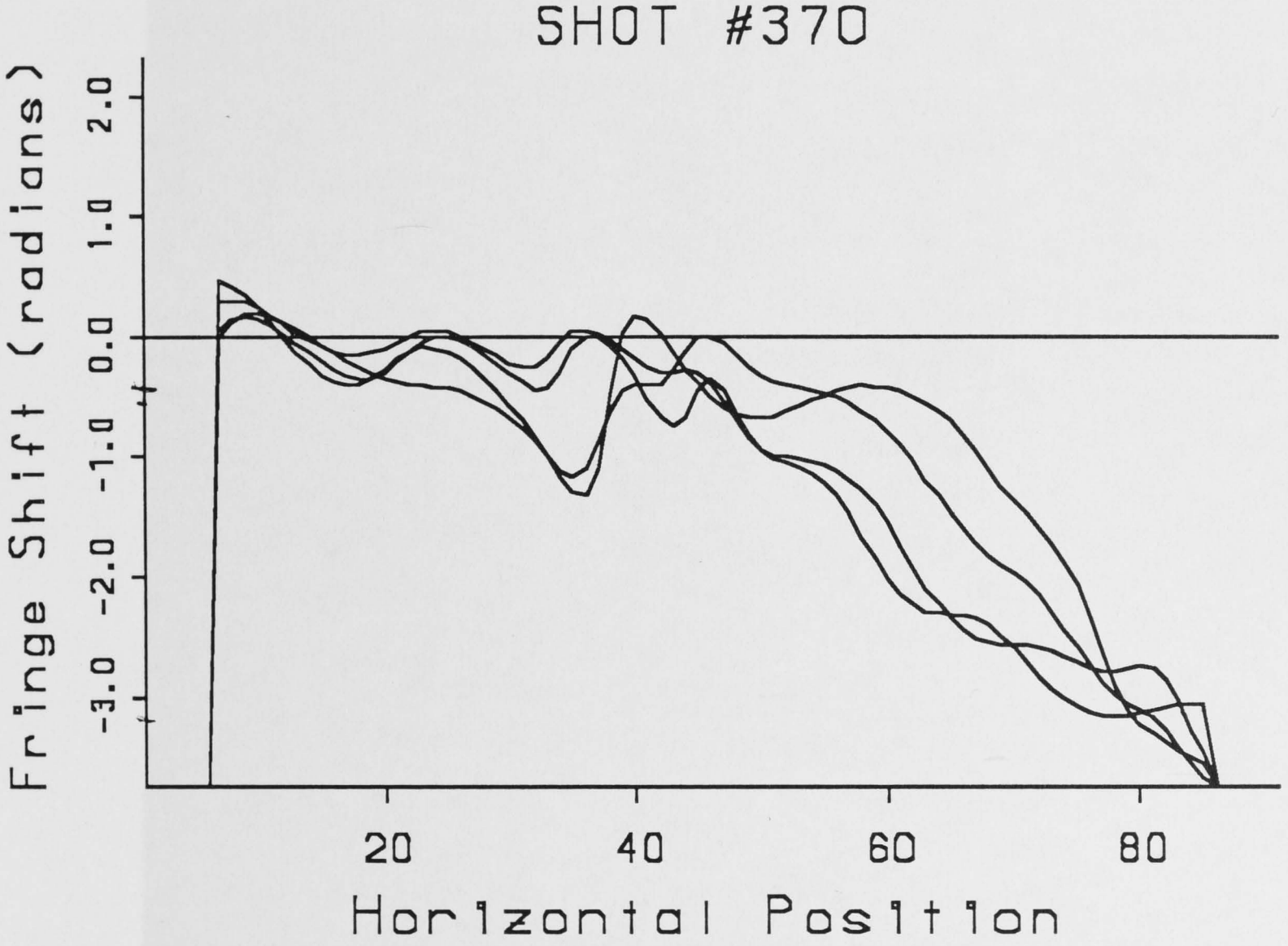

FIGURE 7.15d Shot #370, An overlay of the four vertical slices taken at 5, 10, 15 and 20 mm behind the incident shock. This gives the phase shift across the reflected shock. The horizontal position is given in pixels.

Direction of
Shock
Propagation

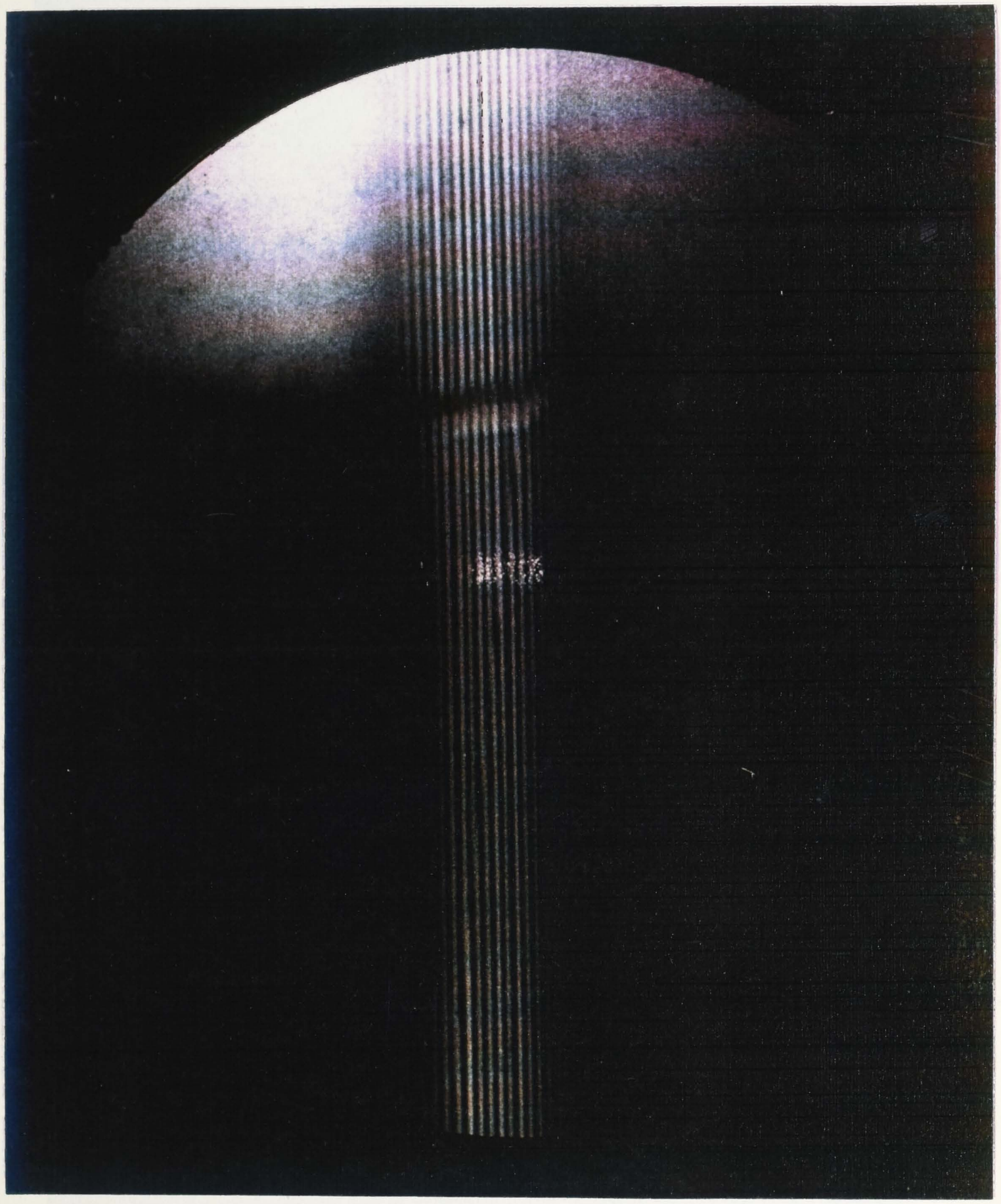

FIGURE 7.16a Shot #387, The original interferogram.
Gas temperature = 298 K
Iodine vapour pressure = 0 Kpa
Shock velocity = 595.6 m/s
Mach # ~ 1.73
Laser wavelength = 632.8 nm

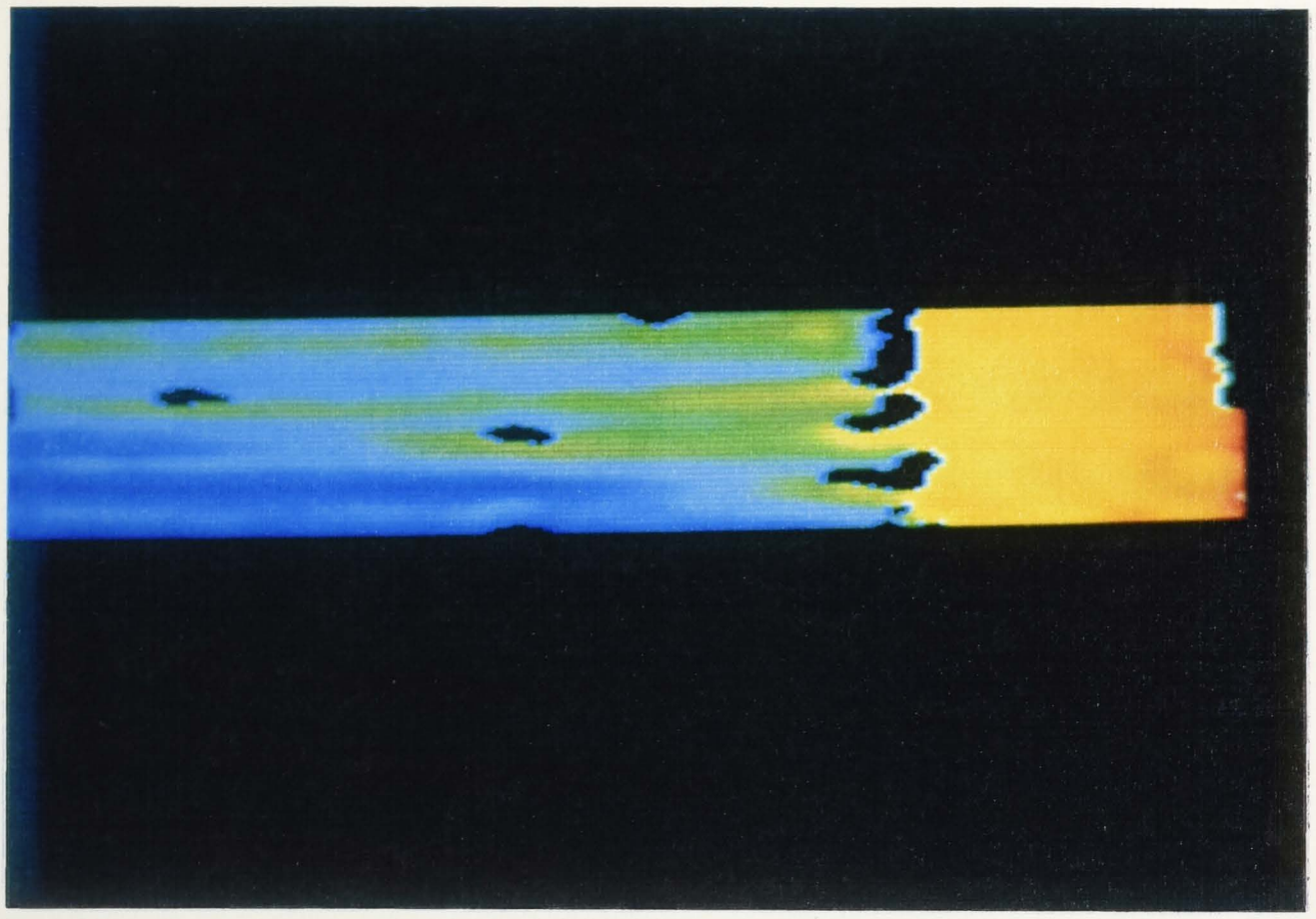

FIGURE 7.16b Shot #387, The filtered picture.
(1 - 256 pixel display)

Direction of
Shock
Propagation

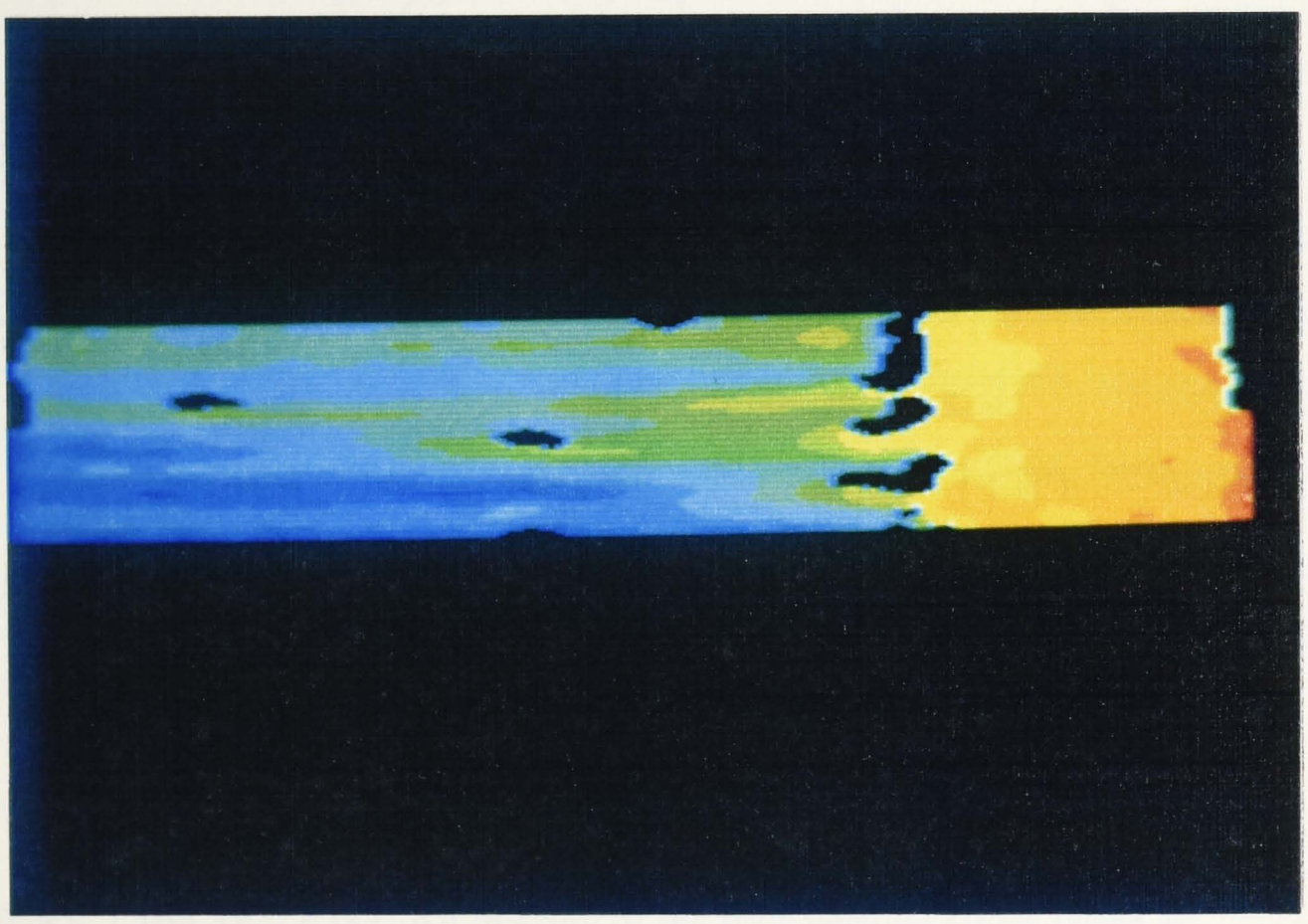

FIGURE 7.16c Shot #387, The filtered picture.
(1 - 56 pixel display)

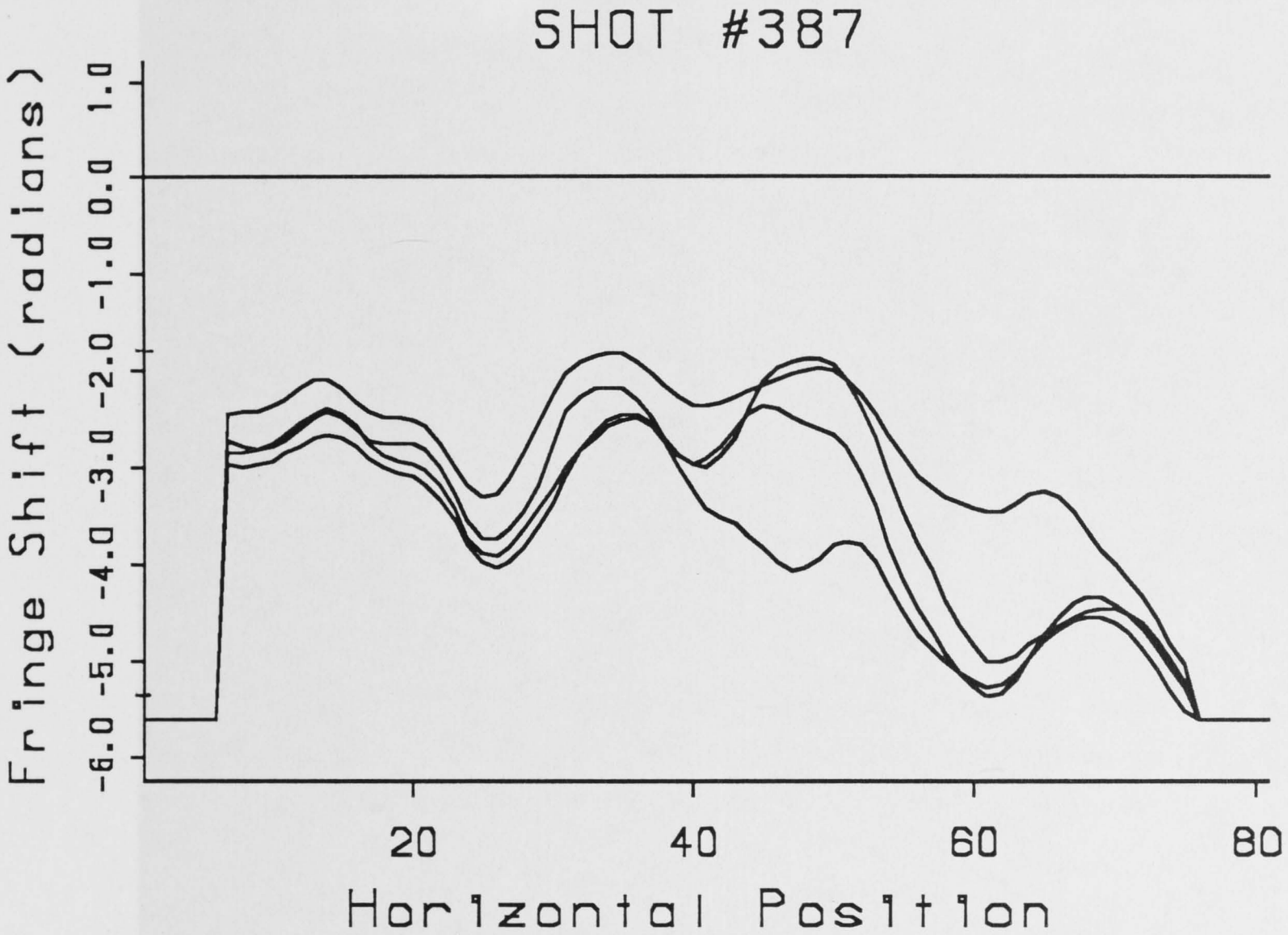

FIGURE 7.16d Shot #387, An overlay of the four vertical slices taken at 5, 10, 15 and 20 mm behind the incident shock. This gives the phase shift across the reflected shock. The horizontal position is given in pixels.

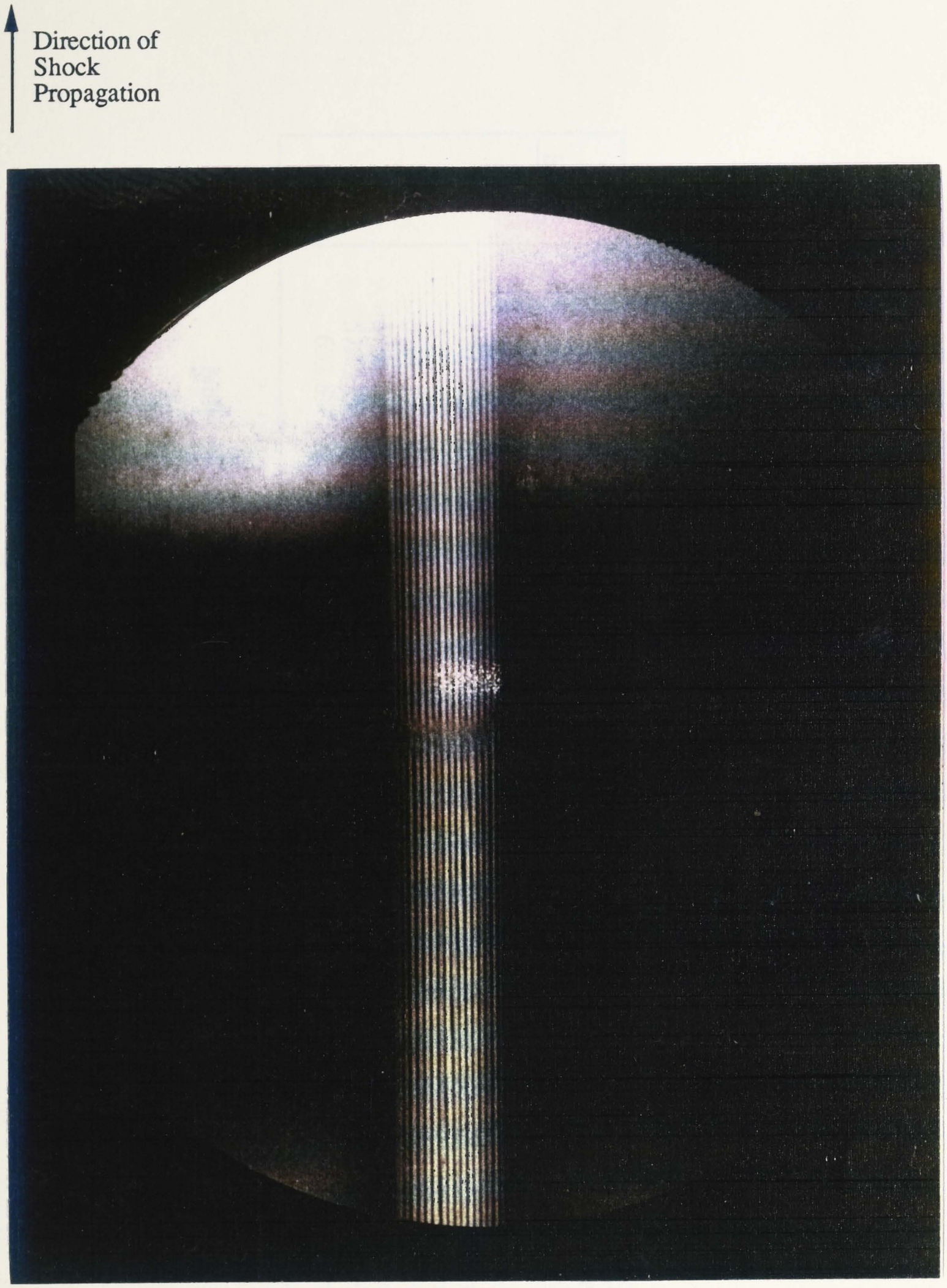

FIGURE 7.17 Shot #393, The original interferogram.
Gas temperature = 298 K
Iodine vapour pressure = 0 Kpa
Shock velocity = 616.0 m/s
Mach # ~ 1.79
Laser wavelength = 632.8 nm

TABLE 7.2
Wavelength Versus Fringe Shift

Shot #	Wavelength (nm)	Phase Shift (radians) (5 mm *)	Phase Shift (radians) (10 mm *)	Phase Shift (radians) (15 mm *)	Phase Shift (radians) (20 mm *)	Average Phase Shift (radians)
371	570.513	2.24	2.98	2.78	2.41	2.60 +/- 0.38
364	570.515	4.41	5.07	4.63	4.23	4.59 +/- 0.49
365	570.17	1.97	2.57	2.76	2.62	2.48 +/- 0.51
368	570.519	3.4	3.15	3.65	2.75	3.24 +/- 0.49
369	570.521	2.85	2.48	2.24	2.18	2.44 +/- 0.41
370	570.523	3.12	3.65	2.42	2.84	3.01 +/- 0.64
387	632.8	3.04	3.08	2.74	2.74	2.90 +/- 0.18

*** behind the incident shock**
Note: a phase shift of 6.28318 radians = 1 fringe shift

T A B L E 7.3
Operating Conditions Versus Shot #

Shot #	h.p.r. press. (kPa)	s.t. press. (kPa)	Gas Temp. (Celsius)	Iodine vap. press. (kPa)	Shock Velocity (m/s)	Sound Speed (m/s)	Mach #	Laser Wavelength (nm)
364	115.2 +/- 5%	9.98 +/- 5%	68 +/- 5%	1.07 +/- 10%	509.4 +/- 3.4%	274.2 +/- 36%	1.86*	570.515 +/- 0.01
365	115.2	9.98	66	0.866	506.3	286	1.77	570.517
368	115.2	9.98	58	0.533	509.4	308.3	1.65	570.519
369	115.2	9.98	59	0.6	512.7	302.9	1.69	570.521
370	115.2	9.98	63	0.706	512.7	296	1.73	570.523
371	115.2	9.98	62	0.667	506.3	298.7	1.7	570.513
387	115.2	9.98	-	-	595.6	345	1.73	632.8

*** An error of 36%**

Error quoted for the first entry in each column is the typical error for for all values in that column

Chapter 8. DISCUSSION

8.1 Absorption and Refractive Index Measurements

The refractive index scans shown in figures 7.7 and 7.8 indicate there was no resolvable fringe shift achieved in scanning through the regions of the spectrum occupied by the $B^3\Pi_{0u^+} \leftrightarrow X^1\Sigma_g^+$ (16,0) bandhead, λ = 570.519 nm or the isolated R(20) line of the $B^3\Pi_{0u^+} \leftrightarrow X^1\Sigma_g^+$ (18,1) transition at λ = 571.226 nm.

A number of experimental problems were encountered whilst trying to measure the fringe shifts due to the iodine spectral lines when tuning through with the laser. The major problem was fringe movement due to convection currents in the test arm of the MZ. The outside diameter of the shock tube test section was 0.28 metres. However, the separation between the first mirror (M1) and the second beamsplitter (BS2) (see figure 5.5) was 1.4 metres. This meant that in the test arm of the MZ there existed a 1.1 m air gap subject to density variations that caused fringe shifts unrelated to the detuning of the laser through the iodine spectral lines. This effect is clearly seen in figure 7.9, where no iodine was present in the shock tube (verified by the absorption scan) but light intensity variations were measured by the photo-diode. If this background noise from figure 7.9 was overlaid across the absorption traces from figures 7.7 and 7.8, the result would be very close to what is observed in the refractive index scans of figures 7.7 and 7.8. The second problem encountered was that of absorption during the refractive index scans. It was possible that any fringe shift that was occurring was unresolvable due to its amplitude being reduced by the absorption to such a point that any change was unmeasurable.

Theoretical calculations (completed after the scans) of the expected fringe shift, however, shed new light on the problem of no detectable fringe shifts for the refractivity scans. These calculations couldn't be completed satisfactorily until an absolute number density for the lower levels involved in the transitions of interest could be determined accurately. The installation of a thermistor gauge that allowed an estimation of the upper limit for these values wasn't completed until the later stages of the experiment.

The theoretically determined fringe shifts were validated by comparison between the theoretically determined optical depths and the observed values for the transition lines in question. (See Appendix A for the method of calculation for both the theoretical optical depth and refractivity or section 4.7 for discussion of the computer code.)

The comparison between the theoretical and the experimental values of optical depth for the R(20)(18,1) transition at λ = 571.226 nm was good, with the theoretical value approximately 5% lower than the experimental value. However, the theoretical optical depth values for the (16,0) bandhead were approximately 100% too low. This discrepancy led to a more detailed investigation than that undertaken at the commencement of this experiment of overlapping lines in the bandhead region. Another line was found to coincide exactly with the bandhead at λ = 570.519 nm. This transition line corresponded to the Q(50)(23,3) transition in molecular iodine. The added absorption from this line caused an increase in the optical depth at the bandhead of about 70%, thereby resulting in a difference of about 25% between the theoretical value and the experimental value for optical depth at λ = 570.519 nm. The difference still present after the summing of these two lines is assumed to be due to additions from the wings of a number of other lines found lying very close to the bandhead. These are ignored here due to their small contributions to the refractivity in this region, i.e. the Q(50)(23,3) transition that increases the optical depth in the bandhead region by approximately 70% contributes no fringe shift greater than about 1/20 of a fringe to the refractivity.

The theoretical calculations for the (16,0) bandhead and the Q(50)(23,3) isolated line indicate that when detuning from λ = 570.527 nm there is no resolvable fringe shift, i.e. no fringe shift > 1/10 of a fringe. When detuning from the bandhead at λ = 570.519 nm to λ = 570.515 nm, there is a negative fringe shift of 0.0031 or ~ 1/300 of a fringe and a positive fringe shift of 0.0825 or ~ 1/12 of a fringe.

Calculations for the Q(50)(23,3) transition show that when detuning from λ = 571.228 nm to λ = 571.220 nm there is a negative fringe shift of 0.2325 or ~ 1/4 of a fringe and a positive fringe shift of 0.1768 or ~ 1/6 of a fringe.

This indicates that the fringe shifts were too small to be resolved, given the experimental set up and the resolution of approximately 1 fringe shift. It also implies that the enhancement effect was much smaller than was hoped for.

8.2 Flow Visualization

The reflected shock fringe shifts seen in the filtered pictures of the shots taken for the (16,0) bandhead series are unresolvable in the original interferograms. Fringe shifts of the order 1/20 of a fringe in the original interferogram are resolvable using the Fourier transform filtering technique, when the original is of good quality. Unfortunately, due to a number of circumstances the quality of the interferograms obtained in the (16,0) bandhead series are poor.

From table 7.2, it can be seen that for shot #364 (λ = 570.515 nm), the fringe shift across the reflected shock is approximately 67% greater than the average excluding that particular value, 75% greater than the fringe shift seen for shot #371 (λ = 570.513 nm), where presumably no fringe shift enhancement effects are occurring and 37% larger than the fringe shift seen in shot #387, where the fringe shift was due solely to density changes in the air.

There is some variation in shock strength amongst the shots but there exists no correlation between shock strength and fringe shift across the reflected shock. This would seem to indicate some enhancement effect has occurred at the wavelength, λ = 570.515 nm, perhaps due to the detuning from the bandhead.

Theoretical calculations of the expected fringe shift across the reflected shock, completed for the region about the (16,0) bandhead, indicate that no enhancement effects should be present for shots #371 and #364 (λ = 570.513 nm and 570.515 nm) and the greatest fringe shift should occur for shot #369 (λ = 570.521 nm). (See table 8.1.) It can be seen from table 8.1 that this is not the case. The greatest fringe shift occurred at λ = 570.515 nm and the smallest at λ = 570.521 nm. No relationship between fringe shift and wavelength can be made and of the six shots taken in the (16,0) bandhead series. Half the shots show a fringe shift across the

TABLE 8.1
Wavelength Versus Phase Shift

Shot #	Wavelength (nm)	Average Phase Shift (radians)	Average Phase Shift (fringes)	Max. Theor. Phase Shift (fringes)	Min. Theor. Phase Shift (fringes)
371	570.513	2.60 +/- 0.38	0.41 or (2/5)	-	-
364	570.515	4.59 +/- 0.49	0.73 or (3/4)	-	-
365	570.17	2.48 +/- 0.51	0.39 or (2/5)	1/100	1/220
368	570.519	3.24 +/- 0.49	0.52 or (1/2)	1/158	1/380
369	570.521	2.44 +/- 0.41	0.39 or (2/5)	1/45	1/105
370	570.523	3.01 +/- 0.64	0.48 or (1/2)	-	-
387	632.8	2.90 +/- 0.18	0.46 or (4/9)	-	-

reflected shock that is less than that for a test gas of air only (shot #387). It should also be noted from table 7.3 that the Mach number for shot #364 (λ = 570.515 nm) was the strongest for all shots, including the reference shot (shot #387), by about 8%.

As mentioned above, the interferograms produced for the (16,0) bandhead series were of poor quality. The lack of fringe sharpness and contrast was a major contributor to the degradation of the (16,0) bandhead interferograms; however this effect wasn't present in early interferograms using the same experimental equipment and optical set-up. The interferogram of shot #215 (figure 8.1) is an example. This was the first shot in air using the MZ and streak camera that showed Mach reflection. Another good image of Mach reflection, this time in iodine, is seen in the interferogram of Shot #256, shown in figure 8.2. Approximately 0.267-0.667 KPa of iodine has been introduced into the shock tube. At this early stage of the experiment, no temperature measuring device had been attached to the shock tube and later temperature measurement, indicate that for the period of heating allowed for these shots, a temperature range of approximately 293 K < T < 343 K existed. All other conditions were unchanged, with air pressure in the shock tube reduced appropriately.

The comparison of figures 8.1 and 8.2 shows that a new problem has emerged: extra fringe shifts in the flow. It can be seen that the MR configuration has undergone a radical change. The laser used for this shot (and the other shots mentioned below unless otherwise stated) was the Spectra/Coherent ring dye laser with the wavelength for this shot being λ = 571.488 nm. This was ~ 4.8 GHz from line centre (17498.02 cm^{-1} or 571.493 nm) for two transitions, the Q(71)(23,3) and R(38)(18,1). (The linewidth of the laser is not known for this shot). Another fringe shift is present in figure 8.2 that is mirroring the incident shock and looks very much like a relaxation region. The incident shock in figure 8.2 has all the appearance of a dispersed shock, with the secondary fringe shift due to resolvable vibrational relaxation of the diatomic iodine molecule. Honma *et al.* (1987) observed what seems to be a similar effect occurring for weak shock reflection (both RR and MR) for pseudo-steady flow in a test gas of CO_2. A second reflected shock also exists (in figure 8.2), originating

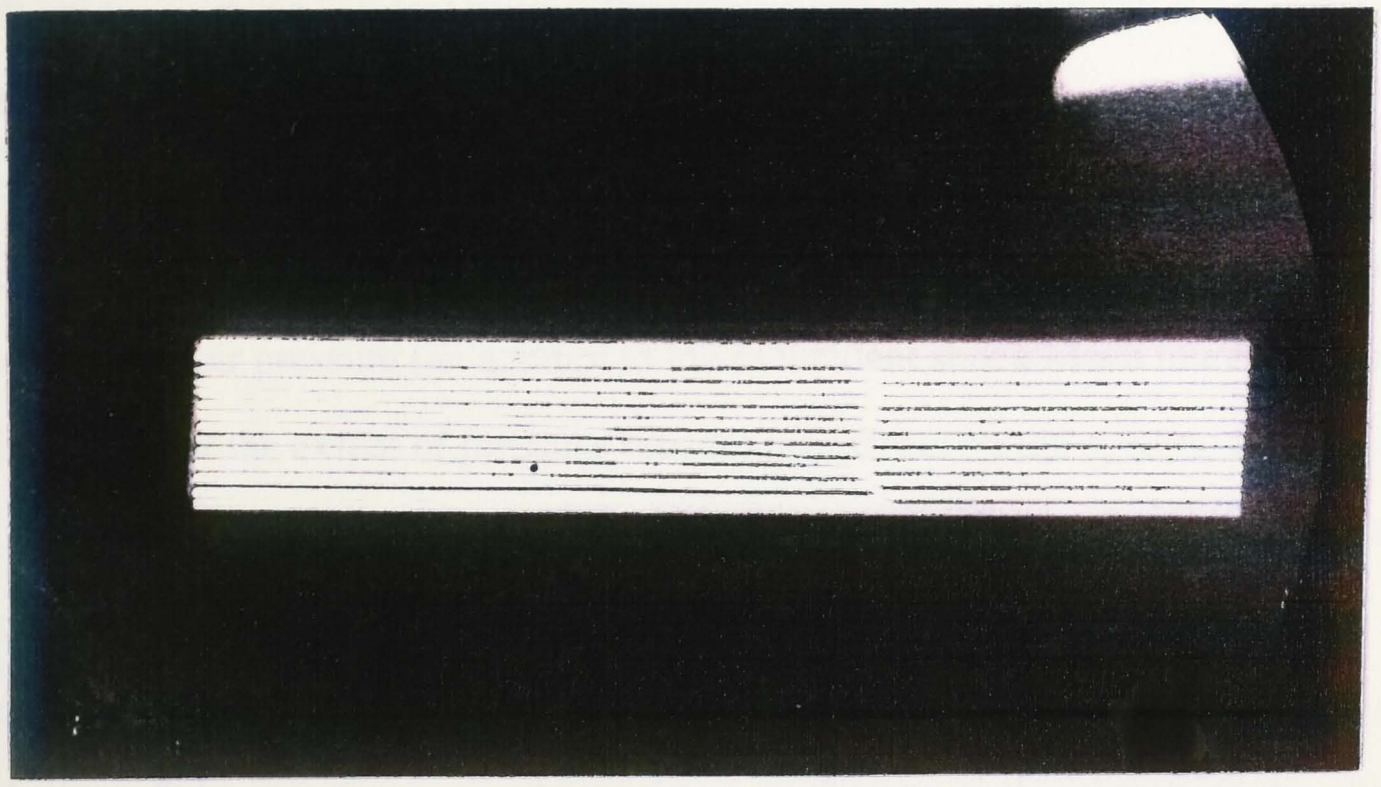

FIGURE 8.1 Shot #215, the first successful shot of Mach reflection in the shock tube. The test gas was air only.
h.p.r. = 481 KPa, s.t. = 9.98 KPa
shock velocity = 639 m/s, Mach # = 1.85
λ = 514.5 nm

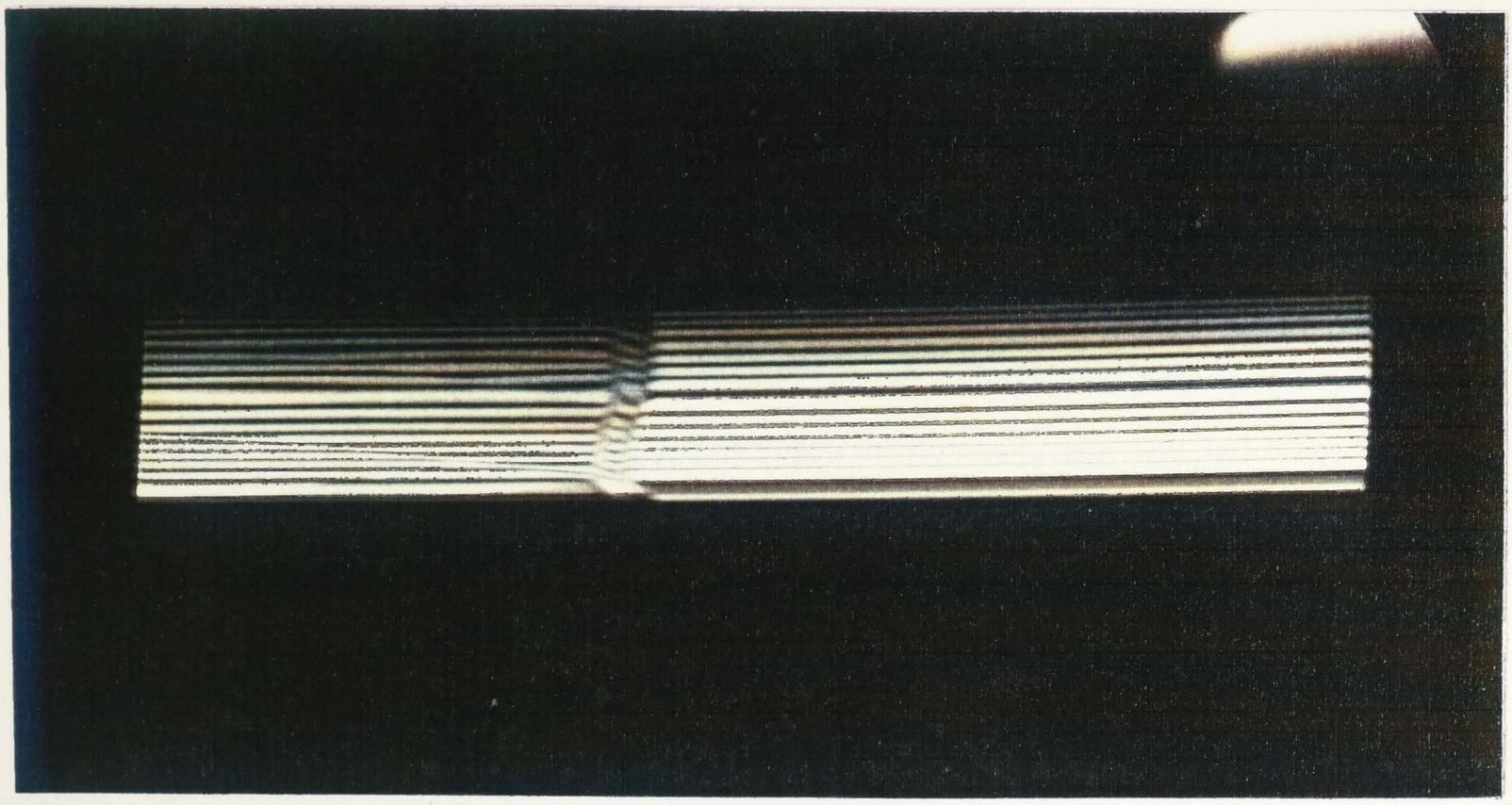

FIGURE 8.2 Shot #256, an early interferogram of Mach reflection in an iodine vapour and air buffer.
h.p.r. = 446 KPa, s.t. = 9.98 KPa
gas temp. = unknown, I_2 vapour press. = unknown
shock velocity = 544 m/s, Mach # = 1.79 - 2.00
λ = 571.488 nm

nearly midway up the incident shock. Possible causes of this extra reflected shock are unknown.

Secondary fringe shifts existed in the flow at a number of different operating conditions. An increased shock tube pressure in conjunction with a decreased high pressure reservoir pressure (an attempt to lower incident shock Mach number prior to the discovery of the extent of pressure broadening effects on the spectral linewidths) resulted in the interferogram shown in figure 8.3 (shot #275). The incident shock is noticeably increased in curvature and the secondary fringe shift associated with the incident shock is now adjacent to it and is seen as a broadening of the shock. A close inspection of the interferogram shows fringe curvature in the region of the shock duplicating what was observed in the experiments of Honma *et al.* (1987) and shown in figure 5 of their paper. The second reflected shock, originating midway up the incident shock, is still present and seems stronger. This extra reflected shock was also present in some N_2 pumped dye laser shots (Rhodamine 6G, broadband lasing in the yellow, $\lambda \sim 571$ nm) using a differential interferometer at the operating conditions of high pressure reservoir = 239 KPa (20 p.s.i. gauge) air and shock tube = 90 KPa (900 mbars) air and iodine. The laser used for Shot #275 was an Ar^+ laser that had a wavelength of $\lambda = 514.5$ nm and a linewidth of greater than 20 MHz. (This is near a major absorption band in iodine.)

At another set of conditions figure 8.4 (shot #281) was the result. The laser wavelength was $\lambda = 569.020$ nm and since this was near an absorption line, an overall drop off in the fringe intensity occurred. The incident shock appears as a shadow with complete absorption in the region of the incident shock and the Mach stem. The reflected shock is now broader in its appearance and very distinct. The extra reflected shock originating midway up the incident shock is still present but extremely hard to see. The shadow effect persisted from this shot on and is perhaps an effect of increased shock curvature at slower shock speeds (the shock curvature is a 2-dimensional effect that will appear to broaden the shock in the x-direction) or of increased absorption in the relaxation zone associated with the incident shock. The

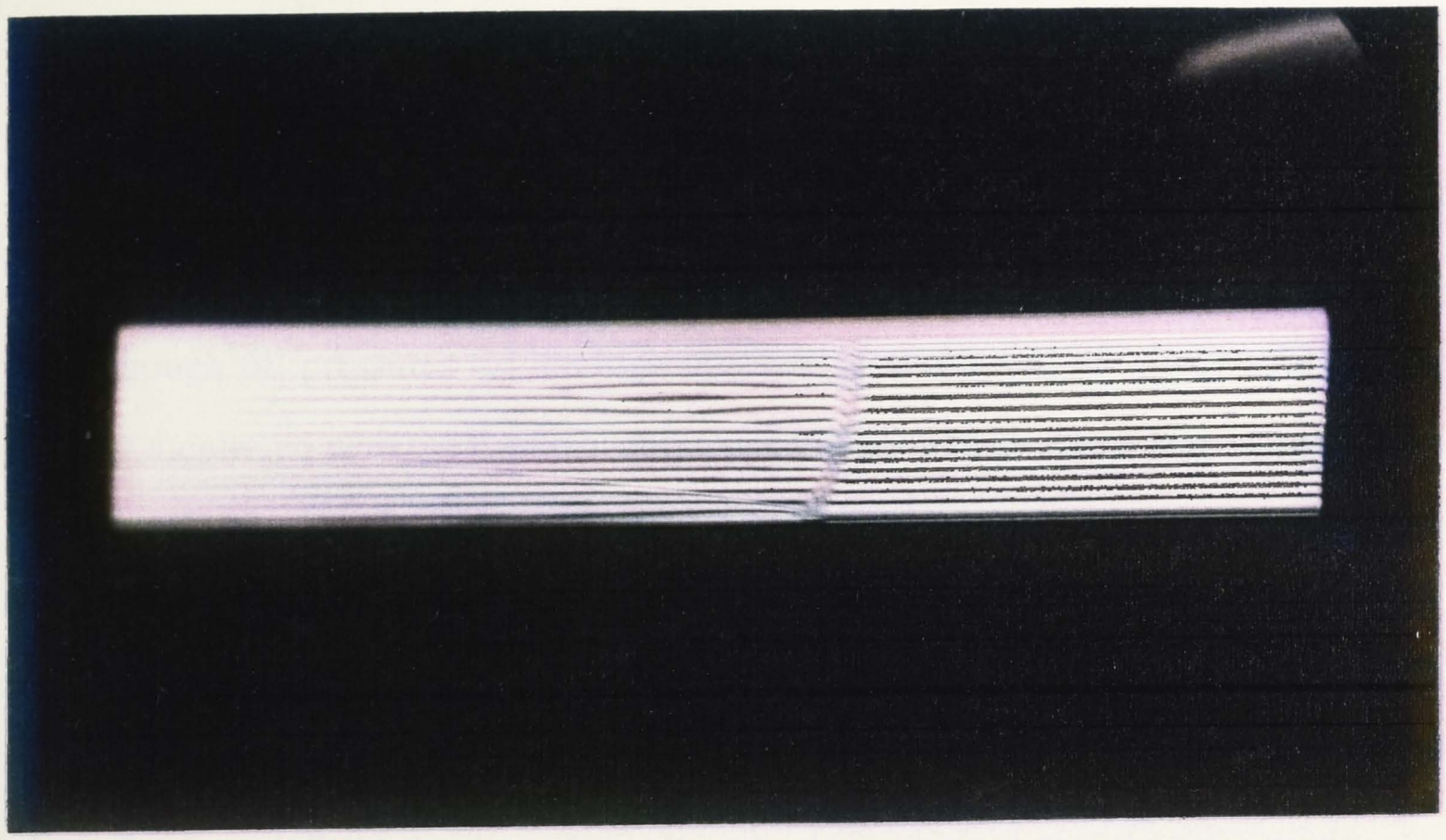

FIGURE 8.3 Shot #275
h.p.r. = 239 KPa, s.t. = 50 KPa
gas temp. = unknown, I_2 vapour press. = unknown
shock velocity = 462 m/s, Mach # = 1.31 - 1.65
λ = 514.5 nm

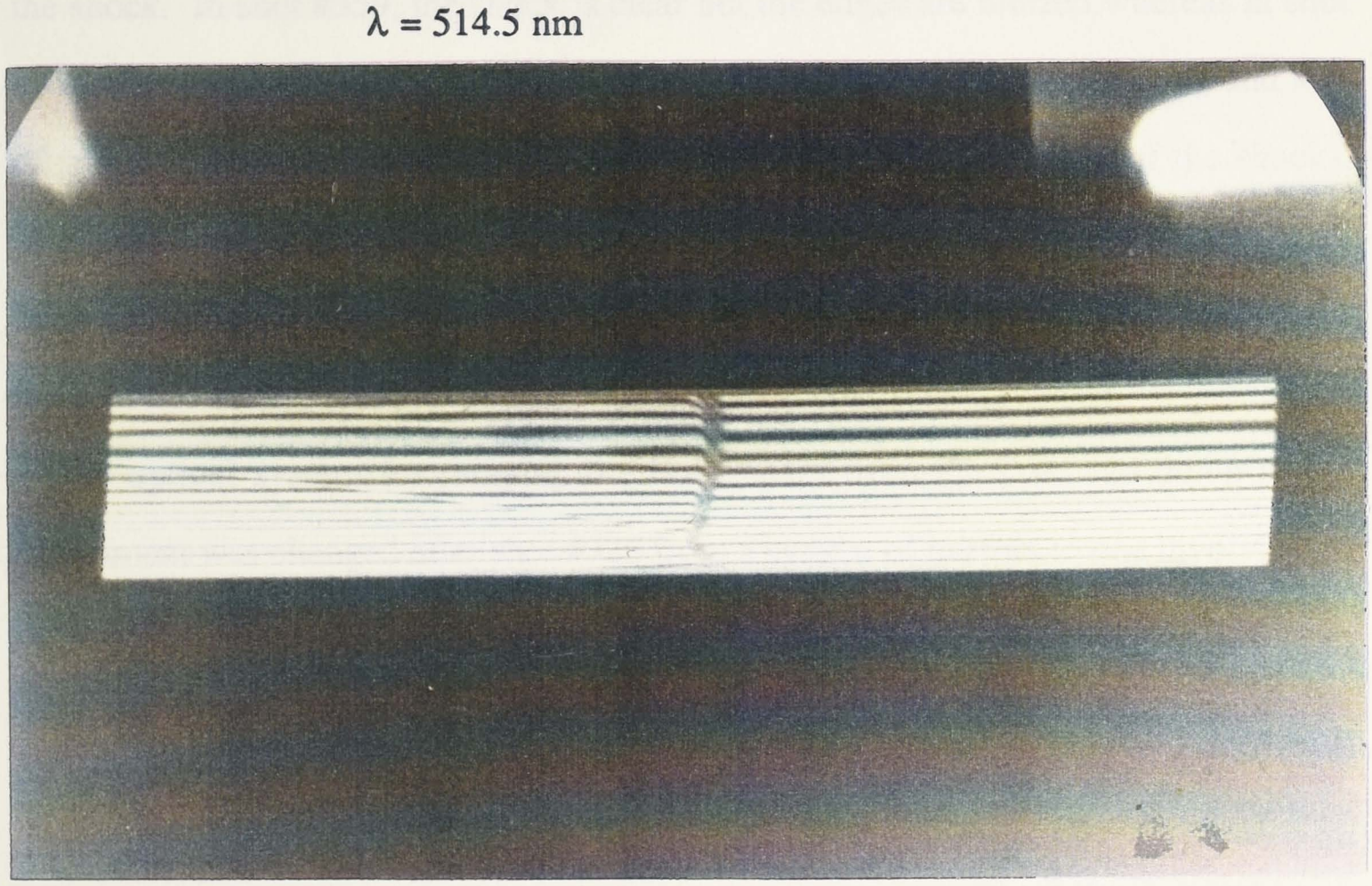

FIGURE 8.4 Shot #281
h.p.r. = 239 KPa, s.t. = 50 KPa
gas temp. = unknown, I_2 vapour press. = unknown
shock velocity = 469 m/s, Mach # = 1.33 - 1.68
λ = 569.020 nm

shadow effect seemed greater for weak shocks than for strong shocks.(i.e. a similar effect is occurring for shot #256, a stronger shock (see figure 8.2), but is resolvable as a relaxation zone with two separate fringe shifts.)

The shock tube also had an inability to produce a consistent shock configuration even though fill pressures for the high pressure reservoir and the shock tube were closely monitored with the resultant shock speed variation kept to a minimum. This variation in shock reflection configuration can be seen in the interferograms from shots #358 - #361 (see figures 8.5-8.8). The average shock speed for the four shots was 515.19 m/s, with the greatest difference from the mean being 7.41 m/s (a variation of ~ 1.4% over the four shots). Possible reasons for this inconsistency in the reflection configuration is unclear. It is also interesting to note the poor quality of the shock image in shot #358 (see figure 8.5) when compared to shot #359 (see figure 8.6). There is a difference in overall fringe intensity as well as in the appearance of the shock. In shot #359, the shock is clear but the edges are blurred whereas in shot #358, the shock isn't very well defined due to a combination of edge blurring and loss of fringe resolution (possibly as a result of absorption in the region of the shock). The laser wavelength for shot #358 was λ = 570.523 nm, right in the middle of an iodine absorption region (near the 16,0 bandhead). On the other hand, the wavelength for shot #359 was λ = 570.544 nm, which is clear of any such regions.

The optical system for relaying the laser beam from the laser lab down to the experiment was changed after shot #326 from a system of mirrors to one involving an optic fibre (no changes were made to the optical system on the output side of the MZ). This was tested in place but produced unsatisfactory results due to the poor quality of the optic fibre used. (Only one fibre of sufficient length was available.) Therefore, the mirror system was re-installed for shots #344 onwards. During this process a lens was replaced on the output side of the MZ and incorrectly positioned. This wasn't discovered until shot #390 and was at first thought responsible for the blurring and broadening of the shock in shots #364 to #387 (see figures 7.10 to 7.16). However, a closer inspection of some of the interferograms taken after the optical system

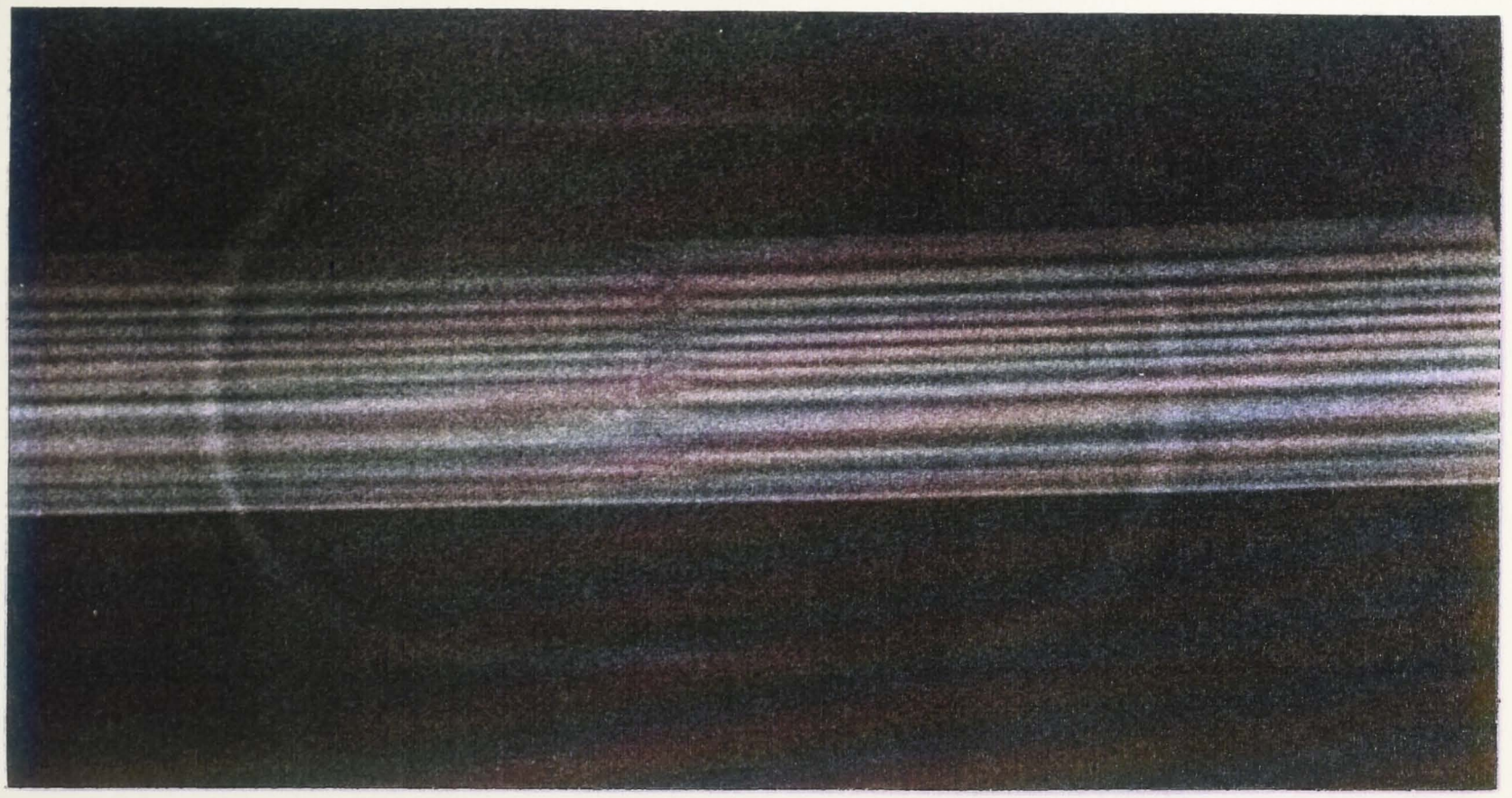

FIGURE 8.5 Shot #358
h.p.r. = 115.2 KPa, s.t. = 9.98 KPa
gas temp. = 50 °C, I_2 vapour press. = 0.35 KPa
shock velocity = 519.2 m/s, Mach # = 1.60
λ = 570.523 nm

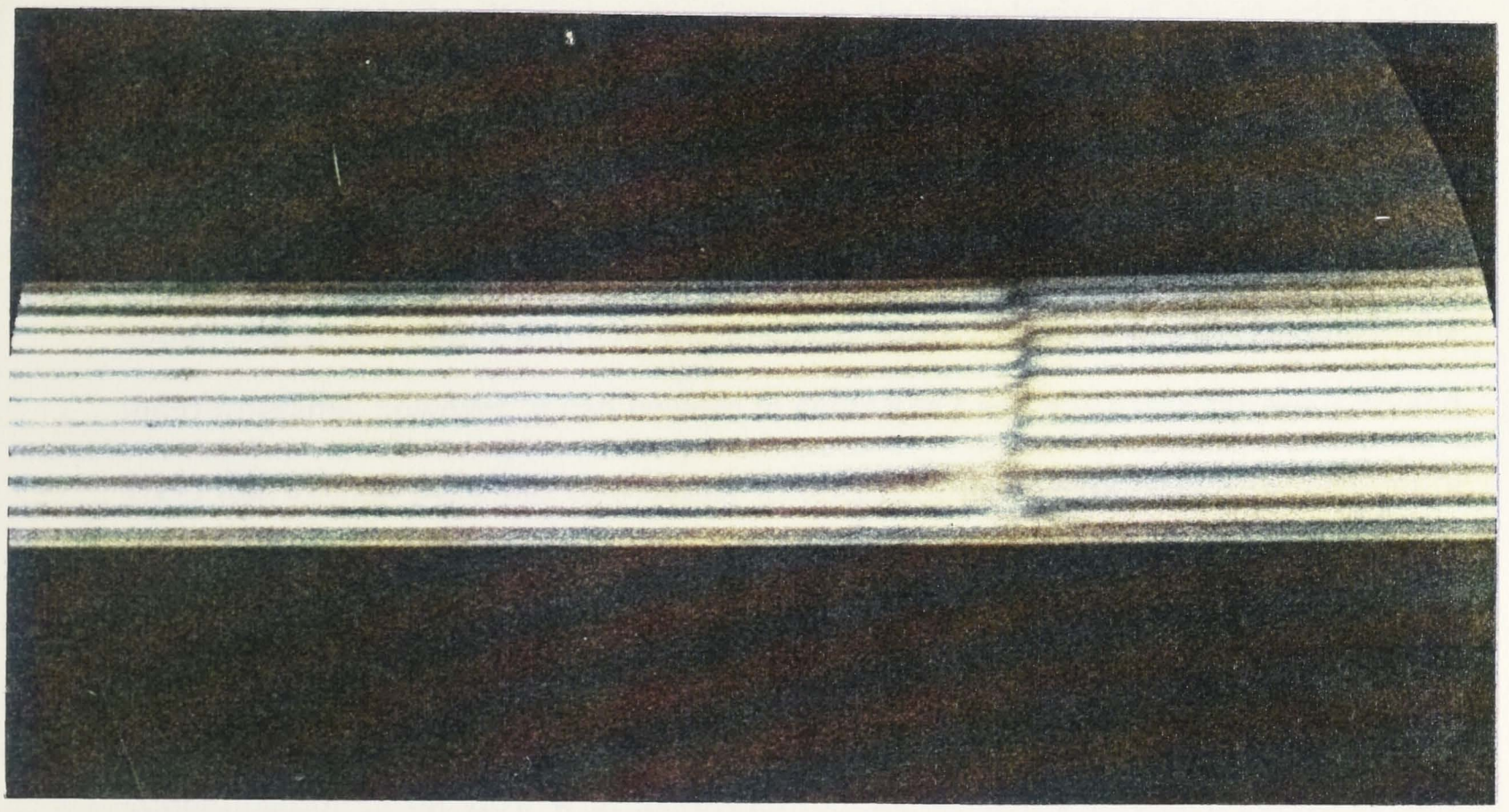

FIGURE 8.6 Shot #359
h.p.r. = 115.2 KPa, s.t. = 9.98 KPa
gas temp. = 44 °C, I_2 vapour press. = 0.23 KPa
shock velocity = 512.7 m/s, Mach # = 1.52
λ = 570.544 nm

alteration but prior to shot #364, for example shots #356, 357 and 359 (see figures 8.9, 8.10 and 8.6), shows a reasonably well defined incident shock and Mach stem, with shots #356 and #357 also showing a well defined reflected shock. The incorrect positioning of the lens was therefore not the major contributing factor to this shock blurring and broadening effect.

It should also be noted that the streak camera was streaking at 1.6 times the indicated (and assumed) streak speed of 10 μs/cm. This was not determined until after shot #387, when measurements were done to determine the actual streak speed of the camera. This increase in streak speed would have the effect of broadening the shock in the interferogram. The Imacon streak camera did break down after shot #326 and underwent a major overhaul to determine the problem. It may be possible that the streak speed was altered unknowingly during this process since the speed may be altered internally by a screw adjustment for calibration purposes. However, there exists no data on the streak speed of the camera before the breakdown so it is not possible to determine if this was a factor in the broadening of the shocks in the interferograms after shot #326.

After the completion of shot #371, no more use of the tunable c.w. lasers was possible and so additional shots were done using a He-Ne laser. These shots were completed at conditions that had previously produced sharp and clear shocks in the interferograms; however, it can be seen in shots #387 and #393 (see figures 7.16 and 7.17) that even at these old conditions, where previous interferograms of the quality of shot #275 and #281 were obtained (see figures 8.3 and 8.4), the incident shock and the Mach stem are still extremely broad. The reflected shock is again visible but it is weaker than it was for shots #275 and #281. This would seem to suggest contamination of the flow with molecular iodine. Over the extended period of time taken for the experiment, the interior of the shock tube became corroded. This was especially true of the shock reflecting wedge in the test section. The surface of the wedge became extremely pitted and by the time some thought was given to its replacement it had become bonded irremovably to the test section due to this

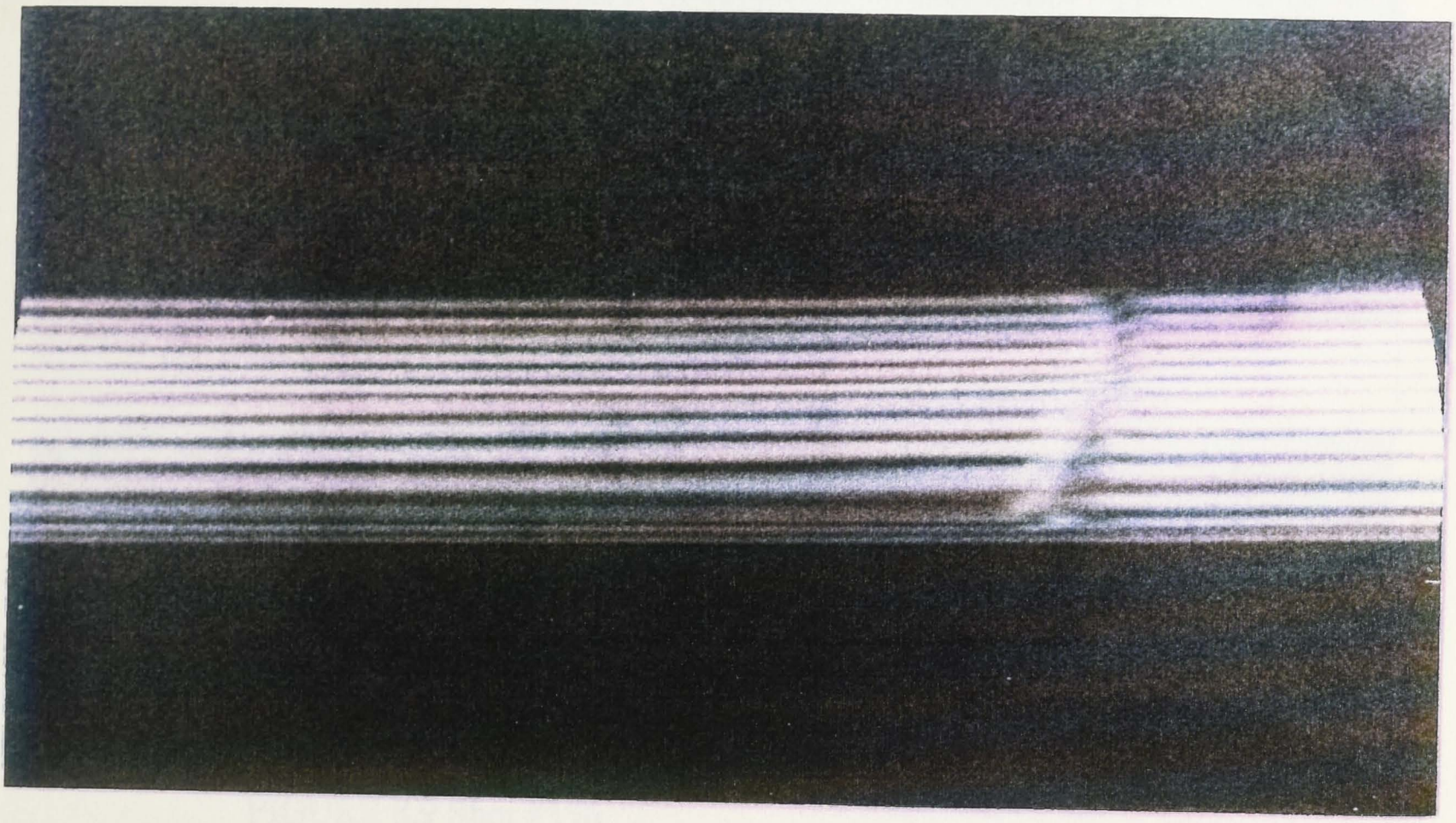

FIGURE 8.7 Shot #360
h.p.r. = 115.2 KPa, s.t. = 9.98 KPa
gas temp. = 52 °C, I_2 vapour press. = 0.40 KPa
shock velocity = 522.6 m/s, Mach # = 1.60
λ = 570.543 nm

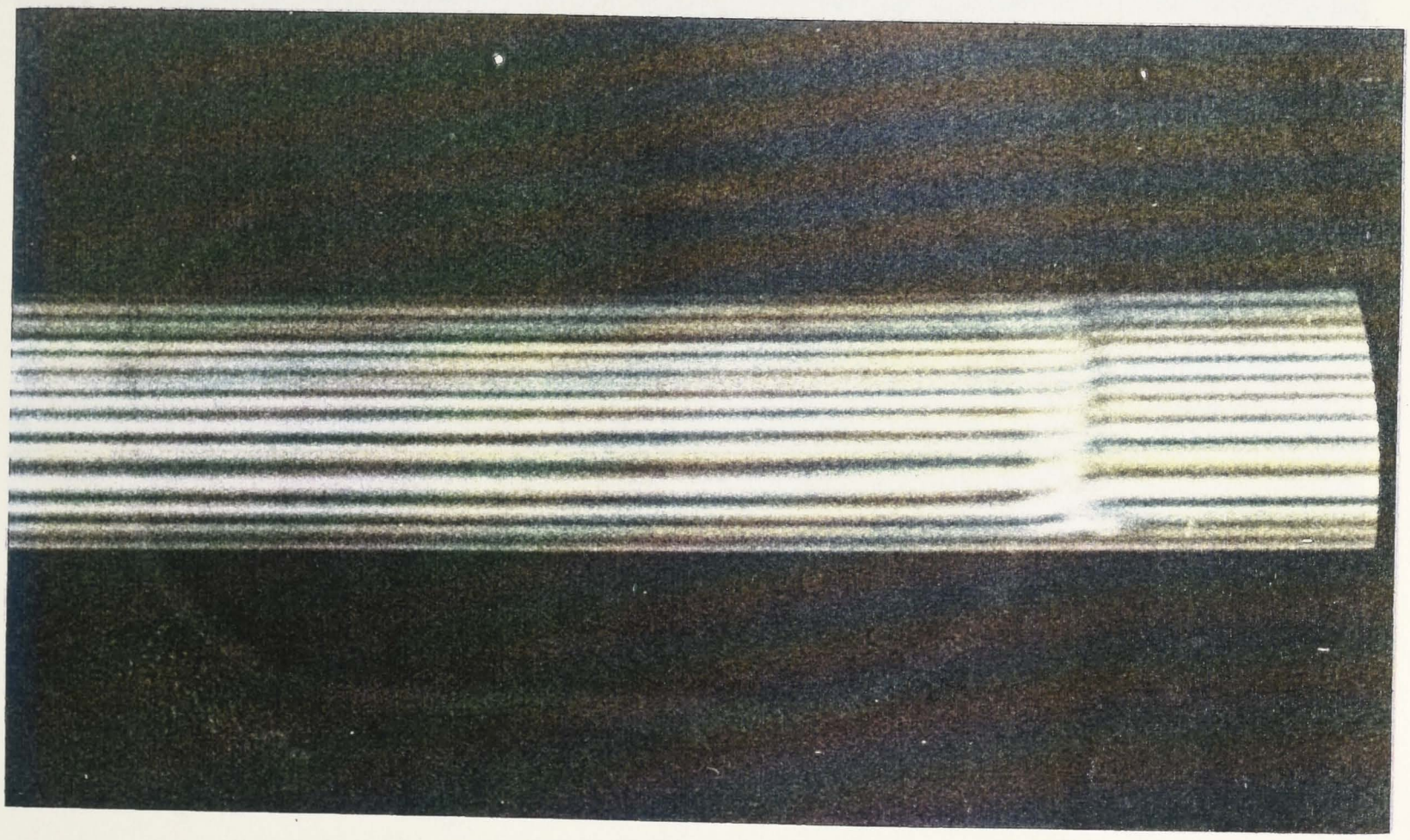

FIGURE 8.8 Shot #361 (test gas of air only)
h.p.r. = 115.2 KPa, s.t. = 9.98 KPa
shock velocity = 506.3 m/s, Mach # = 1.5

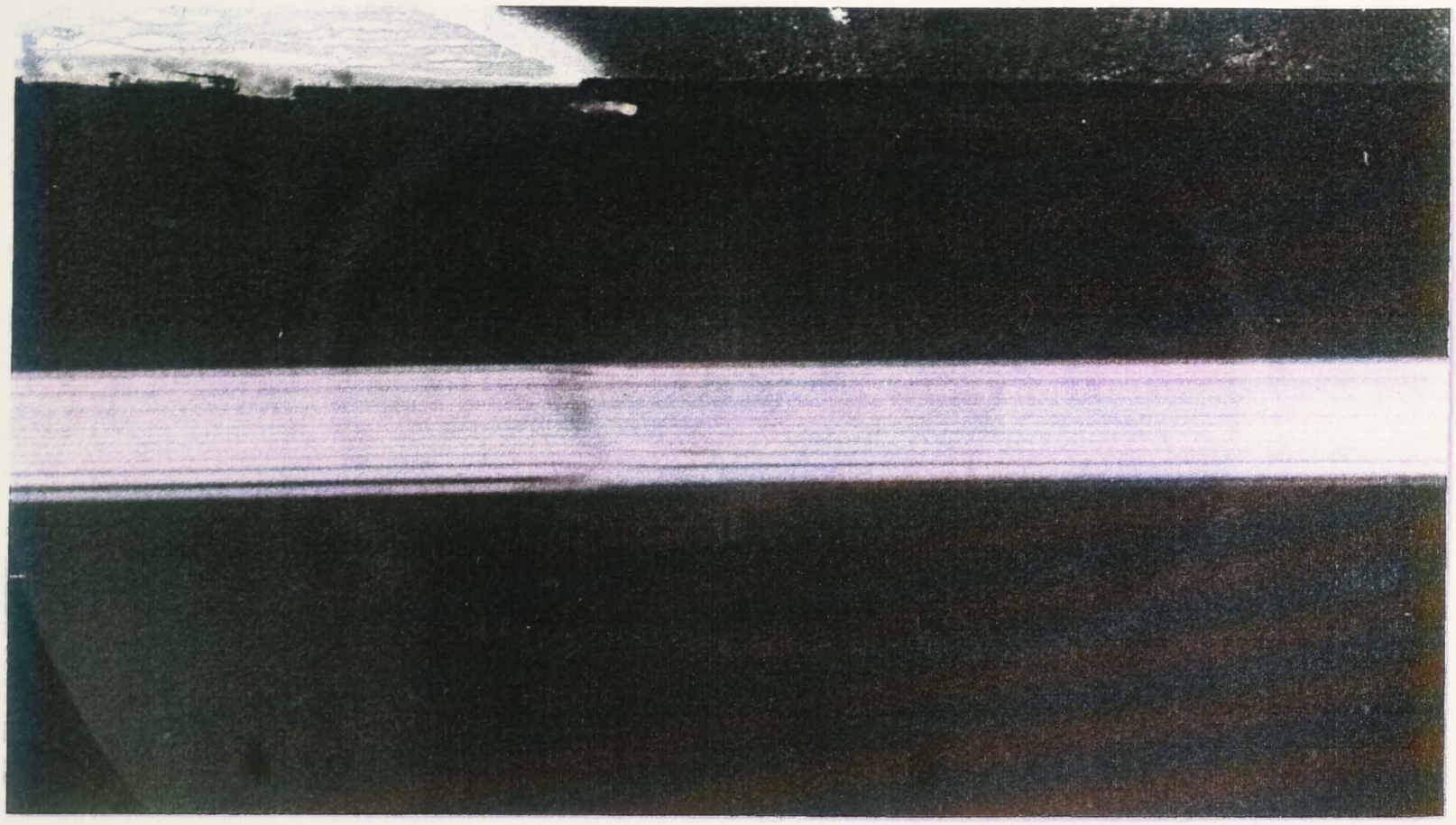

FIGURE 8.9 Shot #356

h.p.r. = 115.2 KPa, s.t. = 9.98 KPa

gas temp. = 49 °C, I_2 vapour press. = 0.35 KPa

shock velocity = 536.4 m/s, Mach # = 1.62

λ = 570.515 nm

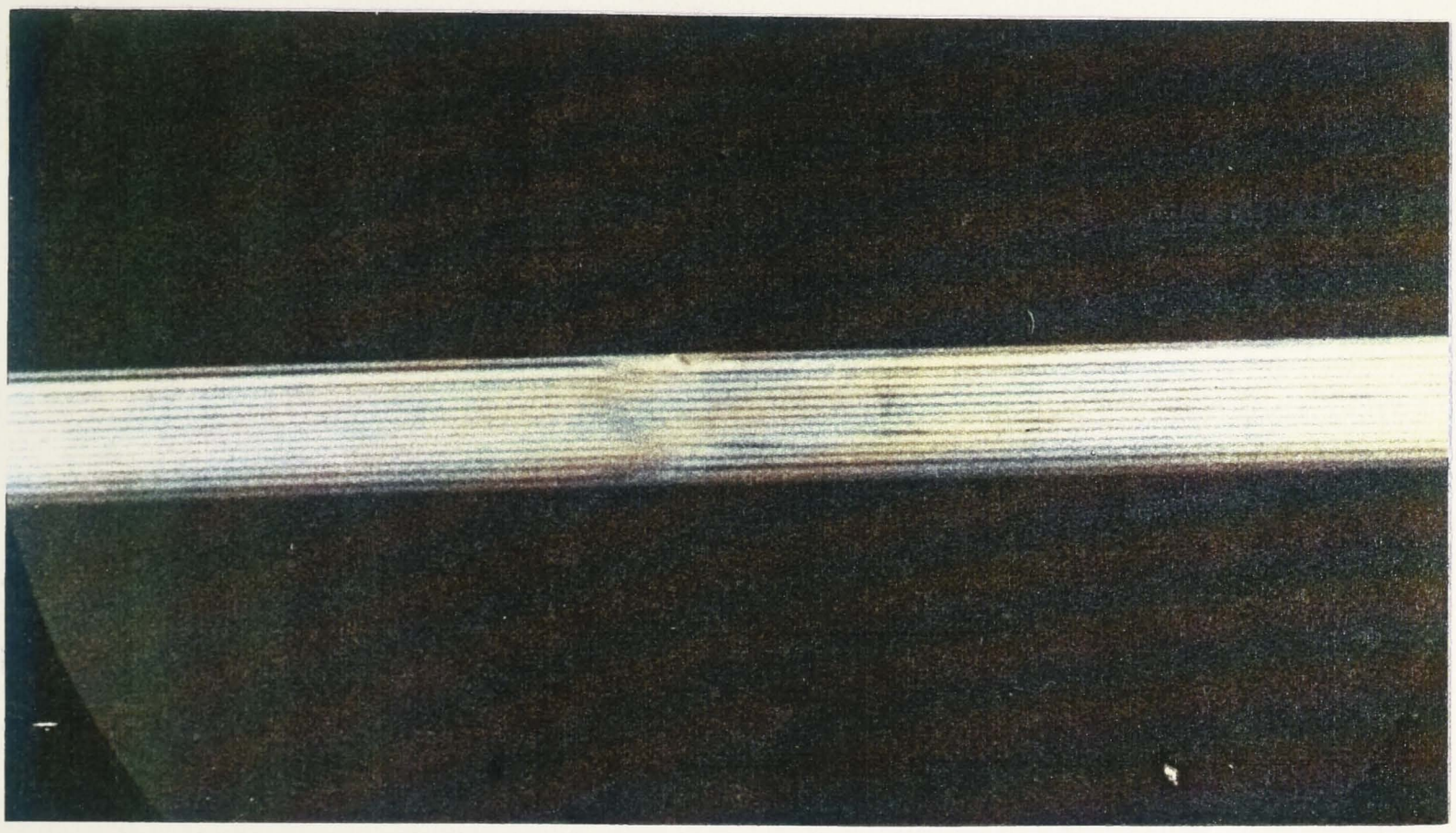

FIGURE 8.10 Shot #357

h.p.r. = 115.2 KPa, s.t. = 9.98 KPa

gas temp. = 47 °C, I_2 vapour press. = 0.31 KPa

shock velocity = 522.6 m/s, Mach # = 1.57

λ = 570.523 nm

corrosion.

It can be seen from the above that a number of possibly conflicting and unexpected processes were occurring in the shock tube during the experiment and this has not aided the primary goal of the experiment, that of the investigation of weak Mach reflection using spectral line interferometry.

9. CONCLUSION

The results of the experimental work presented here have implications for the application of spectral line interferometry to weak Mach reflection using iodine vapour as a test gas impurity.

(1) The percentage of iodine used in the test gas raised the Mach number of the incident shock outside the range generally accepted for weak shock reflection.

(2) The total iodine number density produced by the heating system was too small to allow significant enhancement of the fringe shift across the reflected shock to occur.

(3) The use of iodine in the test gas caused dispersion of the shock due to vibrational relaxation effects.

Shot #364 showed a significantly larger fringe shift across the reflected shock (the shift was 3/4 of a fringe) in comparison to the other shots analysed. The reason for this enhancement was unclear since the computer code that was written for this experiment predicted no detectable fringe shift at the flow conditions used. In the final analysis, it was not possible to determine the wavelength region of maximum fringe shift sensitivity in the iodine spectrum for the tuning of the laser wavelength (i.e. a bandhead or an isolated line), due to equipment failure and time limitations.

The computer code that was developed throughout the time of this experiment provided theoretical values for the wavelength position, absorption and refractivity for the rotational transition lines (of a given vibrational transition) that agreed well with those values observed experimentally. The optical depth and fringe shift sections of the code, used in retrospect after no significant fringe shift effect was observed experimentally, confirmed that no fringe shift enhancement due to spectral line interferometry, was occurring. More programming development could still be done, (i.e. allowing for contributions over the entire vibrational spectrum to the calculation of absorption and refractivity at a particular wavelength rather than just a single vibrational mode as is currently done) however the code in its present state worked satisfactorily for this experiment.

Spectral line interferometry in theory, lends itself readily to the production of

improved interferograms due to the large fringe shifts obtained, however some experimental limitations exist. A spectral line of sufficient oscillator strength must lie in the wavelength region of the recording medium and the population number density of the atoms/molecules involved in the transition must be large. Attention must also be paid to laser beam quality, especially in the region of maximum sensitivity for the method since fringe contrast and sharpness is reduced as the absorption increases.

APPENDIX A

From Pery-Thorne and Banfield (1970), the oscillator strength for a given vibrational band (v',v") can be expressed as

$$f_{v'v"} = \frac{8\pi^2 mc}{3he^2 g"} \sigma_{v'v"} q_{v'v"} R_e^2(r_{v'v"}) \qquad (A1)$$

where g" is the statistical weight of the lower state, $\sigma_{v'v"}$ is the wavenumber of the band origin, $q_{v'v"}$ is the Frank-Condon factor and R_e is the electronic transition moment, a function of the r-centroid $r_{v'v"}$ for the band concerned.

From Measures (1970), the real refractive index n at frequencies close to a spectral line having a dispersive profile is written as

$$n-1 = \frac{2\pi\, Nfe^2}{m} \times \frac{\omega_0^2 - \omega^2}{\left(\omega_0^2 - \omega^2\right)^2 + \omega^2\gamma^2} \cong \frac{Nfr_0\lambda_0^2\omega_0}{4\pi} \times \frac{\omega_0 - \omega}{(\omega_0 - \omega)^2 + \frac{\gamma^2}{4}} \qquad (A2)$$

where N is the number density of the lower level of the transition, f is the oscillator strength, e is the charge of an electron, m is the electronic mass, ω_0 is the line centre angular frequency, γ is the effective line width and r_0 is the classical electron radius given by $r_0 = e^2/mc^2$. If the molecules associated with the transition line of interest are in thermal motion, then it is possible that appreciable doppler broadening will occur and the refractive index close to the transition line will be given by

$$n-1 = \frac{1}{2} \frac{Nfr_0\lambda_0^2 c}{\sqrt{\pi}\beta} \times \int_{-\infty}^{+\infty} \frac{(y-x)e^{-y^2}dy}{(y-x)^2 + a^2} \qquad (A3)$$

where $y = 2\sqrt{\ln 2}\left(\nu_0^* - \nu_0\right)/\delta\nu_D$, $x = 2\sqrt{\ln 2}(\nu - \nu_0)/\delta\nu_D$, $a = \sqrt{\ln 2}\ \delta\nu_L/\delta\nu_D$ $\beta = \pi\delta\nu_D/\sqrt{\ln 2}$, ν_0 is the frequency of the line centre, $\delta\nu_L$ is the FWHM and $\delta\nu_D$ the doppler width.

As a check for our value of the refractivity, calculated theoretically, a calculation of the optical depth $K(\nu)\ell$ was compared to experimental values. (i.e. if the theoretical optical depth equalled the experimental value, it was assumed the theoretical method of calculation was correct and therefore the refractivity calculations were accurate.)

The expression for the optical depth, also from Measures (1970) is given by

$$k\ell = 2\sqrt{\pi}Nf\ell r_0 c\frac{\alpha}{\beta}\times\int_{-\infty}^{+\infty}\frac{e^{-y^2}dy}{(y-x)^2+a^2} \qquad \text{(A4)}$$

where ℓ is the optical length and $\alpha = \sqrt{\ln 2}\delta\nu_L / \pi\delta\nu_D$.

APPENDIX B

For the determination of the number density N of the lower level of the transition, the energy levels of the anharmonic oscillator are considered. The term values are given by

$$G(v) = \omega_e\left(v+\frac{1}{2}\right) - \omega_e x_e\left(v+\frac{1}{2}\right)^2 + \omega_e y_e\left(v+\frac{1}{2}\right)^3 \qquad \text{(B1)}$$

where v is the vibrational quantum number and ω_e, $\omega_e x_e$ and $\omega_e y_e$ are vibrational parameters related to the anharmonicity of the oscillator.

All energy levels are referenced to the lowest level (as zero) and so

$$G_0(v) = G(v) - G(0) = \omega_0 v - \omega_0 x_0 v^2 + \omega_0 y_0 v^3 - .... \qquad \text{(B2)}$$

with $\omega_0 = \omega_e'' - \omega_e x_e'' + \frac{3}{4}\omega_e y_e''$, $\omega_0 x_0 = \omega_e x_e'' - \frac{3}{2}\omega_e y_e''$, $\omega_0 y_0 = \omega_e y_e''$.

For the populations of the vibrational levels, a Maxwell-Boltzmann distribution is assumed and the number of molecules dN_E that have a classical vibrational energy between E and E+dE is proportional to exp(-E/kT) dE, where k is Boltzmann's constant and T is the absolute temperature. Therefore, the quantity $G_0(v)/kT$ gives the relative number density of molecules in the different vibrational levels referenced to the number density of the lowest level. Therefore, the total number density is given by the relative number density divided by the "state sum" or partition function,

$$Q_v = 1 + e^{-G_0(1)hc/kT} + e^{-G_0(2)hc/kT} + ... \qquad \text{(B3)}$$

and

$$N_v = \frac{N_T}{Q_v} e^{-G_0(v)hc/kT} \qquad \text{(B4)}$$

where N_T is the number density of iodine molecules.

There is a degeneracy associated with each rotational level of 2J + 1, where J is the

rotational quantum number. Thus the number of molecules N_J in the rotational level of J of the lowest vibrational state at a temperature T is proportional to

$$(2J+1)e^{-F(J)hc/kT}. \tag{B5}$$

Assuming a rigid rotator, ($\Lambda = 0$),

$$N_J = \frac{N_v}{Q_r}(2J+1)e^{-BJ(J+1)hc/kT} \tag{B6}$$

where B is the internuclear separation for a particular level and Q_r is the rotational state sum,

$$Q_r = 1 + 3e^{-2Bhc/kT} + 5e^{-6Bhc/kT} + ... \tag{B7}$$

similar to that for vibration. An assumption can be made for Q_r for sufficiently large values of T or small values of B:

$$Q_r \approx \int_0^\infty (2J+1)e^{-BJ(J+1)hc/kT} = \frac{kT}{hcB} \tag{B8}$$

Therefore, the expression for the lower rotational number density is

$$N_J = N_v \frac{hcB}{kT}(2J+1)e^{-BJ(J+1)hc/kT} \tag{B9}$$

The above equation is valid for $\Lambda = 0$ (i.e. rigid rotator) and must be altered slightly for an electronic transition. The 2J + 1 term only applies for the rotational transition and must be replaced by a new term given by the Honl-London formula, S_J. (See section 4.4.2). Thus, the correct expression for the number density in a given rotational level of a given vibrational level is

$$N_J = N_v \frac{hcB}{kT} S_J e^{-BJ(J+1)hc/kT} \qquad (B10)$$

REFERENCES

Banwell, C.N. 1972 *Fundamentals of Molecular Spectroscopy* McGraw-Hill

Bargmann, V. and Montegomery, D. 1945 *O.S.R.D.* No. 5011.

Bazhenova, T.V., Gvozdeva, L.G. and Nettleton, M.A. 1984 *Prog. Aerospace Sci.* 21 : 249-331

Ben-Dor, G. and Glass, I.I. 1979 *J. Fluid Mech.* 92 : 459-96

Ben-Dor, G. and Glass, I.I. 1980 *J. Fluid Mech.* 96 : 735-56

Bleakney, W. and Taub, A.H. 1949 *Rev. Mod. Phys.* 21 : 584-605

Bone, D.J., Bachor, H.A. and Sandeman, J 1986 *Appl. Optics* 25 : 1653-1660

Brewer, L. and Tellinghuisen, J. 1971 *J. Chem. Phys.* 56 No. 8 : 3929-3938

Bryson, A.E. and Gross, R.F.W. 1961 *J. Fluid Mech.* 10 : 1-16

Courant, R. and Freiderichs, K.O. 1948 *Supersonic Flow and Shock Waves.* New York : Interscience. 464 pp.

Dewey, J.M. and McMillen, D.J. 1985 *J. Fluid Mech.* 152 : 67-81

Glass, I.I. and Patterson, A.J 1955 *J. Aero. Sci.* 22 No. 2 : 73

Gurderly, K.G. 1947 *Wrigt Field Report* F-TR-2168-ND.

Henderson, L.F. and Gray, P.M. 1981 *Proc. R. Soc. London Ser. A* 377 : 363-78

Henderson, L.F. and Lozzi, A. 1975 *J. Fluid Mech.* 68 : 139-55

Henderson, L.F. and Lozzi, A. 1979 *J. Fluid Mech.* 94 : 541-59

Herzberg, G. 1950 *Spectra of Diatomic Molecules* New York : Von Nostrand Reinhold

Honma, H.,Yoshida, H. and Inomata, K. 1987 *Shock Tube and Waves.* Proceedings 16th Int. Symp. Shock Tube and Waves Aachen pp 581-587

Hornung, H.G. 1986 *Ann. Rev. Fluid Mech.* 18 : 33-58

Hornung, H.G. and Kychakoff, G. 1977 *Shock Tube and Shock Wave Research,* ed. B. Ahlborn, A. Herzberg, D. Russell pp 297-302. Seattle : Univ. Wash. Press

Hornung, H.G., Oertel, H. and Sandeman, R.J. 1979 *J. Fluid Mech.* 90 : 541-60

Hornung, H.G., Robinson, M.L. 1982 *J. Fluid Mech.* 123 : 155-64

Hornung, H.G., Taylor, J.R. 1982 *J. Fluid Mech.* 123 : 143-53

Huber, M.C.E. 1971 *Modern Optical Methods in Gas Dynamics Research* ed. D.S. Dosanjh pp 85-112 New York : Plenum

Huber, M.C.E. and Herzberg, G. 1979 *Constants of Diatomic Molecules.* New York : Von Nostrand Reinhold

Hund, F. 1927 *Z. Phyzik* 42 : 93

Hund, F. 1930 *Z. Phyzik* 63 : 719

Kawamura, R. and Saito, H. 1956 *J. Phys. Soc. Jpn.* 11 : 584-92

Kuhn, H.G. 1969 *Atomic Spectra.* Longmans

Landau, L.D. and Lifshitz, F.M. 1959 *Fluid Mechanics.* Wiley

Law, C.K. and Glass, I.I. 1971 *CASI Trans.* 4 : 2-12

Liepmann, H.W. and Roshko, A. 1957 *Elements of Gas Dynamics.* Wiley

Mach, E. 1878 *Sitzungsber. Akad. Wiss. Wein* 78 : 819-38

Measures, R.M. 1970 *Appl. Optics* 9 : 737-741

Mitchell, A.C.G. and Zemansky, M.S. 1934 *Resonance Radiation and Excited Atoms.* Cambridge Univ. Press

Pery-Thorne, A. and Banfield, 1970 *J. Phys. B : Atom. Molec. Phys.* 3 : 1011-1019

Smith, L.G. 1945 *O.S.R.D. Rep.* No. 6271, Off. Sci. Res. Dev. Washington, D.C.

Smith, W.R. 1959 *Phys. Fluids* 2 : 533-41

Sternberg, J. 1959 *Phys. Fluids* 2 : 179

Takayama, K.,Gotoh, J.and Ben-Dor, G. 1981 *Shock Tubes and Waves,* ed. C.F. Treanor, J.G. Hall, pp 326-334 Albany: State Univ. N. Y. Press

Tellinghuisen, J. 1978 *J. Quant. Radiat. Transfer* 19 : 149-161

Thorne, A.P. 1974 *Spectraphysics* 1st ed. Chapman and Hall

Thorne, A.P. 1989 *Spectraphysics* 2nd ed. Chapman and Hall

von Neumann, J. 1943 *See Collected Works,* 6 : 238-99. Pergamon (1963)

Walker, 1981

White, D.R. 1951 *Princeton Univ. Dept. Phys. Tech. Rep.* II-10,
Princeton, N.J.